Nanoporous Anodic Aluminum Oxide/Silicon – Polyester Hybrid Systems for the Detection of Bacterial Enzymes

DISSERTATION
zur Erlangung des Grades eines Doktors der Naturwissenschaften

vorgelegt von
M.Sc. Qasim Alhusaini

eingereicht bei der Naturwissenschaftlich-Technischen Fakultät
der Universität Siegen
Siegen 2024

Betreuer und erster Gutachter

Prof. Dr. Holger Schönherr

Universität Siegen

Zweiter Gutachter

Prof. Dr. Ulrich Jonas

Universität Siegen

Tag der mündlichen Prüfung

05.03.2025

Table of Contents

Zusammenfassung

Die Entwicklung gezielter Diagnostik- und Therapieansätze zur Behandlung bakterieller Infektionen steht weltweit im Fokus der Forschung, motiviert durch die zunehmende Ausbreitung antibiotikaresistenter Bakterien. Einer der vielversprechenden diagnostischen Ansätze basiert auf der Verwendung Stimuli-responsiver Materialien, sogenannten "intelligenten Materialien". In dieser Dissertation wurde ein Stimuli-responsives biologisch abbaubares Polymer zusammen mit anodisiertem Aluminiumoxid (AAO) und porösen Silizium Rugate Filtern (pSiRF) zur optischen Detektion von Pilz- und Bakterienenzymen verwendet.

Zunächst wurden AAO-Nanostrukturen durch verfeinerte Anodisierungsprozesse hergestellt. Die Anodisierungsparameter wurden angepasst, um die Struktur des AAO an die Anforderungen der Sensorik anzupassen. Die hergestellten AAO-Nanomaterialien mit gut geordneten hexagonalen Porenstrukturen wurden weiter mit Phosphorsäure nasschemisch behandelt, um die Porendurchmesser zu vergrößern. Der Durchmesser und die Länge der Poren wurden mittels Feldemissionsrasterelektronenmikroskopie (FESEM) analysiert. Die Daten zeigen, dass die Porosität linear mit der Einwirkzeit der Phosphorsäure zunahm. Die Abhängigkeit der Porenlänge von der Anodisierungszeit war ebenfalls linear. Die Herstellung von porösen Silizium (pSi) Nanostrukturen wurde ebenfalls im Detail untersucht. Der Herstellungsprozess wurde optimiert, um die gewünschten photonischen Strukturen zu erhalten, die die Anforderungen für die Erkennung des Sensorsignals mit bloßem Auge erfüllen. Die elektrochemische Ätzung von pSi wurde in HF/Ethanol-Gemischen durchgeführt und ergab Nanoporen mit Porendurchmessern und Porenlängen, die sich jeweils linear mit den Stromdichten und der Ätzzeit erhöhten. Das optimale Regime für die elektrochemische Ätzung in Flusssäure/Ethanol (1:2 v/v) zur Synthese von pSiRF-Sensoren mit einem hohen Qualitätsfaktor war eine Periodenzeit von 7 Sekunden für 100 Zyklen bei minimalen und maximalen Stromdichten von 15 und 50 mA cm^{-2}. Spin-Coating und Beschichtung aus Lösung wurden verwendet, um die AAO-, planaren Si- und pSiRF-Sensoren mit dem biologisch abbaubaren Polymer Poly(lactid) (PLA) zu modifizieren. Die Modifikation der Sensoren wurde mittels FESEM, energiedispersiver Röntgenspektroskopie (EDX), thermogravimetrischer Analyse (TGA), Ellipsometrie, Kontaktwinkelmessung und reflektometrischer Interferenz-Spektroskopie (RIfS) untersucht.

Die enzymatische Zersetzung von PLA in den Sensoren wurde durch das Pilzenzym Proteinase K und von *Pseudomonas aeruginosa* (PAO1) (*P. aeruginosa* (PAO1)) sezernierte Proteasen katalysiert. Der Wasserkontaktwinkel wies auf eine Veränderung der Benetzbarkeit nach der enzymatischen Behandlung hin, was mit einer Reduktion der Carbonyl-Banden in den Fourier-Transformations-Infrarotspektren (FTIR) übereinstimmt. Die Rauigkeitsdaten der Rasterkraftmikroskopie (AFM) und die RIFs Daten bestätigten ebenfalls den Abbau der PLA-Filme bzw. des PLA in den Nanoporen. Die optischen RIfS Daten zeigten eine Blauverschiebung der Werte der effektiven optischen Dicke (*EOT*) und der Wellenlänge nach der Behandlung mit Proteinase K. Schließlich wurden die AAO- und pSiRF-Sensoren in Kulturen des Bakteriums *P. aeruginosa* (PAO1) und den entsprechenden sterilen Kulturüberständen getestet. Das Ergebnis zeigte, dass die enzymatische Reaktion von PLA im Vergleich zur freien Enzymlösung nachweisbar war. Interessanterweise gab es bemerkenswerte Farbverschiebungen im pSiRF-Sensor, die von grün zu blau übergingen, nachdem der Sensor reiner Proteinase K Lösung oder *P. aeruginosa* (PAO1)-Kulturen ausgesetzt wurde. Diese Farbänderung konnte mit bloßem Auge nach der Behandlung des Sensors mit dem Enzym, dem Waschen und Trocknen erkannt werden, was darauf hindeutet, dass dieses Prinzip zukünftig verbessert und potenziell genutzt werden könnte, um bakterielle Enzyme klinisch relevanter bakterieller Krankheitserreger visuell und schnell zu erkennen.

Abstract

The development of targeted diagnostics and therapy approaches aiming at treating bacterial infections are in the focus of research worldwide, driven by the increasing impact of antibiotic-resistant bacteria. One of the diagnostic approaches is based on stimuli-responsive materials, so-called "smart materials". In this Thesis, a stimuli-responsive biodegradable polymer was combined with anodic aluminum oxide (AAO) and porous silicon rugate filters (pSiRF) for the optical detection of fungal and bacterial enzymes.

Firstly, AAO nanostructures were produced via refined anodization processes. The anodization parameters were adjusted to tailor the structure of the AAO to the sensing requirements. The fabricated AAO nanomaterials with well-ordered hexagonal pore structures were further treated with phosphoric acid to widen the pores. The pore diameter, length, and porosity were evaluated by field emission scanning electron microscopy (FESEM). The data showed that the porosity increased linearly with widening time. The dependence of the pore length on the anodization time was also studied, showing also a linear tendency. The fabrication of porous silicon (pSi) nanostructures was also studied in detail. The fabrication process was optimized to obtain the desired structures that fulfill the sensing requirements for bare eye detection. The electrochemical etching of pSi was carried out in HF/ethanol mixtures and afforded nanopores with pore diameters and pore lengths that increased linearly with the current densities and the etching time, respectively. The optimal regime for electrochemical etching to synthesize pSiRF sensors with a high-quality factor was a 7 sec period time for 100 cycles at minimum and maximum current densities of 15 and 50 mA cm^{-2}, respectively, in hydrofluoric acid/ethanol (1:2 v/v). Spin coating and solvent casting methods were then utilized to modify the AAO, planar Si, and pSiRF sensors with the biodegradable polymer poly(lactic acid) (PLA). The modification of those sensors was investigated using FESEM, energy-dispersive X-ray spectroscopy (EDX), thermogravimetric analysis (TGA), ellipsometry, contact angle, and reflectometric interference spectroscopy (RIfS) techniques.

The enzymatic degradation of PLA in these sensors, catalyzed by proteinase K, a fungal enzyme, and proteases secreted by the pathogen *Pseudomonas aeruginosa* (PAO1) (*P. aeruginosa*) (PAO1), was studied. The water contact angle showed a change in the wettability after the enzymatic reaction, which is consistent with a reduction in the calculated carbonyl band observed in Fourier transform infrared (FTIR) spectra. Atomic force microscopy (AFM) roughness data also confirmed the PLA film degradation. RIfS emphasized the occurrence of the degradation of PLA-modified pores of AAO and pSiRF. The data showed a decrease in effective optical thickness (*EOT)* and a blue-shift in wavelength after treatment with proteinase K. Finally, the AAO and pSiRF sensors were tested in the *P. aeruginosa* (PAO1) cultures and their corresponding sterile-filtered culture supernatants. The results revealed that the enzymatic reaction of PLA was detectable compared to the free enzyme solution (LB medium). Interestingly, there were noticeable color shifts in the pSiRF sensor, transitioning from green to blue, when exposed to pure proteinase K solution or *P. aeruginosa* (PAO1) cultures. This color change could be detected by the bare eye after treating the sensor with the enzyme, washing, and drying, suggesting that this principle may be improved and potentially utilized to sense bacterial enzymes of clinically relevant bacterial pathogens visually and rapidly.

List of Abbreviations and Acronyms

AAO	anodic aluminum oxide
AFM	atomic force microscopy
APTES	(3-aminopropyl)triethoxysilane
ATR	attenuated total reflectance
a.u.	arbitrary units
aq	aqueous (solution)
ATR	attenuated total reflection
CA	contact angle
cDNA	complementary deoxyribonucleic acid
°C	degree celsius
CFU	colony forming unit
CVD	chemical vapor phase deposition
Da	Dalton
D_i	interpore distance
DCM	dichloromethane
DMSO	dimethylsulfoxide
DNA	deoxyribonucleic acid
D	pore diameter
dsDNA	double-stranded deoxyribonucleic acid
$\mathrm{d}W/\mathrm{d}T$	mass derivative
E. coli	*Escherichia coli*
EDX	energy-dispersive X-ray spectroscopy
eff	effective
EOT	effective optical thickness
FESEM	field emission scanning electron microscope
FDTS	1H,1H,2H,2H-Perfluorododcyltrichlorosilane
FFT	fast Fourier transformation
FTIR	Fourier-transform infrared
FWHM	full width at half maximum
h	hour

HA	hard anodization
IUPAC	international union of pure and applied chemistry
L	length
LB	Luria–Bertani medium
LOD	limit of detection
kPa	kilopascal
MA	mild anodization
m	mass
mA	milliampere
mg	milligram
min	minute
mL	milliliter
msec	millisecond
Mw	weight average molar mass
OD	optical density
P	porosity
P. aeruginosa	*Pseudomonas aeruginosa*
PBS	phosphate buffer saline
PCR	polymerase chain reaction
pM	picomolar
PLA	poly(lactic acid)
PMMA	poly(methyl methacrylate)
PS	polystyrene
pSi	porous silicon
pSiRF	porous silicon rugate filter
PoC	point of care
PVA	poly(vinyl alcohol)
PVC	poly(vinyl chloride)
λ	wavelength
RIfS	reflectometric interference spectroscopy
SAM	self-assembled monolayer

S. aureus	*Staphyloccocus aureus*
sec	second
SD	standard deviation
SEM	scanning electron microscopy
SLIM	spectroscopic liquid infiltration method
Si	silicon
ssDNA	single-stranded deoxyribonucleic acid
t	time
TGA	thermogravimetric analysis
TRIS	tris-(hydroxymethyl)-aminomethane
UV	ultraviolet
V	volt
Vis	visible
v%	volume percent
wt%	weight percent

Chapter 1. Introduction and Motivation

In recent decades, nanoporous materials have received significant attention due to their applications, which include molecular separation[1], drug delivery[2], energy storage[3], chemical sensing[4], and biosensing[5]. Due to their larger specific surface area, it is possible to load more bio-recognition elements onto porous substrates than planar substrates, and hence, high sensitivity can be achieved[6]. Notable examples of nanoporous substrates include anodic aluminum oxide (AAO) and porous silicon (pSi). They can be fabricated via anodization/electrochemical processes with adjustable pore diameters, ranging from sub-nanometers to hundreds of nanometers and hundreds of micrometers in length[7,8,9]. Furthermore, the porosity of those substrates can also be adjusted. For instance, pSi can be fabricated with 40 to 80 % porosity[10]. In contrast, for AAO, a porosity of 10 % could be achieved under mild anodization (MA) conditions and reached up to 40 % by post-chemical treatment[11,12]. It is worth noting that pSi usually has irregular pore shapes and is in less order compared to AAO, which has circular, hexagonal shape and well-ordered pores[10,11].

AAO is utilized in many applications, such as drug delivery[13], templating-based material[14], bone implants[15], and sensing[16]. pSi is mainly applied to drug delivery[17] and sensing[18]. AAO and pSi are particularly promising materials for sensing because of their biocompatibility[19,20,21] tunable nanoporous structure[22,23] and optical properties[24,25].

Several studies have been conducted in which AAO and pSi were utilized as transducer surfaces to design label-free sensors[26,27]. Bacterial detection is highly desirable in many fields due to the increasing occurrence of bacteria that are resistant to antibiotics[28]. Therefore, several methods have been developed to detect bacteria directly and indirectly, particularly by employing nanoporous materials[29]. This Thesis focuses on the fabrication and functionalization of porous nanostructures with biodegradable polymers to assess their potential as transducers for detecting enzymes and bacterial enzymes.

Firstly, the anodization of aluminum (Al) was investigated to achieve the optimized anodization conditions to fabricate AAO with regular circular pores with desirable pore diameters, as described in Chapter 4. Subsequently, it is well-known that the surface wettability of the AAO surface has an impact on the coating of the pores with a polymeric material or on the penetration of the biological media into the pores; thus, the systematic investigation of the wetting of AAO using opened and closed pores is discussed at the end of Chapter 4.

In Chapter 5, the AAO sensor and planner Si were coated with poly(lactic acid) (PLA) to design a composite system to detect a bacterial enzyme. The fungal enzyme proteinase K was used as a model enzyme for proteases secreted by bacteria. The PLA modification on the top surface of AAO (covering the pore gate) and on planar Si was intensively investigated. Additionally, the enzymatic degradation of PLA film on those substrates was monitored using numerous techniques.

In Chapter 6, the response of polymer-modified AAO for sensing enzymes was optimized by filling the pores of AAO with PLA and removing the PLA film from the top side of the AAO surface before performing the enzymatic degradation. Furthermore, the modification process of PLA inside the pores was investigated using reflectometric interference spectroscopy (RIfS). The degradation of PLA by proteinase K was also studied. Furthermore, the AAO sensor was tested in the sterile *Pseudomonas aeruginosa* (PAO1) (*P. aeruginosa* (PAO1)) supernatant.

In Chapter 7, the fabrication pSi and porous silicon rugate filter (pSiRF) were fabricated via electrochemical etching. The etching process was optimized by applying the optimal etching parameters, which were experimentally investigated to obtain the desired pSiRF structures. Then, PLA was loaded into the pores of pSiRF using the casting method. The energy-dispersive X-ray spectroscopy (EDX), RIfS, and thermogravimetric analysis (TGA) techniques were conducted to investigate the loaded PLA inside the pores.

Finally, Chapter 8 discussed the bacterial detection approach using the pSiRF sensors loaded with PLA. The pSiRF sensors were utilized as optical transducers to detect enzymes, including proteinase K, and those secreted by *P. aeruginosa*. The enzymatic degradation of PLA by proteinase K and both supernatant and suspension of *P. aeruginosa* was investigated. Additionally, the potential use of this approach for visual detection was investigated.

References

---

[1] Song, Y.; Bao, H.; Shen, X.; Li, X.; Liang, X.; Wang, S. Emerging Nanoporous Materials for Biomolecule Separation. *Advanced Functional Materials* **2022**, *32* (20). https://doi.org/10.1002/adfm.202113153.

[2] Gulati, K.; Ramakrishnan, S.; Aw, M. S.; Atkins, G. J.; Findlay, D. M.; Losic, D. Biocompatible Polymer Coating of Titania Nanotube Arrays for Improved Drug Elution and Osteoblast Adhesion. *Acta Biomaterialia* **2012**, *8* (1), 449–456. https://doi.org/10.1016/j.actbio.2011.09.004.

[3] Wei, Q.; Fu, Y.; Zhang, G.; Yang, D.; Meng, G.; Sun, S. Rational Design of Novel Nanostructured Arrays Based on Porous AAO Templates for Electrochemical Energy Storage and Conversion. *Nano Energy* **2018**, *55*, 234–259. https:// doi.org/10.1016/j.nanoen.2018.10.070.

[4] Kumeria, T.; Rahman, M. M.; Santos, A.; Ferré-Borrull, J.; Marsal, L. F.; Losic, D. Nanoporous Anodic Alumina Rugate Filters for Sensing of Ionic Mercury: Toward Environmental Point-of-Analysis Systems. *ACS Applied Materials & Interfaces* **2014**, *6* (15), 12971–12978. https://doi.org/10.1021/am502882d.

[5] Pla, L.; Santiago-Felipe, S.; Tormo-Mas, M. Á.; Ruiz-Gaitán, A.; Pemán, J.; Valentín, E.; Sancenón, F.; Aznar, E.; Martínez-Máñez, R. Oligonucleotide-Capped Nanoporous Anodic Alumina Biosensor as Diagnostic Tool for Rapid and Accurate Detection of Candida Auris in Clinical Samples. *Emerging Microbes & Infections* **2021**, *10* (1), 407–415. https://doi.org/10.1080/22221751.2020.1870411.

[6] Jane, A.; Dronov, R.; Hodges, A.; Voelcker, N. H. Porous Silicon Biosensors on the Advance. *Trends in Biotechnology* **2009**, *27* (4), 230–239. https://doi.org/ 10.1016/j.tibtech.2008.12.004.

[7] Asoh, H.; Nishio, K.; Nakao, M.; Yokoo, A.; Tamamura, T.; Masuda, H. Fabrication of Ideally Ordered Anodic Porous Alumina with 63 nm Hole Periodicity using Sulfuric Acid. *Journal of Vacuum Science & Technology B Microelectronics and Nanometer Structures Processing Measurement and Phenomena* **2001**, *19* (2), 569–572. https://doi.org/10.1116/1.1347039.

[8] Li, C.; He, L.; Jiang, S.; Mo, R.; Yan, X.; Qian, Z.-J.; Zhou, C.; Sun, S.; Hong, P.; Huang, Y. Ultrasensitive Detection of MicroRNA Using an Array of Au Nanowires Deposited within the Channels of a Porous Anodized Alumina Membrane. *Electrochemistry Communications* **2019**, *102*, 19–24. https://doi.org/10.1016/j.elecom.2019.03.008.

[9] Steinhart, M.; Murano, S.; Schaper, A. K.; Ogawa, T.; Tsuji, M.; Gösele, U.; Weder, C.; Wendorff, J. H. Morphology of Polymer/Liquid-Crystal Nanotubes: Influence of Confinement. *Advanced Functional Materials* **2005**, *15* (10), 1656–1664. https://doi.org/10.1002/adfm.200500139.

[10] Anglin, E.; Cheng, L.; Freeman, W.; Sailor, M. Porous Silicon in Drug Delivery Devices and Materials. *Advanced Drug Delivery Reviews* **2008**, *60* (11), 1266–1277. https://doi.org/10.1016/ j.addr.2008.03.017.

---

[11] Nielsch, K.; Choi, J.; Schwirn, K.; Wehrspohn, R. B.; Gösele, U. Self-ordering Regimes of Porous Alumina: The 10 Porosity Rule. *Nano Letters* **2002**, *2* (7), 677–680. https://doi.org/10.1021/ nl025537k.

[12] Lee, W.; Ji, R.; Gösele, U.; Nielsch, K. Fast Fabrication of Long-range Ordered Porous Alumina Membranes by Hard Anodization. *Nature Materials* **2006**, *5* (9), 741–747. https://doi.org/10.1038/nmat1717.

[13] Jeon, G.; Yang, S. Y.; Byun, J.; Kim, J. K. Electrically Actuatable Smart Nanoporous Membrane for Pulsatile Drug Release. *Nano Letters* **2011**, *11* (3), 1284–1288. https://doi.org/10.1021/nl104329y.

[14] Schulte, A.; Alhusaini, Q. F. M.; Schönherr, H. Anodic Aluminum Oxide Nanopore Template-Assisted Fabrication of Nanostructured Poly(vinyl alcohol) Hydrogels for Cell Studies. *ACS Applied Bio Materials* **2020**, *3* (4), 2419–2427. https://doi.org/10.1021/acsabm.0c00153.

[15] Walpole, A. R.; Briggs, E. P.; Karlsson, M.; Pålsgård, E.; Wilshaw, P. R. Nano-porous Alumina Coatings for Improved Bone Implant Interfaces. *Materialwissenschaft Und Werkstofftechnik* **2003**, *34* (12), 1064–1068. https://doi.org/10.1002/mawe.200300707.

[16] Santos, A.; Kumeria, T.; Losic, D. Nanoporous Anodic Aluminum Oxide for Chemical Sensing and Biosensors. *TrAC Trends in Analytical Chemistry* **2013**, *44*, 25–38. https://doi.org/ 10.1016/j.trac.2012.11.007.

[17] Vasani, R. B.; McInnes, S. J. P.; Cole, M. A.; Jani, A. M. M.; Ellis, A. V.; Voelcker, N. H. Stimulus-Responsiveness and Drug Release from Porous Silicon Films ATRP-Grafted with Poly(N-isopropylacrylamide). *Langmuir* **2011**, *27* (12), 7843–7853. https://doi.org/10.1021/la200551g.

[18] Kilian, K. A.; Lai, L. M. H.; Magenau, A.; Cartland, S.; Böcking, T.; Di Girolamo, N.; Gal, M.; Gaus, K.; Gooding, J. J. Smart Tissue Culture: in Situ Monitoring of the Activity of Protease Enzymes Secreted from Live Cells Using Nanostructured Photonic Crystals. *Nano Letters* **2009**, *9* (5), 2021–2025. https://doi.org/10.1021/nl900283j.

[19]. Low, S. P.; Voelcker, N. H.; Canham, L. T.; Williams, K. A. The Biocompatibility of Porous Silicon in Tissues of the Eye. *Biomaterials* **2009,** *30* (15), 2873–2880. https://doi.org/10.1016/j.biomaterials.2009.02.008.

[20]. Secret, E.; Smith, K.; Dubljevic, V.; Moore, E.; Macardle, P.; Delalat, B.; Rogers, M.-L.; Johns, T. G.; Durand, J.-O.; Cunin, F.; Voelcker, N. H. Antibody-Functionalized Porous Silicon Nanoparticles for Vectorization of Hydrophobic Drugs. *Advanced Healthcare Materials* **2013,** *2* (5), 718–727. https://doi.org/10.1002/adhm.201200335.

[21] Xifre-Perez, E.; Ferre-Borrull, J.; Marsal, L. F. Oligonucleotic Probes and Immunosensors Based on Nanoporous Anodic Alumina for Screening of Diseases. *Advanced Materials Technologies* **2022**, *7* (9). https://doi.org/10.1002/admt.202101591.

[22]. Janshoff, A.; Dancil, K.-P. S.; Steinem, C.; Greiner, D. P.; Lin, V. S.-Y.; Gurtner, C.; Motesharei, K.; Sailor, M. J.; Ghadiri, M. R. Macroporous p-Type Silicon Fabry–Perot Layers.

Fabrication, Characterization, and Applications in Biosensing. *Journal of the American Chemical Society.* **1998,** *120* (46), 12108–12116. https://doi.org/10.1021/ja9826237.

[23]. Santos, A.; Vojkuvka, L.; Alba, M.; Balderrama, V. S.; Ferré-Borrull, J.; Pallarès, J.; Marsal, L. F. Understanding and Morphology Control of Pore Modulations in Nanoporous Anodic Alumina by Discontinuous Anodization. *physica status solidi (a)* **2012**, *209* (10), 2045–2048. https://doi.org/10.1002/pssa.201228150.

[24]. Rendina, I.; Rea, I.; Rotiroti, L.; Stefano, L. de. Porous Silicon-Based Optical Biosensors and Biochips. *Physica E: Low-dimensional Systems and Nanostructures* **2007,** *38* (1-2), 188–192. https://doi.org/10.1016/j.physe.2006.12.050.

[25]. Rajeev, G.; Xifre-Perez, E.; Prieto Simon, B.; Cowin, A. J.; Marsal, L. F.; Voelcker, N. H. A Label-Free Optical Biosensor Based on Nanoporous Anodic Alumina for Tumour Necrosis Factor-Alpha Detection in Chronic Wounds. *Sensors and Actuators B: Chemical* **2018**, *257*, 116–123. https://doi.org/10.1016/j.snb.2017.10.156.

[26]. Szili, E. J.; Jane, A.; Low, S. P.; Sweetman, M.; Macardle, P.; Kumar, S.; St. Smart, R. C.; Voelcker, N. H. Interferometric Porous Silicon Transducers Using an Enzymatically Amplified Optical Signal. *Sensors and Actuators B: Chemical* **2011,** *160* (1), 341–348. https://doi.org/10.1016/j.snb.2011.07.059.

[27]. Rai, V.; Deng, J.; Toh, C.-S. Electrochemical Nanoporous Alumina Membrane-Based Label-Free DNA Biosensor for the Detection of Legionella Sp. *Talanta* **2012**, *98*, 112–117. https://doi.org/10.1016/j.talanta.2012.06.055.

[28] MacFadden, D. R.; McGough, S. F.; Fisman, D.; Santillana, M.; Brownstein, J. S. Antibiotic Resistance Increases with Local Temperature. *Nature Climate Change* **2018**, *8* (6), 510–514. https://doi.org/10.1038/s41558-018-0161-6.

[29] Li, S.; Huang, J.; Cai, L. A Porous Silicon Optical Microcavity for Sensitive Bacteria Detection. *Nanotechnology* **2011**, *22* (42), 425502. https://doi.org/10.1088/0957-4484/22/42/425502.

Chapter 2. State of Knowledge

2.1 Introduction

With the increasing occurrence of bacteria that are resistant to antibiotics, particularly multiply resistant bacteria[1], new methods of targeted diagnostics and therapies are the focus of research activities worldwide. This Thesis focuses on fabricating and functionalizing porous nanostructures with biodegradable polymers for bacterial enzymes and, thus, indirect bacteria detection. This Chapter first discusses the underlying principles of bacteria detection using conventional and advanced techniques. Then, the fabrication, characterization, and modification of anodic aluminum oxide (AAO) and porous silicon (pSi)/photonic structures will be described. The enzymatic degradation of biodegradable polymers will also be highlighted. Finally, the white light interferometric technique will be introduced to investigate the sensing of enzymes.

2.2 Methods for Detection and Identification of Enzymes and Bacteria

Accurate detection of bacterial cells in various sample types, including food, water, and blood, is essential[2]. Consequently, numerous effective methods have been developed to fulfill this requirement, primarily for laboratory use. These methods are now widely recognized as the standard for identifying bacteria and are commonly used in laboratories worldwide[3]. The widely used techniques include culture and colony counting[4,5], polymerase chain reaction (PCR)[6,7] and enzyme-linked immunosorbent assay (ELISA)[8].

The culture and colony counting method involves adding bacteria to agar media. After incubation, bacterial growth can be quantified by counting the colonies formed on the agar surface. Although this method is the oldest for detecting bacteria, it is time-consuming because colonies require at least several hours for bacteria to become observable[9].

The PCR technique relies on isolating, amplifying, and quantifying a short chain of DNA of the targeted bacteria[10]. After the isolation and purification of DNA, the denaturation step takes place by applying heat to the extracted and purified DNA. As a result, a single-strand DNA will be formed. This single-strand DNA will then bind to a target-specific primer, resulting in double-strand DNA, which undergoes an extension. This cycle continues until an amplified double-strand DNA is obtained. Finally, the gel electrophoresis technique is utilized to detect this amplified double-strand DNA of the targeted bacteria. The PCR technique may provide misleading information because, for instance, the DNA will be found both in alive and dead cells, making it difficult to determine whether the cells are alive or dead[11]. Additionally, the method requires highly trained personnel and might be costly to operate[12]. Due to its high selectivity, the ELISA method is an effective method to detect various pathogens, such as bacteria[13] and viruses[14]. It relies on specific antibody-antigen interactions[15]. However, ELISA also has disadvantages; for instance, it is a time consuming, complicated, and costly method[16] and antigen cross-reactions might occur[17,18]. Furthermore, it cannot detect bacteria or viruses in real-time and is also susceptible to interference[19]. Therefore, rapid, direct, low-cost, and reliable methods are necessary for detecting pathogens, especially bacteria. Thus, scientists have explored, studied and examined biosensors and sensors as platforms for the detection of bacteria (Figure 2.1)[20,21].

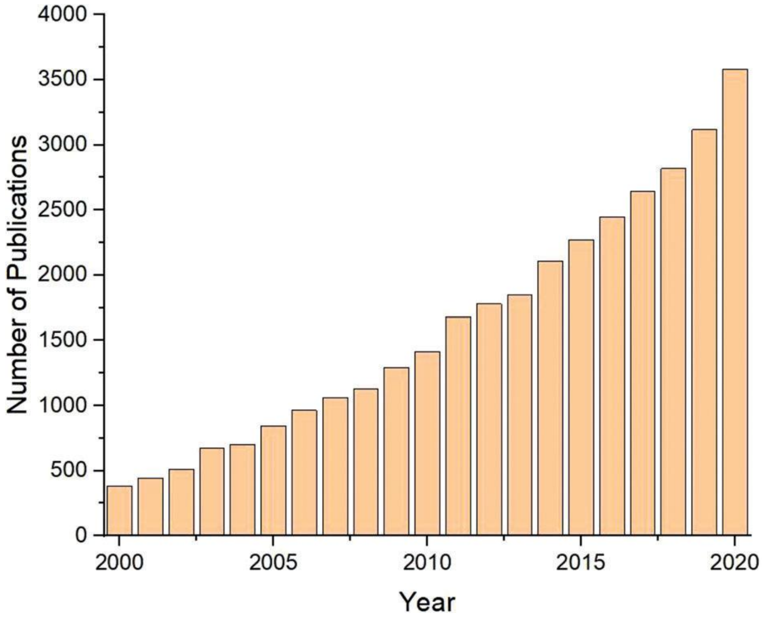

Figure 2.1: *Statistics of publications on biosensors for bacterial detection. This Figure was reproduced with permission from reference [20]: Gopal, A.; Yan, L.; Kashif, S.; Munshi, T.; Roy, V. A. L.; Voelcker, N. H.; Chen, X. Biosensors and Point-of-Care Devices for Bacterial Detection: Rapid Diagnostics Informing Antibiotic Therapy. Advanced Healthcare Materials* ***2021****, 11 (3). Copyright 2021. John Wiley & Sons, Inc.*

Biosensors or sensors offer real-time or rapid detection strategies, and additionally, they exhibit remarkable versatility due to their ability to use different chemical, physical, and biological tools to detect and identify the presence of particular bacteria or biomarkers[22].

Biosensors/sensors can be used as a label-free sensing strategy, which is preferable to reduce the detection time as well as reduce undesired interferences[23]. However, these can be highly selective and sensitive detection approaches, if they are integrated with particular sensing techniques.

In recent years, porous nanoporous structured materials, including AAO[24], pSi[25], porous metal oxides[26], porous organo-silica[27], and porous polymers[28] have emerged as novel platforms for developing biosensors and sensors[29,30,31] due to their high specific surface to volume ratio, which enhances the sensor's sensitivity by increasing the number of immobilized receptors and available binding sites. Utilizing porous nanomaterials as sensor platforms enhances sensitivity and offers high selectivity, making them a good choice for identifying and quantifying analytes in complex samples. AAO and pSi are among the most utilized porous materials in sensing applications due to their chemical, optical, mechanical, electrical, biocompatible properties and controllable structures[32,33,34].

AAO is fabricated by electrochemical anodization of a pure Al substrate in acidic electrolytes[35]. Its well-defined structure has pores produced perpendicular to the Al substrate in a honeycomb shape[36]. The surface chemistry of AAO allows different functional groups to be bonded to the surface, permitting the binding of different analytes to be used in further sensing applications[37,38].

Researchers utilized AAO as a versatile platform for chemical sensing and biosensing[39,40,41]. For instance, Kumeria *et al.* used the optimized AAO structure to detect volatile sulphur compounds and hydrogen gas[42,43]. Here, AAO structures were fabricated and coated with gold and platinum to provide a specific binding site for the detection of hydrogen sulphide gas and hydrogen gas, respectively. Further study demonstrates the optimization of the surface modification of the gold-coated surface of AAO with mercaptoundecanoic acid. The data showed that the sensor’s signal was very sensitive to the change in thiol concentrations[44]. Li and co-workers efficiently designed a DNA label-free detection sensor based on AAO[45]. They developed an electrochemical detector by coating the top side of the AAO surface with a layer of gold, whereas the pores were functionalized with the single-strand DNA. Upon the DNA hybridization, the diffusion of ferricyanide ions through the AAO pores will be slowed and, thus, can be measured. This sensor offers a highly sensitive, selective, and rapid method for DNA analysis. Smirnov’s group conducted a similar study;

they used small and large AAO pores to monitor the effect of pore geometry on the diffusion and hybridization of DNA inside the pores[46]. Dhathathreyan reported on a protocol using AAO as an enzyme sensor[47]. This author utilized AAO to study the kinetics of the reaction of the enzyme invertase by functionalizing the AAO pores with invertase. The activity of the enzyme inside the pores was monitored with confocal laser scanning microscopy (CLSM) and surface plasmon spectroscopy (SPR) during the injection of different sucrose at pH ranging from 3.0 to 6.5. The data exhibited that the optimal activity of invertase was reached at pH 4, and the kinetic was biphasic for the adsorption of the invertase and its interaction with the sucrose.

The methods of employing AAO and pSi for bacterial sensing can be divided into indirect and direct. Figure 2.2 demonstrates the differences between these two methods. In indirect methods, bacterial detection relies on targeting only specific components of the bacterial cells, such as fragments of DNA, proteins, or enzymes released by bacteria. On the other hand, in direct methods, bacteria detection is achieved by directly attaching the whole bacteria to the surface of the porous materials[48,49].

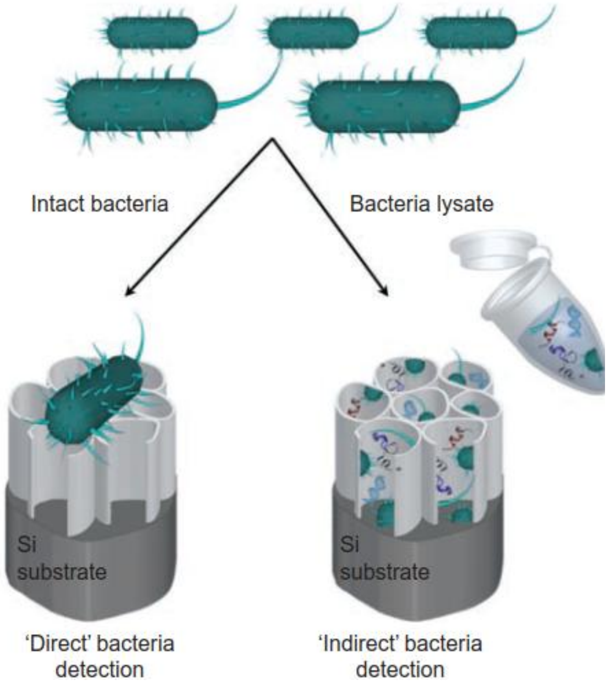

Figure 2.2: *Schematic of 'indirect' and 'direct' bacteria detection based on pSi. This Figure was reproduced with permission from reference [49]: Srinivasan, S.; Leonard, F.; Kuncewicz, T. M.; Godin, B. In Vivo Imaging Assessment of Porous Silicon. Porous Silicon for Biomedical Applications* ***2014****, 223–252. Copyright 2014. Elsevier.*

The detection of bacteria via a DNA-based sensor is achieved by modifying the porous structures with a ssDNA sequence. If a cDNA of the target bacteria is introduced to this ssDNA, the hybridization of DNA will take place. As a result, the sensor response can be recorded. Toh *et al.* demonstrated a DNA-modified AAO sensor for bacteria sensing[50]. They proposed an electrochemical method to detect the target DNA of *Legionella sp.* by pre-immobilized ssDNA inside AAO pores. The sensor signal was recorded based on the redox process that happened due to the hybridization of cDNA of bacteria with the functionalized ssDNA inside AAO pores. This sensor provided a sensitive method with detection of limit 3.1×10^{-13} M.

In another study, Escosura-Muñiz *et al.* designed an AAO based sensor to electrically evaluate bacterial virulence by detecting the enzyme hyaluronidase (HYAL) secreted by live *Staphylococcus aureus* and *Pseudomonas aeruginosa (P. aeruginosa)* cultures on AAO[51]. These researchers functionalized the pores of AAO with (3-aminopropyl)triethoxysilane (APTES) followed by activation with [*N*-(3-dimethylamino)propyl)]-*N*-ethylcarbodimide/ sulfo-NHS, sulfo *N*-hydroxysuccinimide and finally the reaction with an anti-HYAL antibody. HYAL secreted by bacteria entered the pores and blocked them due to HYAL immunorecognition (bound to the antibody); in contrast, in the absence of enzyme or for reduced enzyme activity (by inhibition), no closing of the pores took place, which was proved by voltametric measurements.

Other researchers developed an AAO-polymer composite structure to detect “indirectly” *P. aeruginosa* by employing its secreted proteinases[30]. The pores of AAO were coated with poly(sodium-4-styrenesulfonate) and poly-L-lysine polymers via layer-by-layer approach[52]. Due to the enzymatic degradation, a layer of poly-L-lysine was degraded after exposure to proteinase; the reaction was monitored by Interferometry, as discussed later in this Chapter.

pSi was also used as a platform for enzyme and bacteria detection. The work by Grooms’s group fabricated a DNA-pSi based sensor to detect *Salmonella enteritidis*[53]. The pSi was coated with polypyrrole by electropolymerization. Then, ssDNA was introduced to the polypyrrole-pSi surface for interaction between the negatively charged ssDNA and positively charged polymer film without further chemical modification. Exposure of this sensor to the cDNA probe of *Salmonella enteritidis* led to the formation of dsDNA, and the current density was measured. The data revealed that the reaction was selective, and the limit of detection (LOD) was 1 ng mL^{-1}. Alocilja and co-workers reported a pSi sensor for indirectly sensing *E. coli* based on secreted enzymes[54]. The study demonstrated a luminescence protocol for sensing bacterial enzymes. The pores of pSi were modified with dioxetane and Polymyxin B. The β-galactosidase enzyme, which is secreted from *E. coli,* among other molecules during the metabolism, reacted with dioxetane/Polymyxin B inside the pores. This reaction produced light at 350 nm with higher emissions than the reference sensor. This pSi-enzyme sensor exhibits a sensitivity for bacteria of 100 CFU mL^{-1}.

Other authors proposed a pSi sensor that was based on enzyme-responsive material for *Staphylococcus aureus* detection[55]. Thermally hydrocarbonized pores of pSi were coated with hyaluronic acid methacrylate (HYAMA) via crosslinking. When the sensor was exposed to HYAL, an enzyme produced by *Staphylococcus aureus*, enzymatic degradation occurred and was monitored by voltammetry. The result revealed that the enzyme could successfully degrade the HYAMA; furthermore, the reaction response increased with the increase in the enzyme concentration.

Recent research conducted by Francis and co-workers developed a new sensing protocol using pSi to detect bacteria indirectly via their lysate[56]. The top surface pSi film was coated with a layer of TiO_2 layers, which serves as a passivating film and enhances the reflectivity of pSi. In this method, the lytic enzyme, which is utilized as a recognition component, attaches only the specific bacteria, and, as a result, bacterial lysate will be released, which then penetrates the pore, causing an increase in the film's refractive index. They could use this to detect the Gram-positive rod-shaped bacteria *Bacillus cereus* using an enzyme model called bacteriophage-encoded PlyB221 endolysin. The sensitivity of the sensor reached 1000 CFU mL^{-1}.

Some methods for detecting bacteria require pre-treatment or extraction processes. These processes might be time-consuming or can only be performed in a specific laboratory. Therefore, the use of direct detection methods could overcome these challenges. The sensing of bacteria using AAO/pSi could be implemented by testing with bacterial suspensions containing different concentrations of bacteria fragments. In these methods, the bacteria cells are directly attached to the AAO or pSi surface either by a specific surface design or surface chemistry. Thus, there is no need for the presence of secreted molecules by bacteria, such as enzymes or antibodies, to serve as sensing analytes[57].

Lee *et al.* fabricated a chip based on AAO for label-free detection of bacteria[58]. They covered the top side of the AAO surface with a thin layer of gold to provide a plasmon resonance and enhance the Interferometry. The sensing concept relies on changes in reflectivity due to the immobilization of bacteria cells on the surface. The chip-AAO-coated gold was functionalized with thiolated specific aptamers. Different cell concentrations of *P. aeruginosa* were exposed to aptamers functionalized and nonfunctionalized chips. In aptamer-modified AAO, the reflectivity dropped over the increase of cell concentrations compared to bare ones. The result demonstrated that the functionalized sensor could detect *P. aeruginosa* cells, whereas no physical absorption occurred in the untreated sensor. Li *et al.* also suggested using an AAO sensor for direct and selective detection of *Listeria monocytogenes*[59]. This sensor employs AAO combined with a specific aptamer supported by electrochemical detection. The data showed a reduction in current response due to charge repulsive and steric hindrance, which occurred in the presence of *Listeria monocytogenes*.

The use of pSi in direct bacteria detection was also reported[60]. For instance, Massad-Ivanir and colleagues suggested a sensing method for direct bacteria detection by functionalizing the pSi surface with a biorecognition element, i.e., antibody[61]. The target bacteria (*E. coli*) was captured on the modified pSi sensor via antibody-antigen binding, and the process was monitored by interferometry techniques, as shown in Figure 2.3. The data confirmed that the drop in the reflectivity of the maximum peak was due to binding *E. coli* on the pSi surface compared to the free *E. coli* sample.

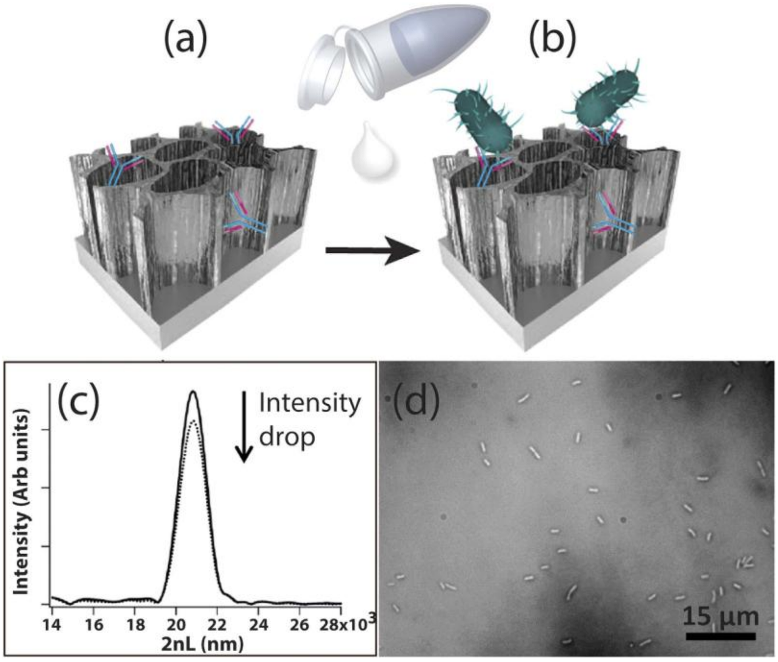

Figure 2.3: *a) and b) Schematic of antibody binding and bacteria capturing on pSi, respectively. c) Reflectivity spectra before and after bacteria capture, d) Image of the presence of E. coli on pSi surface measured by scanning electron microscopy. This Figure was reproduced with permission from reference [61]: Massad-Ivanir, N.; Shtenberg, G.; Raz, N.; Gazenbeek, C.; Budding, D.; Bos, M. P.; Segal, E. Porous Silicon-Based Biosensors: Towards Real-Time Optical Detection of Target Bacteria in the Food Industry. Scientific Reports* ***2016,*** *6 (1). Copyright 2016. Springer Nature.*

Segal and co-workers proposed another rapid, free-label, direct-sensing bacteria approach[62]. This approach is based on directly capturing the large bacteria (the whole bacteria) inside a pore of pSi and analyzing the process with reflective interferometric Fourier transform spectroscopy. They fabricated macro-sized pSi substrates and chemically oxidized them in a diluted ammonia–hydrogen peroxide solution under heating for 1 h. Finally, the oxidized substrates were functionalized with APTES, providing a positively charged surface. Different concentrations of *E. coli* were introduced to this pSi sensor. Due to the negative charge of the bacterial surface, *E. coli* cells adhered to the charged inner pore surface, promoting accurate measurements. They concluded that this system could be used for real-time sensing of large biological analytes.

2.3 Fabrication of Anodic Aluminum Oxide (AAO)

The anodization process of aluminium (Al) has been studied since 1953[63]. Depending on the anodization conditions, two structures of the Al_2O_3 could be formed: the non-porous Al_2O_3 layer and the porous Al_2O_3 layer (AAO). The geometry of the AAO can be schematically described as a honeycomb structure[64,65] characterized by a close-packed array of hexagonal circular pores (Figure 2.4a)[66]. Highly ordered AAO nanostructures are often fabricated using the 2-step anodization method, which was developed by Masuda et al[36].

The structure of AAO is defined by structural parameters pore diameter (D_p), wall thickness (W_t), interpore distance D_{int}, porosity (P), pore density and pore length, as shown in Figure 2.4b[66]. The pore diameter and pore length can range from a few nm to more than a hundred nm[67,68,69] and from a few hundred nm to a hundred µm[70,71], respectively.

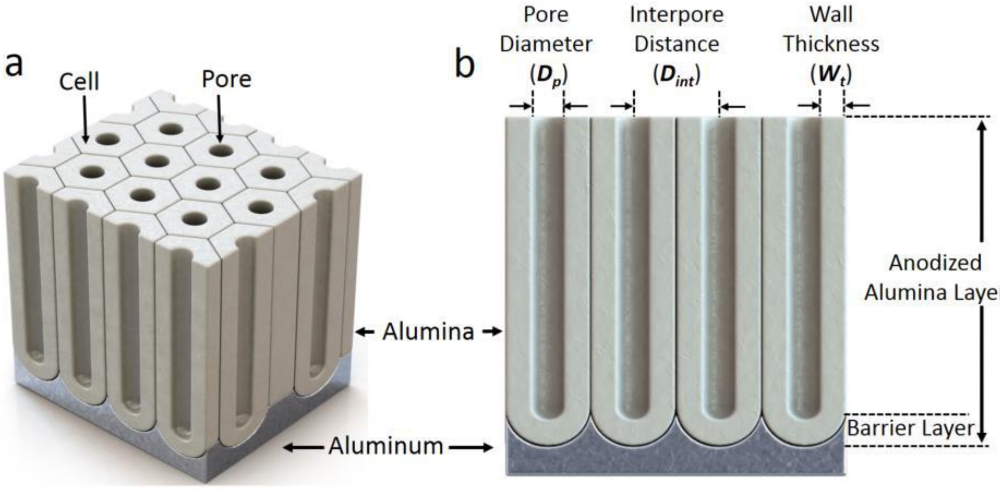

Figure 2.4: *a) Schematic of the structure of AAO obtained from the anodization of Al. b) Schematic of the cross-sectional view of the AAO showing its structural parameters. This Figure was reproduced with permission from reference [66]: Jeong, C.; Jung, J.; Sheppard, K.; Choi, C.-H. Control of the Nanopore Architecture of Anodic Alumina via Stepwise Anodization with Voltage Modulation and Pore Widening. Nanomaterials* ***2023****, 13 (2), 342. Copyright 2023. MDPI.*

The porosity of AAO refers to the ratio of the surface area occupied by pores to the whole surface area, which can be calculated as follows[72].

$$P = 0.907 \, (D_p / D_{int})^2 \quad \text{.. (Eq. 2.1)}$$

The formation of AAO involves two chemical reactions taking place simultaneously: Al_2O_3 layer formation and Al_2O_3 layer dissolution. The Al_2O_3 layer formation process takes place at both the Al/ Al_2O_3 and electrolyte/ Al_2O_3 interfaces due to the migration of Al^{3+} ions towards the electrolyte and the migration of O^{2-} and OH^- from the electrolyte towards the Al/ Al_2O_3 interface through the barrier layer (Figure 2.5). The field-enhanced dissolution of the Al_2O_3 layer occurs at the bottom of pores (at the electrolyte/Al_2O_3 interface) due to an enhanced electric field, which forces Al^{3+} ions to move to the Al/ Al_2O_3 interface. The dissolution process is slower than the formation process. Thus, the rates of these two chemical processes determine the pore formation of AAO[73].

The reactions taking place during the anodization process of Al can be expressed by the equations Eq. 2.1-2.4. The Al oxidation at the anode is displayed in Eq.2.2.

$$2Al \longrightarrow 2Al^{3+} + 6e^- \quad \text{...} \ (Eq.\ 2.2)$$

Other anodic reactions taking place at Al/ Al_2O_3 and electrolyte/ Al_2O_3 interfaces are presented in Eq. 2.3 and Eq. 2.4, respectively.

$$2Al + 3O^{2-} \longrightarrow Al_2O_3 + 6e^- \quad \text{...} \ (Eq.\ 2.3)$$

$$2Al^{3+} + 3H_2O \longrightarrow Al_2O_3 + 6H^+ \quad \text{...} \ (Eq.\ 2.4)$$

The chemical reaction at the cathode can be expressed by Eq. 2.5.

$$6H^+ + 6e^- \longrightarrow 3H_2 \quad \text{...} \ (Eq.\ 2.5)$$

The overall chemical reaction during the anodization of Al can be written as:

$$2Al + 3H_2O \longrightarrow Al_2O_3 + 3H_2 \quad \text{...} \ (Eq.\ 2.6)$$

A dissolution of Al_2O_3 by the acidic electrolyte may also occur, according to Eq. 2.7.

$$Al_2O_3 + 6H^+ \longrightarrow 2Al^{3+} + 3H_2O \quad \text{...} \ (Eq.\ 2.7)$$

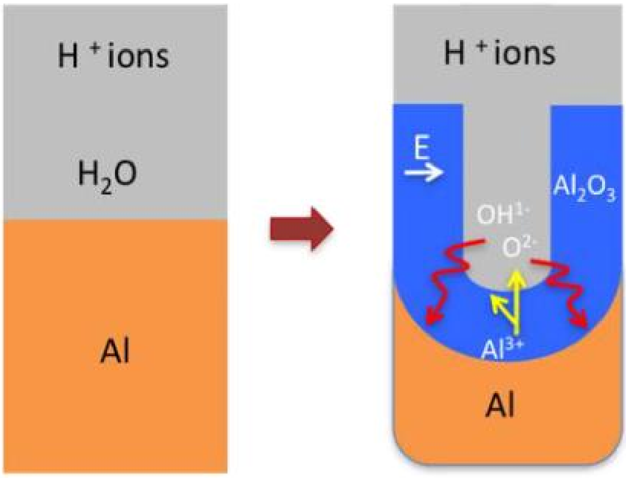

Figure 2.5: *Schematic of the anodization of Al and formation of AAO in the acidic electrolyte showing the migration of the reactive ions across the barrier layer. This Figure was reproduced with permission from reference [74]: Poinern, G. E. J.; Ali, N.; Fawcett, D. Progress in Nano-Engineered Anodic Aluminum Oxide Membrane Development. Materials* ***2011****, 4 (3), 487–526. Copyright 2011. MDPI.*

The structure of AAO can be controlled by optimizing the anodizing parameters applied voltage, temperature, anodization time, and type of electrolyte[75], offering an advantage feature of AAO that makes it one of the most desired nanostructures in nanotechnology[76]. For instance, Lin and co-workers studied the effect of applied voltage on the formation of pores and stated that the pore diameter and interpore distance increased linearly with the applied voltage[77]. Other authors investigated in detail the impact of different voltages on the pore formation during the anodization process of Al. They found a similar trend and explained it by considering the velocity of migrated ions under the impact of an electric field during the formation and dissolution of the Al_2O_3 layers. The relationship between the pore diameter and interpore distance can be written as follows[78]:

$$D_p = \lambda_p U \quad \text{..........} \quad \text{(Eq. 2.8)}$$

$$D_{int} = \lambda_c U \quad \text{..........} \quad \text{(Eq. 2.9)}$$

where λ_p *and* λ_c are constants, U is the applied voltage. For anodization under mild anodization conditions in oxalic, sulfuric, and phosphoric acids, λ_p *and* λ_c are 0.9 and 2.5 nm/V, respectively[78]. The pore wall thickness and barrier layer thickness (*B*) can be calculated by Eq. 2.10 and 2.11, respectively.

$W_t = ½ (D_{int} - D_p)$ ………………………………………………………… (Eq. 2.10)

$B = \lambda_b W_t$ ………………………………………………………… (Eq. 2.11)

where λ_b is constant, and its value depends on the type of electrolyte, for example, $\lambda_b \sim 1.33$ and 1.12 for sulfuric and oxalic acids, respectively.

The effect of temperature on the pore formation was also investigated. A study by Chowdhury's group showed that the anodization of Al took place at 15, 19, and 25 V under different temperatures[79]. The data revealed that the porosity and the pore diameter of AAO increased with the increase in temperature. For example, the anodization at 15 V provided two porosities: 28 % and 45 % when electrolyte temperatures were 3 ˚C and 15 ˚C, respectively. However, this effect on porosity might be limited at elevated temperatures (at constant voltage) due to the dissolution of Al_2O_3 at the pore wall with no change in the interpore distance[80].

The anodization time has an essential role in the growth of AAO, which was supported by the work of Jaskuła and his group[78]. They performed a series of anodization experiments with varied anodization times ranging from 4 to 16 h using different electrolytes and purities. The result, presented in Figure 2.6, displays a significant increase in the pore length of AAO with time. Furthermore, the researchers concluded that the type of used electrolytes directly affected the growth rate of AAO.

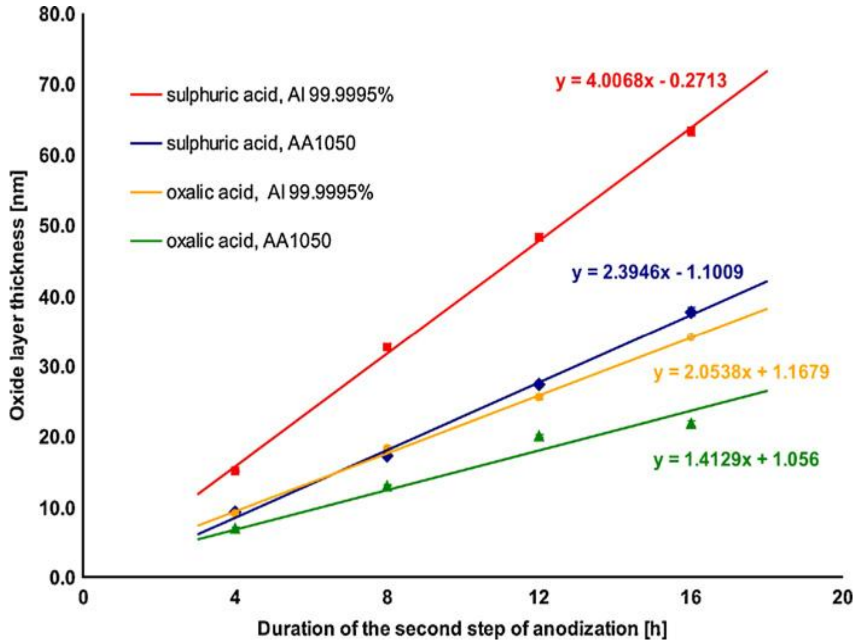

Figure. 2.6: *Dependence of the thickness AAO on the anodization time. Sulfuric and oxalic acids with different purities were used in the anodization of Al. This Figure was reproduced with permission from reference [78]: Zaraska, L.; Sulka, G. D.; Szeremeta, J.; Jaskuła, M. Porous Anodic Alumina Formed by Anodization of Aluminum Alloy (AA1050) and High Purity Aluminum. Electrochimica Acta* ***2010****, 55 (14), 4377–4386. Copyright 2016. Elsevier.*

This behaviour was also investigated by Dobosz, who reported on the relation of the anodization time, type of electrolyte, and temperature with the thickness of AAO[81]. He compared the growth rate of AAO produced with sulfuric, oxalic, and phosphoric acids. The result revealed that a thicker AAO film prepared in sulfuric acid was observed at a constant time and temperature compared to other electrolytes, which could be explained by the difference in the migration rate of the active ions through the barrier layer[82]. Furthermore, the same study recorded a linear increase in the thickness of AAO with a limited anodization time. However, a non-linear relationship was observed when the anodization time exceeded 40 h. The latter was explained by the limited diffusion of the ions when the pores are long, which makes it difficult for the reactant ions to move from the electrolyte along the pore to reach the bottom of the pores[82].

Generally, there are two types of anodization processes: mild anodization (MA)[36] and hard anodization (HA)[83]. In the MA, the voltage is kept constant during the anodization, while in the HA, higher applies and increases gradually until reaching the desired value[84]. The growth of AAO pores produced in HA is faster than in MA. For example, Gösele and colleagues prepared AAO in MA and HA at 40 and 140 V using 0.3 M oxalic acid as an electrolyte. They found that the thicker AAO film (more than 100 µm) was prepared for 2 h compared to AAO film prepared at 40 V (3.8 µm). They also reported a non-linear trend when the pores become longer.

Based on these processes, AAO can be fabricated using one, two, or three steps[85,86,87,88]. In the one-step anodization process, the disordered nanopores may form due to the random nature of the initial formation of pores[89]. In the two or three anodization step methods, the first AAO layer is removed by chemical etching, leaving the Al surface with highly ordered periodic indentations, which serve as the initiation sites for forming pores in the following anodization steps; consequently, a high-ordered and hexagonal nanoporous structure of AAO could be achieved[90]. Figure 2.7 displays the fabrication steps of AAO, starting with the electropolishing of the Al surface, which reduces the roughness and, hence, reduces the undesired enhanced current density during the anodization process and ends with a hexagonally ordered structure of AAO.

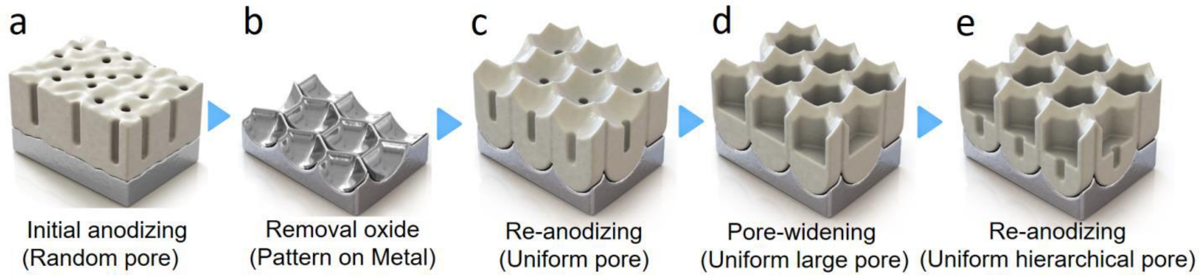

Figure 2.7: *Schematic of the steps used in MA for fabrication of AAO. a) Initial anodization showing the first AAO layer with random pores, b) Al substrate after removal of the first AAO layer by chemical etching. c) Formation of the ordered structure after the second anodization. d) Pore widening process to expend the pore diameter. e) An additional anodization step to produce hierarchical pore structures. This Figure was reproduced with permission from reference [66]: Jeong, C.; Jung, J.; Sheppard, K.; Choi, C.-H. Control of the Nanopore Architecture of Anodic Alumina via Stepwise Anodization with Voltage Modulation and Pore Widening. Nanomaterials* ***2023****, 13 (2), 342. Copyright 2023. MDPI.*

As shown in Figure 2.7, after the second anodization, the pore diameter of AAO can be widened by wet chemical treatment without affecting the interpore distance. The research performed by Carroll *et al.* aimed to prepare AAO with 28 nm in diameter at 40 V in oxalic acid in two-step anodization and to expand the pore diameter by post-treatment[91]. After the second anodization step, the as-made pores were enlarged to 90 nm after immersion in a solution containing 5 wt% phosphoric acid at 19 ˚C for 40 min. They also concluded that the pore diameter is directly proportional to the widening time, offering an advantage in designing an AAO with the desired pore size[91].

2.4 Fabrication and Stabilization of Porous Silicon (pSi)

PSi has attracted attention in recent years because of its biocompatibility and adaptability to different structural and chemical properties, particularly in biosensing applications[92,93]. The pSi has an advantage over the flat Si because it has a high surface area, which improves the sensitivity of the sensor, i.e., lowering the LOD[94]. The most popular method of producing pSi is electrochemical anodization, also known as electrochemical etching, which was discovered in the 1950s[95,96]. The electrochemical etching of the Si wafer is carried out in a Teflon cell using a mixture of hydrofluoric acid (HF) and ethanol as the etching solution. The wafer is placed on a conductive layer, usually an Al or Pt sheet, which serves as the anode (Figure 2.8). In order to provide a consistent electron flow and, consequently, pSi films with a homogeneous length of the porous layer, the cathode is often composed of Pt in the form of a rounded wire parallel to the Si substrate.

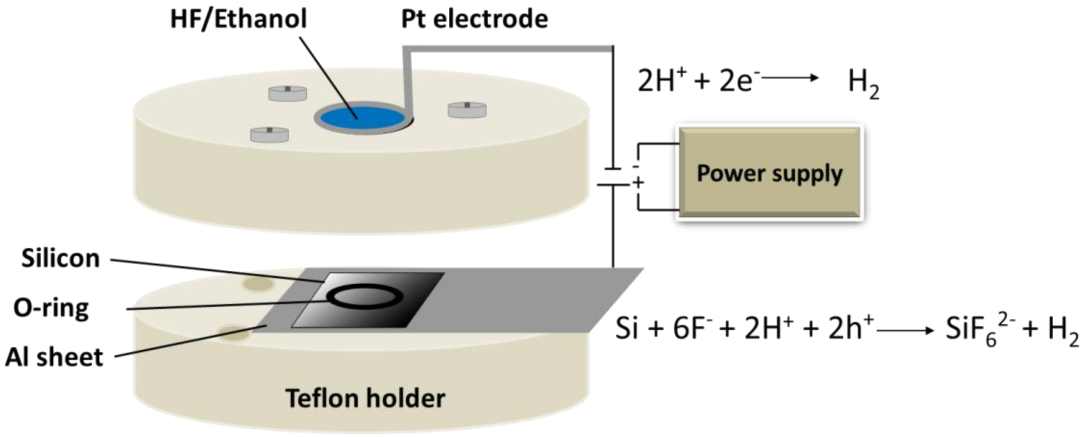

Figure 2.8: *Schematic of an electrochemical etching cell to pSi using HF/ethanol mixture as an electrolyte (etching solution). The anode (Si wafer) and cathode (Pt wire) are connected to a power supply. The inserted equations represent the main oxidation and reduction half-reactions taking place during the etching of Si.*

The electrochemical etching process of Si using HF has already been reported[97,98]. This process includes the following steps: the migration of positive holes from the bulk silicon to the Si/electrolyte interface, pore nucleation, and propagation. These three steps continue until pores in the Si substrate are developed, as displayed in Figure 2.9a-c.

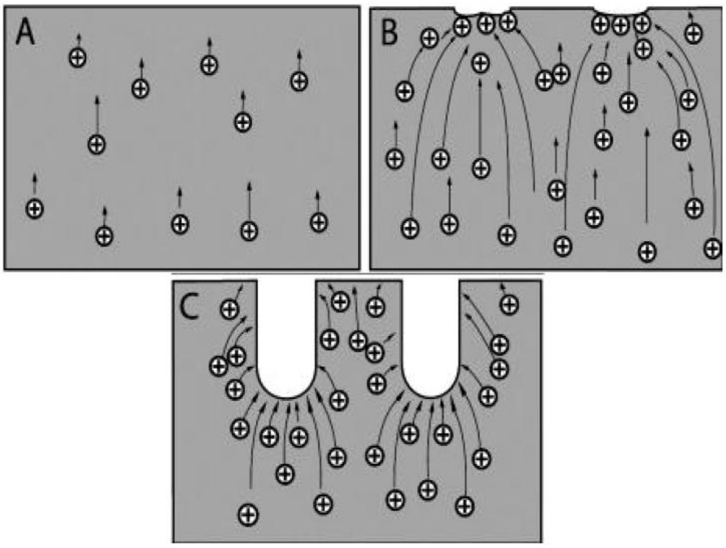

Figure 2.9: *Schematic pore formation during electro-etching process of Si. The process includes the following steps: A) Migration of positive holes in the bulk Si to Si/electrolyte interface, B) random pore nucleation, and C) pore formation and propagation. This Figure was reprinted with permission from reference [99]: Ressine, A.; Ekström, S.; Marko-Varga, G.; Laurell, T. Macro-/Nanoporous Silicon as a Support for High-Performance Protein Microarrays. Analytical Chemistry* ***2003****, 75 (24), 6968–6974. Copyright 2003. American Chemical Society.*

As shown in Figure 2.9a, the positive holes move toward the cathode surface when an electric current is supplied, which can be expressed by Eq. 2.12. When the holes reach the Si/electrolyte interface, the reaction in Eq. 2.13 occurs, and dips on the surface are created, as demonstrated in Figure 2.9b.

$Si + 2\,HF + h^+ \longrightarrow SiF_2 + 2\,H^+ + e^-$ .... (Eq. 2.12)

$SiF_2 + 2\,HF \longrightarrow SiF_4 + H_2$ .... (Eq. 2.13)

$SiF_4 + 2\,HF \longrightarrow H_2SiF_6$ .... (Eq. 2.14)

As the current flow continues, more holes will be attracted at the bottom of the dip, forming more dips and creating pores, as shown in Figure 2.9c and presented in Eq. 2.14.

The structure and morphology of PSi are usually governed by the type and concentration of the dopant in the Si substrate, the current density, the composition of the electrolyte, and the duration of the etching process[100,101,102,103,104,105]. The morphology of the pSi is widely defined as the pore diameter, the pore length, and the porosity. The pSi can be classified based on its pore size. They are called micropores, mesopores, and macropores if the pore sizes are up to 2 nm, from 2 to 50 nm, and more than 50 nm, respectively[106].

Despite observable morphological changes when specific parameters are tuned, there is no formula for predicting the parameters that precisely determine the pore size, length, and porosity to achieve the desired pSi structure. To produce a desirable pSi structure, it is recommended that the fabrication parameters and resulting pSi structure should be studied. For instance, the concentration of dopants, which is inversely proportional to the wafer's resistivity, affects the pore size. The higher the dopant concentration, the larger the pore is produced102. Also, the dopant type affects the pore size; N-type dopant wafers, often doped with phosphorus, generally have a greater pore diameter (> 50 nm) compared to p-type wafers (< 50 nm)[107].

Current density is a critical parameter in the etching process of pSi. It was reported that the current density directly influences the pore size[108,109]. Ogata *et al.* studied the effect of varying the current density on the pore diameter of pSi[110]. They observed that pore diameters increased with increasing the current density (Figure 2.10). The increasing current density will also accelerate the etching rate[111]. For the same etching time, the pore length is thus increased.

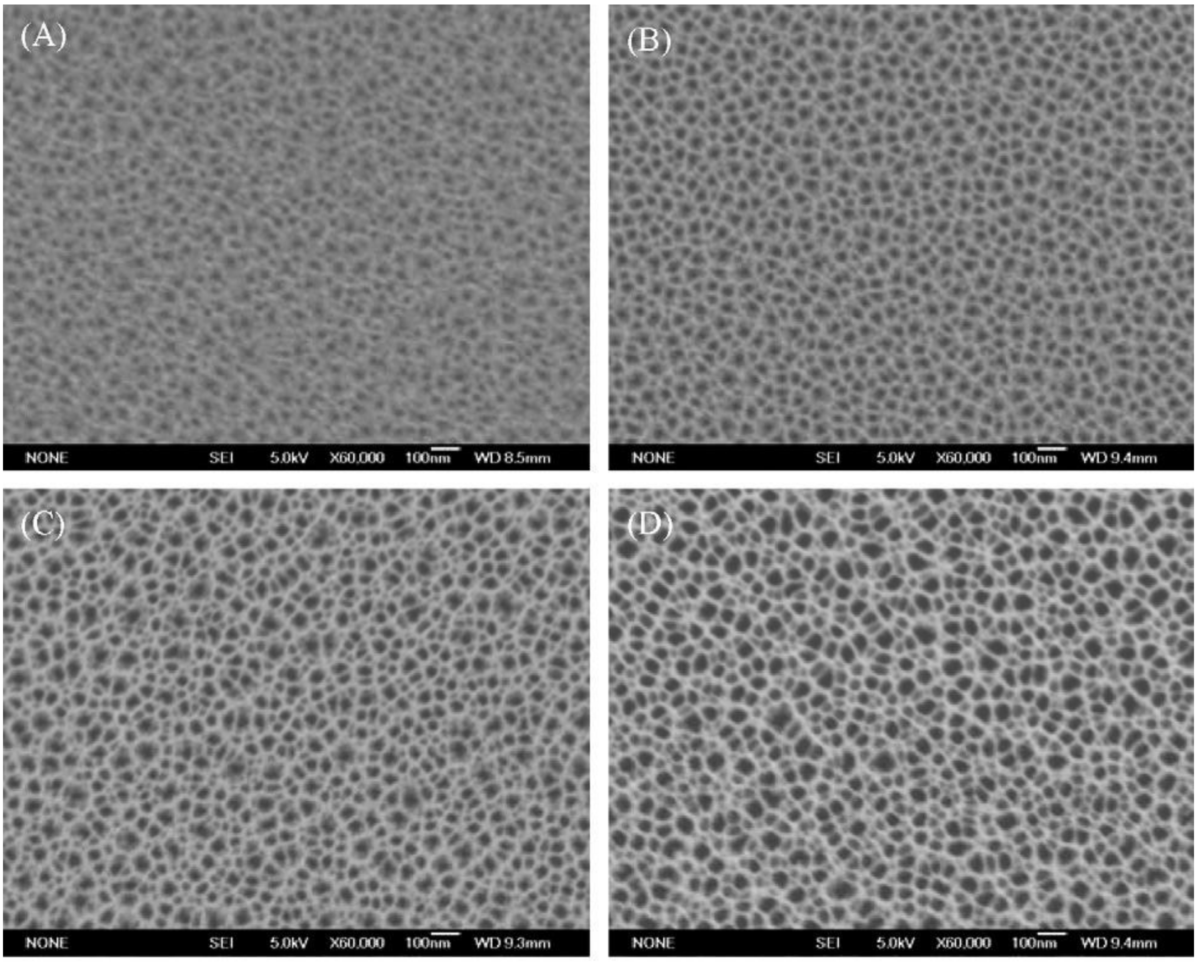

Figure 2.10: *Top-view SEM images of the dependence of pore diameter on current density: A) 5, B) 10, C) 15, and (D) 20 mA cm^{2-}. This Figure was reprinted with permission from reference [110]: Harraz, F. A.; El-Sheikh, S. M.; Sakka, T.; Ogata, Y. H. Cylindrical Pore Arrays in Silicon with Intermediate Nano-Sizes: A Template for Nanofabrication and Multilayer Applications. Electrochimica Acta **2008**, 53 (22), 6444–6451. Copyright 2008. Elsevier.*

The etching time is also considered an essential factor in electrochemical etching. It determines the pore length, also known as the thickness of the pSi film. The pore length is directly proportional to the etching time of the etching process[112]. It was observed that the pore length increased linearly with the etching time under a constant current density[113]. It is worth mentioning that this may not be applicable for a longer time (long pores) due to the restriction of the transport of ions in the long pores of porous materials[114].

Another essential structural term is porosity. The IUPAC defines porosity as “the ratio of the total pore volume to the apparent volume103. The porosity of pSi film also has an essential role in the sensing application since it determines the accommodation of the biomolecule of interest into the porous material. Therefore, the etching parameters must be chosen carefully to produce the desired structures. Lee *et al.* investigated the effect of current density on the porosity of pSi as single- and double-layer structures using HF as an electrolyte[115]. They observed that the higher the current density, the larger the porosity.

The porosity of the pSi film can be assessed by several methods such as electron microscopy[116], gravimetric method[117,118], and spectroscopic liquid infiltration method (SLIM)[119,120]. In the electron microscopy method, the pore geometry is measured from the top side as well as a cross-section along the pore depth (thickness of the porous layer). Thus, the porosity can be estimated based on the pore size. However, this method is limited; it only measures the porosity at the pore surface (top side of pSi) and not the entire bulk film[121,122] which can be misleading if defects or inhomogeneous pores are formed in the fabricated film.

In the gravimetric method, the porosity is determined by measuring the mass of the Si sample before and after the etching process and then after the removal of the porous layer of Si by chemical etching in NaOH[103]. These three masses are expressed in Eq. 2.15 as m_1, m_2, and m_3, respectively.

$$P = (m_1 - m_2)/(m_1 - m_3) \quad \text{..} \quad \text{(Eq. 2.15)}$$

where P is the porosity.

The pSi film thickness can also be determined by the gravimetric method by applying Eq. 2.16103.

$$W = (m_1 - m_3)/A\, d_{Si} \quad \text{..} \quad \text{(Eq. 2.16)}$$

where W is the film thickness, A is the surface area of the porous film, and d_{Si} is the density of elemental silicon. However, this method is destructive and might be undesirable if the pSi samples are needed for further experiments.

The last method that enables the determination of film thickness and porosity is SLIM. Compared to the gravimetric method, SLIM is a non-destructive method, as it employs light to analyze the porous samples, which is considered an optical characterization method[123]. In the SLIM method, two reflectance spectra of the pSi filled with air and a liquid, whose refractive index is known, are recorded. To achieve an accurate result, the pores must be completely filled with liquid and no air bubbles left. When liquid infiltrates the pores, the average refractive index of the pSi will increase, which will cause the reflectance spectrum to shift. By applying the two-component effective medium approach, the effective optical thickness (*EOT*) values (for air and liquid), which will be discussed later in detail in this Chapter, can be fitted, and the porosity and thickness of pSi film can be determined[124].

The current density is a critical factor in the fabrication of pSi because it controls the pore size and porosity of the produced pSi film. Therefore, the variation of the current density in real-time will lead to the fabrication of different optical and physical pSi structures. If the current density is fixed during the electrochemical etching of Si, a single-layer pSi structure will be produced[125]. Furthermore, multilayer pSi structures can be produced by varying the current density over time[126]. The double layer pSi can be achieved by applying a higher current density followed by a lower current density (or vice versa) once through the electrochemical etching,[127] as shown in Figure 2.11. This produced pSi structure exhibits a large pore size on one layer and a small pore size on another, offering an advantage in biosensing applications if the selective penetration of the molecules into the pores is required[128]; in other words, the small pores will allow the smaller molecules to penetrate and block the bigger ones.

The variation of the current density during the electrochemical etching process of Si produces numerous photonic crystals (also called 1D photonic structures) such as the Bragg mirror[129], microcavity[130], rugate filter[131] , and apodized rugate filter[132]. The photonic crystals possess a so-called "stop bandgap" that restricts the reflectivity of light to specific wavelengths[133]. The latter feature makes the photonic structures a proper candidate for sensing applications[134].

The Bragg mirror is fabricated by varying the current density with low and high current densities in a stepwise manner. This produces a two-layered structure with two different porosities, resulting in different refractive indices of these layers. The *EOT* of these layers is proportional to one-quarter of the wavelength that the mirror is intended to reflect[135]. The reflectivity spectrum of this structure exhibits a high reflectively broad band located around this wavelength (Figure 2.11).

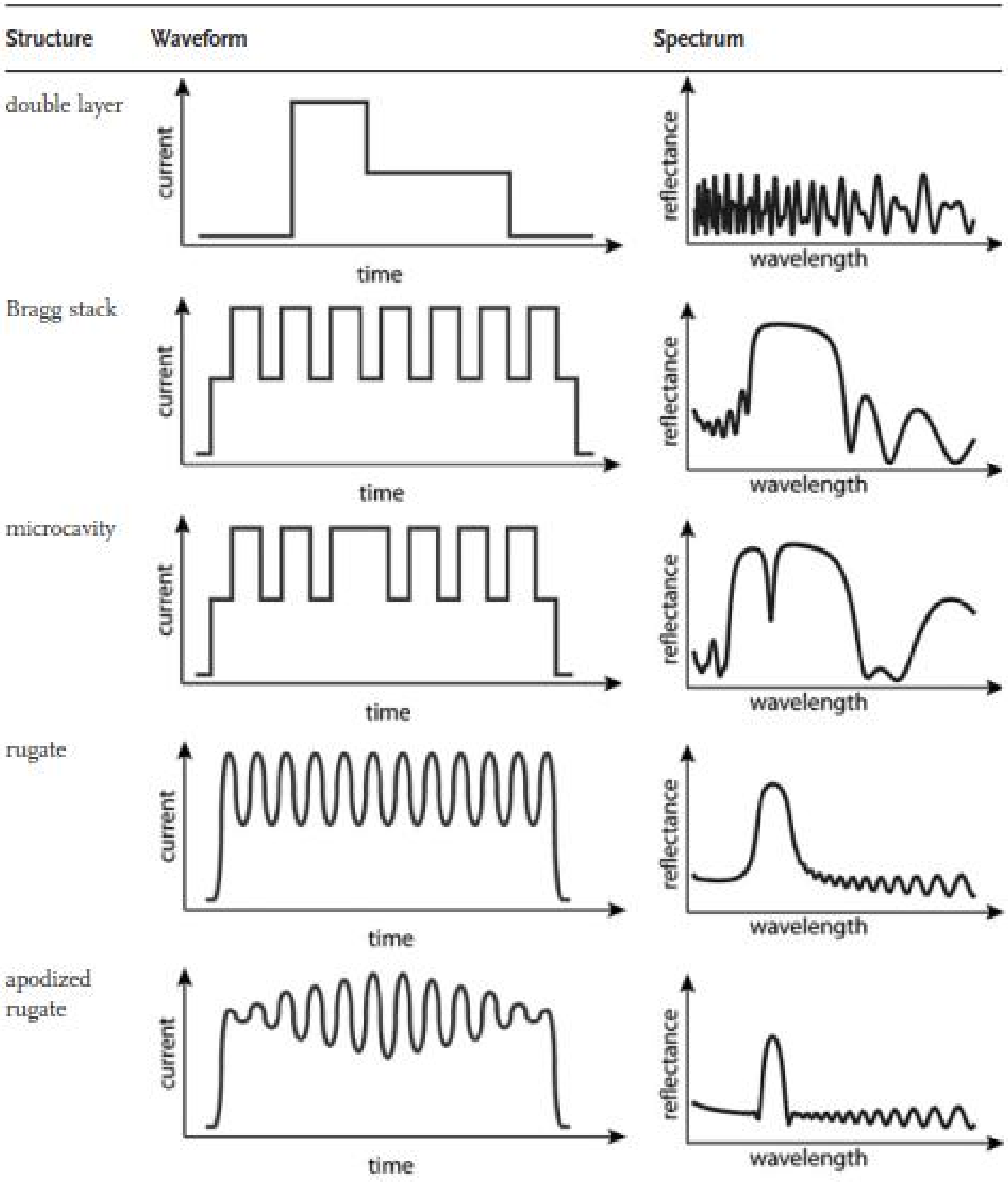

Figure 2.11: *Plots of the current density waveforms for double and multilayer pSi structures and their representative reflectivity spectra. This Figure was reproduced with permission from reference [103]: Sailor, M.J. Porous Silicon in Practice: Preparation, Characterization and Applications, First Edition,* ***2012****, Wiley-VCH, Weinheim, Germany. Copyright 2012. Wiley-VCH Verlag GmbH & Co. KGaA.*

Another multilayered structure fabricated in pSi is the microcavity[136]. This structure is fabricated so that a cavity layer is created into a single Bragg mirror. The resulting structure with alternating layers of different porosities exhibits a very sharp peak in the centre of a broad band of high reflectivity produced by the Bragg mirror in the reflectivity spectrum, as displayed in Figure 2.11. The peak position is associated with the *EOT* of these two layers surrounding the cavity layer.

In contrast to the Bragg mirror, which is produced by using a stepwise alternation between high and low current densities, the rugate filter is fabricated by applying high and low current densities in a sinusoidal waveform during the etching process with maximum and minimum values representing the high and low current densities. It should be noted that the significant change between the refractive indices of the Bragg mirror`s layers leads to the absorption of a broad range of wavelengths, forming a broad spectral band[137]. The pSiRF exhibits an individual, high reflectivity and sharper peak in the reflectance spectrum compared to the Bragg mirror, which is illustrated in Figure 2.11. The apodized rugate filter is the same as the rugate filter, but the sinusoidal waveform was apodized with a Gaussian window function to suppress the side lobes located on both sides of the stopband peak in the reflectivity spectrum to enhance the sensitivity of the sensor[138,139].

The chemical composition of the pSi surface affects its stability and capability to bind to biological molecules. The freshly fabricated pSi is reactive and unstable in aqueous media and ambient air due to its hydrogen-terminated surface (Si-H). It has been reported that the freshly etched pSi surface has been passivated with a thin layer of native oxide and subsequently dissolved when exposed to ambient or physiological conditions[140]. The degradation of pSi in the biological environment can be expressed by simplifying the following equations[141].

$$\mathrm{Si} + 2\mathrm{H_2O} \longrightarrow \mathrm{SiO_2} + 2\mathrm{H_2} \quad \text{..} \quad \text{(Eq. 2.17)}$$

$$\mathrm{SiO_2} + 2\mathrm{H_2O} \longrightarrow \mathrm{Si(OH)_4} \quad \text{..} \quad \text{(Eq. 2.18)}$$

Eq. 2.17 and Eq. 2.18 emphasize that the degradation of pSi can also be monitored by liberating hydrogen gas and reducing the pH of the solution, respectively[142].

The formation of an oxide layer on pSi changes its chemical, physical, optical, and electrical properties, providing an improper platform for various applications, especially in biosensing. Thus, stabilizing the pSi surface is necessary to fulfill the conditions of biosensing[143]. There are two approaches to stabilize the pSi: chemical functionalization[144] or oxidation. The chemical functionalization is generally carried out by converting the silicon–hydride to silicon–carbon bonds[145]. It was concluded that hydrosilylation and carbonisation are the most employed chemical protocols to form covalent silicon–carbon bonds on the pSi surface[146,147]. In the hydrosilylation method, the stabilization takes place by adding unsaturated compounds possessing alkenes, alkynes or aldehydes groups to the freshly etched pSi using heat[148], catalyst[149] , or photochemistry[150]. Horrocks *et al.* demonstrated the stabilizing of pSi by heating it in a solution containing an alkene-terminated compound for 20 h, providing a stabilized pSi by a productive monolayer[151]. A similar study was conducted by Buriak *et al.* for converting silicon–hydride to silicon–carbon bonds on pSi[152]. However, the hydrosilylation method does not functionalize the entire pSi surface, making pSi susceptible to chemical dissolution[153]. On the other hand, the carbonization method offers a more stable pSi surface than hydrosilylation ones for a long time period because it provides almost complete surface modification with a strong silicon-carbon bond[154]. Another advantage of this method is forming functional groups on the pSi surface that are used for further chemical functionalization[155].

A study published by Salonen *et al.* first reported using thermal carbonization to stabilize pSi by decomposing acetylene gas at different temperatures, producing three types of bonds covering pSi surfaces, e.i C-H, C=C and C-OH[156]. In this method, the nature of the formed pSi surface is governed by the applied temperature; for instance, if the decomposition of acetylene gas takes place until 520 ˚C, a hydrophobic surface will be generated[157]. In contrast, a pSi surface is considered a hydrophilic surface at a temperature above 700 ˚C[158]. However, this method might not be recommended if a hydrophilic surface is required without further modification. Furthermore, stabilization at elevated temperatures raises the possibility of cracking the pSi skeleton or pore shrinkage[159], which is undesirable in some applications.

The stabilization of the pSi surface can also be performed by oxidation methods, such as thermal oxidation, ozone oxidation, or oxidation by organic solvent methods. Thermal oxidation is a commonly used method of converting pSi hydride surfaces to pSi oxide ones, which changes the surface from hydrophobic to hydrophilic. The oxidation process depends on the applied temperature and the treatment time. Leppävuori and his colleagues observed that at a temperature ranging between 250 and 400 ˚C, the oxygen atoms are inserted into the Si backbone, causing the conversion of Si-Si bonds to Si-O-Si bonds[160]. They confirmed that the inserted oxygen atom between two Si atoms expanded the pSi structure, and subsequently, a minor reduction in the pore diameter was observed. A further increase in temperature led to the oxidation of Si-H to O-Si-OH, as well as the formation of a thicker oxide layer. A total oxidation of Si-H spices on the pSi surface and uniformly distributed oxygen into the pSi backbone was observed at 600 ˚C and above[161]. For high temperatures, from 700 ˚C and above, it was reported that the surface area and the mechanical stability were reduced due to the formation of the oxide layer into the pSi skeleton[159]. The use of thermal oxidation to stabilize the pSi surface in the biosensing was also reported[162,163]. Sailor and co-workers have thermally treated the freshly etched two-layer pSi structures at 600 ˚C for 1.5 h and loaded the enzyme for online monitoring of its activity. In this Thesis, all pSi structures were stabilized by the thermal oxidization process at 600 °C in the air.

2.5 Surface Functionalization of Porous Substrates

As discussed earlier in this Chapter, AAO and pSi have unique advantages, making them ideal for biosensing[164], chemical sensing[165], or solar cell production[166]. However, the surface of AAO or pSi must be functionalized with certain materials to fulfill specific requirements. There are numerous approaches to modify or functionalize the pores of AAO/pSi, such as chemical binding[167, 168], polymerization[169,170], layer-by-layer deposition[171,172] or wetting with polymers (as a solution or melt). Several studies have demonstrated wetting the pores of AAO with polymer melts or solutions as a simple and versatile technique for producing polymer nanotubes or nanowires[173,174,175]. Steinhart and his team have conducted a study to achieve well-defined structures of the soft materials produced on the AAO and pSi[173]. They could fabricate polymeric nanotube structures of polystyrene (PS) and polymethyl methacrylate (PMMA) by wetting AAO and pSi, respectively.

The fabrication of nanostructures, such as nanotubes, nanorods, nanowires, and nanoparticles, is governed by the properties of the polymer and the geometry of the pores[176,177,178,179]. For example, a thin film, known as precursor film, is formed when low-surface energy liquids wet surfaces with high-surface energy[180]. The AAO or oxidized pSi surfaces have high surface energy[181], which can be used to prepare nanotube structures or nanowires by wetting polymer solutions and melts. However, the wetting of nanopores by applying the polymer solution or melting on the top of the porous substrate leads mainly to the formation of nanotubes rather than nanowires[182] because the difference in driving forces dominates the wetting behaviour inside the pores[183]. In other words, the nanotubes are rapidly formed due to the high adhesive forces (van der Waals interactions) compared to the cohesive forces. The latter dominates the complete filling, leading to the formation of nanowires. It was also reported that wall and complete pore wetting could occur on different timescales if the solidification process of polymeric melt/solutions does not happen[182]. Thus, the polymer (as melts/solutions) must be solidified within the nanopores to preserve nanotube structures by cooling the melts below the glass transition/crystallization temperatures or by solvent evaporation for the polymer solution[182]. Figure 2.12 shows the scenarios of the wetting of AAO with polymeric solution/melts that could happen.

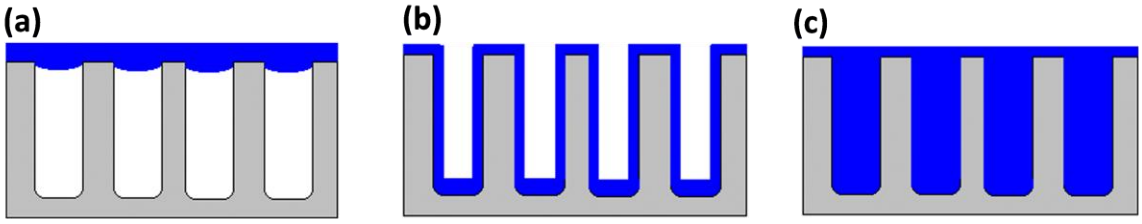

Figure 2.12: *Schematic representation of the wetting of AAO with (a) represents the initial phase when the polymer solution/melt is placed on top of the AAO surface. (b) The polymer solution/melt penetrates into the pores, forming a mesoscopic thin film. (c) If the polymer solidification does not occur, the complete filling of the pores follows stage b and forms polymeric nanorods rather than nanotubes. This Figure was Reprinted with permission from reference [184]: Redón, R.; Vázquez-Olmos, A.; Mata-Zamora, M. E.; Ordóñez-Medrano, A.; Rivera-Torres, F.; Saniger, J. M. Contact Angle Studies on Anodic Porous Alumina. Journal of Colloid and Interface Science* ***2005****, 287 (2), 664–670. Copyright 2005. Elsevier.*

However, various methods have been developed for producing polymeric nanowires, including vacuum infiltration, melt capillary and melt precursor wetting infiltration[185]. Russell and colleagues prepared nanorod and nanotube structures by melting a polymer into the 200 nm nanopores in the diameter of AAO. They investigated the wetting of AAO with PS at different annealing temperatures above the glass transition temperature of PS. Polymeric nanorods and nanotubes were obtained depending on the molecular weight of the PS used and on the annealing temperature. The study shows that short nanorod structures (~5 µm) were produced compared to the pore length (60 µm) under annealing at

130 °C for 2 h; with the extension of this process to ~12 days, the length of 60 µm nanorods was prepared; indicating a completed the wetting of the pores were reached. The authors concluded that the polymer melts wetted the pores at the slow capillary process due to the small pore diameter and the high viscosity of the polymer melts at this low temperature. In contrast, nanotube structures were observed at the elevated temperature (205 °C) within 2 h and had a length of 60 µm, the same as the pore length, indicating a complete pore wetting was reached.

A study by Lee *et al*. shows that polymer concertation impacts the morphology of nanotube structures[186]. Different concentrations of PS and PMMA were applied on the fixed AAO substrates on a spin coater at 3000 rpm. The result confirmed that a thicker wall of nanotubes was obtained with the high polymer solution and vice versa.

The modification of the AAO or pSi with polymer via the wetting approach was also used in sensing and biosensing[187,188]. Chistyakov and co-workers reported on pSi as a new type of sensor for detecting chemical compounds[189]. The proposed pSi sensor was a microcavity modified with organic polyphenylenevinylene and polyfluorene polymers via the wetting solution of pSi. The polymers dissolved in chloroform successfully infiltrated the pores of pSi without applying a vacuum or heat, which was confirmed by the shift in the luminescence spectra before and after polymer infiltration into the nanopores of pSi. This hybrid sensor was able to detect the vapors of nitroaromatic compounds.

Using biodegradable polymers to modify porous materials was considered a promising approach in biosensing, cell study, and drug delivery[190,191]. Biopolymers, such as poly(lactic acid) (PLA), have been used in many applications, such as medical implants and related applications, due to their biocompatibility, low toxicity, and easy cell adhesion[192,193]. PLA is an aliphatic polyester that can be produced from renewable resources such as corn[194]. PLA can be degraded into nontoxic residuals, making it suitable for biological applications. The degradation of PLA takes place at the ester bonds, leading to the production of carboxylic and hydroxyl end-groups on polymer chains. This process is accelerated in the presence of specific proteinases, bacteria and alkali environments[195,196,197]. In this Thesis, the modification of AAO and pSi with PLA via the wetting approach was investigated. This approach was then used for enzyme and bacterial sensing.

2.6 Reflectometric Interference Technique for Enzyme and Bacteria Detection

Reflectometric interference spectroscopy (RIfS) is a sensitive optical detection technique that relies on the interaction between white light and thin films[198]. By illuminating a thin film with white light, the light will be reflected at the film's two interfaces; both consecutively reflected light beams superimpose and cause destructive and constructive interference in dependence on the properties of light and the thin film. As a result, the reflectivity of light will be enhanced specifically at wavelengths located along with the optical modes of the so-called “Fabry-Pérot optical cavity”[199,200]. The interference of the multiple reflections of light through the Fabry-Pérot cavity will create an interference fringe pattern. This Fabry-Perot interference pattern can be used to define the refractive index and thickness of the thin film.

Thin films such as polymers and non-porous metal oxides were considered Fabry-Pérot cavities[201,202]. However, due to their limited surface area for analyte-receptor interactions, nanoporous thin films, such as pSi and AAO, have emerged as excellent alternatives, especially when combined with RIfS. Hence, the light is reflected at air/Al_2O_3 and Al_2O_3/Al interfaces in AAO and at air/SiO_2 and SiO_2/Si interfaces in pSi (Figure 2.13). The wavelength of the peak maxima in the RIfS spectrum is determined by the Fabry-Pérot equation[203]:

$$m\lambda = 2Ln_{eff} \qquad \text{..} \quad \text{(Eq. 2.19)}$$

where m is the interference order, λ is the wavelength, L is the thickness of the thin film i.e., AAO or pSi, and n_{eff} is the effective refractive index of the porous film and its void. The term “$2Ln_{eff}$” in Eq. 2.19 is called the effective optical thickness (*EOT*). Therefore, Eq. 2.19 can be written as:

$$EOT = 2Ln_{eff} \qquad \text{..} \quad \text{(Eq. 2.20)}$$

EOT can be determined by utilizing the fast Fourier transform (FFT) to the RIfS spectrum. The *EOT* value is correlated to the center of the resulting FFT Gaussian peak, as illustrated in Figure 2.13 [204].

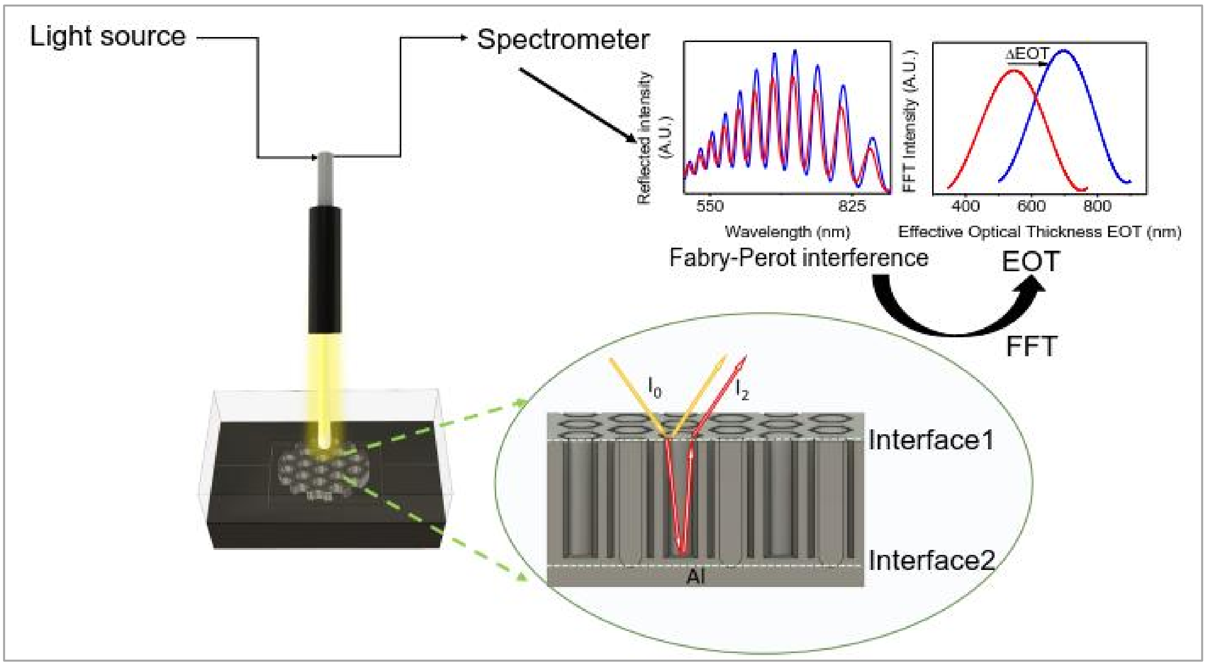

Figure 2.13: *Schematic of the principle of RIfS and the data processing for the porous film displaying the reflected light at the two film interfaces, the resulting spectra and their data processing by FFT to calculate EOT. This Figure was reproduced with permission from reference [204]: Pol, L.; Eckstein, C.; Acosta, L.; Xifré-Pérez, E.; Ferré-Borrull, J.; Marsal, L. Real-Time Monitoring of Biotinylated Molecules Detection Dynamics in Nanoporous Anodic Alumina for Bio-Sensing. Nanomaterials* ***2019****, 9 (3), 478. Copyright 2019. MDPI.*

The detection approach of RIfS coupled with porous film is based on the change in n_{eff} as a result of immobilizing materials into pores of the porous film[205]. When the air-filled pores are filled with, for example, liquid or polymers, the *EOT* increases as a result of the increased refractive index within the pores. This change leads to a red shift (longer wavelength) in the fringe pattern of the RIfS spectrum, as shown in Figure 2.14. Therefore, the change in the *EOT* was used as a trigger in the sensing method for real-time and in-situ monitoring of the binding of molecules to the pore surface.

Gooding *et al.* reported on designing a pSi sensor to detect enzyme activity[206]. The pores of the pSi were coated with a peptide and then exposed to the protease subtilisin. As a result, the peptide was enzymatically digested, which was noticed by observing the blue shift (shorter wavelength) on the reflectivity spectrum. This shift is because of the reduction of *EOT*, which is due to releasing peptide fragments from the pores upon degradation.

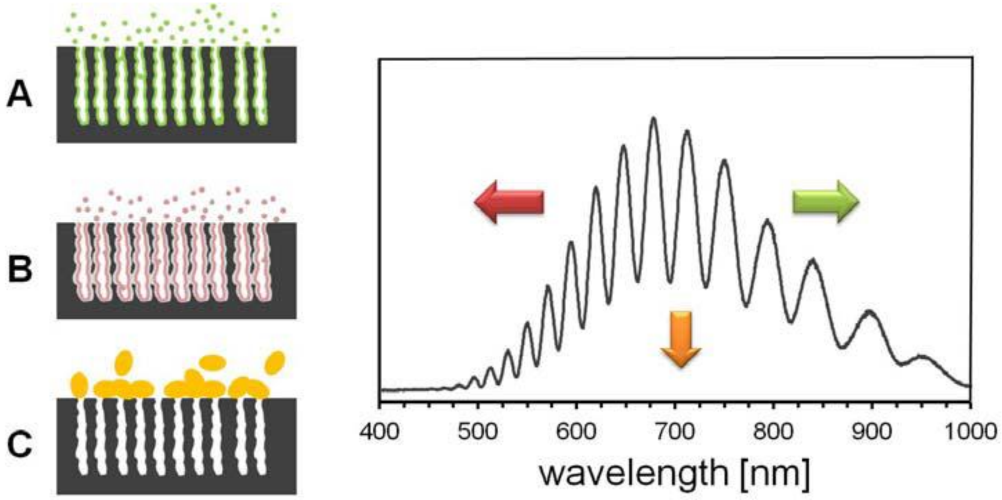

Figure 2.14: *Sensing concept based on pSi (A,B) schematic of the loading and releasing of molecules in/out the pores, which leads to a shift in the fringe pattern of the RIfS spectrum due to a change in EOT, shown on the RIfS spectrum with green and red arrows, respectively. (C) schematic of immobilizing the Analytes on the top side of pSi causes a change in the reflectivity of the light due to the refractive index contrast, as indicated by the orange arrow in the fringe pattern. This Figure was reproduced with permission from reference [207]: Pacholski, C. Photonic Crystal Sensors Based on Porous Silicon. Sensors* ***2013****, 13 (4), 4694–4713. Copyright 2013. MDPI.*

Krismastuti *et al.* used the AAO combined with RIFS to provide a label-free sensing approach for bacterial enzyme detection[30]. The authors experimentally showed that AAO, combined with a biodegradable polymer, could be used to detect pathogenic bacteria by their secreted enzymes. These authors used proteinase K to degrade the poly-L-lysine immobilized inside the AAO pores using a layer-by-layer approach. The deposition and enzymatic degradation of the polymer were monitored in real time by RIfS. The change in the *EOT* value was recorded. The data exhibited that *EOT* increased upon polymer deposition due to an increased refractive index inside the pores.

In contrast, *EOT* decreased when the AAO sensor was exposed to the enzyme solution. The reduction in *EOT* values was confirmed by a measurable blue shift on the RIfS spectrum. They also tested the sensor on human wound fluid samples; the *EOT* dropped after enzyme treatment, which indicated the successful reduction of the polymer amount (Figure 2.15).

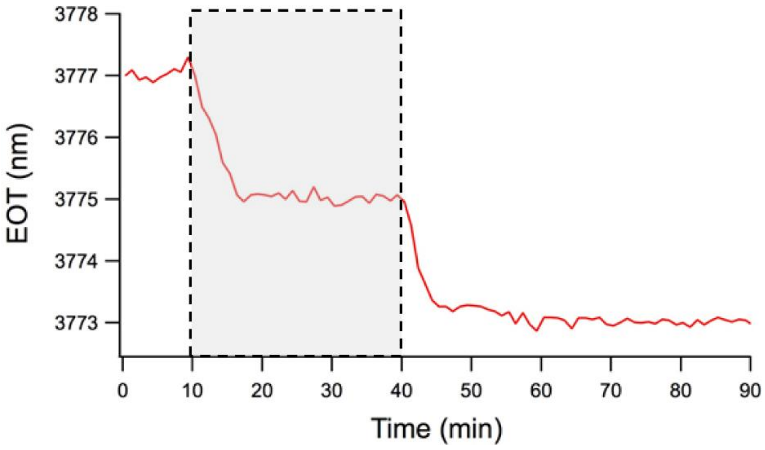

Figure 2.15: *Sensorgram for enzymatic degradation of polymer in the human wound fluid sample. The coated AAO sensor with polymer was exposed to a wound fluid spike with proteinase K enzyme for 30 min. This Figure was reproduced with permission from reference [30]: Krismastuti, F. S. H.; Bayat, H.; Voelcker, N. H.; Schönherr, H. Real Time Monitoring of Layer-by-Layer Polyelectrolyte Deposition and Bacterial Enzyme Detection in Nanoporous Anodized Aluminum Oxide. Analytical Chemistry **2015**, 87 (7), 3856–3863. Copyright 2015. American Chemical Society.*

As discussed above, the change in *EOT* results from the change in n_{eff}, which depends on the refractive index of the pores' void. Fortunately, the change in the refractive index inside the pores (void) can be determined by applying the Maxwell-Garnett approximation[208,209,210,211], which is expressed in Eq. 2.21. Based on this model, the n_{eff} can be used to predict how much the *EOT* would shift if the void is replaced with different materials, for instance, if water infiltrates the air-filled pores of AAO. The *EOT* can be calculated by knowing the porosity, refractive indices, pore length of AAO, and the refractive index of the void. The calculated *EOT* can then be compared with the measured *EOT* (experimental *EOT*) to determine the volume fraction (fractional pore filling in %) of loaded or released materials, such as polymer from AAO pores.

$$n^2_{eff} = n^2_{Al_2O_3} \frac{2n^2_{Al_2O_3} + n^2_{void} + 2P\,(n^2_{void} - n^2_{Al_2O_3})}{2n^2_{Al_2O_3} + n^2_{void} - P\,(n^2_{void} - n^2_{Al_2O_3})} \quad \text{................ (Eq. 2.21)}$$

where P is the porosity of AAO, $n_{Al_2O_3}$, n_{void} are refractive indices of AAO and the void, respectively.

2.7 References

---

[1] MacFadden, D. R.; McGough, S. F.; Fisman, D.; Santillana, M.; Brownstein, J. S. Antibiotic Resistance Increases with Local Temperature. *Nature Climate Change* **2018**, *8* (6), 510–514. https://doi.org/10.1038/s41558-018-0161-6.

[2] Kim, S.; Kim, S. Bacterial Pathogen Detection by Conventional Culture-based and Recent Alternative (Polymerase Chain Reaction, Isothermal Amplification, Enzyme Linked Immunosorbent Assay, Bacteriophage Amplification, and Gold Nanoparticle Aggregation) Methods in Food Samples: A Review. *Journal of Food Safety* **2020**, *41* (1). https://doi.org/10.1111/jfs.12870.

[3] Iqbal, S. S.; Mayo, M. W.; Bruno, J. G.; Bronk, B. V.; Batt, C. A.; Chambers, J. P. A Review of Molecular Recognition Technologies for Detection of Biological Threat Agents. *Biosensors and Bioelectronics* **2000**, *15* (11–12), 549–578. https://doi.org/10.1016/s0956-5663(00)00108-1.

[4] Leoni, E.; De Luca, G.; Legnani, P. P.; Sacchetti, R.; Stampi, S.; Zanetti, F. Legionella Waterline Colonization: Detection of Legionella Species in Domestic, Hotel and Hospital Hot Water Systems. *Journal of Applied Microbiology* **2005**, *98* (2), 373–379. https://doi.org/10.1111/j.1365-2672.2004.02458.x.

[5] Tomasiewicz, D. M.; Hotchkiss, D. K.; Reinbold, G. W.; Read, R. B.; Hartman, P. A. The Most Suitable Number of Colonies on Plates for Counting. *Journal of Food Protection* **1980**, *43* (4), 282–286. https://doi.org/10.4315/0362-028x-43.4.282.

[6] Bej, A. K.; Mahbubani, M. H.; Dicesare, J. L.; Atlas, R. M. Polymerase Chain Reaction-Gene Probe Detection of Microorganisms by Using Filter-Concentrated Samples. *Applied and Environmental Microbiology* **1991**, *57* (12), 3529–3534. https://doi.org/10.1128/aem.57.12.3529-3534.1991.

[7] Caméléna, F.; Moy, A.-C.; Dudoignon, E.; Poncin, T.; Deniau, B.; Guillemet, L.; Le Goff, J.; Budoo, M.; Benyamina, M.; Chaussard, M.; Coutrot, M.; Lafaurie, M.; Plaud, B.; Mebazaa, A.; Depret, F.; Berçot, B. Performance of a Multiplex Polymerase Chain Reaction Panel for Identifying Bacterial Pathogens Causing Pneumonia in Critically Ill Patients with COVID-19. *Diagnostic Microbiology and Infectious Disease* **2021**, *99* (1), 115183. https://doi.org/10.1016/j.diagmicrobio.2020.115183.

[8] Tabatabaei, M. S.; Ahmed, M. Enzyme-Linked Immunosorbent Assay (ELISA). *Methods in Molecular Biology* **2022**, 115–134. https://doi.org/10.1007/978-1-0716-2376-3_10.

[9] Opota, O.; Croxatto, A.; Prod'hom, G.; Greub, G. Blood Culture-Based Diagnosis of Bacteraemia: State of the Art. *Clinical Microbiology and Infection* **2015**, *21* (4), 313–322. https://doi.org/10.1016/j.cmi.2015.01.003.

[10] Lazcka, O.; Campo, F. J. D.; Muñoz, F. X. Pathogen Detection: A Perspective of Traditional Methods and Biosensors. *Biosensors and Bioelectronics* **2007**, *22* (7), 1205–1217. https://doi.org/10.1016/j.bios.2006.06.036.

---

[11] Seinige, D.; Krischek, C.; Klein, G.; Kehrenberg, C. Comparative Analysis and Limitations of Ethidium Monoazide and Propidium Monoazide Treatments for the Differentiation of Viable and Nonviable Campylobacter Cells. *Applied and Environmental Microbiology* **2014**, *80* (7), 2186–2192. https://doi.org/10.1128/aem.03962-13.

[12] Toze, S. PCR and the Detection of Microbial Pathogens in Water and Wastewater. *Water Research* **1999**, *33* (17), 3545–3556. https://doi.org/10.1016/s0043-1354(99)00071-8.

[13] Shih, C.-M.; Chang, C.-L.; Hsu, M.-Y.; Lin, J.-Y.; Kuan, C.-M.; Wang, H.-K.; Huang, C.-T.; Chung, M.-C.; Huang, K.-C.; Hsu, C.-E.; Wang, C.-Y.; Shen, Y.-C.; Cheng, C.-M. Paper-Based ELISA to Rapidly Detect Escherichia Coli. *Talanta* **2015**, *145*, 2–5. https://doi.org/10.1016/j.talanta.2015.07.051.

[14] Ksiazek, T. G.; West, C. P.; Rollin, P. E.; Jahrling, P. B.; Peters, C. J. ELISA for the Detection of Antibodies to Ebola Viruses. *The Journal of Infectious Diseases* **1999**, *179* (s1), S192–S198. https://doi.org/10.1086/514313.

[15] MacMullan, M. A.; Ibrayeva, A.; Trettner, K.; Deming, L.; Das, S.; Tran, F.; Moreno, J. R.; Casian, J. G.; Chellamuthu, P.; Kraft, J.; Kozak, K.; Turner, F. E.; Slepnev, V. I.; Le Page, L. M. ELISA Detection of SARS-CoV-2 Antibodies in Saliva. *Scientific Reports* **2020**, *10* (1). https://doi.org/10.1038/s41598-020-77555-4.

[16] Du, T.; Zhu, G.; Wu, X.; Fang, J.; Zhou, E.-M. <p>Biotinylated Single-Domain Antibody-Based Blocking ELISA for Detection of Antibodies Against Swine Influenza Virus</P>. *International Journal of Nanomedicine* **2019**, *Volume 14*, 9337–9349. https://doi.org/10.2147/ijn.s218458.

[17] Majdinasab, M.; Hayat, A.; Marty, J. L. Aptamer-Based Assays and Aptasensors for Detection of Pathogenic Bacteria in Food Samples. *TrAC Trends in Analytical Chemistry* **2018**, *107*, 60–77. https://doi.org/10.1016/j.trac.2018.07.016.

[18] Richter, Ł.; Janczuk-Richter, M.; Niedziółka-Jönsson, J.; Paczesny, J.; Hołyst, R. Recent Advances in Bacteriophage-Based Methods for Bacteria Detection. *Drug Discovery Today* **2018**, *23* (2), 448–455. https://doi.org/10.1016/j.drudis.2017.11.007.

[19] Meng, J.; Doyle, M. P. Introduction. Microbiological Food Safety. *Microbes and Infection* **2002**, *4* (4), 395–397. https://doi.org/10.1016/s1286-4579(02)01552-6.

[20] Gopal, A.; Yan, L.; Kashif, S.; Munshi, T.; Roy, V. A. L.; Voelcker, N. H.; Chen, X. Biosensors and Point-of-Care Devices for Bacterial Detection: Rapid Diagnostics Informing Antibiotic Therapy. *Advanced Healthcare Materials* **2021**, *11* (3). https://doi.org/10.1002/adhm.202101546.

[21] Amouzadeh Tabrizi, M.; Ferré-Borrull, J.; Marsal, L. F. Remote Sensing of Salmonella-Specific DNA Fragment by Using Nanoporous Alumina Modified with the Single-Strand DNA Probe. *Sensors and Actuators B: Chemical* **2020**, *304*, 127302. https://doi.org/10.1016 /j.snb.2019.127302.

[22] Zhang, C.; Paria, D.; Semancik, S.; Barman, I. Composite-Scattering Plasmonic Nanoprobes for Label-Free, Quantitative Biomolecular Sensing. *Small* **2019**, *15* (38). https://doi.org/10.1002/smll.201901165.

---

[23] Rajeev, G.; Xifre-Perez, E.; Prieto Simon, B.; Cowin, A. J.; Marsal, L. F.; Voelcker, N. H. A Label-Free Optical Biosensor Based on Nanoporous Anodic Alumina for Tumour Necrosis Factor-Alpha Detection in Chronic Wounds. *Sensors and Actuators B: Chemical* **2018**, *257*, 116–123. https://doi.org/10.1016/j.snb.2017.10.156.

[24] Santos, A.; Balderrama, V. S.; Alba, M.; Formentín, P.; Ferré-Borrull, J.; Pallarès, J.; Marsal, L. F. Nanoporous Anodic Alumina Barcodes: Toward Smart Optical Biosensors. *Advanced Materials* **2012**, *24* (8), 1050–1054. https://doi.org/10.1002/adma.201104490.

[25] Antunez, E. E.; Mahon, C. S.; Tong, Z.; Voelcker, N. H.; Müllner, M. A Regenerable Biosensing Platform for Bacterial Toxins. *Biomacromolecules* **2020**, *22* (2), 441–453. https://doi.org/10.1021/acs.biomac.0c01318.

[26] Walcarius, A. Mesoporous Materials and Electrochemistry. *Chemical Society Reviews* **2013**, *42* (9), 4098. https://doi.org/10.1039/c2cs35322a.

[27] Van Der Voort, P.; Esquivel, D.; De Canck, E.; Goethals, F.; Van Driessche, I.; Romero-Salguero, F. J. Periodic Mesoporous Organosilicas: From Simple to Complex Bridges; a Comprehensive Overview of Functions, Morphologies and Applications. *Chem. Soc. Rev.* **2013**, *42* (9), 3913–3955. https://doi.org/10.1039/c2cs35222b.

[28] Wang, J.; Zhou, Y.; Jiang, L. Bio-Inspired Track-Etched Polymeric Nanochannels: Steady-State Biosensors for Detection of Analytes. *ACS Nano* **2021**, *15* (12), 18974–19013. https://doi.org/10.1021/acsnano.1c08582.

[29] Alvarez, S. D.; Schwartz, M. P.; Migliori, B.; Rang, C. U.; Chao, L.; Sailor, M. J. Using a Porous Silicon Photonic Crystal for Bacterial Cell-based Biosensing. *physica status solidi (a)* **2007**, *204* (5), 1439–1443. https://doi.org/10.1002/pssa.200674379.

[30] Krismastuti, F. S. H.; Bayat, H.; Voelcker, N. H.; Schönherr, H. Real Time Monitoring of Layer-by-Layer Polyelectrolyte Deposition and Bacterial Enzyme Detection in Nanoporous Anodized Aluminum Oxide. *Analytical Chemistry* **2015**, *87* (7), 3856–3863. https://doi.org/10.1021/ac504626m.

[31] Pol, L.; Eckstein, C.; Acosta, L.; Xifré-Pérez, E.; Ferré-Borrull, J.; Marsal, L. Real-Time Monitoring of Biotinylated Molecules Detection Dynamics in Nanoporous Anodic Alumina for Bio-Sensing. *Nanomaterials* **2019**, *9* (3), 478. https://doi.org/10.3390/nano9030478.

[32] Kumeria, T.; Santos, A.; Losic, D. Nanoporous Anodic Alumina Platforms: Engineered Surface Chemistry and Structure for Optical Sensing Applications. *Sensors* **2014**, *14* (7), 11878–11918. https://doi.org/10.3390/s140711878.

[33] Santos, A.; Vojkuvka, L.; Alba, M.; Balderrama, V. S.; Ferré-Borrull, J.; Pallarès, J.; Marsal, L. F. Understanding and Morphology Control of Pore Modulations in Nanoporous Anodic Alumina by Discontinuous Anodization. *physica status solidi (a)* **2012**, *209* (10), 2045–2048. https://doi.org/10.1002/pssa.201228150.

[34] Mariani, S.; Strambini, L. M.; Barillaro, G. Femtomole Detection of Proteins Using a Label-Free Nanostructured Porous Silicon Interferometer for Perspective Ultrasensitive Biosensing. *Analytical Chemistry* **2016**, *88* (17), 8502–8509. https://doi.org/10.1021/acs.analchem.6b01228.

---

[35] Raoufi, M.; Schönherr, H. Improved Synthesis of Anodized Aluminum Oxide with Modulated Pore Diameters for the Fabrication of Polymeric Nanotubes. *RSC Advances* **2013**, *3* (32), 13429. https://doi.org/10.1039/c3ra41165f.

[36] Masuda, H.; Fukuda, K. Ordered Metal Nanohole Arrays Made by a Two-Step Replication of Honeycomb Structures of Anodic Alumina. *Science* **1995**, *268* (5216), 1466–1468. https://doi.org/10.1126/science.268.5216.1466.

[37] Asai, N.; Shimizu, T.; Shingubara, S.; Ito, T. Fabrication of Highly Sensitive QCM Sensor Using AAO Nanoholes and Its Application in Biosensing. *Sensors and Actuators B: Chemical* **2018**, *276*, 534–539. https://doi.org/10.1016/j.snb.2018.08.094.

[38] Ferré-Borrull, J.; Xifré-Pérez, E.; Pallarès, J.; Marsal, L. F. Optical Properties of Nanoporous Anodic Alumina and Derived Applications. *Nanoporous Alumina* **2015**, 185–217. https://doi.org/10.1007/978-3-319-20334-8_6.

[39] Kumeria, T.; Rahman, M. M.; Santos, A.; Ferré-Borrull, J.; Marsal, L. F.; Losic, D. Nanoporous Anodic Alumina Rugate Filters for Sensing of Ionic Mercury: Toward Environmental Point-of-Analysis Systems. *ACS Applied Materials & Interfaces* **2014**, *6* (15), 12971–12978. https://doi.org/10.1021/am502882d.

[40] Das, D.; Alhusaini, Q. F. M.; Kaur, K.; Raoufi, M.; Schönherr, H. Enzyme-Responsive Biopolymeric Nanogel Fibers by Extrusion: Engineering of High-Surface-Area Hydrogels and Application in Bacterial Enzyme Detection. *ACS Applied Materials & Interfaces* **2021**, *13* (11), 12928–12940. https://doi.org/10.1021/acsami.1c00136.

[41] Pla, L.; Santiago-Felipe, S.; Tormo-Mas, M. Á.; Ruiz-Gaitán, A.; Pemán, J.; Valentín, E.; Sancenón, F.; Aznar, E.; Martínez-Máñez, R. Oligonucleotide-Capped Nanoporous Anodic Alumina Biosensor as Diagnostic Tool for Rapid and Accurate Detection of Candida Auris in Clinical Samples. *Emerging Microbes & Infections* **2021**, *10* (1), 407–415. https://doi.org/10.1080/22221751.2020.1870411.

[42] Kumeria, T.; Losic, D. Reflective Interferometric Gas Sensing Using Nanoporous Anodic Aluminium Oxide (AAO). *physica status solidi (RRL) – Rapid Research Letters* **2011**, *5* (10–11), 406–408. https://doi.org/10.1002/pssr.201105425.

[43] Kumeria, T.; Parkinson, L.; Losic, D. A Nanoporous Interferometric Micro-Sensor for Biomedical Detection of Volatile Sulphur Compounds. *Nanoscale Research Letters* **2011**, *6* (1). https://doi.org/10.1186/1556-276x-6-634.

[44] Kumeria, T.; Losic, D. Controlling Interferometric Properties of Nanoporous Anodic Aluminium Oxide. *Nanoscale Research Letters* **2012**, *7* (1). https://doi.org/10.1186/1556-276x-7-88.

[45] Li, S.-J.; Xia, N.; Yuan, B.-Q.; Du, W.-M.; Sun, Z.-F.; Zhou, B.-B. A Novel DNA Sensor Using a Sandwich Format by Electrochemical Measurement of Marker Ion Fluxes across Nanoporous Alumina Membrane. *Electrochimica Acta* **2015**, *159*, 234–241. https://doi.org/10.1016/j.electacta.2015.02.010.

---

[46] Vlassiouk, I.; Takmakov, P.; Smirnov, S. Sensing DNA Hybridization via Ionic Conductance through a Nanoporous Electrode. *Langmuir* **2005**, *21* (11), 4776–4778. https://doi.org/10.1021/la0471644.

[47] Dhathathreyan, A. Real-Time Monitoring of Invertase Activity Immobilized in Nanoporous Aluminum Oxide. *The Journal of Physical Chemistry B* **2011**, *115* (20), 6678–6682. https://doi.org/10.1021/jp1122085.

[48] Massad-Ivanir, N.; Segal, E. Porous Silicon for Bacteria Detection. *Porous Silicon for Biomedical Applications* **2014**, 286–303. https://doi.org/10.1533/9780857097156.2.286.

[49] Srinivasan, S.; Leonard, F.; Kuncewicz, T. M.; Godin, B. In Vivo Imaging Assessment of Porous Silicon. *Porous Silicon for Biomedical Applications* **2014**, 223–252. https://doi.org/10.1533/9780857097156.2.223.

[50] Rai, V.; Deng, J.; Toh, C.-S. Electrochemical Nanoporous Alumina Membrane-Based Label-Free DNA Biosensor for the Detection of Legionella Sp. *Talanta* **2012**, *98*, 112–117. https://doi.org/10.1016/j.talanta.2012.06.055.

[51] Escosura-Muñiz, A. de la; Ivanova, K.; Tzanov, T. Electrical Evaluation of Bacterial Virulence Factors Using Nanopores. *ACS Applied Materials & Interfaces* **2019**, *11* (14), 13140–13146. https://doi.org/10.1021/acsami.9b02382.

[52] Lazzara, T. D.; Lau, K. H. A.; Knoll, W.; Janshoff, A.; Steinem, C. Macromolecular Shape and Interactions in Layer-by-Layer Assemblies within Cylindrical Nanopores. *Beilstein Journal of Nanotechnology* **2012**, *3*, 475–484. https://doi.org/10.3762/bjnano.3.54.

[53] Jin, J.-H.; Zhang, D.; Alocilja, E. C.; Grooms, D. L. Label-Free DNA Sensor on Nanoporous Silicon-Polypyrrole Chip for Monitoring Salmonella Species. *IEEE Sensors Journal* **2008**, *8* (6), 891–895. https://doi.org/10.1109/jsen.2008.923182.

[54] Mathew, F. P.; Alocilja, E. C. Porous Silicon-Based Biosensor for Pathogen Detection. *Biosensors and Bioelectronics* **2005**, *20* (8), 1656–1661. https://doi.org/10.1016/j.bios.2004.08.006.

[55] Tücking, K.; Vasani, R. B.; Cavallaro, A. A.; Voelcker, N. H.; Schönherr, H.; Prieto-Simon, B. Porous Silicon: Hyaluronic Acid–Modified Porous Silicon Films for the Electrochemical Sensing of Bacterial Hyaluronidase. *Macromolecular Rapid Communications* **2018**, *39* (19). https://doi.org/10.1002/marc.201870044.

[56] Vercauteren, R.; Leprince, A.; Nuytten, M.; Mahillon, J.; Francis, L. A. Indirect Detection of Bacteria on Optically Enhanced Porous Silicon Membrane-Based Biosensors Using Selective Lytic Enzymes. *ACS Sensors* **2023**, *8* (7), 2627–2634. https://doi.org/10.1021/acssensors.3c00467.

[57] Alvarez, S. D.; Schwartz, M. P.; Migliori, B.; Rang, C. U.; Chao, L.; Sailor, M. J. Using a Porous Silicon Photonic Crystal for Bacterial Cell-based Biosensing. *physica status solidi (a)* **2007**, *204* (5), 1439–1443. https://doi.org/10.1002/pssa.200674379.

[58] Kim, D.-K.; Kim, D. M.; Yoo, S. M.; Lee, S. Y. Controllable Gold-Capped Nanoporous Anodic Alumina Chip for Label-Free, Specific Detection of Bacterial Cells. *RSC Advances* **2017**, *7* (30), 18815–18820. https://doi.org/10.1039/c6ra27130h.

---

[59] Zhou, C.-X.; Mo, R.-J.; Chen, Z.-M.; Wang, J.; Shen, G.-Z.; Li, Y.-P.; Quan, Q.-G.; Liu, Y.; Li, C.-Y. Quantitative Label-Free Listeria Analysis Based on Aptamer Modified Nanoporous Sensor. *ACS Sensors* **2016**, *1* (8), 965–969. https://doi.org/10.1021/acssensors.6b00333.

[60] Massad-Ivanir, N.; Mirsky, Y.; Nahor, A.; Edrei, E.; Bonanno-Young, L. M.; Ben Dov, N.; Sa'ar, A.; Segal, E. Trap and Track: Designing Self-Reporting Porous Si Photonic Crystals for Rapid Bacteria Detection. *The Analyst* **2014**, *139* (16), 3885–3894. https://doi.org/10.1039/c4an00364k.

[61] Massad-Ivanir, N.; Shtenberg, G.; Raz, N.; Gazenbeek, C.; Budding, D.; Bos, M. P.; Segal, E. Porous Silicon-Based Biosensors: Towards Real-Time Optical Detection of Target Bacteria in the Food Industry. *Scientific Reports* **2016**, *6* (1). https://doi.org/10.1038/srep38099.

[62] Mirsky, Y.; Nahor, A.; Edrei, E.; Massad-Ivanir, N.; Bonanno, L. M.; Segal, E.; Sa'ar, A. Optical Biosensing of Bacteria and Cells Using Porous Silicon Based, Photonic Lamellar Gratings. *Applied Physics Letters* **2013**, *103* (3). https://doi.org/10.1063/1.4813740.

[63] Keller, F.; Hunter, M. S.; Robinson, D. L. Structural Features of Oxide Coatings on Aluminum. *Journal of The Electrochemical Society* **1953**, *100* (9), 411. https://doi.org/10.1149/1.2781142.

[64] Eftekhari, A.; Nanostructured Materials in Electrochemistry. *Materials Today* **2008**, *11* (4), 58. https://doi.org/10.1016/s1369-7021(08)70059-2.

[65] Lee, W.; Park, S.-J. Porous Anodic Aluminum Oxide: Anodization and Templated Synthesis of Functional Nanostructures. *Chemical Reviews* **2014**, *114* (15), 7487–7556. https://doi.org/10.1021/cr500002z.

[66] Jeong, C.; Jung, J.; Sheppard, K.; Choi, C.-H. Control of the Nanopore Architecture of Anodic Alumina via Stepwise Anodization with Voltage Modulation and Pore Widening. *Nanomaterials* **2023**, *13* (2), 342. https://doi.org/10.3390/nano13020342.

[67] Md Jani, A. M.; Losic, D.; Voelcker, N. H. Nanoporous Anodic Aluminium Oxide: Advances in Surface Engineering and Emerging Applications. *Progress in Materials Science* **2013**, *58* (5), 636–704. https://doi.org/10.1016/j.pmatsci.2013.01.002.

[68] Raoufi, M.; Tranchida, D.; Schönherr, H. Pushing the Size Limits in the Replication of Nanopores in Anodized Aluminum Oxide via the Layer-by-Layer Deposition of Polyelectrolytes. Langmuir 2012, 28 (26), 10091–10096. https://doi.org/10.1021/la3017062.

[69] Bayat, H.; Raoufi, M.; Zamrik, I.; Schönherr, H. Poly(Diethylene Glycol Methylether Methacrylate) Brush-Functionalized Anodic Alumina Nanopores: Curvature-Dependent Polymerization Kinetics and Nanopore Filling. *Langmuir* **2020**, *36* (10), 2663–2672. https://doi.org/10.1021/acs.langmuir.9b03700.

[70] Schulte, A.; Alhusaini, Q.; Awan, A.; Schönherr, H. Anodic Aluminum Oxide Membrane Assisted Extrusion of Polymer Solutions for Hydrogel Formation. *Macromolecular Symposia* **2023**, *409* (1). https://doi.org/10.1002/masy.202200208.

[71] Petukhov, D. I.; Buldakov, D. A.; Tishkin, A. A.; Lukashin, A. V.; Eliseev, A. A. Liquid Permeation and Chemical Stability of Anodic Alumina Membranes. *Beilstein Journal of Nanotechnology* **2017**, *8*, 561–570. https://doi.org/10.3762/bjnano.8.60.

---

[72] Sulka, G. D. Highly Ordered Anodic Porous Alumina Formation by Self-Organized Anodizing. *In Nanostructured Materials in Electrochemistry*; Eftekhari, A., Ed.; *Wiley-VCH*: Weinheim, Germany, **2008**; pp 1−116.

[73] Zhu, Z.; Garcia-Gancedo, L.; Liu, Q.; Flewitt, A.; Milne, W. I.; Moussy, F. Size-Tunable Porous Anodic Alumina Nano-Structure for Biosensing. *Soft Nanoscience Letters* **2011**, *01* (03), 55–60. https://doi.org/10.4236/snl.2011.13010.

[74] Poinern, G. E. J.; Ali, N.; Fawcett, D. Progress in Nano-Engineered Anodic Aluminum Oxide Membrane Development. *Materials* **2011**, *4* (3), 487–526. https://doi.org/10.3390/ma4030487.

[75] Belwalkar, A.; Grasing, E.; Vangeertryden, W.; Huang, Z.; Misiolek, W. Effect of Processing Parameters on Pore Structure and Thickness of Anodic Aluminum Oxide (AAO) Tubular Membranes. *Journal of Membrane Science* **2008**, *319* (1–2), 192–198. https://doi.org/10.1016/j.memsci.2008.03.044.

[76] Haberkorn, N.; Gutmann, J. S.; Theato, P. Template-Assisted Fabrication of Free-Standing Nanorod Arrays of a Hole-Conducting Cross-Linked Triphenylamine Derivative: Toward Ordered Bulk-Heterojunction Solar Cells. *ACS Nano* **2009**, *3* (6), 1415–1422. https://doi.org/10.1021/nn900207a.

[77] Bai, A.; Hu, C.-C.; Yang, Y.-F.; Lin, C.-C. Pore Diameter Control of Anodic Aluminum Oxide with Ordered Array of Nanopores. *Electrochimica Acta* **2008**, *53* (5), 2258–2264. https://doi.org/10.1016/j.electacta.2007.09.039.

[78] Zaraska, L.; Sulka, G. D.; Szeremeta, J.; Jaskuła, M. Porous Anodic Alumina Formed by Anodization of Aluminum Alloy (AA1050) and High Purity Aluminum. *Electrochimica Acta* **2010**, *55* (14), 4377–4386. https://doi.org/10.1016/j.electacta.2009.12.054.

[79] Sellarajan, B.; Sharma, M.; Ghosh, S. K.; Nagaraja, H. S.; Barshilia, H. C.; Chowdhury, P. Effect of Electrolyte Temperature on the Formation of Highly Ordered Nanoporous Alumina Template. *Microporous and Mesoporous Materials* **2016**, *224*, 262–270. https://doi.org/ 10.1016/ j.micromeso.2015.12.045.

[80] Ono, S.; Saito, M.; Ishiguro, M.; Asoh, H. Controlling Factor of Self-Ordering of Anodic Porous Alumina. *Journal of The Electrochemical Society* **2004**, *151* (8), B473. https://doi.org/10.1149/1.1767838.

[81] Dobosz, I. Influence of the Anodization Conditions and Chemical Treatment on the Formation of Alumina Membranes with Defined Pore Diameters. *Journal of Porous Materials* **2021**, *28* (4), 1011–1022. https://doi.org/10.1007/s10934-021-01052-w.

[82] Jessensky, O.; Müller, F.; Gösele, U. Self-Organized Formation of Hexagonal Pore Arrays in Anodic Alumina. *Applied Physics Letters* **1998**, *72* (10), 1173–1175. https://doi.org/10.1063/1.121004.

[83] Lee, W.; Ji, R.; Gösele, U.; Nielsch, K. Fast Fabrication of Long-Range Ordered Porous Alumina Membranes by Hard Anodization. *Nature Materials* **2006**, *5* (9), 741–747. https://doi.org/10.1038/nmat1717.

---

[84] Liu, J.; Liu, S.; Zhou, H.; Xie, C.; Huang, Z.; Fu, C.; Kuang, Y. Preparation of Self-Ordered Nanoporous Anodic Aluminum Oxide Membranes by Combination of Hard Anodization and Mild Anodization. *Thin Solid Films* **2014**, *552*, 75–81. https://doi.org/ 10.1016/ j.tsf.2013.12.023.

[85] Voon, C. H.; Derman, M. N.; Hashim, U.; Ahmad, K. R.; Ho, L. N. A Simple One-Step Anodising Method for the Synthesis of Ordered Porous Anodic Alumina. *Journal of Experimental Nanoscience* **2012**, *9* (2), 106–112. https://doi.org /10.1080/ 17458080. 2011.630151.

[86] Li, X.; Ni, S.; Zhou, X. Highly Ordered Porous Anodic Alumina with Large Diameter Pores Fabricated by an Improved Two-Step Anodization Approach. *Journal of Nanoscience and Nanotechnology* **2015**, *15* (2), 1725–1731. https://doi.org/10.1166/jnn.2015.9025.

[87] Ateş, S.; Baran, E.; Yazıcı, B. The Nanoporous Anodic Alumina Oxide Formed by Two-Step Anodization. *Thin Solid Films* **2018**, *648*, 94–102. https://doi.org/10.1016/j.tsf.2018.01.013.

[88] Lim, J.-H.; Wiley, J. B. Controlling Pore Geometries and Interpore Distances of Anodic Aluminum Oxide Templates via Three-Step Anodization. *Journal of Nanoscience and Nanotechnology* **2015**, *15* (1), 633–641. https://doi.org/10.1166/jnn.2015.9245.

[89] Mir, M. A.; Shah, M. A.; Ganai, P. A. Nanoporous Anodic Alumina (NAA) Prepared in Different Electrolytes with Different Pore Sizes for Humidity Sensing. *Journal of Solid State Electrochemistry* **2020**, *24* (7), 1679–1686. https://doi.org/10.1007/s10008-020-04683-2.

[90] Absalan, G.; Barzegar, S.; Moradi, M.; Behaein, S. Fabricating Al2O3-Nanopores Array by an Ultrahigh Voltage Two-Step Anodization Technique: Investigating the Effect of Voltage Rate and Al Foil Thickness on Geometry and Ordering of the Array. *Materials Chemistry and Physics* **2017**, *199*, 265–271. https://doi.org/10.1016/j.matchemphys.2017.07.015.

[91] Zhang, J.; Kielbasa, J. E.; Carroll, D. L. Controllable Fabrication of Porous Alumina Templates for Nanostructures Synthesis. *Materials Chemistry and Physics* **2010**, *122* (1), 295–300. https://doi.org/10.1016/j.matchemphys.2010.02.023.

[92] Orosco, M. M.; Pacholski, C.; Sailor, M. J. Real-Time Monitoring of Enzyme Activity in a Mesoporous Silicon Double Layer. *Nature Nanotechnology* **2009**, *4* (4), 255–258. https://doi.org/10.1038/nnano.2009.11.

[93] Nanda Kumar, D.; Freidman, I.; Sionov, E.; Shtenberg, G. Porous Silicon Fabry-Pérot Interferometer Designed for Sensitive Detection of Aflatoxin B1 in Field Crops. *Food Chemistry* **2023**, *405*, 134980. https://doi.org/10.1016/j.foodchem.2022.134980.

[94] Jane, A.; Dronov, R.; Hodges, A.; Voelcker, N. H. Porous Silicon Biosensors on the Advance. *Trends in Biotechnology* **2009**, *27* (4), 230–239. https://doi.org/ 10.1016/j.tibtech. 2008.12.004.

[95] Uhlir, A. Electrolytic Shaping of Germanium and Silicon. *Bell System Technical Journal* **1956**, *35* (2), 333–347. https://doi.org/10.1002/j.1538-7305.1956.tb02385.x.

[96] Turner, D. R. Electropolishing Silicon in Hydrofluoric Acid Solutions. *Journal of The Electrochemical Society* **1958**, *105* (7), 402. https://doi.org/10.1149/1.2428873.

---

[97] Smith, R. L.; Collins, S. D. Porous Silicon Formation Mechanisms. *Journal of Applied Physics* **1992**, *71* (8), R1–R22. https://doi.org/10.1063/1.350839.

[98] Lehmann, V.; Gösele, U. Porous Silicon Formation: A Quantum Wire Effect. *Applied Physics Letters* **1991**, *58* (8), 856–858. https://doi.org/10.1063/1.104512.

[99] Ressine, A.; Ekström, S.; Marko-Varga, G.; Laurell, T. Macro-/Nanoporous Silicon as a Support for High-Performance Protein Microarrays. *Analytical Chemistry* **2003**, *75* (24), 6968–6974. https://doi.org/10.1021/ac034425q.

[100] Canham, L. Handbook of Porous Silicon, second Edition, **2018**, *Springer*, Germany.

[101] Mariani, S.; Pino, L.; Strambini, L. M.; Tedeschi, L.; Barillaro, G. 10 000-Fold Improvement in Protein Detection Using Nanostructured Porous Silicon Interferometric Aptasensors. *ACS Sensors* **2016**, *1* (12), 1471–1479. https://doi.org/10.1021/acssensors.6b00634.

[102] Salonen, J.; Kaukonen, A. M.; Hirvonen, J.; Lehto, V.-P. Mesoporous Silicon in Drug Delivery Applications. *Journal of Pharmaceutical Sciences* **2008**, *97* (2), 632–653. https://doi.org/10.1002/jps.20999.

[103] Sailor, M.J. Porous Silicon in Practice: Preparation, Characterization and Applications, First Edition, **2012**, *Wiley-VCH*, Weinheim, Germany.

[104] Sailor, M.J. Chemical Reactivity and Surface Chemistry of Porous Silicon. Handbook of Porous Silicon,**2014** *Springer*, Cham, Switzerland. https://doi.org/10.1007/978-3-319-04508-5_37-1.

[105] Gong, X.; Bustillo, J.; Blanc, L.; Gautier, G. FEM Simulation on Elastic Parameters of Porous Silicon with Different Pore Shapes. *International Journal of Solids and Structures* **2020**, *190*, 238–243. https://doi.org/10.1016/j.ijsolstr.2019.11.001.

[106] Rouquerol, J.; Avnir, D.; Fairbridge, C. W.; Everett, D. H.; Haynes, J. M.; Pernicone, N.; Ramsay, J. D. F.; Sing, K. S. W.; Unger, K. K. Recommendations for the Characterization of Porous Solids (Technical Report). *Pure and Applied Chemistry* **1994**, *66* (8), 1739–1758. https://doi.org/10.1351/pac199466081739.

[107] Anglin, E.J.; Cheng, L.; Freeman, W.R.; Sailor, M.J. Porous Silicon in Drug Delivery Devices and Materials☆. *Advanced Drug Delivery Reviews* **2008**, *60* (11), 1266–1277. https://doi.org/10.1016/j.addr.2008.03.017.

[108] Peckham, J.; Andrews, G. T. Effect of Anodization Current Density on Pore Geometry in Macroporous Silicon. *Semiconductor Science and* Technology **2013**, *28* (10), 105027. https://doi.org/10.1088/0268-1242/28/10/105027.

[109] Fukami, K.; Tanaka, Y.; Chourou, M. L.; Sakka, T.; Ogata, Y. H. Filling of Mesoporous Silicon with Copper by Electrodeposition from an Aqueous Solution. *Electrochimica Acta* **2009**, *54* (8), 2197–2202. https://doi.org/10.1016/j.electacta.2008.10.024.

[110] Harraz, F. A.; El-Sheikh, S. M.; Sakka, T.; Ogata, Y. H. Cylindrical Pore Arrays in Silicon with Intermediate Nano-Sizes: A Template for Nanofabrication and Multilayer Applications. *Electrochimica Acta* **2008**, *53* (22), 6444–6451. https://doi.org/ 10.1016/ j.electacta. 2008.04.045.

---

[111] Lehmann, V. Electrochemistry of silicon - Instrumentation, Science, Materials and Applications. **2002**, *Wiley-VCH*, Weinheim, Germany.

[112] Wijayanti, S.; Sehati; Suryana, R. The Formation of Porous Silicon (PSi) on p-Type Si (100) Substrate via the Electrochemical Anodization Method with Varying Current Density. *Journal of Physics: Conference Series* **2021**, *1825* (1), 012068. https://doi.org/10.1088/1742-6596/1825/1/012068.

[113] Kleimann, P.; Badel, X.; Linnros, J. Toward the Formation of Three-Dimensional Nanostructures by Electrochemical Etching of Silicon. *Applied Physics Letters* **2005**, *86* (18). https://doi.org/10.1063/1.1924883.

[114] Garcia-Vergara, S. J.; Skeldon, P.; Thompson, G. E.; Habazaki, H. A Flow Model of Porous Anodic Film Growth on Aluminium. *Electrochimica Acta* **2006**, *52* (2), 681–687. https://doi.org/10.1016/j.electacta.2006.05.054.

[115] Chiang, C.-C.; Lee, B. T.-H. Annihilating Pores in the Desired Layer of a Porous Silicon Bilayer with Different Porosities for Layer Transfer. *Scientific Reports* **2019**, *9* (1). https://doi.org/10.1038/s41598-019-49119-8.

[116] Elia, P.; Nativ-Roth, E.; Zeiri, Y.; Porat, Z. Determination of the Average Pore-Size and Total Porosity in Porous Silicon Layers by Image Processing of SEM Micrographs. *Microporous and Mesoporous Materials* **2016**, *225*, 465–471. https://doi.org/10.1016/j.micromeso.2016.01.007.

[117] Massad-Ivanir, N.; Shtenberg, G.; Zeidman, T.; Segal, E. Construction and Characterization of Porous SiO_2/Hydrogel Hybrids as Optical Biosensors for Rapid Detection of Bacteria. *Advanced Functional Materials* **2010**, *20* (14), 2269–2277. https://doi.org/10.1002/adfm.201000406.

[118] Perelman, L. A.; Moore, T.; Singelyn, J.; Sailor, M. J.; Segal, E. Preparation and Characterization of a pH- and Thermally Responsive Poly(N-isopropylacrylamide-co-acrylic Acid)/Porous SiO_2 Hybrid. *Advanced Functional Materials* **2010**, *20* (5), 826–833. https://doi.org/10.1002/adfm.200900822.

[119] Segal, E.; Perelman, L. A.; Cunin, F.; Di Renzo, F.; Devoisselle, J. -M.; Li, Y. Y.; Sailor, M. J. Confinement of Thermoresponsive Hydrogels in Nanostructured Porous Silicon Dioxide Templates. *Advanced Functional Materials* **2007**, *17* (7), 1153–1162. https://doi.org/10.1002/adfm.200601077.

[120] Nirala, N. R.; Asiku, J.; Dvir, H.; Shtenberg, G. N-Acetyl-β-d-Glucosaminidase Activity Assay for Monitoring Insulin-Dependent Diabetes Using Ag-Porous Si SERS Platform. *Talanta* **2022**, *239*, 123087. https://doi.org/10.1016/j.talanta.2021.123087.

[121] Rasson, J.; Poncelet, O.; Mouchet, S. R.; Deparis, O.; Francis, L. A. Vapor Sensing Using a Bio-Inspired Porous Silicon Photonic Crystal. *Materials Today: Proceedings* **2017**, *4* (4), 5006–5012. https://doi.org/10.1016/j.matpr.2017.04.107.

[122] Sassaki, R. M.; Douglas, R. A.; Kleinke, M. U.; Teschke, O. Structure Imaging by Atomic Force Microscopy and Transmission Electron Microscopy of Different Light Emitting Species of Porous Silicon. *Journal of Vacuum Science & Technology B: Microelectronics and*

Nanometer Structures Processing, Measurement, and Phenomena **1996**, *14* (4), 2432–2437. https://doi.org/10.1116/1.588874.

[123] Paes, T. F.; Beloto, A. F.; Galvão, E. C. D. S.; Berni, L. A. Simple Method for Measuring the Porosity, Thickness and Refractive Index of Porous Silicon, Based on the Fabry-Pérot Interference Spectrum. *Revista Brasileira de Aplicações de Vácuo* **2017**, *35* (3), 117. https://doi.org/10.17563/rbav.v35i3.1044.

[124] Massad-Ivanir, N.; Shtenberg, G.; Tzur, A.; Krepker, M. A.; Segal, E. Engineering Nanostructured Porous SiO_2 Surfaces for Bacteria Detection via “Direct Cell Capture.” *Analytical Chemistry* **2011**, *83* (9), 3282–3289. https://doi.org/10.1021/ac200407w.

[125] Segal, E.; Perelman, L. A.; Cunin, F.; Di Renzo, F.; Devoisselle, J. -M.; Li, Y. Y.; Sailor, M. J. Confinement of Thermoresponsive Hydrogels in Nanostructured Porous Silicon Dioxide Templates. *Advanced Functional Materials* **2007**, *17* (7), 1153–1162. https://doi.org/10.1002/adfm.200601077.

[126] Chiang, C.-C.; Lee, B. T.-H. Annihilating Pores in the Desired Layer of a Porous Silicon Bilayer with Different Porosities for Layer Transfer. *Scientific Reports* **2019**, *9* (1). https://doi.org/10.1038/s41598-019-49119-8.

[127] Li, S.; Hu, D.; Huang, J.; Cai, L. Optical Sensing Nanostructures for Porous Silicon Rugate Filters. *Nanoscale Research Letters* **2012**, *7* (1). https://doi.org/10.1186/1556-276x-7-79.

[128] Pacholski, C.; Sartor, M.; Sailor, M. J.; Cunin, F.; Miskelly, G. M. Biosensing Using Porous Silicon Double-Layer Interferometers: Reflective Interferometric Fourier Transform Spectroscopy. *Journal of the American Chemical Society* **2005**, *127* (33), 11636–11645. https://doi.org/10.1021/ja0511671.

[129] Piya, R.; Gupta, B.; Gooding, J. J.; Reece, P. J. Optimising Porous Silicon Bragg Reflectors for Narrow Spectral Resonances. *Journal of Applied Physics* **2018**, *124* (16). https://doi.org/10.1063/1.5048618.

[130] Ivanov, I.; Skryshevsky, V.; Belarouci, A. Engineering Porous Silicon-Based Microcavity for Chemical Sensing. *ACS Omega* **2023**, *8* (23), 21265–21276. https://doi.org/10.1021/acsomega.3c02526.

[131] Chhasatia, R.; Sweetman, M. J.; Prieto-Simon, B.; Voelcker, N. H. Performance Optimisation of Porous Silicon Rugate Filter Biosensor for the Detection of Insulin. *Sensors and Actuators B: Chemical* **2018,** *273*, 1313–1322. https://doi.org/10.1016/j.snb.2018.07.021.

[132] Ilyas, S.; Böcking, T.; Kilian, K.; Reece, P. J.; Gooding, J.; Gaus, K.; Gal, M. Porous Silicon Based Narrow Line-Width Rugate Filters. *Optical Materials* **2007**, *29* (6), 619–622. https://doi.org/10.1016/j.optmat.2005.10.012.

133. Reece, P. J.; Gal, M.; Tan, H. H.; Jagadish, C. Optical Properties of Erbium-Implanted Porous Silicon Microcavities. *Applied Physics Letters* **2004,** *85* (16), 3363–3365. https://doi.org/ 10.1063/1.1808235.

---

[134] Gupta, B.; Guan, B.; Reece, P. J.; Gooding, J. J. Porous Silicon Photonic Crystals for Detection of Infections. *Proc. SPIE Biosensing and Nanomedicine V*; **2012**; 84600Z, 136–143. https://doi.org/10.1117/12.940757.

[135] Ramirez-Gutierrez, C. F.; Martinez-Hernandez, H. D.; Lujan-Cabrera, I. A.; Rodriguez-García, M. E. Design, Fabrication, and Optical Characterization of One-Dimensional Photonic Crystals Based on Porous Silicon Assisted by in-Situ Photoacoustics. *Scientific Reports* **2019**, *9* (1). https://doi.org/10.1038/s41598-019-51200-1.

[136] Reece, P. J.; Lerondel, G.; Mulders, J.; Zheng, W. H.; Gal, M. Fabrication and Tuning of High-Quality Porous Silicon Microcavities. *physica status solidi (a)* **2003**, *197* (2), 321–325. https://doi.org/10.1002/pssa.200306517.

[137] Massad-Ivanir, N.; Bhunia, S. K.; Jelinek, R.; Segal, E. Porous Silicon Bragg Reflector/Carbon Dot Hybrids: Synthesis, Nanostructure, and Optical Properties. *Frontiers in Chemistry* **2018**, *6*. https://doi.org/10.3389/fchem.2018.00574.

[138] Lorenzo, E.; Oton, C. J.; Capuj, N. E.; Ghulinyan, M.; Navarro-Urrios, D.; Gaburro, Z.; Pavesi, L. Porous Silicon-Based Rugate Filters. *Applied Optics* **2005**, *44* (26), 5415. https://doi.org/10.1364/ao.44.005415.

[139] Southwell, W. H. Using Apodization Functions to Reduce Sidelobes in Rugate Filters. *Applied Optics* **1989**, *28* (23), 5091. https://doi.org/10.1364/ao.28.005091.

[140] Cullis, A. G.; Canham, L. T.; Calcott, P. D. J. The Structural and Luminescence Properties of Porous Silicon. *Journal of Applied Physics* **1997**, *82* (3), 909–965. https://doi.org/10.1063/1.366536.

[141] Prestidge, C. A.; Barnes, T. J.; Lau, C.-H.; Barnett, C.; Loni, A.; Canham, L. Mesoporous Silicon: A Platform for the Delivery of Therapeutics. *Expert Opinion on Drug Delivery* **2007**, *4* (2), 101–110. https://doi.org/10.1517/17425247.4.2.101.

[142] Tutov, E. A.; Pavlenko, M. N.; Protasova, I. V.; Kashkarov, V. M. The Interaction of Porous Silicon with Water: A Chemographic Effect. *Technical Physics Letters* **2002**, *28* (9), 729–731. https://doi.org/10.1134/1.1511767.

[143] Tong, W. Y.; Sweetman, M. J.; Marzouk, E. R.; Fraser, C.; Kuchel, T.; Voelcker, N. H. Towards a Subcutaneous Optical Biosensor Based on Thermally Hydrocarbonised Porous Silicon. *Biomaterials* **2016**, *74*, 217–230. https://doi.org/10.1016/j.biomaterials.2015.09.045.

[144] Linford, M. R.; Chidsey, C. E. D. Alkyl Monolayers Covalently Bonded to Silicon Surfaces. *Journal of the American Chemical Society* **1993**, *115* (26), 12631–12632. https://doi.org/10.1021/ja00079a071.

[145] Ciampi, S.; Böcking, T.; Kilian, K. A.; Harper, J. B.; Gooding, J. J. Click Chemistry in Mesoporous Materials: Functionalization of Porous Silicon Rugate Filters. *Langmuir* **2008**, *24* (11), 5888–5892. https://doi.org/10.1021/la800435d.

[146] Layouni, R.; Choudhury, M. H.; Laibinis, P. E.; Weiss, S. M. Thermally Carbonized Porous Silicon for Robust Label-Free DNA Optical Sensing. *ACS Applied Bio Materials* **2019**, *3* (1), 622–627. https://doi.org/10.1021/acsabm.9b01002.

---

[147] Boukherroub, R.; Petit, A.; Loupy, A.; Chazalviel, J.-N.; Ozanam, F. Microwave-Assisted Chemical Functionalization of Hydrogen-Terminated Porous Silicon Surfaces. *The Journal of Physical Chemistry B* **2003**, *107* (48), 13459–13462. https://doi.org/10.1021/jp036530+.

[148] Boukherroub, R.; Morin, S.; Wayner, D. D. M.; Lockwood, D. J. Thermal Route for Chemical Modification and Photoluminescence Stabilization of Porous Silicon. *physica status solidi (a)* **2000**, *182* (1), 117–121. https://doi.org/10.1002/1521-396X(200011)182:1<117::AID-PSSA117>3.0.CO;2-3.

[149] Buriak, J. M.; Allen, M. J. Lewis Acid Mediated Functionalization of Porous Silicon with Substituted Alkenes and Alkynes. *Journal of the American Chemical Society* **1998**, *120* (6), 1339–1340. https://doi.org/10.1021/ja9740125.

[150] Stewart, M. P.; Buriak, J. M. Photopatterned Hydrosilylation on Porous Silicon. *Angewandte Chemie International Edition* **1998**, *37* (23), 3257–3260. https://doi.org/10.1002/(SICI)1521-3773(19981217)37:23<3257::AID-ANIE3257>3.0.CO;2-1.

[151] Bateman, J. E.; Eagling, R. D.; Worrall, D. R.; Horrocks, B. R.; Houlton, A. Alkylation of Porous Silicon by Direct Reaction with Alkenes and Alkynes. *Angewandte Chemie International Edition* **1998**, *37* (19), 2683–2685. https://doi.org/10.1002/(SICI)1521-3773(19981016)37:19<2683::AID-ANIE2683>3.0.CO;2-Y.

[152] Buriak, J. M. Organometallic Chemistry on Silicon Surfaces: Formation of Functional Monolayers Bound through Si–C Bonds. *Chemical Communications* **1999**, No. 12, 1051–1060. https://doi.org/10.1039/a900108e.

[153] Sailor, M. J. Chemical Reactivity and Surface Chemistry of Porous Silicon. *Handbook of Porous Silicon* **2014**, 355–380. https://doi.org/10.1007/978-3-319-05744-6_37.

[154] Salonen, J.; Mäkilä, E. Thermal Stabilization of Porous Silicon. *Porous Silicon for Biomedical Applications* **2021**, 3–26. https://doi.org/10.1016/b978-0-12-821677-4.00003-3.

[155] Guo, K.; Sharma, A.; Toh, R. J.; Alvárez de Eulate, E.; Gengenbach, T. R.; Cetó, X.; Voelcker, N. H.; Prieto-Simón, B. Porous Silicon Nanostructures as Effective Faradaic Electrochemical Sensing Platforms. *Advanced Functional Materials* **2019**, *29* (24). https://doi.org/10.1002/adfm.201809206.

[156] Salonen, J.; Lehto, V.-P.; Björkqvist, M.; Laine, E.; Niinistö, L. Studies of Thermally-Carbonized Porous Silicon Surfaces. *physica status solidi (a)* **2000**, *182* (1), 123–126. https://doi.org/10.1002/1521-396X(200011)182:1<123::AID-PSSA123>3.0.CO;2-F.

[157] Björkqvist, M.; Salonen, J.; Laine, E. Humidity Behavior of Thermally Carbonized Porous Silicon. *Applied Surface Science* **2004**, *222* (1–4), 269–274. https://doi.org/10.1016/j.apsusc.2003.08.025.

[158] Paski, J.; Björkqvist, M.; Salonen, J.; Lehto, V. Effects of Treatment Temperature on Thermally-carbonized Porous Silicon Hygroscopicity. *physica status solidi (c)* **2005**, *2* (9), 3379–3383. https://doi.org/10.1002/pssc.200461175.

[159] Tieu, T.; Alba, M.; Elnathan, R.; Cifuentes-Rius, A.; Voelcker, N. H. Advances in Porous Silicon–Based Nanomaterials for Diagnostic and Therapeutic Applications. *Advanced Therapeutics* **2018**, *2* (1). https://doi.org/10.1002/adtp.201800095.

---

[160] Pap, A. E.; Kordás, K.; George, T. F.; Leppävuori, S. Thermal Oxidation of Porous Silicon: Study on Reaction Kinetics. *The Journal of Physical Chemistry B* **2004**, *108* (34), 12744–12747. https://doi.org/10.1021/jp049323y.

[161] Hadj Zoubir, N.; Vergnat, M.; Delatour, T.; Burneau, A.; de Donato, Ph. Interpretation of the Luminescence Quenching in Chemically Etched Porous Silicon by the Desorption of SiH3 Species. *Applied Physics Letters* **1994**, *65* (1), 82–84. https://doi.org/10.1063/1.113082.

[162] Shtenberg, G.; Massad-Ivanir, N.; Fruk, L.; Segal, E. Nanostructured Porous Si Optical Biosensors: Effect of Thermal Oxidation on Their Performance and Properties. *ACS Applied Materials & Interfaces* **2014**, *6* (18), 16049–16055. https://doi.org/10.1021/am503987j.

[163] Szili, E. J.; Jane, A.; Low, S. P.; Sweetman, M.; Macardle, P.; Kumar, S.; Smart, R. St. C.; Voelcker, N. H. Interferometric Porous Silicon Transducers Using an Enzymatically Amplified Optical Signal. *Sensors and Actuators B: Chemical* **2011**, *160* (1), 341–348. https://doi.org/10.1016/j.snb.2011.07.059.

[164] Caballos, I.; Aranda, M. N.; López-Palacios, A.; Pla, L.; Santiago-Felipe, S.; Hernández-Montoto, A.; Tormo-Mas, M. Á.; Pemán, J.; Gómez-Ruiz, M. D.; Calabuig, E.; Sánchez-Sendra, B.; Francés-Gómez, C.; Geller, R.; Aznar, E.; Martínez-Máñez, R. Aptamer-Capped Nanoporous Anodic Alumina for SARS-CoV-2 Spike Protein Detection. *Advanced Materials Technologies* **2023**, *8* (11). https://doi.org/10.1002/admt.202201913.

[165] Liu, Y.; Wang, H. H.; Indacochea, J. E.; Wang, M. L. A Colorimetric Sensor Based on Anodized Aluminum Oxide (AAO) Substrate for the Detection of Nitroaromatics. *Sensors and Actuators B: Chemical* **2011**, *160* (1), 1149–1158. https://doi.org/10.1016/j.snb.2011.09.040.

[166] Haberkorn, N.; Gutmann, J. S.; Theato, P. Template-Assisted Fabrication of Free-Standing Nanorod Arrays of a Hole-Conducting Cross-Linked Triphenylamine Derivative: Toward Ordered Bulk-Heterojunction Solar Cells. *ACS Nano* **2009**, *3* (6), 1415–1422. https://doi.org/10.1021/nn900207a.

[167] Yantasee, W.; Rutledge, R. D.; Chouyyok, W.; Sukwarotwat, V.; Orr, G.; Warner, C. L.; Warner, M. G.; Fryxell, G. E.; Wiacek, R. J.; Timchalk, C.; Addleman, R. S. Functionalized Nanoporous Silica for the Removal of Heavy Metals from Biological Systems: Adsorption and Application. *ACS Applied Materials & Interfaces* **2010**, *2* (10), 2749–2758. https://doi.org/10.1021/am100616b.

[168] Debrassi, A.; Ribbera, A.; de Vos, W. M.; Wennekes, T.; Zuilhof, H. Stability of (Bio)Functionalized Porous Aluminum Oxide. *Langmuir* **2014**, *30* (5), 1311–1320. https://doi.org/10.1021/la403525z.

[169] Bayat, H.; Raoufi, M.; Zamrik, I.; Schönherr, H. Poly(Diethylene Glycol Methylether Methacrylate) Brush-Functionalized Anodic Alumina Nanopores: Curvature-Dependent Polymerization Kinetics and Nanopore Filling. *Langmuir* **2020**, *36* (10), 2663–2672. https://doi.org/10.1021/acs.langmuir.9b03700.

[170] Müller, S.; Cavallaro, A.; Vasilev, K.; Voelcker, N. H.; Schönherr, H. Temperature-Controlled Antimicrobial Release from Poly(Diethylene Glycol Methylether Methacrylate)-Functionalized Bottleneck-Structured Porous Silicon for the Inhibition of Bacterial Growth.

Macromolecular Chemistry and Physics **2016**, *217* (20), 2243–2251. https://doi.org/10.1002/macp.201600099.

[171] Mariani, S.; Robbiano, V.; Strambini, L. M.; Debrassi, A.; Egri, G.; Dähne, L.; Barillaro, G. Layer-by-Layer Biofunctionalization of Nanostructured Porous Silicon for High-Sensitivity and High-Selectivity Label-Free Affinity Biosensing. *Nature Communications* **2018**, *9* (1). https://doi.org/10.1038/s41467-018-07723-8.

[172] Cho, Y.; Lim, J.; Char, K. Layer-by-Layer Assembled Stimuli-Responsive Nanoporous Membranes. *Soft Matter* **2012**, *8* (40), 10271. https://doi.org/10.1039/c2sm26562a.

[173] Steinhart, M.; Wendorff, J. H.; Greiner, A.; Wehrspohn, R. B.; Nielsch, K.; Schilling, J.; Choi, J.; Gösele, U. Polymer Nanotubes by Wetting of Ordered Porous Templates. *Science* **2002**, *296* (5575), 1997–1997. https://doi.org/10.1126/science.1071210.

[174] Palacios, R.; Formentin, P.; Santos, A.; Pallares, J.; Trifonov, T.; Alcubilla, R.; Marsal, L. F. Synthesis of Ordered Polymer Micro and Nanostructures Via Porous Templates. *2009 Spanish Conference on Electron Devices* **2009**. https://doi.org/10.1109/sced.2009.4800524.

[175] Hoang, X. T.; Nguyen, D. T.; Dong, B. C.; Nguyen, H. N. Fabrication of Carbon Nanostructures from Polymeric Precursor by Using Anodic Aluminum Oxide (AAO) Nanotemplates. *Advances in Natural Sciences: Nanoscience and Nanotechnology* **2013**, *4* (3), 035013. https://doi.org/10.1088/2043-6262/4/3/035013.

[176] Lee, S.; Lee, B.; Choi, J.; Chi, C.-S.; Jeong, Y.; Oh, H.-J. Effects of Various Solution Wetting Conditions on the Morphology and the Crystallization of Poly (Vinylidene Fluoride) Nanotubes. *Journal of the Korean Physical Society* **2009**, *54* (3), 1198–1202. https://doi.org/10.3938/jkps.54.1198.

[177] Palacios, R.; Formentín, P.; Santos, A.; Martínez-Ferrero, E.; Ferré-Borrull, J.; Pallarès, J.; Marsal, L. F. Template-assisted Fabrication and Characterization of Photoluminescent Polymer Nanopillars. *physica status solidi c* **2011**, *8* (9), 2612–2616. https://doi.org/10.1002/pssc.201084122.

[178] Shin, H.-W.; Shin, E.-J.; Cho, S. Y.; Oh, S.-L.; Kim, Y.-R. Enhanced Energy Transfer within PVK/Alq3 Polymer Nanowires Induced by the Interface Effect of Nanochannels in Porous Alumina Membrane. *The Journal of Physical Chemistry C* **2007**, *111* (42), 15391–15396. https://doi.org/10.1021/jp074203m.

[179] Yanagishita, T.; Fujimura, R.; Nishio, K.; Masuda, H. Fabrication of Monodisperse Polymer Nanoparticles by Membrane Emulsification Using Ordered Anodic Porous Alumina. *Langmuir* **2009**, *26* (3), 1516–1519. https://doi.org/10.1021/la903913h.

[180] de Gennes, P. G. Wetting: Statics and Dynamics. *Reviews of Modern Physics* **1985**, *57* (3), 827–863. https://doi.org/10.1103/revmodphys.57.827.

[181] Fox, H. W.; Hare, E. F.; Zisman, W. A. Wetting Properties of Organic Liquids on High-Energy Surfaces. *The Journal of Physical Chemistry* **1955**, *59* (10), 1097–1106. https://doi.org/10.1021/j150532a027.

---

[182] Steinhart, M.; Wendorff, J. H.; Wehrspohn, R. B. Nanotubes à La Carte: Wetting of Porous Templates. *ChemPhysChem* **2003**, *4* (11), 1171–1176. https://doi.org/10.1002/cphc.200300733.

[183] Steinhart, M.; Wendorff, J. H.; Wehrspohn, R. B. Nanotubes à La Carte: Wetting of Porous Templates. *ChemPhysChem* **2003**, *4* (11), 1171–1176. https://doi.org/10.1002/cphc.200300733.

[184] Redón, R.; Vázquez-Olmos, A.; Mata-Zamora, M. E.; Ordóñez-Medrano, A.; Rivera-Torres, F.; Saniger, J. M. Contact Angle Studies on Anodic Porous Alumina. *Journal of Colloid and Interface Science* **2005**, *287* (2), 664–670. https://doi.org/10.1016/j.jcis.2005.02.036.

[185] Martín, J.; Mijangos, C. Tailored Polymer-Based Nanofibers and Nanotubes by Means of Different Infiltration Methods into Alumina Nanopores. *Langmuir* **2008**, *25* (2), 1181–1187. https://doi.org/10.1021/la803127w.

[186] Jin, S.; Lee, Y.; Jeon, S.-M.; Sohn, B.-H.; Chae, W.-S.; Lee, J.-K. Simple Fabrication of Single- and Multi-Layer Polymer Nanotubes by Spin-Casting Method within Anodized Aluminum Oxide (AAO) Templates. *Journal of Materials Chemistry* **2012**, *22* (44), 23368. https://doi.org/10.1039/c2jm34726a.

[187] Ong, P.-L.; Levitsky, I. A. Fluorescent Gas Sensors Based on Nanoporous Optical Resonators (Microcavities) Infiltrated With Sensory Emissive Polymers. *IEEE Sensors Journal* **2011**, *11* (11), 2947–2951. https://doi.org/10.1109/jsen.2011.2150213.

[188] Tokranova, N. A.; Novak, S. W.; Castracane, J.; Levitsky, I. A. Deep Infiltration of Emissive Polymers into Mesoporous Silicon Microcavities: Nanoscale Confinement and Advanced Vapor Sensing. *The Journal of Physical Chemistry C* **2013**, *117* (44), 22667–22676. https://doi.org/10.1021/jp405071n.

[189] Osipov, E. V.; Martynov, I. L.; Dovzhenko, D. S.; Ananev, P. S.; Kotkovskii, G. E.; Chistyakov, A. A. Silicon Photonic Structures with Embedded Polymers for Novel Sensing Methods. *Optics and Spectroscopy* **2017**, *122* (1), 74–78. https://doi.org/10.1134/s0030400x17010222.

[190] Du, K.; Gan, Z. Cellular Interactions on Hierarchical Poly(ε-Caprolactone) Nanowire Micropatterns. *ACS Applied Materials & Interfaces* **2012**, *4* (9), 4643–4650. https://doi.org/10.1021/am301013e.

[191] Gulati, K.; Ramakrishnan, S.; Aw, M. S.; Atkins, G. J.; Findlay, D. M.; Losic, D. Biocompatible Polymer Coating of Titania Nanotube Arrays for Improved Drug Elution and Osteoblast Adhesion. *Acta Biomaterialia* **2012**, *8* (1), 449–456. https://doi.org/10.1016/j.actbio. 2011.09.004.

[192] Kido, Y.; Sakai, R.; John, B.; Okamoto, M.; Seppälä, J. Preparation and Enzymatic Degradation of Porous Crosslinked Polylactides of Biomass Origin. *International Journal of Molecular Sciences* **2014**, *15* (6), 9793–9808. https://doi.org/10.3390/ijms15069793.

[193] Tokiwa, Y.; Calabia, B. P. Biodegradability and Biodegradation of Poly(Lactide). *Applied Microbiology and Biotechnology* **2006**, *72* (2), 244–251. https://doi.org/10.1007/s00253-006-0488-1.

---

[194] Drumright, R. E.; Gruber, P. R.; Henton, D. E. Polylactic Acid Technology. *Advanced Materials* **2000**, *12* (23), 1841–1846. https://doi.org/10.1002/1521-4095(200012)12:23<1841::AID-ADMA1841>3.0.CO;2-E.

[195] Tücking, K.; Grützner, V.; Unger, R. E.; Schönherr, H. Dual Enzyme-Responsive Capsules of Hyaluronic Acid-block-Poly(Lactic Acid) for Sensing Bacterial Enzymes. *Macromolecular Rapid Communications* **2015**, *36* (13), 1248–1254.https://doi.org/10.1002/marc.201500076.

[196] van Nostrum, C. F.; Veldhuis, T. F. J.; Bos, G. W.; Hennink, W. E. Hydrolytic Degradation of Oligo(Lactic Acid): A Kinetic and Mechanistic Study. *Polymer* **2004**, *45* (20), 6779–6787. https://doi.org/10.1016/j.polymer.2004.08.001.

[197] Shinozaki, Y.; Kikkawa, Y.; Sato, S.; Fukuoka, T.; Watanabe, T.; Yoshida, S.; Nakajima-Kambe, T.; Kitamoto, H. K. Enzymatic Degradation of Polyester Films by a Cutinase-like Enzyme from Pseudozyma Antarctica: Surface Plasmon Resonance and Atomic Force Microscopy Study. *Applied Microbiology and Biotechnology* **2013**, *97* (19), 8591–8598. https://doi.org/10.1007/s00253-012-4673-0.

[198] Gauglitz, G.; Ingenhoff, J. Design of New Integrated Optical Substrates for Immuno-Analytical Applications. *Fresenius' Journal of Analytical Chemistry* **1994**, *349* (5), 355–359. https://doi.org/10.1007/bf00326599.

[199] Miller, D. Refractive Fabry-Perot Bistability with Linear Absorption: Theory of Operation and Cavity Optimization. *IEEE Journal of Quantum Electronics* **1981**, *17* (3), 306–311. https://doi.org/10.1109/jqe.1981.1071101.

[200] Huang, K.; Pu, L.; Shi, Y.; Han, P.; Zhang, R.; Zheng, Y. D. Photoluminescence Oscillations in Porous Alumina Films. *Applied Physics Letters* **2006**, *89* (20). https://doi.org/10.1063/1.2390645.

[201] Saenger, K. L.; Tong, H. M. Laser Interferometry: A Measurement Technique for Diffusion Studies in Thin Polymer Films. *Polymer Engineering & Science* **1991**, *31* (6), 432–435. https://doi.org/10.1002/pen.760310608.

[202] Kim, J.; Carnemolla, E. G.; DeVault, C.; Shaltout, A. M.; Faccio, D.; Shalaev, V. M.; Kildishev, A. V.; Ferrera, M.; Boltasseva, A. Dynamic Control of Nanocavities with Tunable Metal Oxides. *Nano Letters* **2018**, *18* (2), 740–746. https://doi.org/10.1021/acs.nanolett.7b03919.

[203] Lin, V. S.-Y.; Motesharei, K.; Dancil, K.-P. S.; Sailor, M. J.; Ghadiri, M. R. A Porous Silicon-Based Optical Interferometric Biosensor. Science **1997**, *278* (5339), 840–843. https://doi.org/10.1126/science.278.5339.840.

[204] Pol, L.; Eckstein, C.; Acosta, L.; Xifré-Pérez, E.; Ferré-Borrull, J.; Marsal, L. Real-Time Monitoring of Biotinylated Molecules Detection Dynamics in Nanoporous Anodic Alumina for Bio-Sensing. *Nanomaterials* **2019**, *9* (3), 478. https://doi.org/10.3390/nano9030478.

[205] Kumeria, T.; Kurkuri, M. D.; Diener, K. R.; Parkinson, L.; Losic, D. Label-Free Reflectometric Interference Microchip Biosensor Based on Nanoporous Alumina for

---

Detection of Circulating Tumour Cells. *Biosensors and Bioelectronics* **2012**, *35* (1), 167–173. https://doi.org/10.1016/j.bios.2012.02.038.

[206] Kilian, K. A.; Böcking, T.; Gaus, K.; Gal, M.; Gooding, J. J. Peptide-Modified Optical Filters for Detecting Protease Activity. *ACS Nano* **2007**, *1* (4), 355–361. https://doi.org/10.1021/nn700141n.

[207] Pacholski, C. Photonic Crystal Sensors Based on Porous Silicon. *Sensors* **2013**, *13* (4), 4694–4713. https://doi.org/10.3390/s130404694.

[208] Garnett, J. C. M. XII. Colours in Metal Glasses and in Metallic Films. *Philosophical Transactions of the Royal Society of London Series a Containing Papers of a Mathematical or Physical Character* **1904**, *203* (359–371), 385–420. https://doi.org/10.1098/rsta.1904.0024.

[209] Lau, K. H. A.; Duran, H.; Knoll, W. In situ Characterization of N-Carboxy Anhydride Polymerization in Nanoporous Anodic Alumina. *The Journal of Physical Chemistry B* **2009**, *113* (10), 3179–3189. https://doi.org/10.1021/jp809593d.

[210] Hierro-Rodriguez, A.; Rocha-Rodrigues, P.; Valdés-Bango, F.; Alameda, J. M.; Jorge, P. a S.; Santos, J. L.; Araujo, J. P.; Teixeira, J. M.; Guerreiro, A. On the Anodic Aluminium Oxide Refractive Index of Nanoporous Templates. *Journal of Physics D Applied Physics* **2015**, *48* (45), 455105. https://doi.org/10.1088/0022-3727/48/45/455105.

[211] Hohlbein, J.; Rehn, U.; Wehrspohn, R. B. In-situ Optical Characterisation of Porous Alumina. *Physica Status Solidi (A)* **2004**, *201* (4), 803–807. https://doi.org/10.1002/pssa.200306781.

Chapter 3. The Objectives of the Thesis

In this Thesis, anodic aluminum oxide (AAO) and porous silicon rugate filter (pSiRF) constitute the target platforms as transducers for detecting fungal and bacterial enzymes. The Thesis focuses on the following points:

1. **Fabrication of AAO, pSi, and pSiRF sensors with optimal structures required for the sensing approach**. This approach relies on using reflectometric interference spectroscopy (RIfS) coupled with nanostructured porous film (i.e., AAO, pSiRF) to track the change in the effective refractive index of the porous film due to the change in the void of the pores. Therefore, an aim was to establish stable and compatible structures for RIfS, which is essential for designing an optical sensing platform for detecting biological species such as enzymes. Secondly, the response of the AAO sensor sealed with stimuli-responsive polymers should be studied in detail.
2. **Modifying the sensor with label-biorecognition elements can be time-consuming or complex**. Therefore, the establishment of a simple, versatile protocol was targeted. The investigation of the modification of nanostructured porous materials with label-free targets, such as biodegradable polymers, using the wetting approach as a filling protocol was pursued.
3. **Investigation of the degradation by fungal and bacteria enzymes of biodegradable polymer filled in the AAO and pSiRF sensors**. The sensors were to be tested in a biological medium using RIfS and other techniques.
4. **Development of a photonic material-based sensor for the bare-eye detection of bacterial enzymes**. The sensor was targeted to be filled with a degradable material, which can be degraded by bacterial enzymes to indicate the presence of pathogens.

Chapter 4. Fabrication and Characterization of Polymer-Sealed AAO Nanopores

4.1 Introduction

Nanoporous anodic aluminum oxide (AAO) nanostructure was employed here to study the modification with polymers for the detection of bacteria. Controllable nanopore dimensions, high surface areas, and large aspect ratios are attributes of AAO that are desirable for designing biosensors[1,2,3,4].

Reflectometric interferometry spectroscopy (RIfS) is an optical detection technique that relies on the interaction between white light and thin films[5]. Combining the RIfS with materials with high surface area would provide a sensitive measurement system that can be used for many applications[6,7,8]. The pSi and AAO nanostructures have a high surface area for analyte-receptor interactions, enhancing the sensor's sensitivity. In this Thesis, the detection approach of RIfS coupled with AAO or pSi is based on the change in n_{eff} as a result of biodegradable polymers or other biological substances entering the pores[9]. The increase in the n_{eff} would lead to an increase in *EOT*, which can then be monitored upon the change in the system. Therefore, the change in the *EOT* was used as a trigger in the sensing method for in-situ or ex-situ monitoring of the modifying AAO with PLA and the consequence enzymatic degradation of PLA.

The AAO/ pSi used for RIfS must have a particular pore size (i.e, pore diameter, pore length, porosity). Therefore, this Chapter addressed the parameters required to prepare a sensor measurable with RIfS. It is worth mentioning that the maximum signal in RIfS using AAO or pSi substrates could be obtained when the void in the pores is replaced with different refractive indices; for instance, liquid replaces air if the pores are initially sealed with polymer and then intentionally opened[10]. Therefore, at the end of this Chapter, this protocol was addressed.

AAO substrates were fabricated by anodizing aluminum in oxalic acid, sulfuric acid, or phosphoric acid electrolytes. The synthesis of ordered AAO requires that the parameters, including the type and concentration of the electrolyte, anodization time, applied voltage, and temperature, are carefully chosen and precisely controlled. For example, the interpore distance is known to increase linearly with the applied voltage, and the increase of the anodization time leads to an increase in the pore length[11,12].

In this Chapter, the synthesis of AAO was performed by the so-called 2-step anodization process or mild anodization (MA)[13]. The anodization setup used and established parameters are first discussed. Then, the morphology of Al before and after the anodization process is analyzed. The pore size of the fabricated AAO substrates was investigated by field emission scanning electron microscopy (FESEM). The AAO fabricated in the three electrolytes provides AAO with three distinct interpore distances and diameters. In addition, the length of the pores was tuned to enable the application of the AAO specimens for RIfS experiments and further biological tests.

4.2 Fabrication of Anodic Aluminum Oxide (AAO)

Prior to anodization, the roughness of the surface of the aluminum sample was reduced by an electropolishing process in a mixture of perchloric acid and ethanol[14]. The aluminum sample, which acted as the anode, was mounted on a copper plate (Figure 4.1a). An aluminum cathode was positioned at a distance of 2.0 cm from the anode. The electropolishing solution was then mixed by a magnetic stirrer to reduce the impact of gas bubbles, which may be generated during the process and accumulate on the surface of the aluminum. The setup is illustrated in Figure 4.1a. The advantage of this configuration was that the volume of the solution, previously cooled to 5 °C, was adequate to maintain a constant temperature during the electropolishing process.

To synthesize AAO by anodization, the electro-polished aluminum samples were placed in a sample holder made of poly(vinyl chloride) (PVC). The sample holder was then inserted into a glass beaker containing the electrolyte solution. The anodization reaction was carried out at a defined constant temperature using a water bath coupled with an external cooling unit. Furthermore, the electrolyte solution was pumped directly toward the aluminum sample to facilitate the effective dissipation of the heat generated during the anodization (see Figure 4.1b).

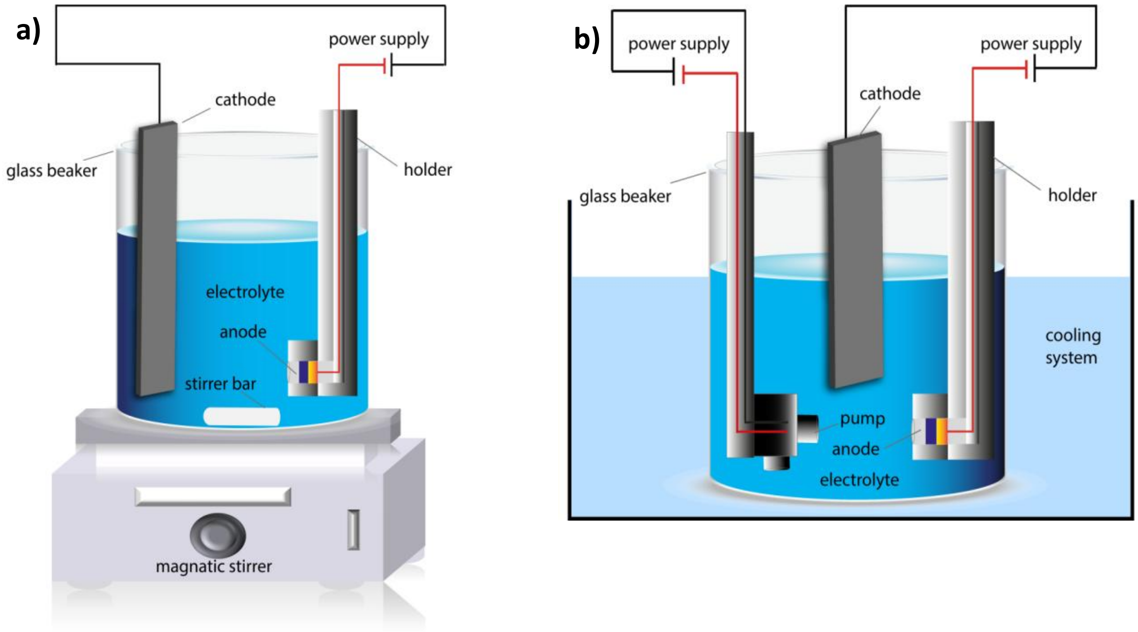

Figure 4.1: *Schemes of a) the electropolishing setup and b) the home-built anodization setup.*

Three sample holders were designed to fabricate different AAO samples. Figure 4.2a shows four Al samples were mounted in one holder to prepare AAO samples with identical pore diameter and pore length. This sample holder was utilized for the anodization at lower voltages, i.e. 25 V and 40 V. By contrast, for the anodization at high voltage (130 V), also called hard anodization (HA), a holder holding one Al sample was built (Figure 4.2b). In this design, the electrolyte was pumped directly to the Al sample, which was necessary to dissipate the heat generated due to the application of the high voltage during the anodization process. It was possible to enlarge the Al sample area by a factor of 7 using a larger sample holder (Figure 4.2c). In order to study the effect of the type of the used electrolyte on the structure of the AAO on the backside of the pores, the remaining Al was removed by a mixture of hydrochloric acid and copper(II)-chloride dihydrate solution[15]. Two specialized holders made of poly(tetrafluorethylene) (PTFE) were built for this purpose, as shown in Figure 4.2d,e.

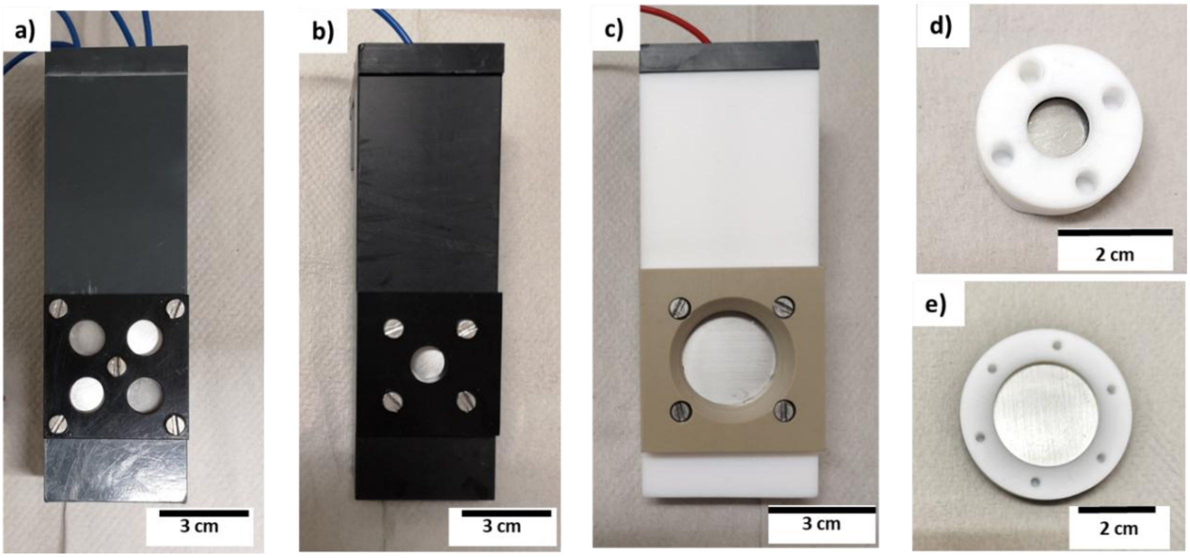

Figure 4.2: *Photographs of sample holders for: a) anodization of four samples, b) anodization of one sample, c) anodization of a large sample, and d, e) removal of aluminum from the backside of small and large samples, respectively.*

4.3 Characterization of AAO

The surface roughness of the Al foil may possess a significant effect on the formation of AAO. Therefore, an electropolishing process was used to reduce the roughness of the surface and to obtain a smoother surface. Figure 4.3a,b shows a top-view FESEM image of an Al foil before and after the electropolishing process.

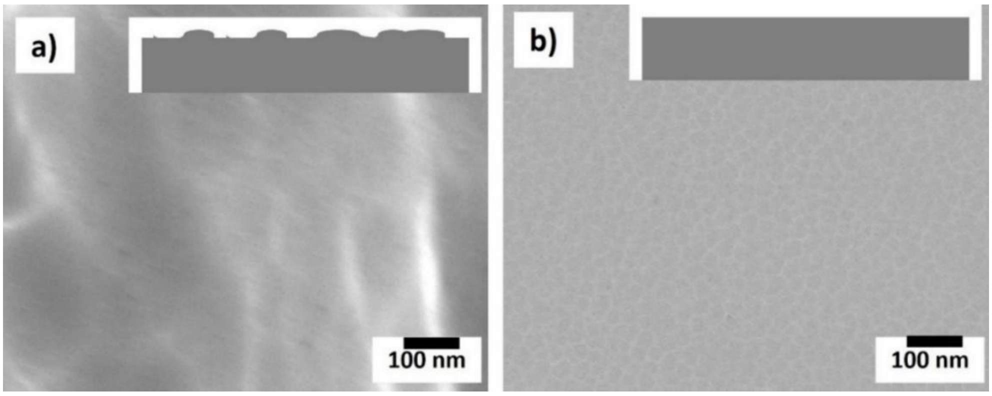

Figure 4.3*: FESEM images of Al foil surface. a) before electropolishing and b) after electropolishing in a mixture of ethanol and perchloric acid at 20 V electropolished at room temperature for 4 min.*

Afterwards, the sample was anodized in the first step. Figure 4.4a shows that the AAO formed in this first anodization step exhibits disordered nanopores. The irregularity of the formed pores, which were prepared in this anodization step, can be seen in the cross-sectional image of FESEM, where branched pores or combined pores could be seen, especially in the first 300 nm long (Figure 4.4b). It can be understood that the pore formation does not start at the same time of the breaking down of the initial oxide layer.

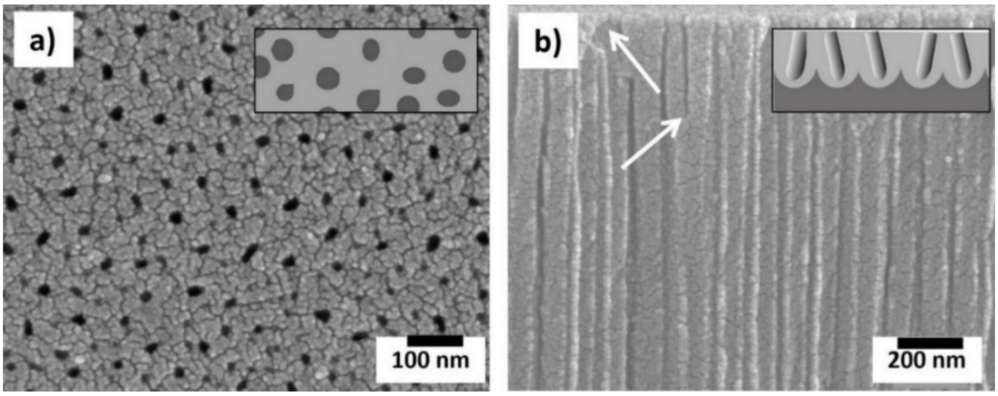

Figure 4.4: *FESEM images of a) the top side of AAO obtained in the first anodization step in oxalic acid (0.30 M) at 40 V and b) the cross-section of the AAO after the first anodization step, white arrows indicate undeveloped pores.*

The porous oxide layer obtained in the first anodization step should be removed to fabricate self-ordered nanopores. This layer was removed by chemical treatment using a mixture of phosphoric acid and chromium oxide solutions[16] (for details, *see the Experimental Part*). Figure 4.5a displays that the barrier layer of the pores, located at the interfaces of the AAO and Al, had ordered hexagonal structures, unlike the top side, where no regular structure was observed.

In Figure 4.5b, the FESEM image reveals the surface corrugations and their hexagonal arrangement on the remaining Al surface.

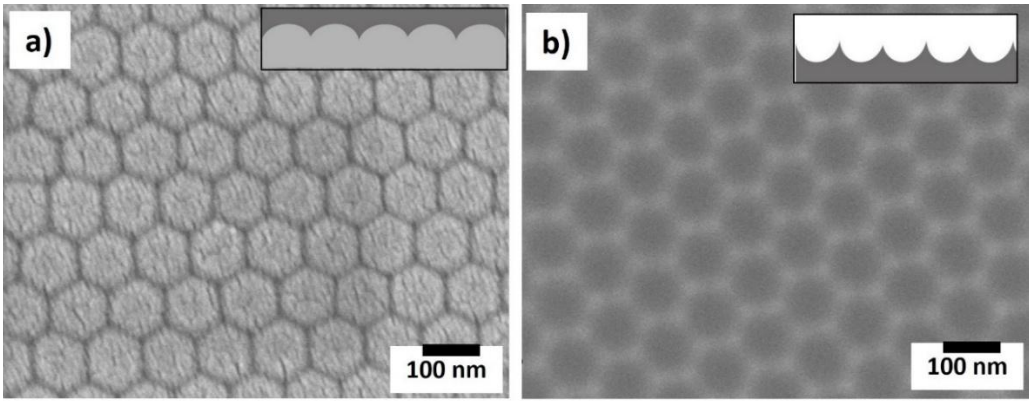

Figure 4.5: *FESEM images of a) the back side of AAO (barrier layer) formed after the first anodization step and b) the Al surface after removal of the first oxide layer by chemical etching in an aqueous solution of phosphoric acid and chromium oxide at 65 °C.*

The structures shown in Figure 4.5b, which stem from the bottom parts of the initially formed pores, can be developed in the second anodization step to form regular pores, as shown in Figure 4.6a, where the pore cell with a honey-shaped structure was prominent.

Furthermore, regular and straight pores along the AAO film were obtained when the second anodization was performed, as revealed in Figure 4.6b.

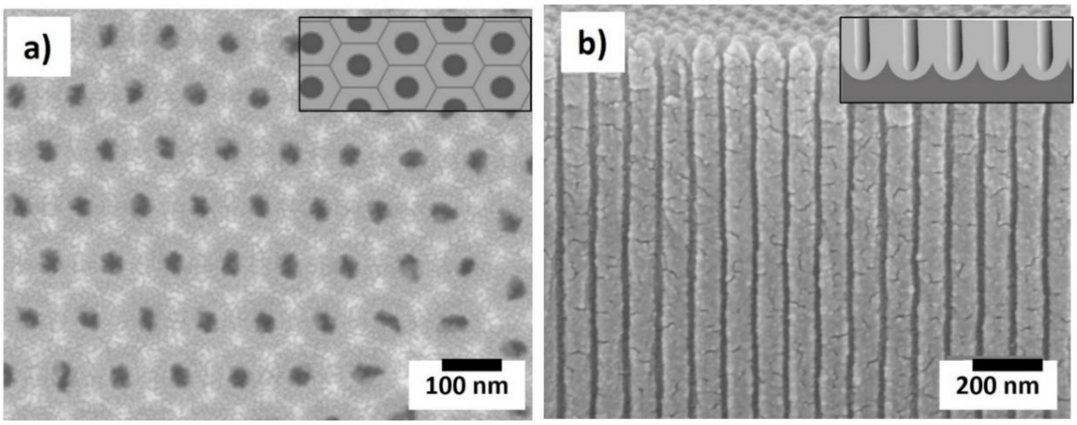

Figure 4.6: *FESEM images of a) the top side of AAO obtained in the 2nd anodization step in oxalic acid (0.30 M) at 40 V and b) the cross-sectional of the AAO after the second anodization step.*

The type of electrolyte and voltage are critical parameters in the anodization process[17,18]. Different acids, such as sulfuric, oxalic, and phosphoric acid, afford stable pore growth with varying voltages, which opens the way to AAO with different pore diameters and interpore distances[19]. Depending on the required structure of AAO, a proper acid with a corresponding voltage must be chosen carefully to get ordered pores. Thus, different AAO substrates were fabricated in sulfuric, oxalic, and phosphoric acids at 25 V, 40 V, and 195 V, respectively[20,21,22]. The FESEM images of the synthesized AAO samples are shown in Figure 4.7a,b,c. As can be seen, the pore diameters and the interpore distances differed depending on the acid used and the voltage applied. The interpore distance was ranging from 66 ± 5 nm to 450 ± 20 nm. Figure 4.7d displays a plot of voltages and the corresponding interpore distances. The interpore distance was found to be linearly proportional to the anodization voltage. The obtained interpore distances agree with the previous values reported by Martín and coworkers (2.4 ± 0.1 nm V^{-1}) [23].

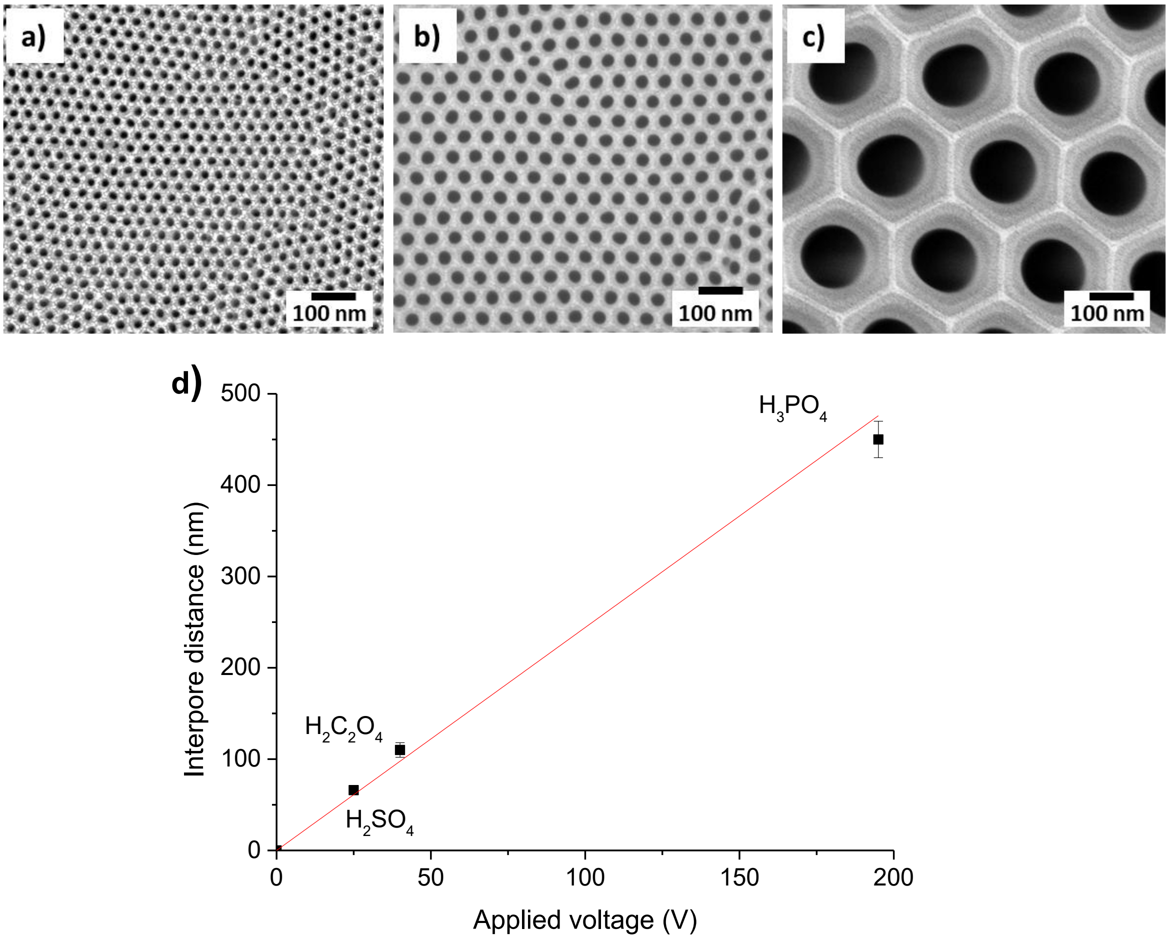

Figure 4.7: *FESEM images of available interpore distances (Di) of AAO mild anodization. a) D_i = 64 ± 5 nm, mild anodization in sulfuric acid at 25 V, b) Di = 110 ± 8 nm, in oxalic acid at 40 V, c) Di = 450 ± 20 nm, in phosphoric acid at 195 V, and d) Plot of interpore distance versus applied voltage, the solid line corresponds to a linear least squares fit of 0 V to 195 V revealing a slope of 2.4 ± 0.1 nm V^{-1}.*

The pore size of AAO plays a significant role in many applications[24,25,26,27]. Fortunately, the pore diameter can be increased after the anodization process to desired values without significantly changing the pore length. In this work, the pore-widening was performed by chemical etching in phosphoric acid. For the AAO obtained with a voltage of 40 V in oxalic acid, the samples were immersed in 0.5 M phosphoric acid at 35 °C from 5 to 35 min[28]. In Figure 4.8a there is a clear trend of increasing pore diameter with increasing widening time. The pore diameter was enlarged from 30 nm to 84 nm after 35 min (Figure 4.8b, 4.8c). As shown in Figure 4.8d, the synthesized AAO had a porosity of 8 %. This value slightly differed from the value of the porosity reported in the literature[12]. This variation is attributed to the sputtered gold layer on AAO; the pore diameter is reduced from 37 ± 3 to 32 ± 2 nm to overcome the charging effect during the FESEM measurement. The porosity of the widened AAO for 35 min was 58 %, which was higher than the non-treated ones by a factor of 7. The interpore distance was 110 ± 4 nm and was constant during the widening process. In comparison, the pore wall thickness decreased from 40 ± 3 to 20 ± 2 nm after 25 min widening.

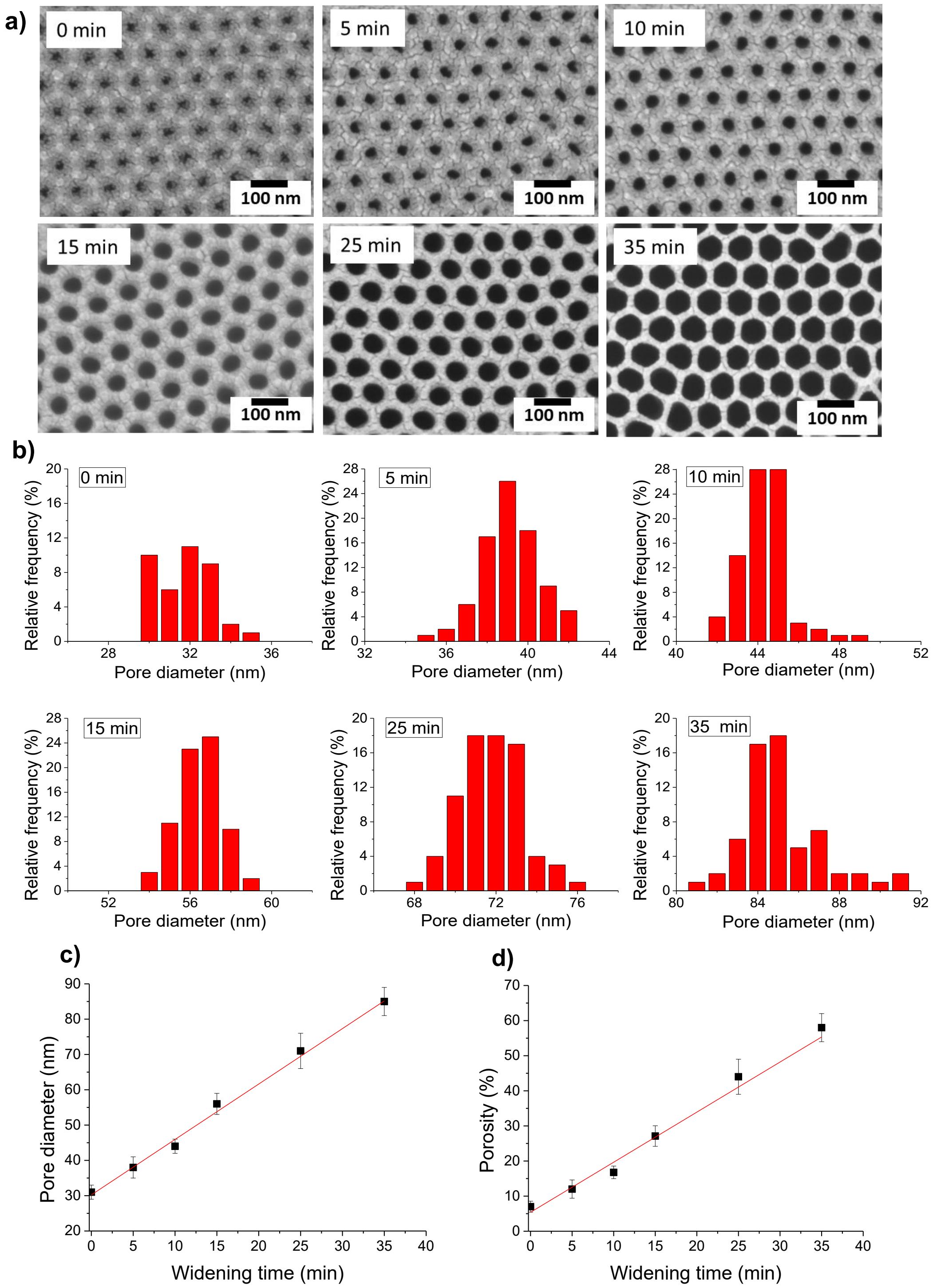

Figure 4.8: *Determination of the pore diameter upon the widening process of the AAO in oxalic acid (0.3 M, 40 V). a) FESEM images of AAO after immersion in phosphoric acid (0.5 M) at 35 °C for 0, 5, 10, 15, 25, and 35 min. b) The corresponding histograms of the pore diameter distributions. The solid line is the non-linear fit. c) Plot of the pore diameter calculated from the Gaussian fitting with the full width at half maximum (FWHM) as an error. b) The porosity versus the widening time estimated from the pore diameter. The solid lines in c and d correspond to linear least-squares fits of the data with slopes of 1.6 nm min^{-1} and 1.5 nm^{-1}, respectively.*

The pore length of AAO can be tuned to achieve a desirable AAO structure by varying the anodization time. The longer the anodization time, the thicker the AAO film. Figure 4.9a displays FESEM images of AAO prepared in 0.3 M oxalic acid at 40 V for anodization ranging from 0.5 h to 4.0 h. As the anodization time increased from 0.5 to 4.0 h, the pore depth of the AAO increased from 1.6 ± 0.3 to 12.8 ± 0.5 µm. The data shows that the pore length increased linearly with the anodization time with a growth rate of 3.2 µm h^{-1} (Figure 4.9 b). This value is higher than that reported by Nielsch and his group, who reported a growth rate of 2.0 µm h^{-1}. This difference might be due to the temperature where anodization took place in these two studies; in this Thesis, we used 8 °C compared to 1 °C in Nielsch´s work. In our group, Dr. Müller reported a growth rate of 3.25 and 4.00 µm h^{-1} for short (1 h) and long (65 h) anodization time, respectively. Generally, the pore length is proportional to the total current passed to the anode at oxide/Al interfaces. It was noticed that the limited diffusion of the electrolyte in long pores led to a non-linear pore length growth rate[29]. Lee et al. reported that pore lengths of more than 50 µm limited the diffusion of anions reaching the oxide/Al interfaces and that the oxidation rate consequently decreased with the anodization time[30]. The pore length is governed by two processes, namely, Al oxidation and chemical dissolution of oxide. The oxide formation process is dominant because it depends on the availability of the cationic and anionic species (H_3O^+ and OH^-) at the oxide/Al interfaces.

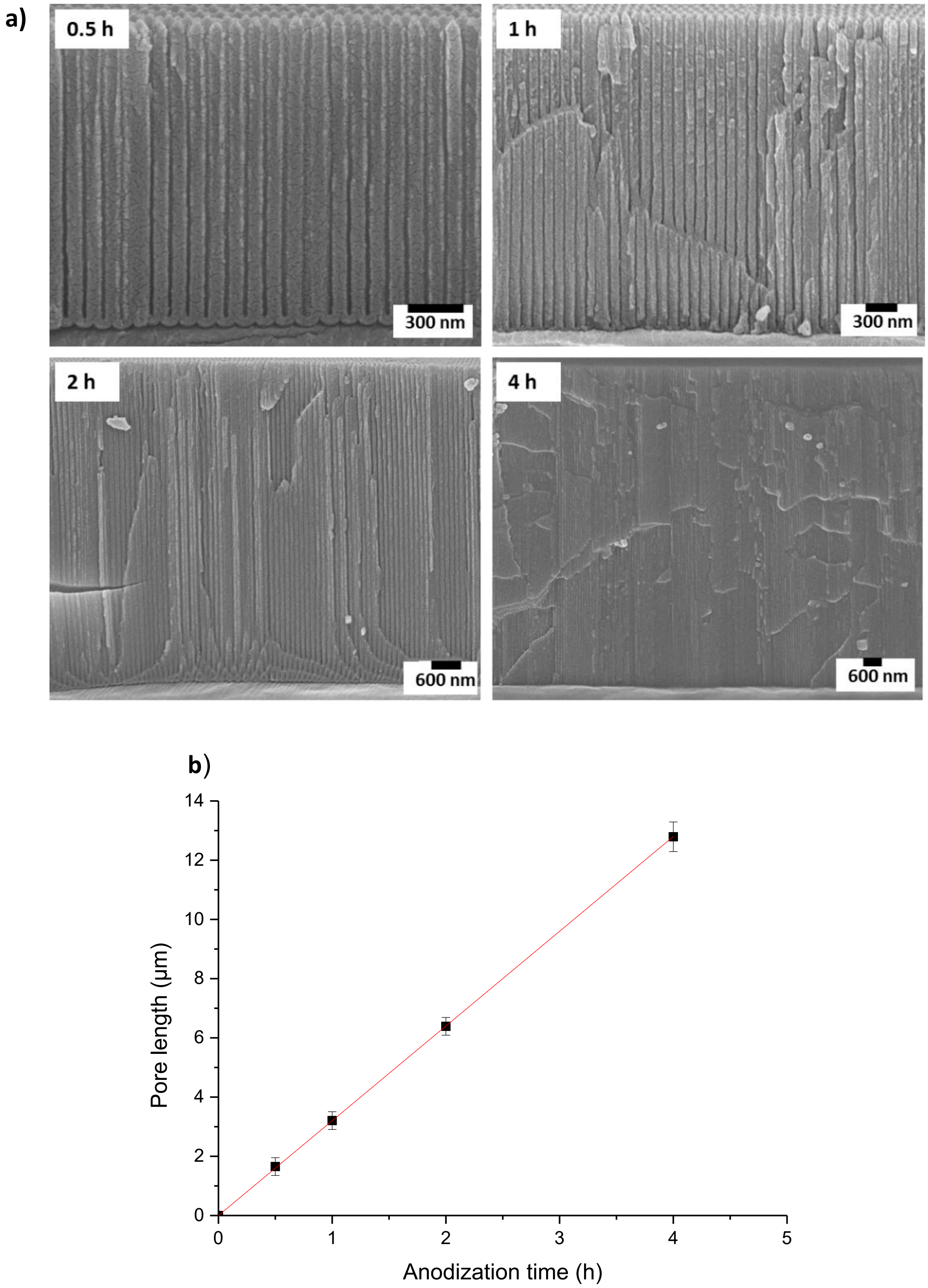

Figure 4.9: *Dependence of the pore length on the anodization time (in 0.3 M oxalic acid at 40 V). a) FESEM cross-section images for anodization times b) Linear fitted graph between mean pore length of AAO (n = 3, the error bars denote the standard deviation) and the anodization time. The solid line corresponds to linear least squares fit of 0 to 4 h, revealing a slope of 3.2 µm* h^{-1}.

While the two-step MA forms ordered circular pores along the entire length, the synthesis of long pores is very time consuming due to the low anodization current. By contrast, HA yields long AAO pores in a short time. For HA, the anodization is started at a lower voltage of 40 V to create a protective oxide layer, which is not ordered (Figure 4.10). Then, the voltage is slowly increased to the final voltage of 130 V. After removing the aluminum from the backside and the barrier oxide layer, a free-standing membrane is obtained, which is well-ordered at the backside.

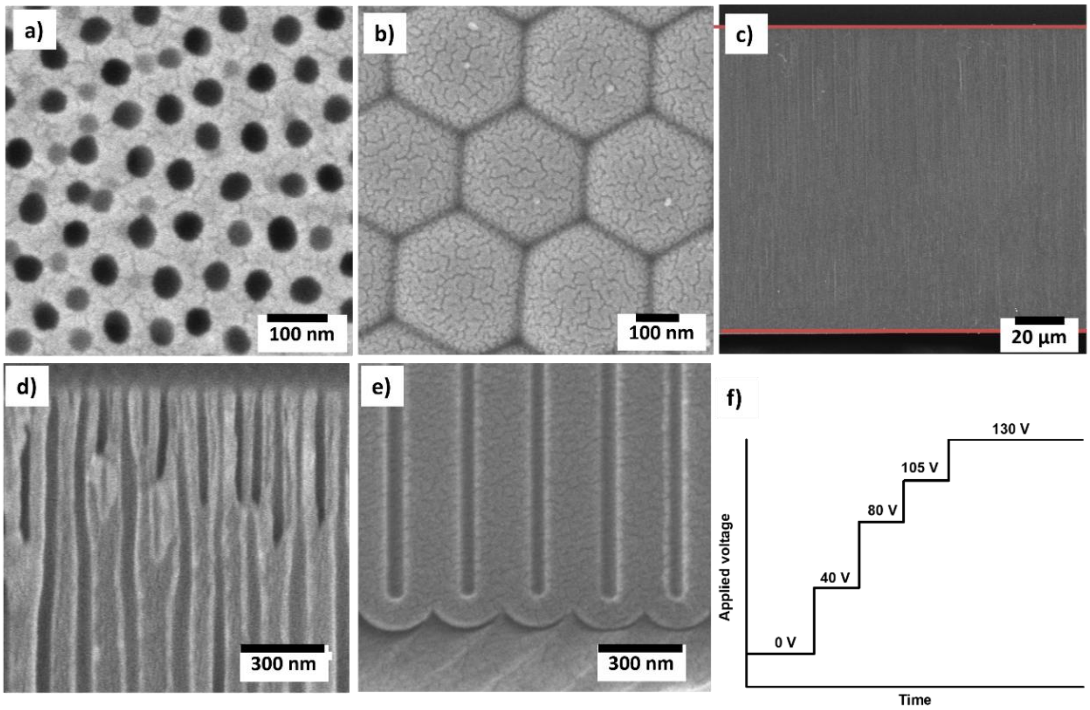

Figure 4.10: *FESEM images of HA anodized AAO in oxalic acid (0.3 M) at 130 V for 4 h. a) topside forming the protective layer for the anodization at high voltage (formed at 40 V) and b) backside after removal of the aluminum, c) cross-sectional view of AAO with low magnification, two red lines were used to determine the top and bottom of AAO film, and d,e) high magnified cross-sectional view of top and bottom of the pores, respectively. f) A plot showing schematic programming of the applied voltage in the HA.*

4.4 Wetting of AAO

The wetting of the AAO pores was investigated using RIfS. Prior to the measurement, the top side of the AAO samples was sputter-coated with 7-8 nm of gold to enhance the reflectivity of the light at the air-AAO interface. The initially air-filled pores were filled with water, and the *EOT* was measured before and after pore filling. Figure 4.11 displays that the

EOT was increased when the pores were filled with water. The Δ*EOT* value was found to be 585 ± 2 nm. The expected *EOT* values were also calculated for both air-filled and water-filled pores using the Maxwell-Garnett equation[31,32]. To calculate the effective refractive index, the refractive indices of bulk Al_2O_3 and air were considered as 1.760 and 1.000, respectively[33]. The refractive index of water was 1.333, which was measured using a refractometer. The porosity and pore length values were determined from FESEM images and were found to be 28 ± 2 % and 3.250 ± 0.050 µm, respectively. Finally, the expected Δ*EOT* was calculated to be 590 nm. The fractional pore filling with water was calculated using Eq. 4.1:

$$\text{Pore filling (\%)} = \frac{\Delta EOT_{\text{experimental}}}{\Delta EOT_{\text{calculated}}} \times 100 \quad \text{.................} \quad \text{(Eq. 4.1)}$$

According to equation 4.1, the pore filling was found to be 98 ± 2 %. The result shows no significant difference between the expected and experimental *EOT*, which means that the pores were entirely filled with water.

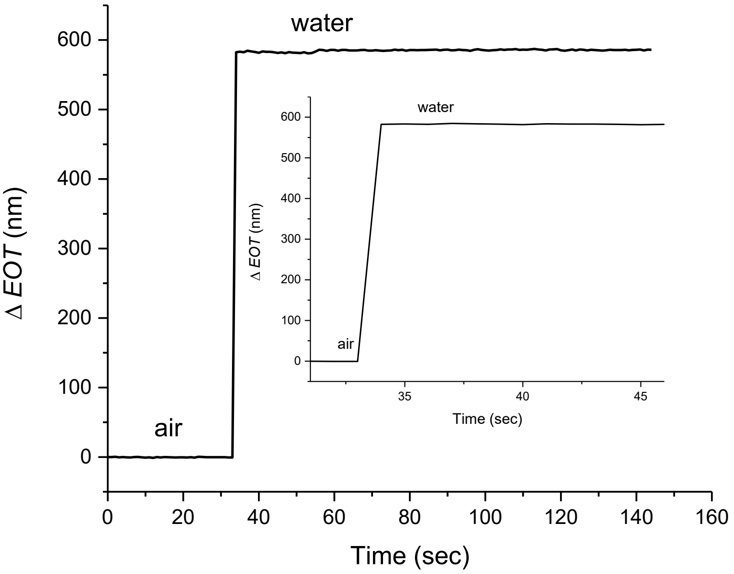

Figure 4.11: *Plot of in-situ- RIfS measurement of the filling of air-filled AAO pores with water. The AAO was fabricated in 0.3 M oxalic acid at 40 V, 60 min second anodization, 17 min pore widening in 0.5 M phosphoric acid at 35 °C, which afforded a pore diameter, interpore distance, pore length, and porosity of 58 ± 2 nm, 108 ± 3 nm, 3.250 ± 0.050 µm and 28 ± 2 %, respectively. The inset shows the transient of filling the pores with water.*

It is not surprising that water wetted AAO pores because the surface of AAO is highly hydrophilic, which was suggested by the measured static contact angle value of 10 ± 3°, close to the value reported by Lee and colleagues (14˚)[34].

Influence of Refractive Index of the Pore Content (void) on RIfS Measurements

To study the effect of the refractive index of the solution on the *EOT*, an experiment using a water/glycerol mixture with different concentrations, i.e., 0.0, 2.5, 5.0, and 7.5 wt% of glycerol in water, was performed. These solutions were introduced into the AAO pores, and the *EOT* was recorded as a function of increasing the refractive index of solutions (Figure 4.12a). All the RIfS measurements were conducted at room temperature, as refractive indices of the solutions are known to depend on the temperature[35,36].

Firstly, water was introduced into the AAO pores, and the *EOT* was recorded *in-situ*. An increase in the Δ*EOT* value by 5 nm was observed after exchanging water with the 2.5 wt% glycerol in water. After 1 min, the cell with the AAO specimen was flushed with water, and a decrease in *EOT* value of 5 nm was observed. The same procedure was repeated for solutions of 5.0 wt% and 7.5 wt% of glycerol in water. The Δ*EOT* as glycerol was replaced by water (or vice versa) due to the increase in the refractive index of the solution inside the pores. As shown in Figure 4.12b, the Δ*EOT* increased linearly with increasing refractive index. Since the length of the AAO pores remains constant during the experiment, the *EOT* value depends upon the refractive index of the pore content of the AAO pores. It can be concluded that *EOT* was found to be sensitive to the change in the refractive index of the solution present inside the AAO pores.

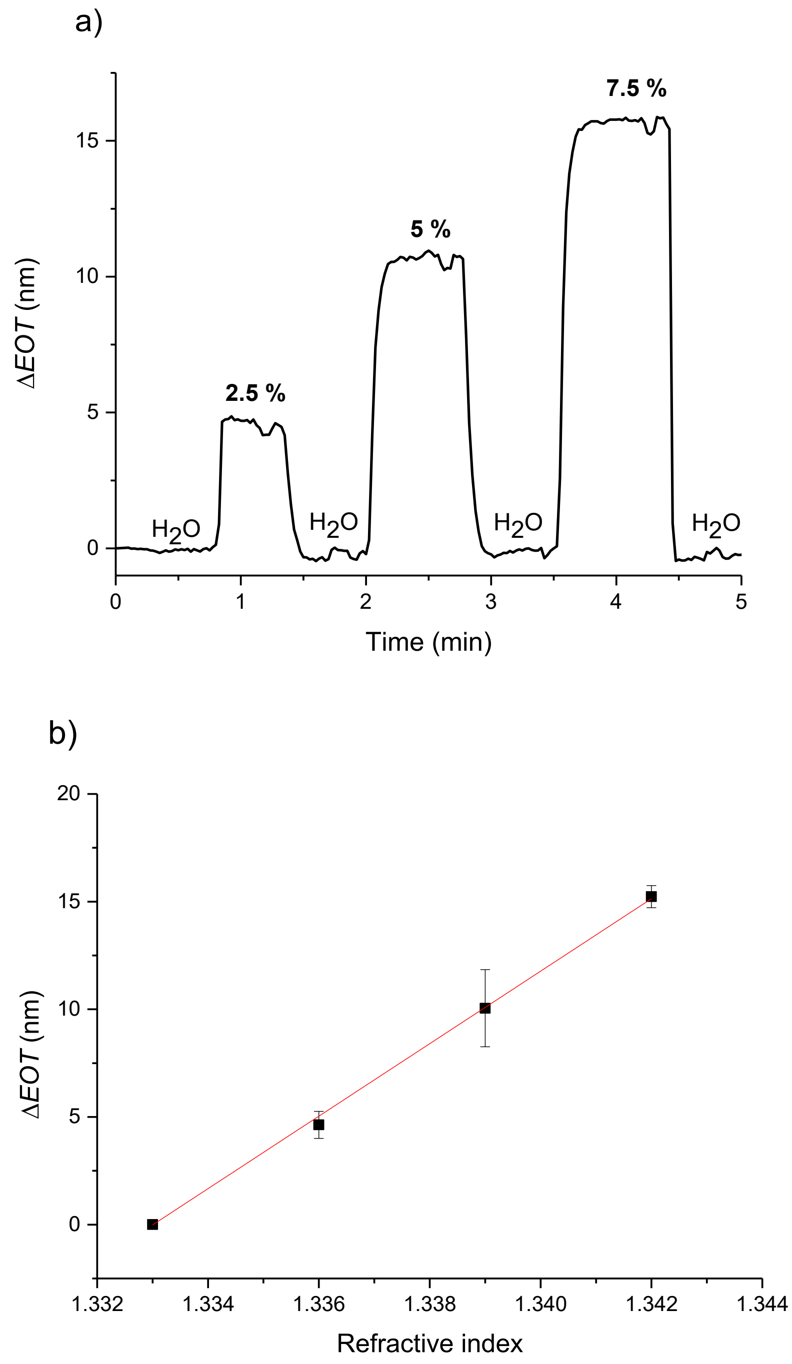

Figure 4.12: *a) ΔEOT values versus time obtained after injecting water/glycerol aliquots of different concentrations. b) Plot of ΔEOT values vs. refractive indices of the solutions used to fill the AAO pores (the solid line represents a least linear squares fit of the data points (n = 3, the error bars denote the standard deviation of ΔEOT). The AAO was fabricated in 0.3 M oxalic acid at 40 V for 60 min, and the pore widening was for 7 min in 0.5 M phosphoric acid at 35 °C which afforded a pore diameter, interpore distance, pore length, and porosity of 42 ± 2 nm, 108 ± 3 nm, 3.250 ± 0.050 µm and 13.7 ± 1.4 %, respectively.*

4.5 Covering the AAO with the Free-Standing Film of Poly(lactic Acid) (PLA)

The strategy to close the nanopores with a thin layer of PLA was to transfer a free-standing thin film of the polymer. To fabricate such a layer, a PLA sheet was prepared on Si wafers, according to Takeoka and co-workers[37]. In order to reduce the adhesion of PLA to the native oxide covered Si surface, the pre-cleaned Si (2 cm x 2 cm) was functionalized with 1H,1H,2H,2H-Perfluorododcyltrichlorosilane (FDTS)[38] via vapor phase deposition. Afterwards, 150 µL of a 3 wt% of PLA prepared in chloroform was spin-coated for 20 sec at 1000 rpm onto the Si wafer. The dry thickness, measured by ellipsometry, of the free-standing PLA film was 350 ± 20 nm. The static water contact angle was measured after each functionalization step. The result reveals that the Si surface was successfully covered with a thin layer of FDTS, which was evident by converting the surface from hydrophilic (13 ± 2°) to hydrophobic (114 ± 3˚) nature. The contact angle dropped to 65 ± 3˚ after spin coating a layer of PLA (Figure 4.13). These values are consistent with previously observed values of bare Si[39], FDTS[40], and PLA film[41] (10-20°, 118°, 72°, respectively).

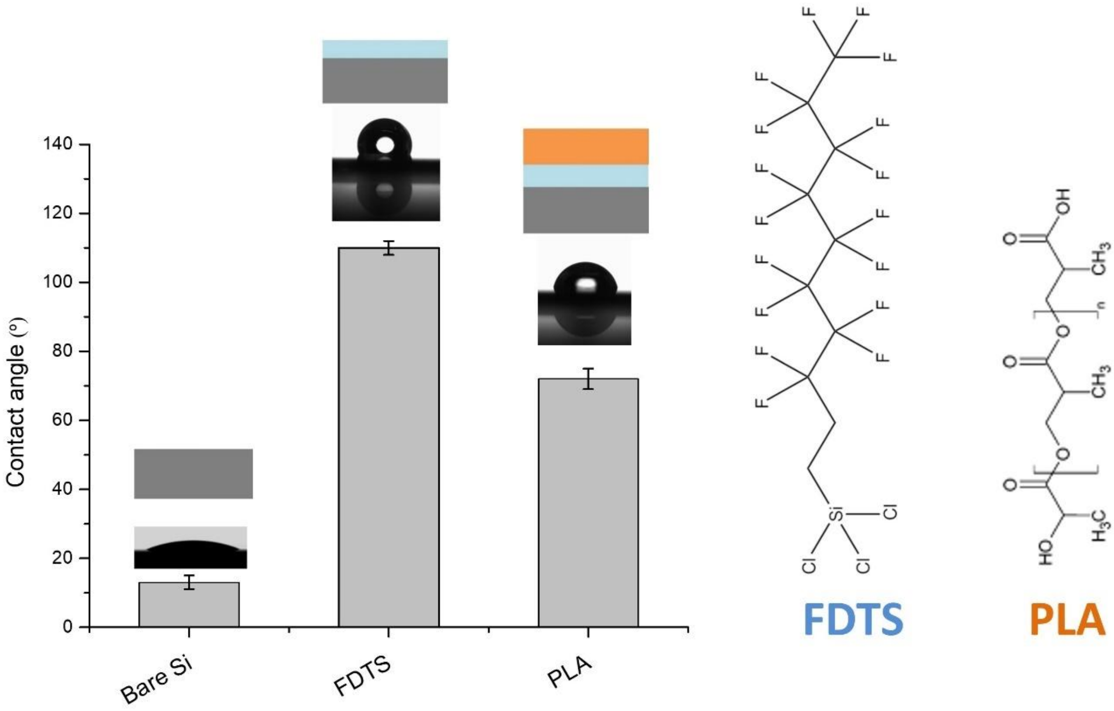

Figure 4.13: *Water contact angle for bare Si, functionalization with FDTS, and for PLA spin coated on Si surface. The chemical structures for FDTS and PLA are inserted.*

Transfer of the free-standing PLA film requires detachment of the PLA film from the Si substrate. Unfortunately, the detachment of this thin film was challenging to achieve without damaging the PLA film. Hence, a second support layer was employed. It was reported that poly(vinyl alcohol) (PVA) was a good choice to support PLA sheets because PVA is water-soluble, and PVA/PLA layers were found to peel off relatively easily from the previously functionalized planar Si with FDTS[42]. Therefore, PVA was utilized as a supporting film. It was thus cast from the solution on the Si wafer that was previously covered with FDTS and PLA. After the drying process, the PVA/PLA film could be peeled off intact and suspended in water to dissolve the PVA (Scheme 4.2).

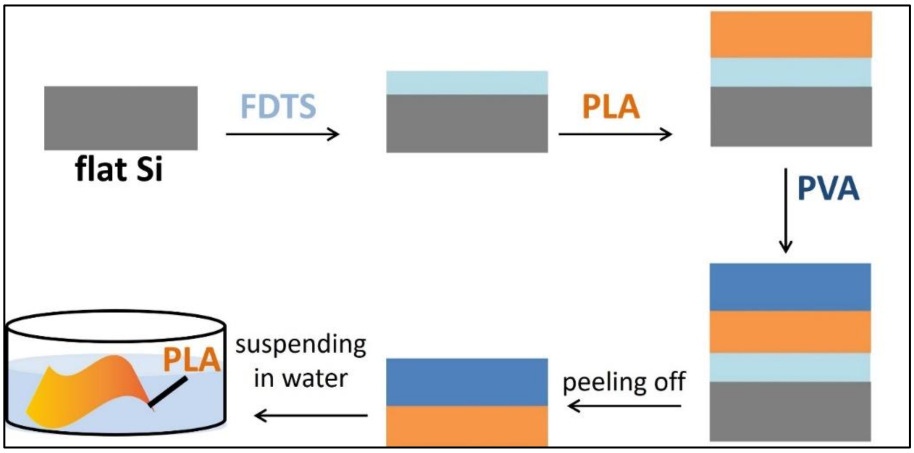

Scheme 4.2: *Schematic of Fabrication of the free-standing PLA film. A planar Si substrate was functionalized with FDTS. Then PLA dissolved in chloroform was dropped on the Si wafer and spin-coated. The Si-FDTS-PLA substrates were coated with PVA, and left to dry at room temperature. Next, the PLA-PVA film was peeled off from Si (support) and suspended in water for 2 h to release the PLA sheet from water-soluble PVA, obtaining a free-standing PLA flooding on water.*

Figure 4.14a shows the suspended PLA film in water, which could be scooped up with AAO. The PLA film was transparent and flexible, as shown in Figure 4.14b. Afterwards, the AAO covered with the free-standing PLA film was heated at 50 ˚C to promote the adhesion of the PLA to the AAO surface. The covered AAO with the free-standing film was analyzed by FESEM.

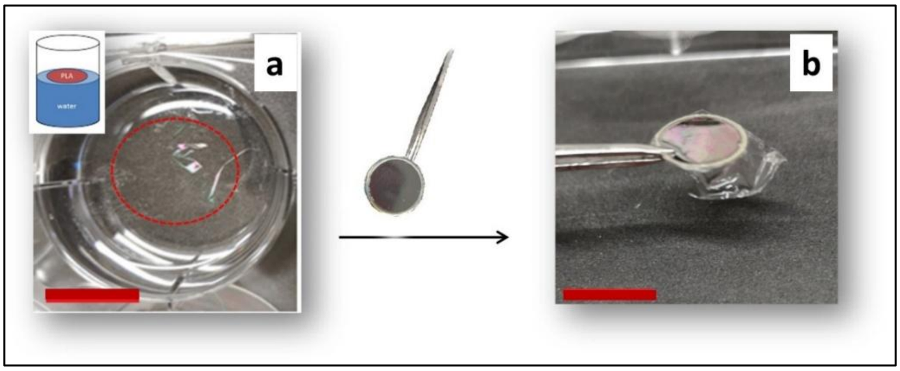

Figure 4.14 *Photograph of the PLA film a) suspended in water, b) covering the AAO. Scale bar = 1 cm*.

Figure 4.15 displays the FESEM image of the PLA film laying on the AAO surface. The FESEM data confirmed that a homogeneous and defect-free PLA thin film could be successfully prepared and transferred onto AAO. The defect-free PLA film was guaranteed by using FDTS since employing this material provides the surface hydrophobic and enables a defect-free detachment of the film and its support[43]. The FESEM shows no PVA layer attached to the PLA layer, which suggests that PVA was dissolved in water and PLA was released. The latter was supported by comparing the thickness of PLA film on the AAO with the thickness of the PLA measured by ellipsometry. These observations confirmed that the thickness of this film did not significantly change before or after detachment from the Si surface (Figure 4.15). The observed crack in the FESEM image could be attributed to the broken underlying support, which might have happened during the mechanical cutting of the AAO for FESEM.

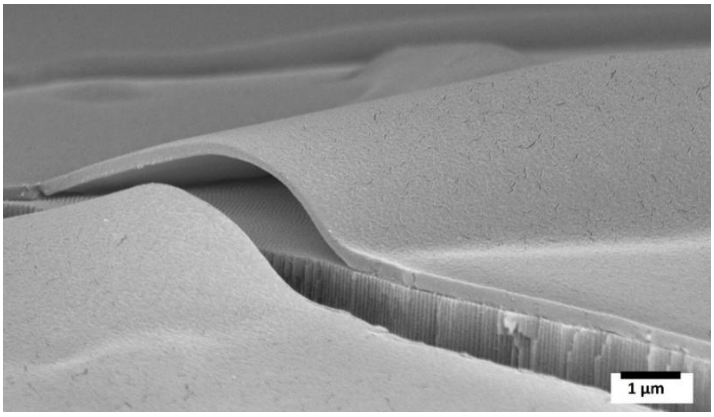

Figure 4.15: *FESEM image of AAO covered with PLA sheet. The AAO was fabricated in 0.3 M oxalic acid at 40 V, 60 min, 7 min pore widening in 0.5 M phosphoric acid at 35 °C, proving pore diameter and pore length of 42 ± 2 nm, 3.250 ± 0.050 µm, respectively. To enhance the attachment of PLA film, the covered AAO with PLA free-standing film was placed on a hot plate for 1 min at 50 ˚C.*

Tests of the PLA/AAO Sensor

To test whether the pores of the AAO were tightly sealed with PLA film, the PLA/AAO system was investigated by RIfS. The RIfS signal was recorded before and after water injection into the RIfS cell, and the Δ*EOT* values were calculated (Figure 4.16a). The data showed that Δ*EOT* increased gradually after injecting water and reached a plateau after 35 min. The increase in the Δ*EOT* value was due to water penetration into the AAO pores. It means that the pores were not permanently sealed with film. This might be either due to (i) cracks in the PLA film that were not detectable in FESEM images, (ii) water, which could get under the PLA film from the edges and fill the pores either directly or by capillary condensation, or (iii) transport of water through the PLA film. These defects might have been formed during the peeling off of the PLA film or during the heating process. The transport of water through the PLA film was excluded as this should occur on much longer time scales[44].

A reference experiment was conducted to verify the change in *EOT* in opened pores (without PLA sheet). The data are shown in Figure 4.16b. The increase of Δ*EOT* was very sharp and reached the plateau in a few seconds. By comparison of the Δ*EOT* values in these two experiments, it was clear that pores were filled to the same extent (likely completely) in both systems (with and without PLA film on top of AAO); however, for the polymer-coated samples, this took much longer, it takes 15 min to fill in half of the pores compared to 2 min of the uncovered AAO. From this outcome, this method, covering the AAO pores with a PLA free-standing sheet, was unsuitable for our sensing design[10]. Therefore, an alternative protocol to achieve a maximum RIfS signal for sensing using PLA deposited into the pores of AAO was established and discussed later in this Thesis.

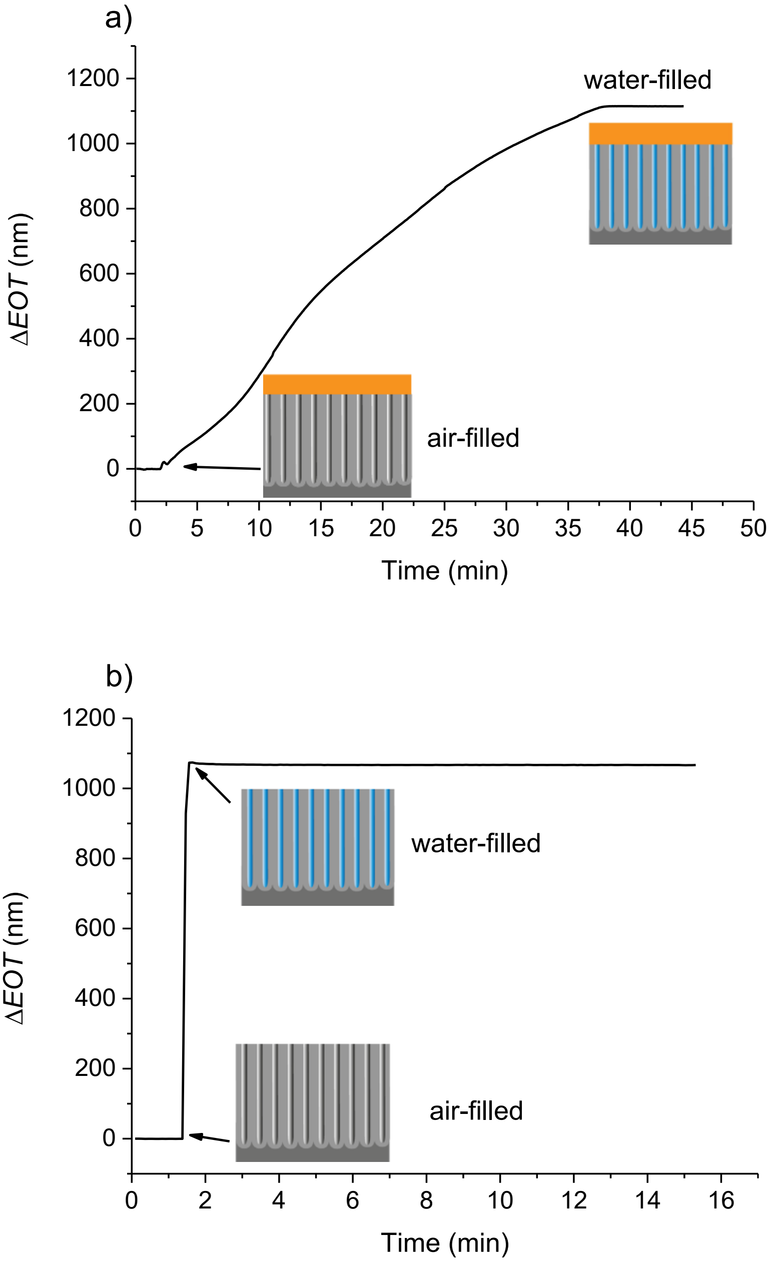

Figure 4.16: *Plot of ΔEOT against the time of the online water- wetting of a) AAO covered with PLA layer, b) neat AAO. The pore diameter, pore length, and porosity of AAO were 59 ± 2 nm, 3.350 ± 0.050 µm, and 28 %, respectively. The AAO was fabricated in 0.3 M oxalic acid at 40 V for 90 min, with 21 min pore widening in 0.5 M phosphoric acid at 35 °C.*

4.6 Conclusion

In this Chapter, the AAO samples were fabricated under optimized conditions to obtain homogenous circular pores with pore diameters and interpore distances ranging from 20 to 130 nm and 64 to 450 nm, respectively. Cooling the reactor is essential to prevent defects, such as uneven pore diameters, that might be formed due to the fluctuation in temperature.

After the electropolishing or anodization step, the aluminum/AAO was checked with FESEM. The data showed that the surface with reduced roughness provided an optimal requirement for anodization. The synthesized AAO samples obtained via the two-step anodization were well-ordered with hexagonal pore shapes. The anodization parameters were adjusted to fabricate the AAO desired for experimental purposes, and the formed AAO samples were investigated. Sulfuric, oxalic, and phosphoric acids with varying voltages were used as electrolytes, offering different pore diameters and interpore distances. In agreement with the literature, the interpore distance was linearly proportional to the anodization voltage.

The pores of the synthesized AAO in oxalic acid were widened in phosphoric acid. The FESEM data confirmed that the pore diameters increased linearly with the widening time. The pore diameter was widened from 32 nm to 85 nm after immersion in phosphoric acid for 35 min. The porosity was also calculated and scaled linearly with widening time. Additionally, the dependence of the pore length on the anodization time was studied. AAO synthesized in oxalic acid at 40 V exhibited pores ranging from 1.6 to 12.8 µm in length when the anodization was conducted from 0.5 to 4.0 h.

The wetting of the AAO pores was investigated using RIfS. The ΔEOT value dramatically increased when the pores were filled with water. Based on the calculated and experimental ΔEOT, the pore filling was found to be 99.5 %. The latter proved that the pores of AAO were filled with water. Furthermore, the dependence of ΔEOT on the refractive index of the filling solution was studied in RIfS, showing a linear trend of ΔEOT with the refractive index of the pore content.

To control the wetting of AAO for further sensing experiments, the top side of AAO was covered with a 350 ± 20 nm thin PLA free-standing sheet. The PLA sheet was successfully prepared on a pre-treated Si wafer using the spin-coated method and transferred to AAO, which covers the top side (the pore gate).

The impact of the PLA sheet on the wetting on AAO was evaluated using RIfS. Two identical AAO samples were used for comparison, covering one with the PLA sheet. The RIfS was conducted during the infiltration of water into the pores. The data showed that the Δ*EOT* measured on AAO covered with PLA gradually increased and reached the plateau in 35 min. In contrast, on the bare AAO (uncovered), the Δ*EOT* increased rapidly and reached a plateau in a few seconds. The latter indicates that the pores were wet with water faster than in the case of covered pores, where the PLA sheet altered the filling of the pores but did not affect the wettability of the pores, which was proved by the *EOT* values for these samples.

4.7 Materials and Methods

Aluminum sheets (99.999 %, 0.5 mm x 100 mm x 250 mm, Evochem), silicon wafers (<100> orientation, Siegert Wafer), sodium hydroxide (>98.8 %, ChemSolute), perchloric acid (70 %, VWR, AnalaR NORMAPUR), ethanol absolute (99.8 %, VWR), 1H,1H,2H,2H-Perfluorododcyltrichlorosilane (97 %, Sigma Aldrich), oxalic acid dihydrate (Merck, >99.5%), phosphoric acid (Roth, 85 wt%), chromium(VI)-oxide (>99.0 %, Sigma-Aldrich), hydrochloric acid 38 wt% (analytical reagent grade, Fisher Scientific), copper (II)-chloride dihydrate (99 %, Riedel-de Haën), Milli-Q water (Milli-Q Direct 8 with Millipak Express 40 filter, 18 MΩ cm, Merck, Germany).

Instruments

Reflectometric Interferometry Spectroscopy (RIfS)

RIfS spectra were measured on AAO, pSi, and pSiRF samples at ambient temperature. The desired samples were fixed into a home-made flow cell and illuminated with white light at a normal incident angle using a tungsten halogen (LS-1) through one arm of a bifurcated optic fiber. The reflected light was collected through another arm of a bifurcated fiber and analyzed using a charge-coupled device (CCD) detector (USB-2000+VIS-NIR-ES). The measurements were recorded using the software SpectraSuite (Ocean Optics). The RIfS signal was recording intervals of 1-60 sec (depending on the experiment), an integration time of 10 msec, a scan to the average value of 500, and a boxcar width of 5. The data was analyzed using the Igor program (Wavemetrics Inc.).

Field Emission Scanning Electron Microscopy (FESEM)

For the characterization of the morphology of the AAO, pSi, and pSiRF samples, FESEM micrographs were acquired on a Zeiss Ultra 55cv Field Emission Scanning Electron Microscopy (FESEM) (Zeiss, Oberkochen, Germany). The operation voltage for all the measurements was 10 kV, and the detector was the Inlens detector. Prior to the measurements, the AAO surface was sputtered with gold for 40 sec, providing a layer of ~ 8 nm, to enhance the conductivity of the surface. The FESEM micrographs were analyzed using ImageJ software (v1.50d).

Fabrication of AAO

If not stated otherwise, the aluminum substrates were degreased in acetone for 3 min and then were rinsed with Milli-Q water and dried in a nitrogen stream. To remove the native oxide layer, the aluminum substrates were immersed in an aqueous solution of NaOH (0.5 M) for 5 min, then rinsed with Milli-Q water and dried in a nitrogen stream. Afterwards, the samples were electropolished at room temperature in a 3:1 mixture (v %) of ethanol and perchloric acid at a constant voltage of 20 V using a power supply (EA-PSI 8160-04T, Electro-Automatic GmbH, Viersen) for 4 min.

The anodization process was performed under a controlled temperature using a cooling system (LAUDA PK20). The reaction temperatures were 5 and -5 °C for the mild and hard anodization, respectively. In the mild anodization, the AAO was fabricated in two steps. In the first step, AAO was anodized in the aqueous solution of oxalic acid (0.3 M) for 5 h at 40 V. The first layer of Al_2O_3 was etched in a solution of phosphoric acid (7.06 g) and chromium oxide (1.53 g) in Milli-Q water (91.42 g) at a temperature of 65 °C. The second anodization step was conducted in the same oxalic acid solution under the same conditions as in the first step.

To achieve the desired pore diameter, the AAO was widened in 0.5 M phosphoric acid at 35 °C for a given time (as mentioned in this Chapter).

The hard anodization was conducted in oxalic acid (0.3 M) at 130 V. In this process, the voltage gradually increased from 40 to 130 V (Table 4.1). Afterwards, the pores were widened for 20 min.

Table 4.1: *Voltage and current program applied for the HA in oxalic acid (0.3 M).*

Time (min)	Voltage (V)	Current (A)
0	40	0.20
8	40	0.20
1	80	0.15
3	105	0.15
1	130	0.15
5	130	0.15
1	130	0.05
240	130	0.05

Fabrication of Free-Standing PLA Film

The flat Si wafers were sonicated in acetone for 5 min by washing them with MQ water and drying them in streaming nitrogen. Afterwards, the cleaned Si wafers were placed in a Uv-Ozone cleaner for 15 min. The functionalization with FDTS was performed by keeping the Si substrates with a vial containing 5 drops of FDTS in the desiccator at a reduced pressure of 16 mbar at room temperature for 12 h. Afterwards, 150 µl of 3 wt% of PLA solution was dropped on a planar Si wafer and spin-coated for 20 sec at 1000 rpm. 1 mL of 10 wt% of PVA (dissolved in distilled water) was cast on the pre-functionalized Si wafer and left to dry at room temperature for 24 h. The PVA/PLA film was peeled off and suspended in water for 2 h. Then, the PLA free-standing sheet was fished by a home-made metal ring. The top side of AAO was covered with this PLA free-standing and placed on a hot plate for 1 min at 50 ˚C.

4.8 References

---

[1] Macias, G.; Ferré-Borrull, J.; Pallarès, J; Marsal, L. 1-D Nanoporous Anodic Alumina Rugate Filters by Means of Small Current Variations for Real-time Sensing Applications. *Nanoscale Research Letters* **2014**, 9 (1), 315. https://doi.org/10.1186/1556-276x-9-315.

[2] Janshoff, A.; Dancil, K.-P. S.; Steinem, C.; Greiner, D. P.; Lin, V. S.-Y.; Gurtner, C.; Motesharei, K.; Sailor, M. J.; Ghadiri, M. R. Macroporous p-Type Silicon Fabry−Perot Layers. Fabrication, Characterization, and Applications in Biosensing. *Journal of the American Chemical Society* **1998**, 120 (46), 12108–12116. https://doi.org/10.1021/ja9826237.

[3] Müller, S.; Cavallaro, A.; Vasilev, K.; Voelcker, N. H.; Schönherr, H. Temperature-Controlled Antimicrobial Release from Poly(diethylene glycol methylether methacrylate)-Functionalized Bottleneck-Structured Porous Silicon for the Inhibition of Bacterial Growth. *Macromolecular Chemistry and Physics* **2016,** *217* (20), 2243–2251. https://doi.org/10.1002/macp.201600099.

[4] Kilian, K. A.; Lai, L. M. H.; Magenau, A.; Cartland, S.; Böcking, T.; Di Girolamo, N.; Gal, M.; Gaus, K.; Gooding, J. J. Smart Tissue Culture: in Situ Monitoring of the Activity of Protease Enzymes Secreted from Live Cells using Nanostructured Photonic Crystals. *Nano Letters* **2009,** *9* (5), 2021–2025. https://doi.org/10.1021/nl900283j.

[5] Gauglitz, G.; Ingenhoff, J. Design of New Integrated Optical Substrates for Immuno-Analytical Applications. *Fresenius' Journal of Analytical Chemistry* **1994**, *349* (5), 355–359. https://doi.org/10.1007/bf00326599.

[6] Lin, V. S.-Y.; Motesharei, K.; Dancil, K.-P. S.; Sailor, M. J.; Ghadiri, M. R. A Porous Silicon-Based Optical Interferometric Biosensor. Science **1997**, *278* (5339), 840–843. https://doi.org/10.1126/science.278.5339.840.

[7] Kumeria, T.; Kurkuri, M. D.; Diener, K. R.; Parkinson, L.; Losic, D. Label-Free Reflectometric Interference Microchip Biosensor Based on Nanoporous Alumina for Detection of Circulating Tumour Cells. *Biosensors and Bioelectronics* **2012**, *35* (1), 167–173. https://doi.org/10.1016/j.bios.2012.02.038

[8] Pacholski, C. Photonic Crystal Sensors Based on Porous Silicon. *Sensors* **2013**, *13* (4), 4694–4713. https://doi.org/10.3390/s130404694.

[9] Kumeria, T.; Kurkuri, M. D.; Diener, K. R.; Parkinson, L.; Losic, D. Label-Free Reflectometric Interference Microchip Biosensor Based on Nanoporous Alumina for Detection of Circulating Tumour Cells. *Biosensors and Bioelectronics* **2012**, *35* (1), 167–173. https://doi.org/10.1016/j.bios.2012.02.038.

[10] Orosco, M. M.; Pacholski, C.; Miskelly, G. M.; Sailor, M. J. Protein-Coated Porous-Silicon Photonic Crystals for Amplified Optical Detection of Protease Activity. *Advanced Materials* **2006**, *18* (11), 1393–1396. https://doi.org/10.1002/adma.200502420.

[11] Kumeria, T.; Losic, D. Controlling Interferometric Properties of Nanoporous Anodic Aluminium Oxide. *Nanoscale Research Letters* **2012**, 7 (1),88. https://doi.org/10.1186/1556-276X-7-88.

---

[12] Nielsch, K.; Choi, J.; Schwirn, K.; Wehrspohn, R.; Gösele, U. Self-ordering Regimes of Porous Alumina: the 10 Porosity Rule. *Nano letters* **2002,** 2 (7), 677–680. https://doi.org/10.1021/nl025537k.

[13] Masuda, H.; Fukuda, K. Ordered Metal Nanohole Arrays Made by a Two-Step Replication of Honeycomb Structures of Anodic Alumina. *Science* **1995**, *268* (5216), 1466–1468. https://doi.org/10.1126/science.268.5216.1466.

[14] Raoufi, M.; Schönherr, H. Improved Synthesis of Anodized Aluminum Oxide with Modulated Pore Diameters for the Fabrication of Polymeric Nanotubes. *RSC Advances* 2013, *3* (32), 13429. https://doi.org/10.1039/c3ra41165f.

[15] Hopkins, P. D.; Farrer, R. A. A Green Method to Produce Nanoporous Aluminum Oxide Templates and the Direct Application in the Synthesis of Nanowires. *Applied Materials Today* **2023**, *32*, 101768. https://doi.org/10.1016/j.apmt.2023.101768.

[16] Huang, W.; Yu, M.; Cao, S.; Wu, L.; Shen, X.; Song, Y. Fabrication of Highly Ordered Porous Anodic Alumina Films in 0.75 M Oxalic Acid Solution without Using Nanoimprinting. *Materials Research Bulletin* **2019**, *111*, 24–33. https://doi.org/10.1016/j.materresbull.2018.11.002.

[17] Zaraska, L.; Sulka, G. D.; Szeremeta, J.; Jaskuła, M. Porous Anodic Alumina Formed by Anodization of Aluminum Alloy (AA1050) and High Purity Aluminum. *Electrochimica Acta* **2010**, *55* (14), 4377–4386. https://doi.org/10.1016/j.electacta.2009.12.054.

[18] Bai, A.; Hu, C.-C.; Yang, Y.-F.; Lin, C.-C. Pore Diameter Control of Anodic Aluminum Oxide with Ordered Array of Nanopores. *Electrochimica Acta* **2008**, *53* (5), 2258–2264. https://doi.org/10.1016/j.electacta.2007.09.039.

[19] Li, A. P.; Müller, F.; Birner, A.; Nielsch, K.; Gösele, U. Hexagonal Pore Arrays with a 50–420 nm Interpore Distance Formed by Self-Organization in Anodic Alumina. *Journal of Applied Physics* **1995**, 84 (11), 6023–6026. https://doi.org/10.1063/1.368911.

[20] Masuda, H.; Hasegwa, F.; Ono, S. Self-Ordering of Cell Arrangement of Anodic Porous Alumina Formed in Sulfuric Acid Solution. *Journal of The Electrochemical Society* **1997**, *144* (5), L127–L130. https://doi.org/10.1149/1.1837634.

[21] Raoufi, M.; Tranchida, D.; Schönherr, H. Pushing the Size Limits in the Replication of Nanopores in Anodized Aluminum Oxide via the Layer-by-Layer Deposition of Polyelectrolytes. Langmuir 2012, 28 (26), 10091–10096. https://doi.org/10.1021/la3017062.

[22] Choi, D. H.; Lee, P. S.; Hwang, W.; Lee, K. H.; Park, H. C. Measurement of the Pore Sizes for Anodic Aluminum Oxide (AAO). *Current Applied Physics* **2006**, *6*, e125–e129. https://doi.org/10.1016/j.cap.2006.01.024.

[23] Martín, J.; Manzano, C.V.; Martín-González, M. In-depth study of self-ordered porous alumina in the 140–400nm pore diameter range. *Microporous and Mesoporous Materials* **2012**, 151, 311–316. https://doi.org/10.1016/j.micromeso.2011.10.018.

[24] Schulte, A.; Alhusaini, Q.F. M.; Schönherr, H. Anodic Aluminum Oxide Nanopore Template-Assisted Fabrication of Nanostructured Poly(vinyl alcohol) Hydrogels for Cell Studies. *ACS Applied Bio Materials* **2020**, 3 (4), 2419–2427. https://doi.org/10.1021/acsabm.0c00153.

---

[25] Nemati, M.; Santos, A.; Losic, D. Fabrication and Optimization of Bilayered Nanoporous Anodic Alumina Structures as Multi-Point Interferometric Sensing Platform. *Sensors* **2018**, 18 (2). https://doi.org/10.3390/s18020470.

[26] Raoufi, M.; Tranchida, D.; Schönherr, H. Pushing the Size Limits in the Replication of Nanopores in Anodized Aluminum Oxide via the Layer-by-Layer Deposition of Polyelectrolytes. *Langmuir* **2018**, 28 (26), 10091–10096. https://doi.org/10.1021/la3017062.

[27] Eckstein, C.; Xifré-Pérez, E.; Porta-I-Batalla, M.; Ferré-Borrull, J.; Marsal, L.F. Optical Monitoring of the Capillary Filling Dynamics Variation in Nanoporous Anodic Alumina toward Sensing Applications. *Langmuir* **2016**, 32 (41), 10467–10472. https://doi.org/ 10.1021/acs.langmuir.6b02459.

[28] Zaraska, L.; Sulka, G. D.; Jaskuła, M. Anodic Alumina Membranes with Defined Pore Diameters and Thicknesses Obtained by Adjusting the Anodizing Duration and Pore Opening/Widening Time. *Journal of Solid State Electrochemistry* **2011**, *15* (11–12), 2427–2436. https://doi.org/10.1007/s10008-011-1471-z.

[29] Garcia-Vergara, S.J.; Skeldon, P.; Thompson, G.E.; Habazaki, H. A Flow Model of Porous Anodic Film Growth on Aluminium. *Electrochimica Acta* **2006**, 52 (2), 681–687: https://doi.org/10.1016/j.electacta.2006.05.054.

[30] Lee, W.; Ji, R.; Gösele, U.; Nielsch, K. Fast Fabrication of Long-Range Ordered Porous Alumina Membranes by Hard Anodization. *Nature materials* **2006**, 5 (9), 741–747. https://doi.org/ 10.1038/nmat1717.

[31] Garnett J. C. M. Colours in Metal Glasses and in Metallic Films. *Philosophical Transactions of* the *Royal Society of London* **1904**, 203, 385–420. https://doi.org/10.1098/rsta.1904.0024.

[32] Sulka, G. D.; Hnida, K. Distributed Bragg Reflector Based on Porous Anodic Alumina Fabricated by Pulse Anodization. *Nanotechnology* **2012**, 23 (7), 75303. https://doi.org/10.1088/0957-4484/23/7/075303.

[33] French, R. H.; Müllejans, H.; Jones, D. J. Optical Properties of Aluminum Oxide: Determined from Vacuum Ultraviolet and Electron Energy-Loss Spectroscopies. *Journal of the American Ceramic Society* **1998**, 81 (10), 2549–2557. https://doi.org/10.1111/j.1151-2916.1998.tb02660.x.

[34] Lee, J.; Jung, S.-Y.; Kumbhar, V. S.; Uhm, S.; Kim, H.-J.; Lee, K. Formation of aluminum oxide nanostructures via anodization of Al3104 alloy and their wettability behavior for self-cleaning application. *Catalysis Today* **2021**, *359*, 50–56. https://doi.org/10.1016/ j.cattod.2019.04.062.

[35] Behrends, R.; Fuchs, K.; Kaatze, U.; Hayashi, Y.; Feldman, Y. Dielectric Properties of Glycerol/Water Mixtures at Temperatures between 10 and 50°C. *The Journal of Chemical Physics* **2006**, 124 (14), 144512. https://doi.org/10.1063/1.2188391.

[36] Jasny, J.; Nickel, B.; Borowicz, P. Wavelength- and Temperature-Dependent Measurement of Refractive Indices. *Journal of the Optical Society of America B* **2004**, 21 (4), 729–738. https://doi.org/10.1364/JOSAB.21.000729.

---

[37] Okamura, Y.; Kabata, K.; Kinoshita, M.; Saitoh, D.; Takeoka, S. Free-Standing Biodegradable Poly(lactic acid) Nanosheet for Sealing Operations in Surgery. *Advanced Materials* **2009**, 21, 4388-4392. https://doi.org/10.1002/adma.200901035

[38] Nishino, T.; Meguro, M.; Nakamae, K.; Matsushita, M.; Ueda, Y. The Lowest Surface Free Energy Based on −CF3 Alignment. *Langmuir* **1999**, 15 (13), 4321–4323. https://doi.org/10.1021/la981727s.

[39] Bryk, P.; Korczeniewski, E.; Szymański, G. S.; Kowalczyk, P.; Terpiłowski, K.; Terzyk, A. P. What Is the Value of Water Contact Angle on Silicon? *Materials* **2020**, *13* (7), 1554. https://doi.org/10.3390/ma13071554.

[40] Arukalam, I. O.; Meng, M.; Xiao, H.; Ma, Y.; Oguzie, E. E.; Li, Y. Effect of Perfluorodecyltrichlorosilane on the Surface Properties and Anti-corrosion Behavior of Poly(dimethylsiloxane)-ZnO Coatings. *Applied Surface Science* **2017**, *433*, 1113–1127. https://doi.org/10.1016/j.apsusc.2017.10.096.

[41] Zereshki, S.; Figoli, A.; Madaeni, S. S.; Simone, S.; Jansen, J. C.; Esmailinezhad, M.; Drioli, E. Poly(lactic acid)/Poly(vinyl pyrrolidone) Blend Membranes: Effect of Membrane Composition on Pervaporation Separation of Ethanol/Cyclohexane Mixture. *Journal of Membrane Science* **2010**, *362* (1–2), 105–112. https://doi.org/10.1016/j.memsci.2010.06.025.

[42] Okamura, Y.; Kabata, K.; Kinoshita, M.; Miyazaki, H.; Saito, A.; Fujie, T.; Ohtsubo, S., Saitoh, D.; Takeoka, S. Fragmentation of Poly(lactic acid) Nanosheets and Patchwork Treatment for Burn Wounds. *Advanced Materials* **2013,** 25, 545-551. https://doi.org/10.1002/adma.201202851.

[43] Lilge, I.; Jiang, S.; Schönherr, H. Long-Term Stable Poly(acrylamide) Brush Modified Transparent Microwells for Cell Attachment Studies in 3D. *Macromolecular Bioscience* **2017**, *17* (5). https://doi.org/10.1002/mabi.201600451.

[44] Xu, H.; Yang, X.; Xie, L.; Hakkarainen, M. Conformational Footprint in Hydrolysis-Induced Nanofibrillation and Crystallization of Poly(lactic acid). *Biomacromolecules* **2016**, *17* (3), 985–995. https://doi.org/10.1021/acs.biomac.5b01636.

Chapter 5. Enzymatic Degradation of Poly(lactic acid) on Planar Si and Nanoporous AAO

5.1 Introduction

In recent years, anodic aluminum oxide (AAO) has been among the interesting nanoporous materials due to its potential applications, including drug delivery[1,2], energy storage[3], and biosensing[4,5,6]. Modifying AAO structures with polymeric materials is one of the protocols for designing enzyme biosensing systems. The concept of enzyme sensors possesses the potential for future (bio)medical applications, e.g., to detect bacterial infections via the detection of hydrolytic bacterial enzymes that may be present in high local concentrations when secreted by bacteria in bacterial biofilms[7]. In this Chapter, AAO was coated with a biodegradable polymer to design a composite system to detect a particular bacterial enzyme. The fungal enzyme proteinase K was used as a model enzyme for proteases secreted, e.g., by *Pseudomonas aeruginosa* (*P. aeruginosa*)[8,9,10]. Nanoporous AAO and planar Si substrates were coated via spin coating with poly(lactic acid) (PLA) and the enzymatic degradation of PLA as a function of film thickness was studied. Scheme 5.1 illustrates the coating of the top side of the AAO specimen surface with PLA and the enzymatic degradation of PLA by exposing the sensor to proteinase K. The degradation of the PLA film was monitored using ellipsometry, contact angle, Fourier transform infrared spectroscopy (FTIR), atomic force microscopy (AFM), reflectometric interference spectroscopy (RIfS), and field emission scanning electron microscopy (FESEM) to provide insight into structure-property relationships.

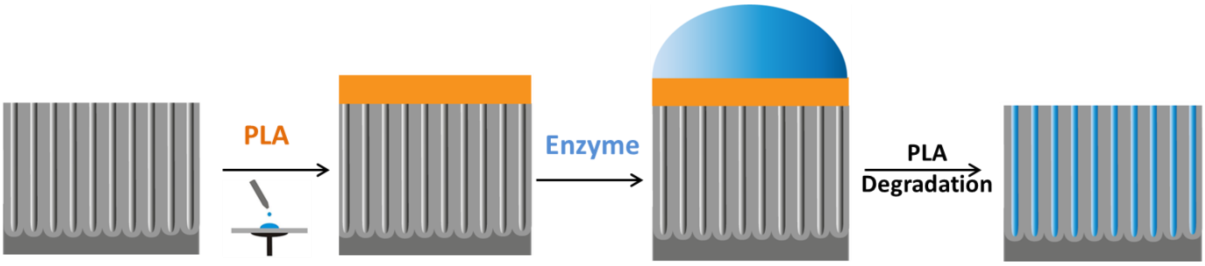

Scheme 5.1: *Schematic of the AAO-based sensor for the detection of enzymes. PLA was spin-coated on AAO before performing the enzymatic degradation, which leads to the opening of the previously closed pore.*

5.2 Modification of Planar Si with PLA by the Spin Coating Method

The spin coating process of PLA was initially performed on planar silicon (Si) wafers. PLA solutions of different concentrations were spin-coated onto pre-cleaned Si wafers at a spinning rate of 1000 rpm for 20 sec. The thicknesses of the resulting films were measured via ellipsometry. Figure 5.1a shows that the dry ellipsometric thickness of the PLA films increased monotonically with the concentration of PLA, in accordance with general observations in spin coating[11]. Specifically, Okamura and his group reported that the film thickness of PLA on planar Si prepared via spin coating increases proportionally to the PLA concentration utilized[12].

Static water contact angle measurements were performed on planar Si surfaces before and after PLA deposition to confirm qualitatively the surface modification. The results of the static water contact angle are presented in Figure 5.2b. The mean value of the measured contact angle of the pre-cleaned Si surface increased from 16 ± 2˚ to 74 ± 3˚ after PLA coating; the latter value is in good agreement with data reported in the literature[13]. It is well known that the higher the water contact angle, the lower the hydrophilicity of the surface[14]. Therefore, the change in contact angle agrees with the presence of the PLA on the Si surface, which changes the surface wettability of oxide covered Si (wettable with water).

The effect of the PLA thickness on contact angle values was also investigated. As shown in Figure 5.1b, there is no significant change in the contact angle values of PLA-coated Si for the film thickness ranging from 14 ± 2 to 172 ± 6 nm, which suggests that homogenous PLA films on the Si wafers were prepared.

Noteworthy, the wettability of the substrate-supported polymer thin film could be thickness-dependent for ultrathin films. Petek and co-workers studied the effect of the film thickness on van der Waals interactions[15]. Their study explored how the underlying substrates (beneath the polymeric thin film) or a homopolymer bilayer system result in van der Waals interactions through the top layer (film). They found that the wetting of a PS thin film with a thickness of 10 nm and below (critical thickness) is mainly dominated by the van der Waals forces, whereas there is no effect of the van der Waals on the wetting of the thicker film. Other researchers reported another value of the critical film thickness. They argued that the van der Waals interactions had no effect on the wettability of an epoxy resin film if the film thickness was below 18 nm[16].

It is worth pointing out that parameters other than the van der Waals interactions may affect the wettability of the thicker polymer film, such as polymer chain mobility[17] or surface roughness[18]. For instance, Hirt et al. reported that a change in the wettability of PLA thin film was observed after manipulating the surface chemical properties and roughness by treating the film with UV radiation[19]. These authors found that the water contact angles decreased with UV exposure time. Another study conducted by Schimmel and coworkers proved that surface wettability changes with surface roughness[20]. They reported that the measured water contact angle of the porous polymer film was reduced by 30° after smoothing the polymer film by isothermal annealing near the glass transition temperature.

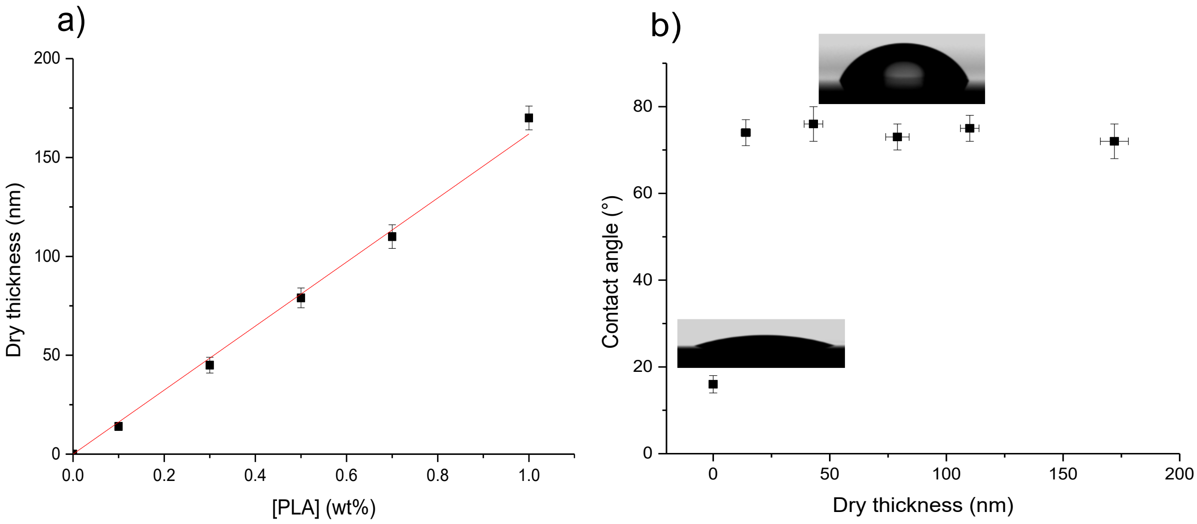

Figure 5.1: *a) Dry ellipsometric thickness versus concentration of PLA solutions (0.1, 0.3, 0.5, 1.0 wt% in chloroform) spin-coated at 1000 rpm for 20 sec on planar oxide covered Si substrates. The solid line corresponds to a linear least-squares fit of the data, which are presented as mean values. The error bars denote the standard deviations (n = 3). b) Values of static water contact angle (sessile drop) versus the thickness of PLA films. The insets are photographs of water droplets on a pristine and a PLA-coated Si wafer, respectively.*

The chemical structure of the PLA spin-coated films on Si was confirmed by FTIR in transmission mode. In the FTIR spectrum shown in Figure 5.2a, the bands at 2997 cm^{-1} and 2946 cm^{-1} are attributed to the CH stretching region[21]. The band at 1759 cm^{-1} is due to the stretching vibrations of C=O bonds[22]. The band at 1456 cm^{-1} is assigned to the -CH$_3$ groups, whereas the bands at 1381 cm^{-1} and 1363 cm^{-1} are related to the -CH groups[23]. The bands at 1189 cm^{-1} and 1090 cm^{-1} correspond to the stretching vibrations of C-O-C groups[21]. FTIR spectroscopy was also performed on different PLA films with different thicknesses. As the different PLA thicknesses displayed essentially very similar spectral characteristics in the region 2000-1500 cm^{-1}, the FTIR spectra of these PLA films are presented as a stack plot in Figure 5.2b. As shown in Figure 5.2b, the absorbance of the band attributed to the C=O bond vibration increased dramatically with the dry thickness of PLA films. The peak areas of C=O groups were determined from the corresponding FTIR spectra and are shown in Figure 5.3c. The values increase linearly with increasing PLA film thickness. The data confirms that PLA was deposited on the Si surface, whereas no peak of the C=O bond was detected in the neat Si substrate.

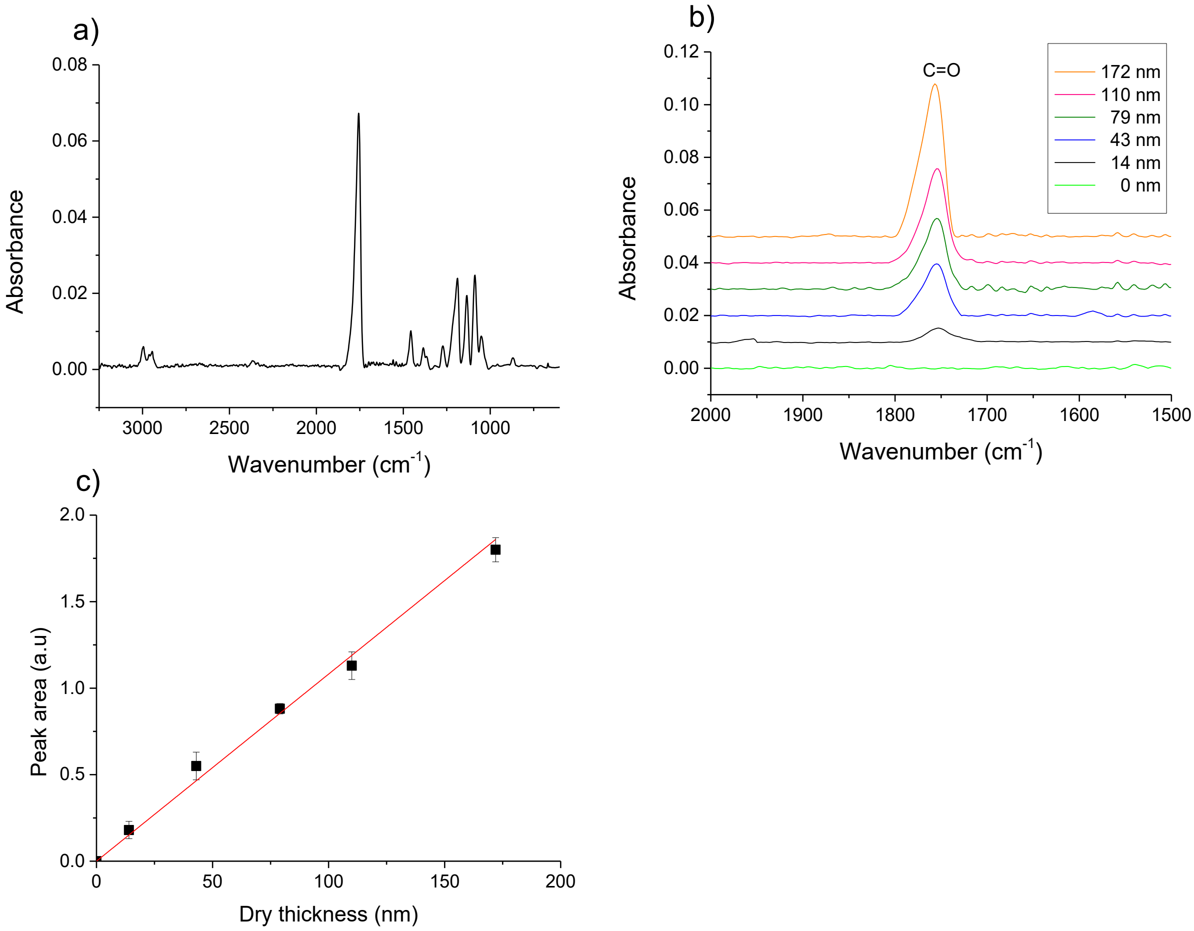

Figure 5.2: *a) FTIR spectrum of PLA film (1.0 wt% PLA solution in chloroform) that was spin-coated at 1000 rpm for 20 sec on planar Si substrates. b) FTIR spectra stack plot for the region 2000-1500 cm^{-1} (where the peak of carbonyl groups is shown) of different thicknesses of PLA films (prepared with PLA solutions of 0.1, 0.3, 0.5, 1.0 wt% in chloroform). c) Dependence of carbonyl peak area on the PLA film thickness. The solid line corresponds to linear least-squares fits of the data. The error bars denote the standard deviations (n = 3).*

5.3 Modification of AAO with PLA by the Spin Coating Method

Subsequently, PLA was utilized to cover the top side of AAO (i.e., the top side with open pores). The coating of PLA onto AAO was performed using the spin coating method. A series of PLA concentrations were chosen to examine the minimum film thickness of PLA that could effectively seal the AAO pores against the ingress of water. This was also done because it has been reported that the thickness of the deposited polymer on the AAO pores impacts the designing of sensor-based AAO[24]. Such a PLA film was supposed to be exposed to an enzyme aqueous solution to study the degradation process catalyzed by the enzyme. Therefore, the smaller the PLA film thickness, the shorter the expected degradation time, which is necessary for sensing.

The deposited PLA on AAO sensors was first investigated by FESEM. Figure 5.3a-d shows FESEM images of AAO before and after the coating with solutions of different concentrations of PLA. The FESEM data revealed that the pores of AAO were not covered when the low PLA concentrations (3 and 4 wt% in chloroform) were used, whereas in the case of the higher concentration of 5 wt% in chloroform, the top side of AAO was covered and no pores were visible. The disappearance of discernible pores on the AAO surface demonstrates that the spin coating method produces a PLA film that successfully covers the pores of the AAO (here, with a mean diameter of 42 ± 3 nm).

A thicker PLA layer is required to seal the AAO pores because of the difference in porosity and roughness between AAO and the planar Si. Jennings and his group observed a variation in the thickness of the polymer coating on porous and nonporous substrates despite employing the same quantity of polymer[25]. These authors attributed this variation to the differences in the surface morphologies of the porous and nonporous substrates.

Figure 5.3e,f shows cross-sectional images of bare AAO and PLA film atop the AAO. Only the AAO sample that was covered with a higher concentration (5 wt%) of PLA solution is shown. The data reveals that the PLA film successfully covers the top side of the AAO surface with a film thickness of 340 ± 30 nm. Based on the FESEM images, the spin coating method can be utilized to prepare a uniform polymer film on both planar and porous surfaces.

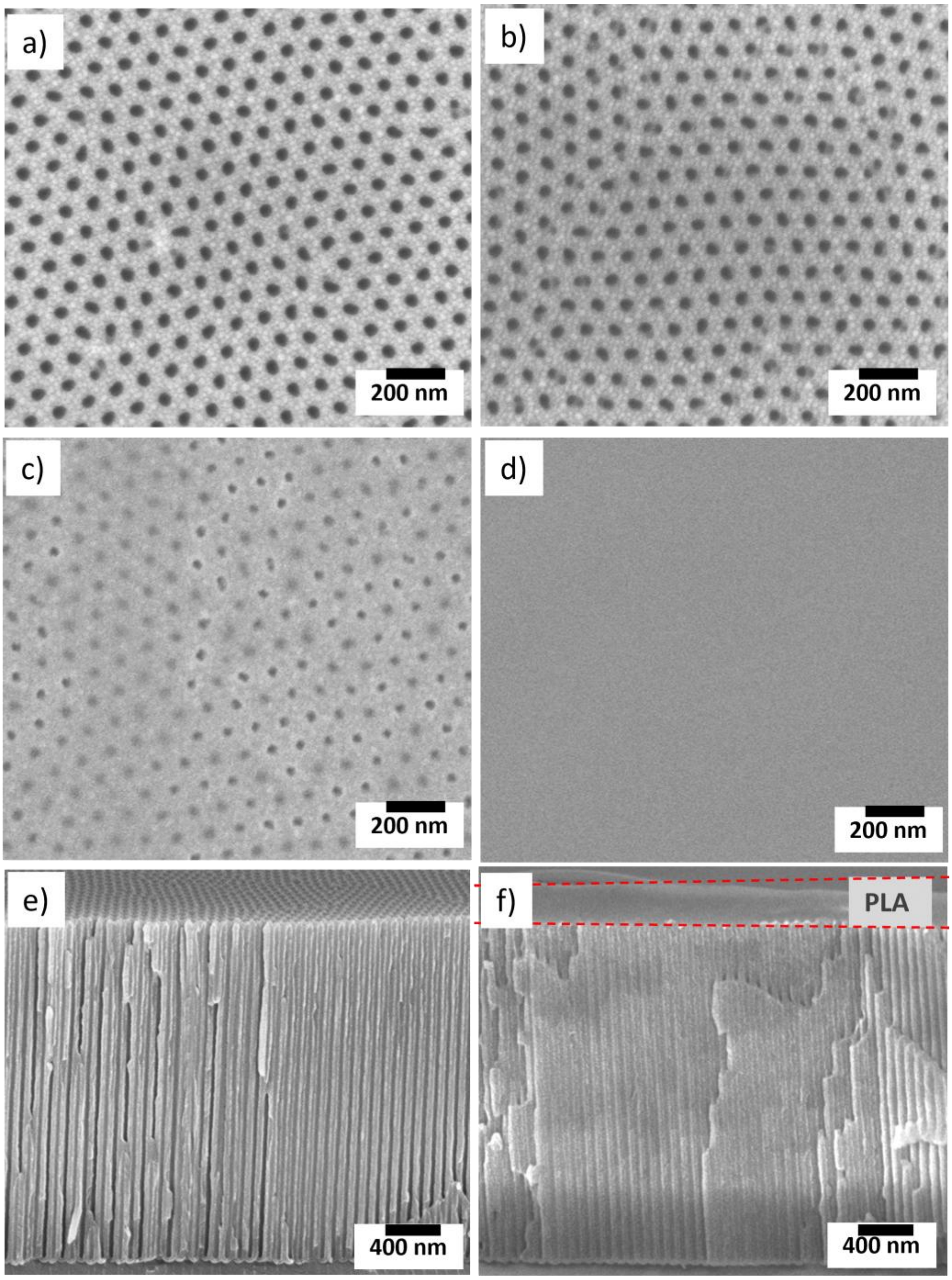

Figure 5.3: *Top view and cross-sectional FESEM images of AAO (D_i = 103 nm, D_p = 42 nm, l = 3.2 µm; 40 V, 0.3 M oxalic acid, 2nd anodization: 60 min, widening: 7 min in H_3PO_4 at 35 °C). a,e) bare AAO, b,c) spin-coated of 3, 4 wt% PLA, and d,f) spin-coated of 5 wt% PLA in chloroform.*

Attenuated total reflectance FTIR (ATR-FTIR) spectroscopy measurements were performed on the top side of the AAO surface covered with different amounts of PLA. The AAO samples were measured by ATR-FTIR spectroscopy before and after PLA coating and the recorded spectra are presented in Figure 5.4a. As discussed previously in this Chapter, the absorbance at 1759 cm^{-1}, which was assigned to C=O groups in PLA, was used to evaluate the coating process. The ATR-FTIR spectroscopy measurement on the neat AAO could not detect any band at 1759 cm^{-1} compared to the coated AAO with PLA. The FTIR spectra confirmed that the prominent carbonyl absorption band increased with PLA concentration due to the increase in the thickness of the PLA film. The area under the band of the carbonyl group stretching vibration showed a linear relationship with PLA concentration from 1 to 4 wt% in chloroform. By contrast, a maximum height and peak area for the carbonyl peak was observed at the higher PLA concentration (5 wt% in chloroform); additionally, a deviation from the linear trend was observed (Figure 5.4b). The latter phenomenon is attributed to the higher viscosity of the polymer solution at the high concentration[26]. Torkelson and co-workers investigated the effect of the viscosity of the PS and PMMA solutions on the film thickness using the spin coating method[26]. They reported that the high viscosity of the polymer solution (higher concentration) hinders the flow (of the solution) on the substrate; subsequently, the solvent's evaporation will occur before the film thinning process, which is necessary to prepare a homogenous polymer film[26]. Therefore, the more viscous the polymer solution, the thicker the film is formed[27]. Mattoli´s group conducted a study to prepare a free-standing PLA film for cell-polymer interaction; the data showed a non-linear behaviour of the prepared PLA film with the higher polymer concentrations[28].

The PLA film coated on AAO may differ in thickness from that on the planar Si surface even if the same concentration of polymer is used due to the difference in the wetting behaviour of those surfaces, as they have different properties and morphologies[29].

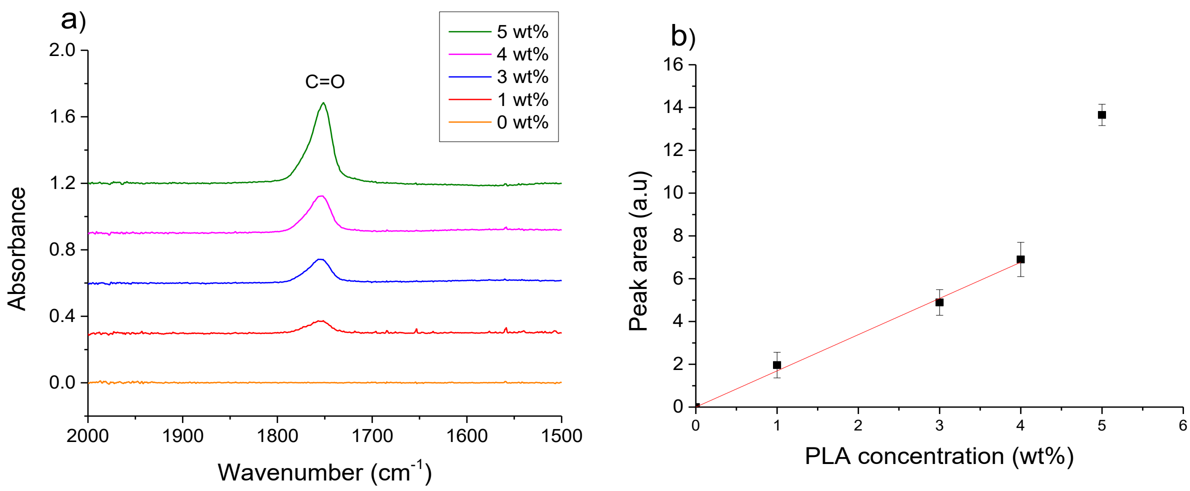

Figure 5.4: *a) ATR- FTIR spectra stack plot for PLA thin films prepared by spin coating using different concentrations of PLA in chloroform on AAO. b) Dependence of carbonyl peak area at 1755 cm^{-1} on the PLA film thickness. The solid line corresponds to linear least-squares fits of the data. The error bars denote the standard deviations (n = 3).*

The thermal degradation behaviour of the neat PLA and PLA-covered AAO is shown in Figure 5.5a,b. PLA is thermally unstable and exhibits a reduction in molar mass during the thermal treatment[30]. This reduction is due to the tendency of ester linkages of PLA to break down during the thermal process[31]. The TGA measurement of neat PLA exhibited a rapid change in its mass with elevated temperature. Figure 5.5a shows the thermal degradation of neat PLA starting at a temperature of 281 °C and continuing up to 460 °C, where 99 % of PLA was thermally degraded. The onset of decomposition of PLA was found to be around 335 °C. There was an inflection point at 370 °C, and the PLA was degraded completely below 460 °C.

Figure 5.5b shows the TGA data acquired from PLA coated on AAO as well as neat AAO. Initially, a weight loss (expressed as weight %) was observed for neat AAO between 100 and 175 °C, with no further reduction. For AAO coated with PLA, weight loss occurred between 100 °C and 275 °C. These losses for both systems could be attributed to the absorbed water or adsorbed species besides the chloroform residuals in the PLA/AAO composite. The degradation of PLA slowly started at a temperature of 280 °C, and most of the PLA was degraded below 450 °C, but the thermal degradation of PLA continued even beyond 550 °C. It is worth mentioning that the remaining weight % (thermogram of spin-coated PLA in Figure 5.5b) corresponds to the AAO template, which is the majority of the PLA/AAO composite being measured.

The difference in decomposition behaviours of the polymer as bulk and as coated on AAO could be associated with the tightly bound polymer on the top AAO surface and inside the pores[32]. Zhong and his colleagues measured TGA on the AAO filled with poly(methacrylic acid)[32]. Their data revealed that although most of the polymer was decomposed below 420 °C, the decomposition of the polymer continued at further temperatures (e.g., above 600 °C) compared to the bulk polymer. Furthermore, the decomposition of the polymer deposited inside the pores may affect the mass transport of gaseous residual products and volatile residual products from the pores, leading to a delay in the thermal decomposition process[33].

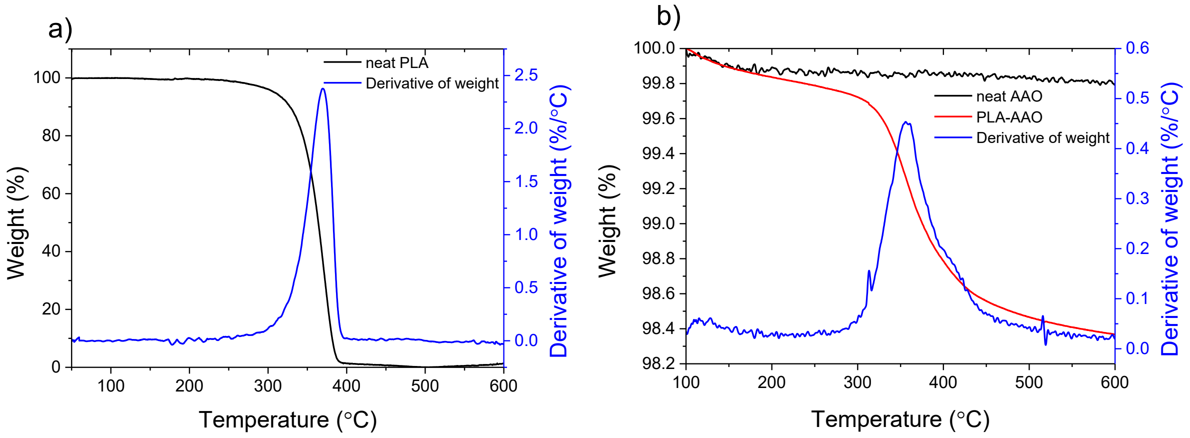

Figure 5.5: *TGA thermograms of PLA a) in bulk (as powder), b) spin-coated PLA on AAO, which was prepared in oxalic acid at 40 V for 1 h and widened in phosphoric acid for 7 min with an average pore diameter of 42 ± 4 and pore length 3.2 ± 0.3 µm. The heating ramp was conducted from 100 to 600 °C with a heating rate of 10 °C per minute in a 15 mL min^{-1} nitrogen gas flow. A 5 wt % PLA solution was spin-coated on AAO at 1000 rpm for 20 sec.*

To assess the distribution and presence of PLA within the pores, a cross-sectional view of the PLA-filled AAO sample was analyzed using energy dispersive x-ray spectroscopy (EDX). Figure 5.6a shows a cross-sectional FESEM image of AAO marked with four points: three along the pores and one on the PLA layer on the top side of AAO. Those points were targeted by the point mode measurement in EDX, resulting in four separated EDX spectra being recorded from those four points, as shown in Figure 5.6b-e.

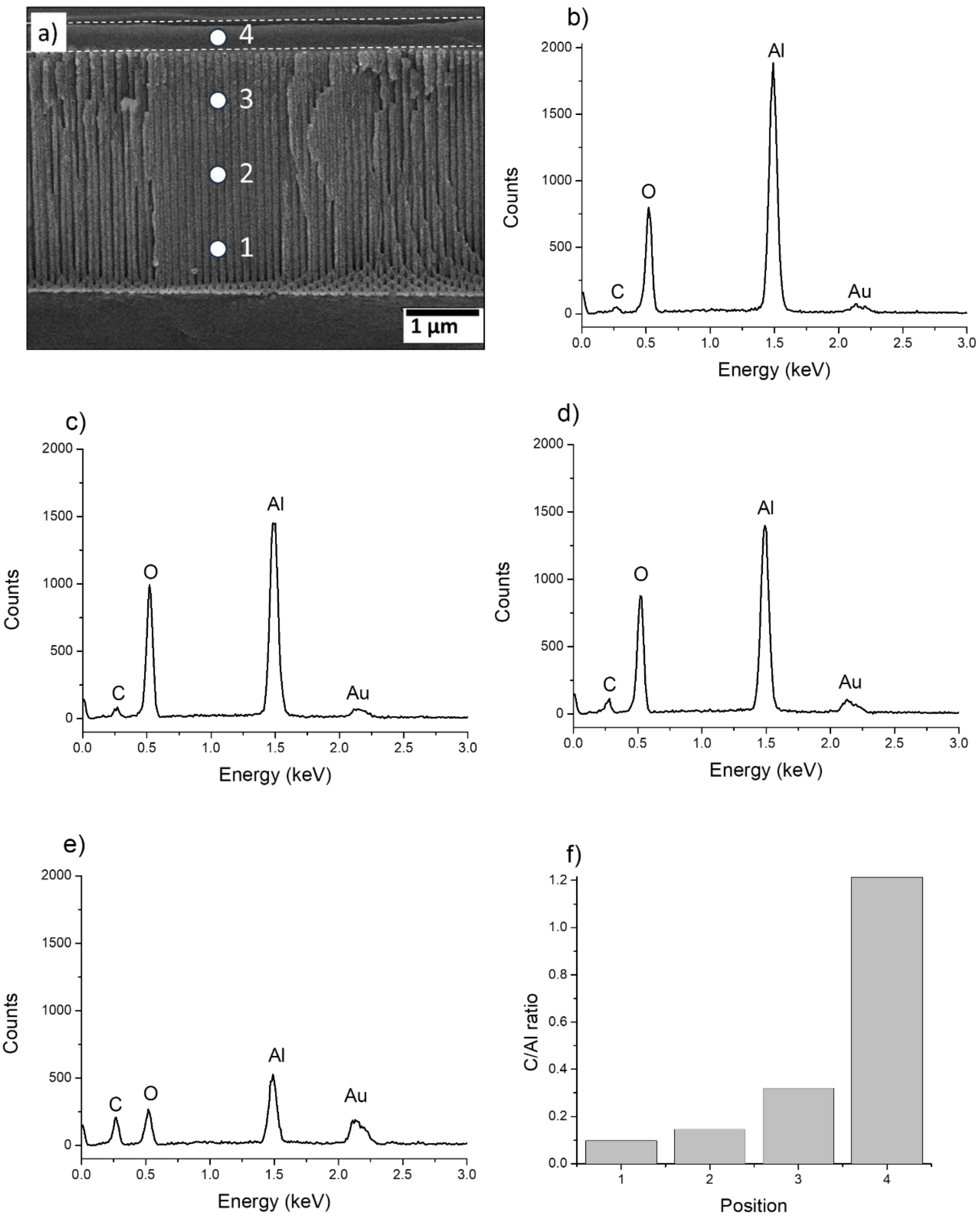

Figure 5.6: *a) Cross-sectional FESEM image of AAO covered with PLA and the EDX measurements were conducted on four position points (numbered 1-4) across the pores. b-e) EDX spectra for these points 1, 2, 3, and 4, respectively. f) C/Al weight elemental ratio calculated from the EDX spectra for those four positions points shown in a.*

The EDX spectra demonstrate four detectable peaks belonging to the carbon, oxygen, aluminum, and gold elements. The carbon signal located at 0.277 keV, beside the oxygen at 0.525 keV, is the essential building element of PLA[34]. The Al signal at 1.486 keV came from the building element of AAO, together with O[35]. The observed signal at 2.120 keV resulted from the passivated layer of Au[36], which was used as a conductive layer for FESEM measurement[37]. The elements observed for the PLA and AAO agree with previous studies[38,39]. Thus, EDX analysis confirms the presence of PLA in the pores and not only on the pore gate/top side of AAO. The C/Al weight elemental ratio was calculated and shown in Figure 5.6f. The EDX data displays that the PLA was distributed along the pores and that the quantity of PLA was low in regions placed more profoundly into the pores.

However, EDX was also conducted on neat AAO, specifically in the middle of the cross-sectional AAO film, as shown in Figure 5.7a, and the EDX spectrum was recorded (Figure 5.7b). The analysis of the EDX spectrum indicated that the C/Al ratio is four times smaller than that observed in the spectrum of PLA-filled AAO shown in Figure 5.6c. The presence of the C peak on the EDX spectrum of the neat AAO could be attributed to contaminations during sample preparation under the ambient environment[40] or the oxalic impurities incorporated into the AAO film during the anodization of Al[41,42,43]. Zhang and coauthors studied the photoluminescence (PL) of AAO prepared in oxalic acid[44]. They reported that the AAO showed a PL band at 470 nm, which was caused by oxalic impurities found after the fabrication of AAO. Other researchers fabricated the AAO in a mixture of malonic and sulfuric acid and found a similar behaviour[45].

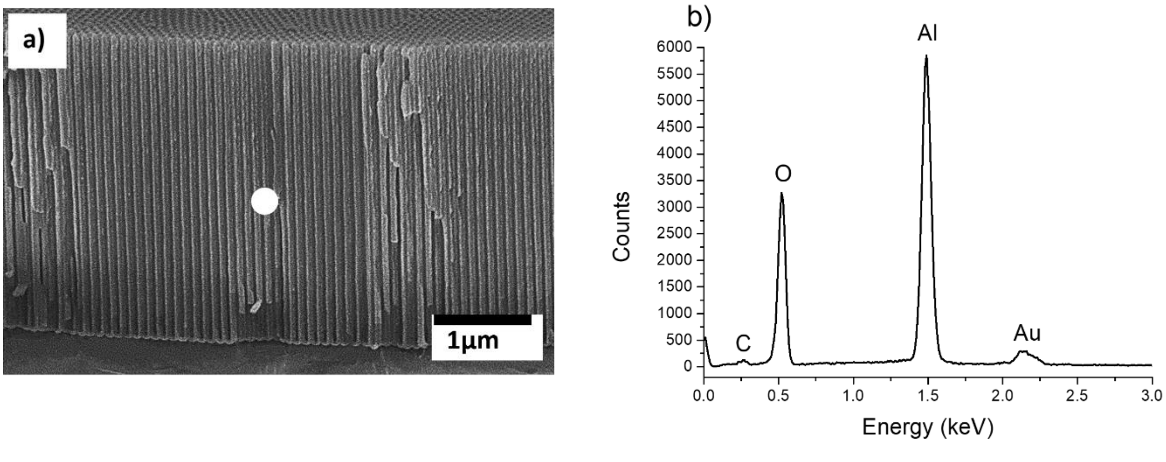

Figure 5.7: *a) Cross-sectional FESEM image of neat AAO showing one point where EDX was measured, b) EDX spectrum obtained from a. The C/Al ratio was calculated to be 0.05.*

5.4 Enzymatic Degradation of PLA on Nonporous and Porous Substrates

5.4.1 Enzymatic Degradation of PLA on the Planar Si

As discussed in Chapter 2, the presence of bacteria can be indirectly determined via their secreted enzymes, specifically by the degradation of a polymer by the enzyme. In this Chapter, proteinase K was used as a model enzyme to degrade the PLA coatings on planar Si and AAO substrates. The degradation of PLA on planar Si was studied using ellipsometry, contact angle (CA), FTIR spectroscopy, FESEM and AFM. The degradation of a PLA film with 68 ± 3 nm thickness was investigated by ellipsometry to determine the change in the dry PLA film thickness (Figure 5.8). The PLA film was incubated in the proteinase K solution for different interval times, and the dry film thickness was measured every 7 min. The data in Figure 5.8 showed that the thickness of the PLA film decreased linearly with incubation times. The dry thickness of PLA film (prepared by spin coating a 0.5 wt% solution of PLA in chloroform), decreased from 68 to 54 nm within 7 min. After 22 min incubation time, the thickness was lowered to 19 nm; a similar degradation rate and trend were also reported in literature[46]. The degradation rate was evaluated from the linear fit of the data in Figure 5.8, which yielded 2.27 nm min^{-1}. The enzymatic degradation time is expected to be longer for the degradation of the thick PLA films.

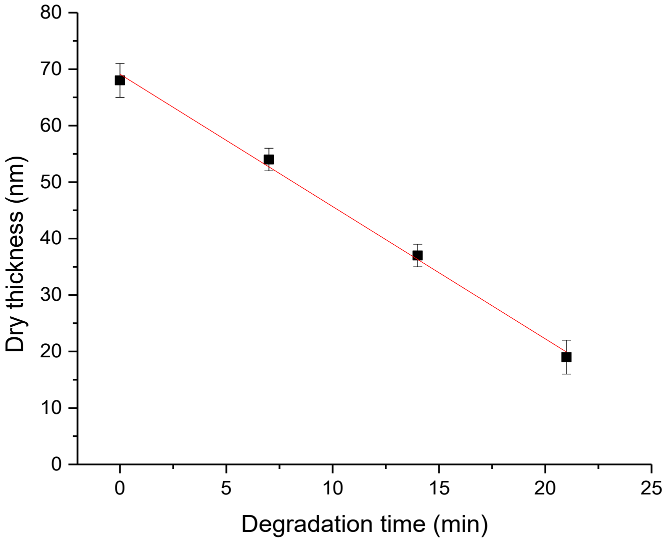

Figure 5.8: *Dry ellipsometric thickness of PLA film spin-coated on planar Si versus the enzymatic degradation in 1 mg* mL^{-1} *proteinase K for 7, 14 and 22 min. (*$D = 858\text{ nm} - 2.27 \times t_{deg}$*,* $R^2 = 0.97$*). The solid red line corresponds to a linear least-squares fit of the ellipsometric data. The error bars denote the standard deviations (n = 3).*

The static water contact angle of PLA films on planar Si was monitored after each degradation time. Figure 5.9 shows that the PLA film becomes slightly more hydrophilic after treatment with proteinase K. This can be explained by the increase in carboxylic acid and hydroxyl residues on the surface due to degradation, causing a change in the surface morphology[47].

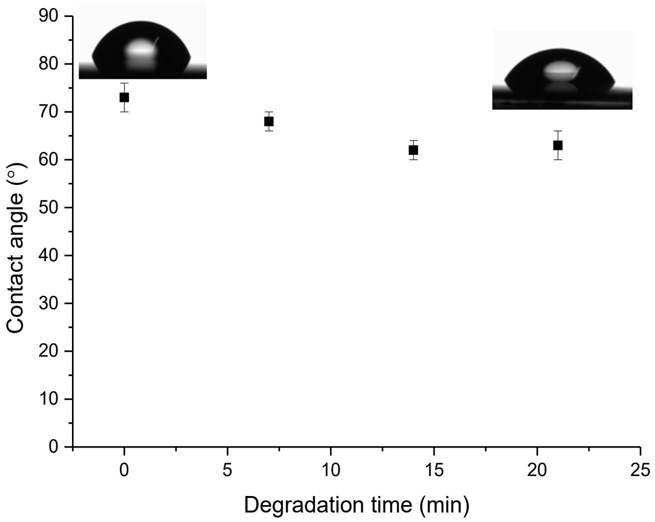

Figure 5.9: *Static water contact angle of PLA film on planar Si surface versus the enzymatic degradation in 1 mg mL^{-1} proteinase K for 7, 14 and 22 min. The insets are the contact angle photograph before and after degradation for 22 min. The error bars denote the standard deviations (n = 3).*

FTIR spectroscopy was performed to monitor the effect of the degradation time on the PLA film spin-coated on planar Si. As demonstrated in Figure 5.10a, the characteristic band of PLA is located at 1754 cm^{-1} (C=O stretching vibration of the carbonyl group). The calculated area of the carbonyl peak from the FTIR bands decreased linearly with the increasing degradation time (Figure 5.10b). The reduction in the band area of carbonyl is associated with the reduction of the PLA film thickness after being subjected to enzymatic degradation, subsequently confirming the occurrence of the degradation process. This effect was consistent with the ellipsometric data discussed in the previous section.

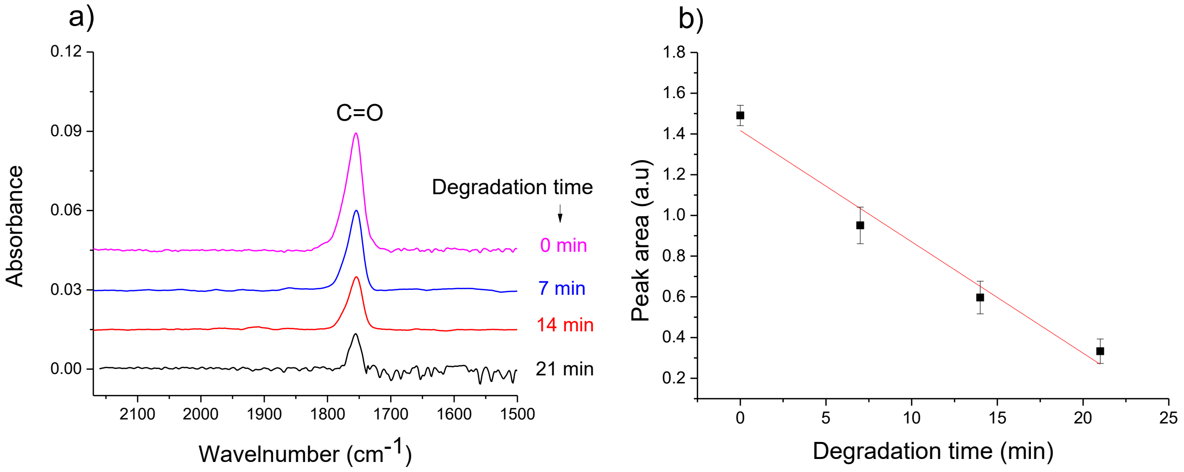

Figure 5.10: *a) FTIR spectra stack plot for PLA thin films spin-coated on planar Si after incubation in 1 mg* mL^{-1} *proteinase K at different times. b) Dependence of carbonyl peak area at 1755* cm^{-1} *on the degradation time (A = 1.42 nm – 0.055 ×* t_{deg}*,* $R^2 = 0.96$*). The solid line corresponds to linear least-squares fits of the data. The error bars denote the standard deviations (n = 3).*

The surface morphology of the PLA-covered Si before and after performing the enzymatic degradation was analyzed by FESEM and AFM. To minimize potential morphological variations between different samples, the FESEM and AFM measurements were conducted on the same Si-PLA sample, which was divided into halves; one-half of the covered Si with PLA was immersed in the proteinase K solution, and another half was left out of the enzyme solution as demonstrated in Figure 5.11.

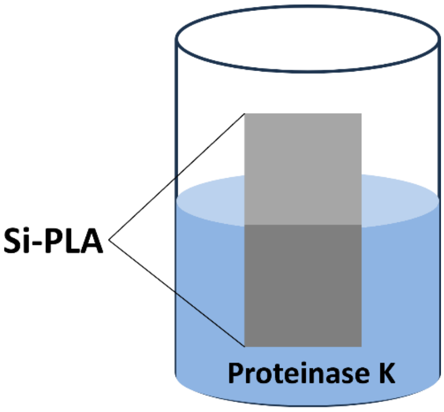

Figure 5.11: *Scheme of performance of the enzymatic degradation of PLA-covered planar Si; only half of the sample was immersed in proteinase K solution.*

Figure 5.12 displays the photograph of PLA film spin-coated on planar Si and the corresponding FESEM images. The light grey and dark areas on the Si-PLA sample represent areas before and after immersion in the enzyme solution for 22 min (Figure 5.12a). According to the research conducted by Reynolds and co-workers[48], the color of a polymer thin film is directly associated with its thickness; therefore, the change in the color of the PLA films after degradation is due to the change in the film thickness upon the film degradation. As shown in Figure 5.12b,c, the FESEM images exhibit no significant erosion on the surface of the PLA film despite the reduction in the film thickness, as confirmed by ellipsometry. This can be explained by PLA degradation occurring homogeneously by erosion of the PLA surface within this time scale[49]. Furthermore, the FESEM images show no difference in the morphology of PLA on the planar surface before and after degradation. The tiny cracks visible on both surfaces are probably from the sputtered gold used to enhance the conductivity of the surface for FESEM measurement, or they formed during the FESEM measurement due to the focused current beam used for high-resolution images, which leads to local heating, or could also be caused by measurement artifacts[50].

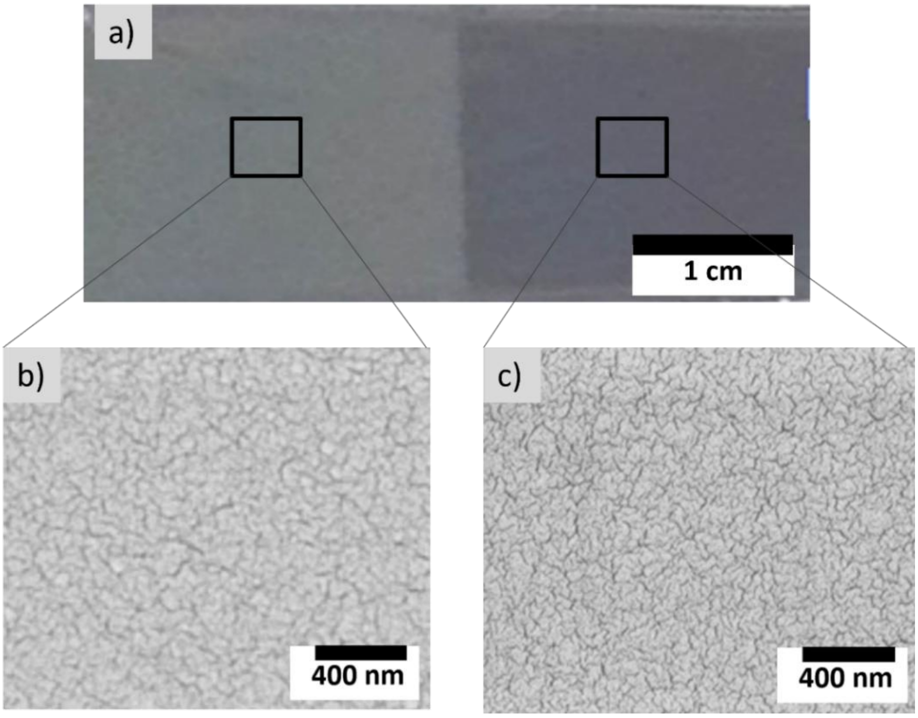

Figure 5.12: *Spin-coated PLA on the planar Si, a) Photograph, b) and c) FESEM images before (light grey part) and after immersion in proteinase K (1 mg mL^{-1}) for 22 min (dark grey part), respectively. Enzymatic degradation of the PLA film was performed as depicted in Figure 5.11.*

AFM measurements were conducted in tapping mode under ambient conditions to assess the impact of the enzymatic degradation on the PLA surface morphology that previously covered the planar Si. As described in the FESEM above, the AFM was also conducted on the Si-PLA sample (Figure 5.13a) and the change in roughness of the treated and untreated parts with the enzyme was evaluated. The AFM data showed that the *Rq* surface roughness of PLA film was 1.19 ± 0.02 nm and increased after the enzyme treatment with the enzyme to 1.31 ± 0.09 nm (scan size 25 µm²), as shown in Figure 5.13b,c. The change in the surface roughness is expected when the PLA film undergoes a dissolution, which can be due to chemical or biological effects[51,52]. Doi and co-workers observed that the *Rq* surface roughness of the PLA film increased from 0.2 to 0.5 nm after exposure to proteinase K for 14 min[46]. Thus, the slightly increasing surface roughness implicated the degradation of PLA.

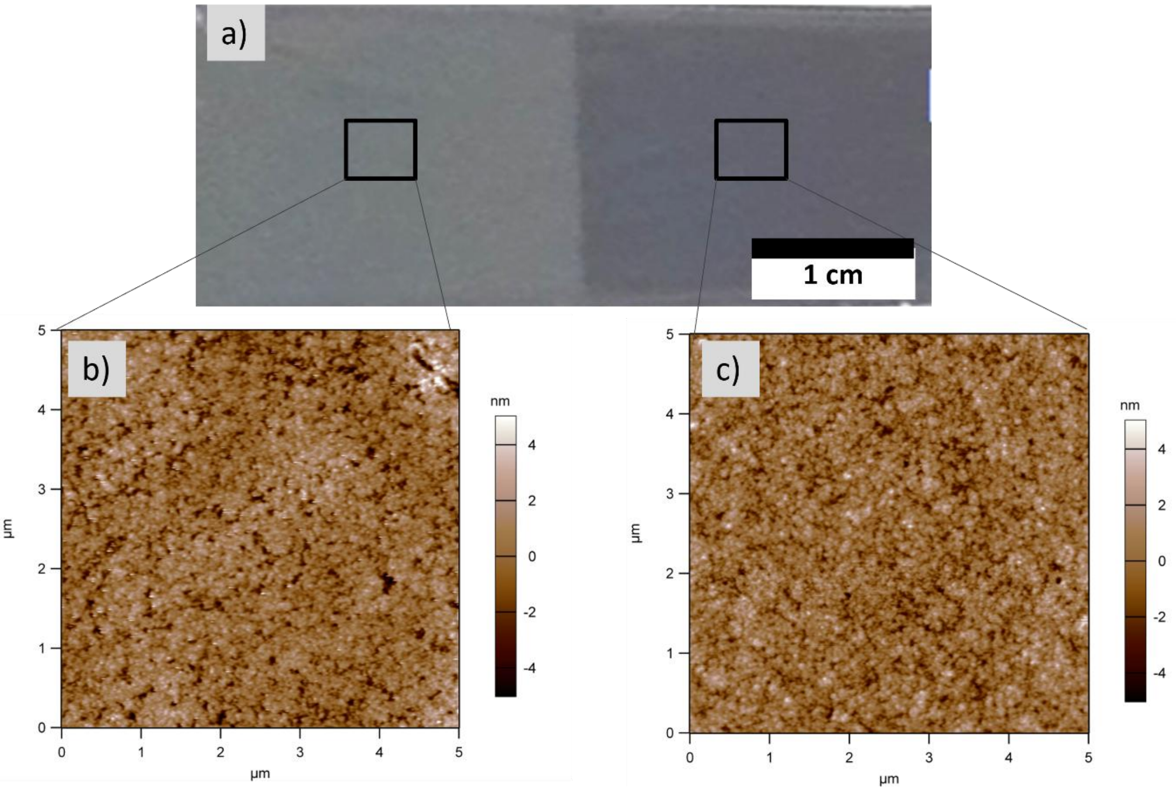

Figure 5.13: *Spin-coated PLA on the planar Si, a) Photograph, b) and c) AFM images before (light grey part) and after immersion in proteinase K (1 mg mL^{-1}) for 22 min (dark grey part), respectively. Enzymatic degradation of the PLA film was performed as depicted in Figure 5.11.*

5.4.2 Enzymatic Degradation of PLA on the AAO

The degradation of the PLA-covered AAO via the enzyme was also investigated. FESEM, contact angle, AFM, and RIfS techniques were used to evaluate the degradation process.

The degradation reaction occurred under the same conditions for degrading PLA on Si planar substrates except for the degradation time. Figure 5.14 demonstrates the setup for treating the AAO substrates (covered with PLA) with Tris-HCl buffer and proteinase K. Two sets of experiments were performed: one set was incubated in Tris-HCl buffer as a reference, and another set was incubated in Proteinase K for 300 min.

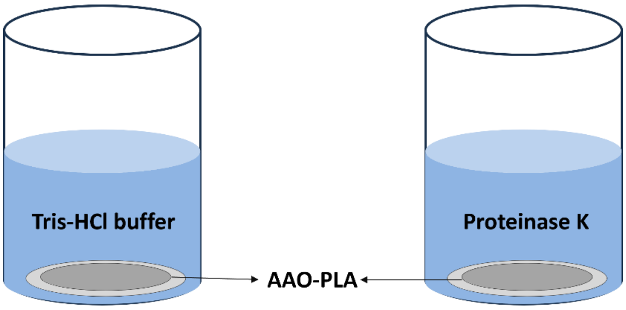

Figure 5.14: *Scheme of the configuration of the immersion of the PLA-covered samples in Tris-HCl buffer (left) and proteinase K (1 mg mL^{-1}) (right) solutions for 300 min, respectively.*

The FESEM measurement was conducted before and after treatment with proteinase K and the buffer solution for 300 min (Figure 5.15). The top-view and cross-sectional FESEM images of the PLA-covered AAO sample are shown in Figure 5.15a,b. After incubation of this sample in the buffer solution, the PLA film survived, as displayed in Figure 5.15c,d. However, it was not the case, when a similar sample was treated with proteinase K; the PLA film was degraded, leaving the pores of AAO clearly visible in the FESEM images (Figure 5.15 e,f).

This data confirmed that the PLA was stable throughout the incubation in buffer solution, and no significant effect on the PLA film morphology was observed. It can be concluded that the disappearance of the PLA was due to enzymatic degradation. Furthermore, the data was consistent with PLA films on planar Si, where no significant change in surface morphology was observable after degradation. This observation confirmed that the enzymatic degradation took place homogenously by surface erosion. Song and his group also reported such observation[52]. They noted that the PLA surface did not change after being degraded by the enzyme esterase for 7 days, despite a weight loss of PLA fibers, but a slight change in the morphology was observed for a longer incubation time (14 days and above).

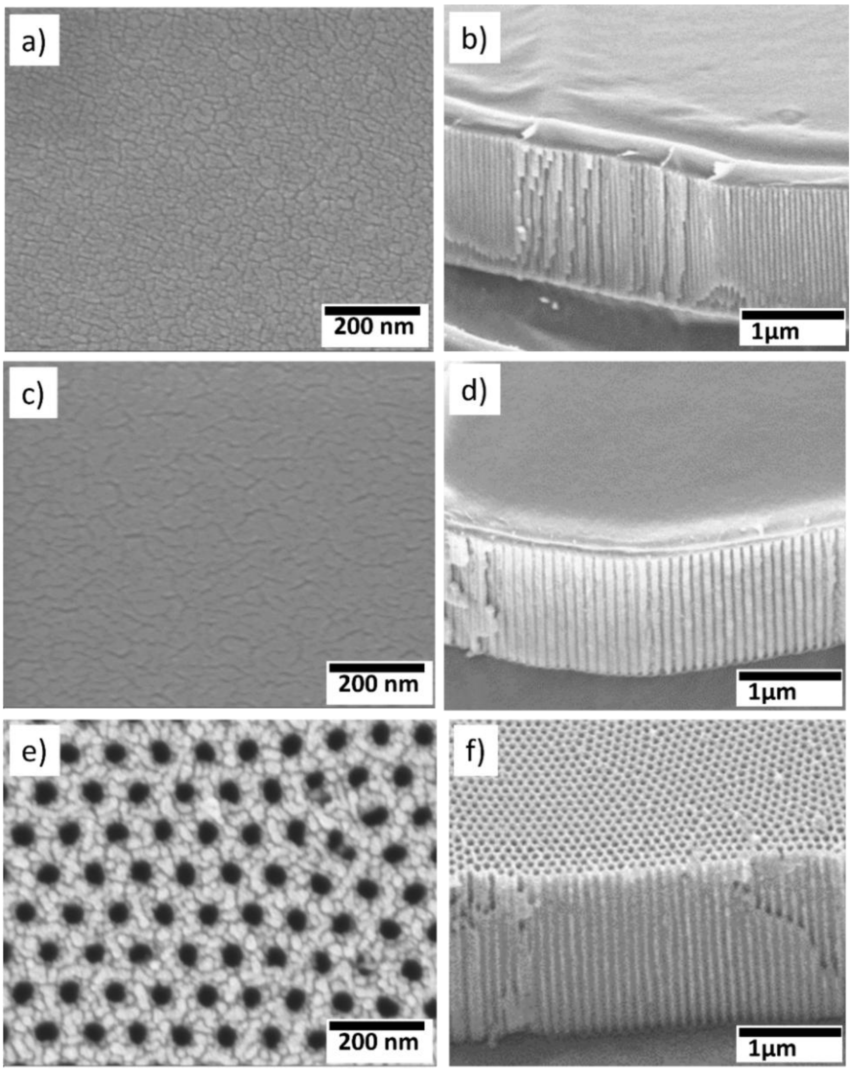

Figure 5.15: *Top-view and cross-sectional FESEM images of the AAO (fabricated in 0.3 M oxalic acid at 40 V for 50 min), a,b) after PLA deposition, c,d) after immersion in Tris-HCl buffer for 300 min, e,f) after immersion in proteinase K (1 mg mL^{-1}) for 300 min.*

The static water contact angles were analyzed to evaluate the effect of the treatment of the AAO and PLA surfaces. The measurements were conducted on the AAO sample before and after PLA deposition and enzymatic degradation. Initially, the water contact angle measurement was performed on bare AAO. The result displays a water contact angle value of 10 ± 3˚ (Figure 5.16), indicating that the bare AAO's surface is hydrophilic. It was reported that the freshly prepared AAO has a hydrophilic surface[53]. For instance, Lee and colleagues stated that the water contact angle on bare AAO was 14˚, which is close to the value reported in this Chapter[54]. The wettability of the AAO changed after the PLA deposition and the water contact angle increased by 61˚. Thus, suggesting that the AAO surface was covered with PLA, which matches the contact angle data of the covered planar Si with PLA, which was discussed initially in this Chapter. It is worth mentioning that this value is independent of the underlying surface (i.e., AAO) due to the full coverage of the AAO by a thick PLA film, which was thick enough to exclude the effect of the AAO surface on the wettability[55]. The water contact angle measurement after immersion of the AAO-PLA sample in buffer solution had a value of 73 ± 2°, which is close to the value before the immersion (71 ± 2°), indicating that the PLA film remained on the AAO surface. Although there is a slight difference in contact angle values, it cannot be concluded that no degradation occurred because, as was discussed earlier in this subchapter, the deviation in the contact angle values of PLA film during the degradation is insignificant.

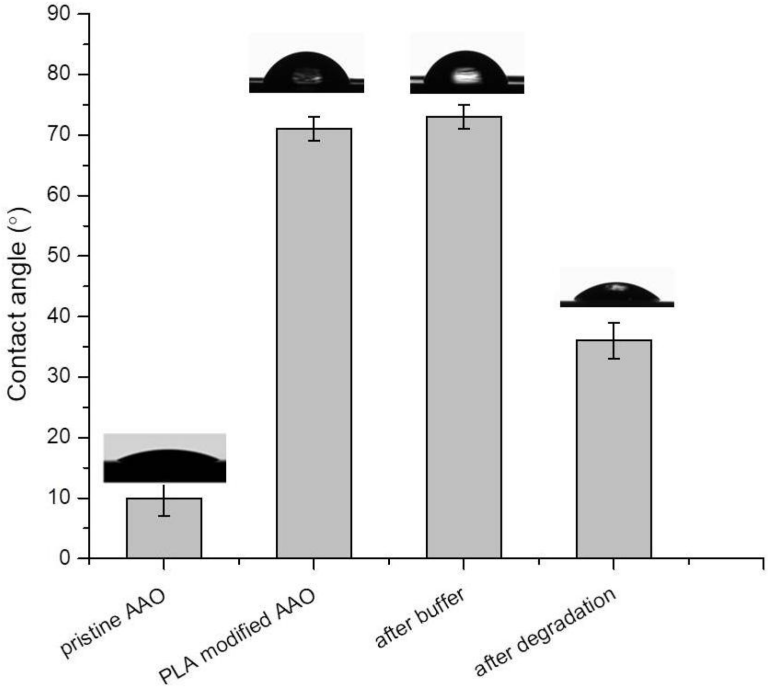

Figure 5.16: *The water contact angle of bare AAO, PLA spin-coated on AAO, before and after degradation by proteinase K (1 mg mL^{-1}) for 300 min.*

By contrast, the value of the static water contact angle dropped to 37 ± 3° after enzymatic degradation for 300 min. The reduction of the contact angle values indicated a change in the surface morphology after immersion in the enzyme solution. This can be explained by removing the PLA film from atop AAO due to the degradation process by proteinase K. As shown in Figure 5.15e, the PLA film was degraded, and the AAO was exposed, which changed the wettability because the AAO is more hydrophilic than the PLA film. It is worth noting that the contact angle value of the AAO after PLA degradation did not match its original value (before PLA deposition), which could be explained by the presence of the small amount of PLA or its fragments or other contaminations on the AAO surface after enzymatic degradation.

AFM measurements were also conducted before and after the enzymatic degradation of PLA on AAO. Figure 5.17 displays AFM images after the deposition of PLA on AAO, after PLA incubation in the buffer solution and after enzymatic degradation, respectively. The *Rq* surface roughness of PLA film before the treatment with the buffer or with the enzyme was 0.48 ± 0.91 nm (scan size 1 μm^2), respectively (Figure 5.17a). Whereas the *Rq* of the treated sample with the buffer was 0.54 ± 1.2 nm. The high standard deviation value could be due to the slight swelling of the PLA film[56]. In contrast, the *Rq* value increased significantly after the treatment with the enzyme (7.24 ± 0.66 nm) due to removing PLA, and the pores were uncovered.

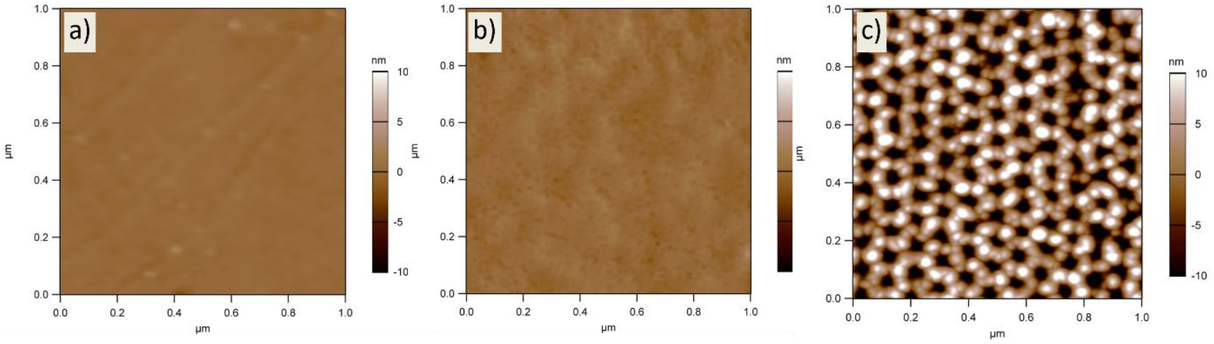

Figure 5.17: *AFM images of spin-coated PLA on AAO Di = 103 nm, l = 3,0 µm; 40 V, 0.3 M oxalic acid, 2nd anodization: 50 min), a) after PLA deposition, b) after immersion in Tris-HCl buffer for 300 min, c) after immersion in proteinase K (1 mg* mL^{-1}*) for 300 min.*

The RIfS technique also proved the enzymatic degradation of PLA on the AAO. The RIfS measurements were conducted on the AAO before and after PLA deposition as well as after incubation in buffer and the enzyme solutions for 300 min. The effective optical thickness (*EOT*) curves, which were acquired from RIfS spectra by applying a fast Fourier transformation (FFT), are shown in Figure 5.18. The *EOT* values for the bare AAO samples ranged between 9975 and 9995 nm. This slight variation could be due to a minor difference in the pore geometry during the AAO fabrication or the pore widening. However, an increase in the *EOT* values was observed after the spin coating of PLA on the AAO. As discussed in this Chapter, the concentration used to cover the AAO was 5 wt% in chloroform. The spin coating of 5 wt% of PLA on the AAO causes a shift in *EOT* at about 494 nm (AAO-filled PLA/air). However, this change in *EOT*, upon PLA deposition, is more significant than the calculated one for 100 % pore filling, which was determined by applying the Maxwell-Garnett equation described in Chapter 2 and comparing the maximum *EOT* of the bare AAO. Based on the calculated *EOT* value and corresponding calculated pore filling (assuming 100 % PLA filling), the pore filling of the AAO sample (with spin-coated PLA) was estimated to be 132 %. This overestimation can be understood by considering the polymer's location in the porous material. The calculated *EOT* represents only AAO and the polymer infiltrating the pores (100 % PLA filling). In the current case, the experimental *EOT* represents the AAO with the PLA located atop and inside the pores, as confirmed by SEM and EDX data. The formation of a PLA layer on top of the AAO pores results in a maximum *EOT* value due to the sum of both layers (AAO plus PLA and the PLA top layer).

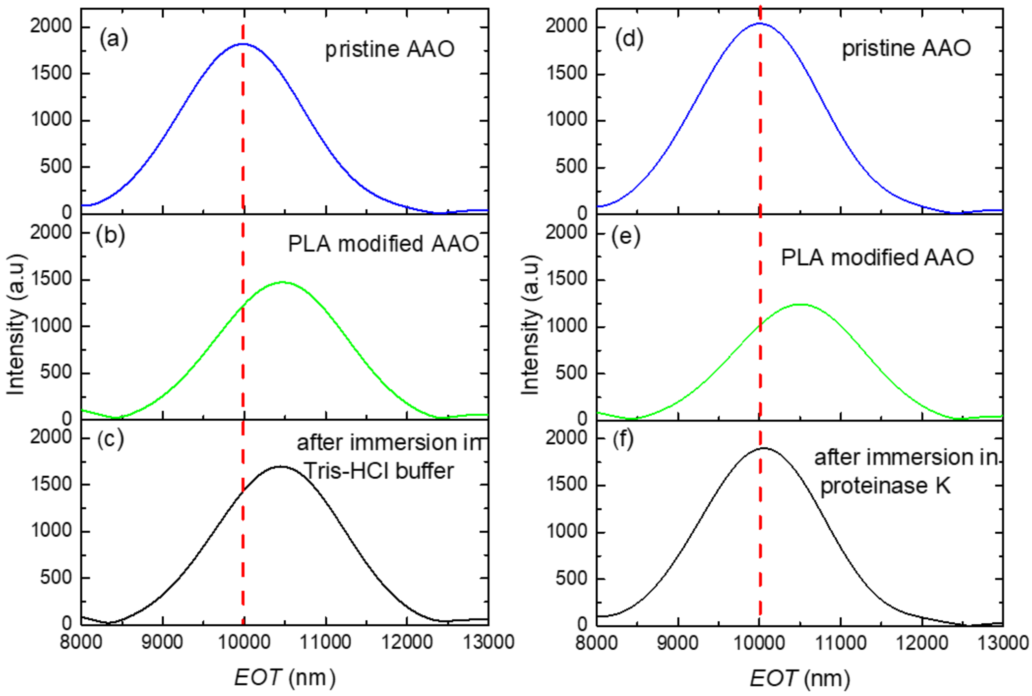

Figure 5.18: *EOT curves obtained from AAO samples (Di = 103 nm, l = 3,0 µm; 40 V, 0.3 M oxalic acid, 2nd anodization: 50 min). Pore diameter: 42 nm (widening: 7 min in H_3PO_4 at 35 °C). a-c) From bare AAO, after PLA spin coating and after immersion in Tris-HCl buffer for 300 min, respectively. d-f) From bare AAO, after PLA spin coating and after immersion in proteinase K (1 mg mL^{-1}) for 300 min, respectively. All the samples were measured in the dried state.*

Despite this issue, the enzymatic degradation of PLA atop AAO could be investigated using RIfS. The *EOT* of the PLA/AAO samples was determined after incubation in the Tris-HCl buffer and proteinase K solutions. Figure 5.19 displays the change in *EOT* (Δ*EOT*) after PLA deposition of AAO as well as after enzymatic degradation. To assess the buffer's effect on the PLA film, the Δ*EOT* values were compared before and after immersion. The data show a decrease in Δ*EOT* by 7 % (from 492 ± 10 to 454 ± 13 nm) after 300 min immersion of PLA-coated AAO in Tris-HCl solution. This reduction in Δ*EOT* could be explained by removing a small amount of PLA from the PLA/buffer interface during the immersion in the buffer or during the post-process, e.g., washing the PLA/AAO sample. Although one could not observe this slight change in the FESEM, AFM, or contact angle data, the RIfS could detect it, making this technique a good candidate for investigating the enzymatic reaction in porous materials.

By contrast, the value of Δ*EOT* of the sample treated with the enzyme solution was enormous compared to that in the buffer. The Δ*EOT* value was decreased by 447 ± 13 nm, which gives a reduction of 91 % compared to 7% in the buffer. This drop in Δ*EOT* is explained by water entering the air-filled pores and confirmed that the enzyme could degrade most of the PLA at this time. It was clear that Δ*EOT* did not recover its original value (i.e., that for bare AAO). This could be due to the remaining residual PLA, as non-degraded or not washed out polymer, inside the pores excluding and change in the morphology of AAO substrates during the enzymatic degradation, since the AAO is stable in the basic environment, as discussed in Chapter 4. In the next Chapter, the enzymatic degradation of PLA coated in AAO will focus on the PLA inside the pores by removing the PLA from the top side of AAO prior to the enzymatic degradation, which offers an advantage such as a response time or sensitivity of the AAO sensor.

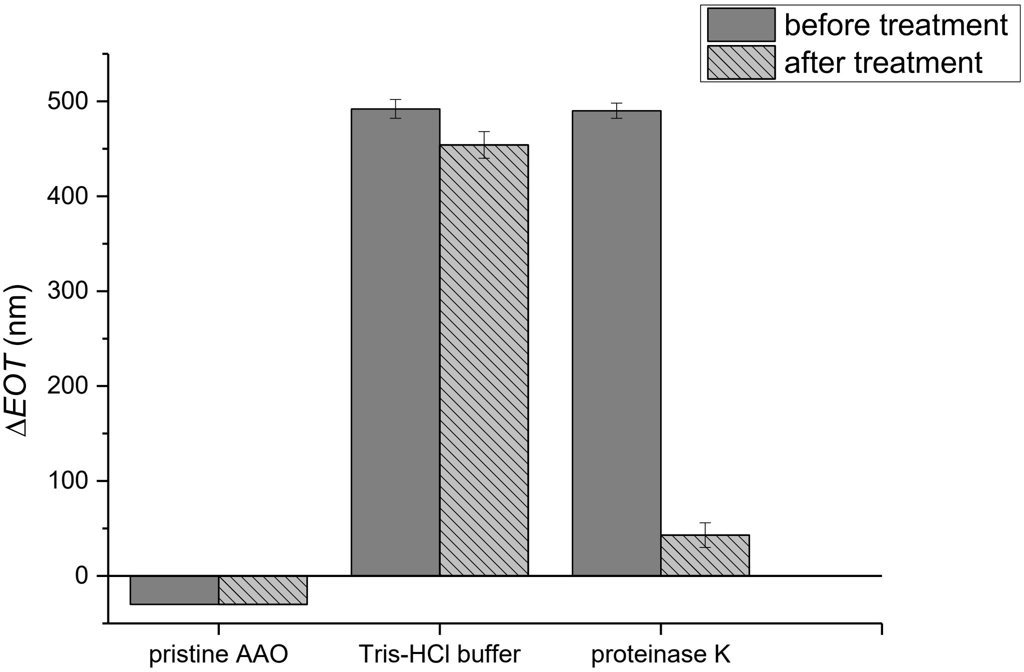

Figure 5.19: *Evaluation of the ΔEOT from Figure 5.18 demonstrating the dependence of the EOT on change in the PLA amount when immersion in the Tris-HCl buffer (PH 8.5) and proteinase K (1 mg mL^{-1})solutions for 300 min. The error bars denote the standard deviations (n = 3). All the measurements were performed after washing and drying PLA/AAO sensors.*

5.5 Conclusion

This Chapter investigated the deposition and enzymatic degradation of PLA on the planar Si and AAO. The PLA deposition process was performed using the spin coating method. Different concentrations of PLA solution were spin-coated on both planar Si and AAO and measured using ellipsometry, water contact angle, and FTIR techniques.

The dry thickness of the PLA film on a planar Si increased linearly with the concentration in the spin coating solution. The water contact angle data confirmed the presence of the PLA on the surface due to the change in wettability. Moreover, the FTIR data were consistent with the ellipsometric and contact angle data where the PLA layer was successfully deposited on the Si surface. The carbonyl band area increased linearly with the dry PLA thickness. The deposition of the PLA on the AAO substrates was examined using the same techniques: contact angle, FESEM, ATR-FTIR, EDX, and TGA. In this Chapter, the intended protocol was to cover the AAO pores entirely with the PLA layer to seal them and reopen them using a specific stimulus (such as an enzyme), enabling their use as a bacterial enzyme sensor. Different concentrations of the PLA solutions were used to ensure optimal pore coverage. The optimal PLA concentration was 5 wt% in chloroform, resulting in 300 nm film thickness estimated from FESEM images.

The FTIR spectroscopy data revealed that as the PLA concentration increased, a deviation from the linear dependence was observed, presumably due to the increase in the viscosity when the concentrated PLA solution was utilized. The TGA data also confirmed the presence of the PLA in the AAO substrate but did not confirm whether the PLA was only on the top side or inside the pores of the AAO sample. Therefore, the EDX measurement was conducted on the coated AAO at four points along the AAO (from top to bottom). The EDX analysis confirms the presence of PLA inside the pores and on the pore gate/top side of AAO. The C/Al weight elemental ratio was calculated from those four points, and it was concluded that the PLA was distributed along the pores, but the quantity of PLA was low in regions placed more profoundly into the pores.

After confirming the presence of PLA on planar Si and AAO substrates, the enzymatic degradation of PLA on those substrates was investigated. The degradation was conducted by proteinase K, which could cleave the ester bond on the PLA backbone. Firstly, the enzymatic degradation of PLA was tested on planar Si substrates. A reduction in dry thickness was observed with an increase in degradation time. The ellipsometric data showed that 73 % of the PLA film with a thickness of 68 ± 3 nm was degraded in 22 min by the enzyme.

Moreover, the contact angle measurements showed a slight change in wettability after the enzymatic degradation, with no further significant change in wettability throughout the degradation process. The FTIR spectroscopy data supported the ellipsometric data by showing a linear trend with the degradation time. FESEM and AFM were performed on the PLA film before and after degradation. The FESEM could not qualitatively differentiate between the PLA film before and after treatment with the enzyme, suggesting that the degradation was homologous on the entire surface. AFM could provide more information about the surface roughness, whereas the PLA film treated with the enzyme was rougher than the untreated one. The enzymatic degradation of the PLA was then investigated on the AAO. The FESEM images showed that the enzyme totally degraded the PLA film on the AAO surface. The reference experiment using an enzyme-free solution showed no degradation, and the PLA film remained intact. The contact angle data also confirmed this process, where a significant reduction in the contact angle was observed before and after the degradation (from 73 ± 2 to 37 ± 3˚). The AFM data showed a slight increase in *Rq* value after immersion in the buffer solution for 300 min. However, this change was prominent after treatment with the enzyme for the same incubation time, which is also clearly displayed in the AFM images. Finally, the degradation of PLA on the AAO substrate was investigated with the RIfS. The *EOT* data confirmed that the PLA was deposited on the AAO substrate due to the increase in the effective refractive index. Furthermore, the *EOT* was decreased after treatment with proteinase K due to the occurrence of the degradation of PLA film, suggesting a reduction in the pore filling by 91 % in 300 min, which was more significant than that of the sample treated with buffer (7 %).

The data presented in this chapter suggest that further investigation into the enzymatic degradation of PLA and other biodegradable polymers across varying pore morphologies would be beneficial for optimizing sensor performance. Another recommendation would be to use this system, PLA covers the AAO pores, to design a platform for drug delivery with an enzyme-triggered gate. This system would mean the pore could be loaded with a drug/dye and sealed with PLA film. The latter could be enzymatically degraded, releasing the drug from the pores to treat, for instance, the infected area.

5.6 Materials and Methods

Chemicals, materials, and instruments, which have already been mentioned in Chapter 4, will not be stated here again.

Fabrication of AAO Sensors

A series of AAO samples were fabricated in oxalic acid at (40 V) for 1 h. Then, they were widened at 35 °C in phosphoric acid for 7 min. The pore diameter and the pore length were around 42 nm and 3.2 µm, respectively. Then, the surface of the AAO sensor was sputtered with gold for 40 sec, providing a layer of ~ 8 nm. The covering process of PLA on the top side of AAO was performed using a spin coating method. A series of PLA concentrations (1, 3, 4, and 5 wt%) were prepared in chloroform.

Static Contact Angle Measurements

The static water contact angle was measured using a sessile drop method (Dataphysics OCA-15, Filderstadt, Germany). A 2 µL of the Milli-Q water droplet was dispensed onto the planar

Si or AAO substrates covered with PLA, and the images were taken directly. The CA measurements were conducted on three positions on each sample. The obtained result is presented as the arithmetic mean with the standard deviation as an error in the data.

Ellipsometry

The thickness measurements of the thin films were done with an alpha-SE variable angle spectroscopic ellipsometer (J.A.Woolam Co., Lincoln, NE) with EASE software. Three different incidence angles, i.e., 65°, 70°, and 75°, were chosen to perform measurements at three different points in the center area of each sample. The data was then fitted using the Cauchy model with a bare Si wafer taken as background. The obtained result is presented as the arithmetic mean with the standard deviation as an error in the data.

Fourier Transform Infrared (FTIR)/Attenuated Total Reflectance Fourier Transform Infrared (ATR-FTIR) Spectroscopy

The measurements of PLA thin films coated on planar Si wafer before and after enzymatic degradation were done with the IFS 66 v spectrometer (Bruker Optics, Ettlingen, Germany), which was equipped with a liquid nitrogen-cooled MCT detector (1000 scans with spectral resolution 4 cm^{-1}) in transmission mode. The background spectrum was collected by scanning a cleaned planar Si wafer. The ATR-FTIR spectra for spin-coated PLA on AAO were recorded in a range between 600 cm^{-1} and 4000 cm^{-1} with a resolution of 0.5 cm^{-1} using a Bruker Tensor 27 (Ettlingen, Germany) with a diamond lens ATR module. The ATR-FTIR measurements were performed by Dr. Maximilian Meier.

Field Emission Scanning Electron Microscopy (FESEM)

Prior to the FESEM measurements, the PLA films coated on the planar Si and on the AAO surface were sputtered with gold for 40 sec, providing a layer of ~ 8 nm, to enhance the conductivity of the surface. The FESEM analysis was conducted using a Zeiss Ultra 55cv field emission scanning electron microscope (FESEM, Zeiss, Oberkochen, Germany) with the Inlens detector. The measurements were performed with two operation voltages: 5 kV and 10 kV. The FESEM images were analyzed using the ImageJ software (v1.50d).

Atomic Force Microscopy (AFM)

The AFM measurements were conducted on the planar Si and AAO samples using Asylum Research MFP-3D Bio AFM (Asylum Research, Santa Barbara, California) in tapping mode. The resolution of the images was set to 512 pixels x 512 pixels. A Si cantilever with a nominal tip radius of 7 nm and a resonance frequency of 300 ± 100 Hz was used (AC160TS, Olympus, Japan). The AFM Measurements were performed and analyzed by Dr. Anna Schulte.

Preparation of PLA Thin Films

Pieces of Si wafers (with a size of 1.2 x 1.2 cm^2) were cleaned in a beaker containing ethanol for 15 min and then in Milli-Q water for 10 min in a sonication bath. The wafers were then dried with a nitrogen stream, followed by cleaning in UV-Ozone cleaner (ProCleaner TM system, supplied by BIOFORCE NANOSCIENCES) for 30 min. 1 wt% PLA solution was prepared in chloroform (99 %, purchased from Carl Roth), and serial dilutions with chloroform were made to prepare PLA solutions with concentrations of 0.1, 0.3, 0.5 and 1.0 wt%. The spin coating technique was used to prepare PLA thin films from different concentrations on cleaned Si-wafers. In each case, the spinning time and spinning speed of the spin-coater were 20 sec and 1000 rpm, respectively. A volume of 300 µL from the PLA solution was deposited on the planar Si and the spin coater. For the AAO, 80 µL from the PLA solution was deposited on the AAO substrate, and the spin coater (ELV, Ostfriesland, Germany) was immediately run for 20 sec at 1000 rpm. Afterwards, the PLA/AAO/Si was left for 24 h under ambient temperature for drying. Prior to each experiment, those samples were vacuumed for 2 h for further drying.

Enzymatic Degradation of PLA with Proteinase K

The AAO and planar Si substrates coated with PLA were placed in a 6-well plate containing 2 mL of Tris-HCl buffer with pH 8.5 or 1 mg mL^{-1} proteinase K solutions at 25 °C. For the planar Si, the samples were kept in the enzyme solution for 7, 14, and 22 min, whereas for AAO samples, the degradation time was 300 min. Afterwards, the samples were washed with Milli-Q water and dried in a stream of nitrogen, then kept in the desiccator at 5 mbar for 2 h, followed by the intended analysis.

5.7 References

---

[1] Sinn Aw, M.; Kurian, M.; Losic, D. Non-Eroding Drug-Releasing Implants with Ordered Nanoporous and Nanotubular Structures: Concepts for Controlling Drug Release. *Biomater. Sci.* **2014**, *2* (1), 10–34. https://doi.org/10.1039/c3bm60196j.

[2] Porta-i-Batalla, M.; Xifré-Pérez, E.; Eckstein, C.; Ferré-Borrull, J.; Marsal, L. 3D Nanoporous Anodic Alumina Structures for Sustained Drug Release. *Nanomaterials* **2017**, *7* (8), 227. https://doi.org/10.3390/nano7080227.

[3] Han, F.; Meng, G.; Zhou, F.; Song, L.; Li, X.; Hu, X.; Zhu, X.; Wu, B.; Wei, B. Dielectric Capacitors with Three-Dimensional Nanoscale Interdigital Electrodes for Energy Storage. *Science Advances* **2015**, *1* (9). https://doi.org/10.1126/sciadv.1500605.

[4] Kumeria, T.; Santos, A.; Losic, D. Nanoporous Anodic Alumina Platforms: Engineered Surface Chemistry and Structure for Optical Sensing Applications. *Sensors* **2014**, *14* (7), 11878–11918. https://doi.org/10.3390/s140711878.

[5] Law, C. S.; Lim, S. Y.; Abell, A. D.; Marsal, L. F.; Santos, A. Structural Tailoring of Nanoporous Anodic Alumina Optical Microcavities for Enhanced Resonant Recirculation of Light. *Nanoscale* **2018**, *10* (29), 14139–14152. https://doi.org/10.1039/c8nr04263b.

[6] Álvarez, J.; Sola, L.; Cretich, M.; Swann, M. J.; Gylfason, K. B.; Volden, T.; Chiari, M.; Hill, D. Real Time Optical Immunosensing with Flow-through Porous Alumina Membranes. *Sensors and Actuators B: Chemical* **2014**, *202*, 834–839. https://doi.org/10.1016/j.snb.2014.06.027.

[7] Kumeria, T.; Wang, J.; Chan, N.; Harris, T. J.; Sailor, M. J. Visual Sensor for Sterilization of Polymer Fixtures Using Embedded Mesoporous Silicon Photonic Crystals. *ACS Sensors* **2018**, *3* (1), 143–150. https://doi.org/10.1021/acssensors.7b00764.

[8] Tücking, K.; Grützner, V.; Unger, R. E.; Schönherr, H. Dual Enzyme-Responsive Capsules of Hyaluronic Acid-block-Poly(Lactic Acid) for Sensing Bacterial Enzymes. *Macromolecular Rapid Communications* **2015**, *36* (13), 1248–1254. https://doi.org/10.1002/marc.201500076.

[9] Sourkouni, G.; Jeremić, S.; Kalogirou, C.; Höfft, O.; Nenadovic, M.; Jankovic, V.; Rajasekaran, D.; Pandis, P.; Padamati, R.; Nikodinovic-Runic, J.; Argirusis, C. Study of PLA Pre-treatment, Enzymatic and Model-Compost Degradation, and Valorization of Degradation Products to Bacterial Nanocellulose. *World Journal of Microbiology and Biotechnology* **2023**, *39* (6). https://doi.org/10.1007/s11274-023-03605-4.

[10] Li, S.; Girard, A.; Garreau, H.; Vert, M. Enzymatic Degradation of Polylactide Stereocopolymers with Predominant D-lactyl Contents. *Polymer Degradation and Stability* **2000**, *71* (1), 61–67. https://doi.org/10.1016/s0141-3910(00)00152-x.

[11] Lawrence, C. J. The Mechanics of Spin Coating of Polymer Films. *The Physics of Fluids* **1988**, *31* (10), 2786–2795. https://doi.org/10.1063/1.866986.

[12] Okamura, Y.; Kabata, K.; Kinoshita, M.; Saitoh, D.; Takeoka, S. Free-Standing Biodegradable Poly(Lactic Acid) Nanosheet for Sealing Operations in Surgery. *Advanced Materials* **2009**, *21* (43), 4388–4392. https://doi.org/10.1002/adma.200901035.

---

[13] Zereshki, S.; Figoli, A.; Madaeni, S. S.; Simone, S.; Jansen, J. C.; Esmailinezhad, M.; Drioli, E. Poly(Lactic Acid)/Poly(Vinyl Pyrrolidone) Blend Membranes: Effect of Membrane Composition on Pervaporation Separation of Ethanol/Cyclohexane Mixture. *Journal of Membrane Science* **2010**,*362*(1–2), 105–112.https://doi.org/10.1016 /j.memsci.2010.06.025.

[14] Yuan, Y.; Lee, T.R. Contact Angle and Wetting Properties. In: Bracco, G., Holst, B. Surface Science Techniques, 2013 *Springer*, Berlin, Germany. https://doi.org/10.1007/978-3-642-34243-1_1.

[15] Petek, E. S.; Katsumata, R. Thickness Dependence of Contact Angles in Multilayered Ultrathin Polymer Films. *Macromolecules* **2022**, *55* (17), 7556–7563. https://doi.org/ 10.1021/acs.macromol.2c01123.

[16] Abbasian, A.; Ghaffarian, S. R.; Mohammadi, N.; Fallahi, D. Sensitivity of Surface Free Energy Analysis Methods to the Contact Angle Changes Attributed to the Thickness Effect in Thin Films. *Journal of Applied Polymer Science* **2004**, *93* (4), 1972–1980. https://doi.org/10.1002/app.20672.

[17] De Gennes, P. G. Wetting: Statics and Dynamics. *Reviews of Modern Physics* **1985**, *57* (3), 827–863. https://doi.org/10.1103/revmodphys.57.827.

[18] Kung, C. H.; Sow, P. K.; Zahiri, B.; Mérida, W. Assessment and Interpretation of Surface Wettability Based on Sessile Droplet Contact Angle Measurement: Challenges and Opportunities. *Advanced Materials Interfaces* **2019**, *6* (18).https://doi.org/ 10.1002/admi.201900839.

[19] Janorkar, A. V.; Metters, A. T.; Hirt, D. E. Modification of Poly(Lactic Acid) Films: Enhanced Wettability from Surface-Confined Photografting and Increased Degradation Rate Due to an Artifact of the Photografting Process. *Macromolecules* **2004**, *37* (24), 9151–9159. https://doi.org/10.1021/ma049056u.

[20] Łojkowski, M.; Walheim, S.; Jokubauskas, P.; Schimmel, T.; Święszkowski, W. Tuning the Wettability of a Thin Polymer Film by Gradually Changing the Geometry of Nanoscale Pore Edges. *Langmuir* **2019**, *35* (17), 5987–5996. https://doi.org/10.1021/acs.langmuir.9b00467.

[21] Singer, F.; Distler, T.; Virtanen, S. Long-Term Corrosion Behavior of Poly-L-Lactic Acid Coated Magnesium in Dulbecco's Modified Eagle Medium at Body Temperature. *International Journal of Electrochemical Science* **2014**, *9* (12), 7965–7976. https://doi.org/10.1016/s1452-3981(23)11019-4.

[22] Vargas-Villagran, H.; Romo-Uribe, A.; Teran-Salgado, E.; Dominguez-Diaz, M.; Flores, A. Electrospun Polylactic Acid Non-Woven Mats Incorporating Silver Nanoparticles. *Polymer Bulletin* **2014**, *71* (9), 2437–2452. https://doi.org/10.1007/s00289-014-1200-8.

[23] Sun, H.; Wang, Y.; Zhang, K.; Zhong, Y.; Lin, L.; Zhou, H.; Chen, L.; Zhang, Y. Hydrophilic and Hydrophobic Poly(L-lactic Acid) Films by Building Porous Topological Surfaces. *Journal of Applied Polymer Science* **2016**, *134* (10). https://doi.org/10.1002/app.44572.

---

[24] Losic, D.; Cole, M. A.; Dollmann, B.; Vasilev, K.; Griesser, H. J. Surface Modification of Nanoporous Alumina Membranes by Plasma Polymerization. *Nanotechnology* **2008**, *19* (24), 245704. https://doi.org/10.1088/0957-4484/19/24/245704.

[25] Parkerson, Z. J.; Prozorovska, L.; Vasuta, M. P.; Oddo, T. D.; Jennings, G. K. Simultaneous Spin Coating and Ring-Opening Metathesis Polymerization for the Rapid Synthesis of Polymer Films. *ACS Applied Materials & Interfaces* **2024**, *16* (13), 16754–16766. https://doi.org/10.1021/acsami.4c00211.

[26] Hall, D. B.; Underhill, P.; Torkelson, J. M. Spin Coating of Thin and Ultrathin Polymer Films. *Polymer Engineering & Science* **1998**, *38* (12), 2039–2045. https://doi.org/ 10.1002/pen.10373.

[27] Peurrung, L. M.; Graves, D. B. Film Thickness Profiles over Topography in Spin Coating. *Journal of The Electrochemical Society* **1991**, *138* (7), 2115–2124. https://doi.org/10.1149/1.2085935.

[28] Fujie, T.; Ricotti, L.; Desii, A.; Menciassi, A.; Dario, P.; Mattoli, V. Evaluation of Substrata Effect on Cell Adhesion Properties Using Freestanding Poly(l-Lactic Acid) Nanosheets. *Langmuir* **2011**, *27* (21), 13173–13182. https://doi.org/10.1021/la203140a.

[29] Ran, C.; Ding, G.; Liu, W.; Deng, Y.; Hou, W. Wetting on Nanoporous Alumina Surface: Transition between Wenzel and Cassie States Controlled by Surface Structure. *Langmuir* **2008**, *24* (18), 9952–9955. https://doi.org/10.1021/la801461j.

[30] Taubner, V.; Shishoo, R. Influence of processing parameters on the degradation of poly(L-lactide) during extrusion. *Journal of Applied Polymer Science,* **2001**, 79 (12), 2128–2135. https://doi.org/10.1002/1097-4628(20010321)79:12<2128::AID-APP1020>3.0.CO;2-#.

[31] Signori, F.; Coltelli, M.-B.; Bronco, S. Thermal Degradation of Poly(Lactic Acid) (PLA) and Poly(Butylene Adipate-Co-Terephthalate) (PBAT) and Their Blends upon Melt Processing. *Polymer Degradation and Stability* **2009**, *94* (1), 74–82. https://doi.org/ 10.1016/j.polymdegradstab.2008.10.004.

[32] Chen, F.; Jiang, X.; Kuang, T.; Chang, L.; Fu, D.; Yang, Z.; Yang, J.; Fan, P.; Fei, Z.; Zhong, M. Effect of Nanoporous Structure and Polymer Brushes on the Ionic Conductivity of Poly(Methacrylic Acid)/Anode Aluminum Oxide Hybrid Membranes. *RSC Advances* **2015**, *5* (86), 70204–70210. https://doi.org/10.1039/c5ra08990e.

[33] Bayat, H.; Raoufi, M.; Zamrik, I.; Schönherr, H. Poly(Diethylene Glycol Methylether Methacrylate) Brush-Functionalized Anodic Alumina Nanopores: Curvature-Dependent Polymerization Kinetics and Nanopore Filling. *Langmuir* **2020**, *36* (10), 2663–2672. https://doi.org/10.1021/acs.langmuir.9b03700.

[34] Dong, Y.; Marshall, J.; Haroosh, H. J.; Mohammadzadehmoghadam, S.; Liu, D.; Qi, X.; Lau, K.-T. Polylactic Acid (PLA)/Halloysite Nanotube (HNT) Composite Mats: Influence of HNT Content and Modification. *Composites Part A: Applied Science and Manufacturing* **2015**, *76*, 28–36. https://doi.org/10.1016/j.compositesa.2015.05.011.

---

[35] Li, S.-Y.; Wang, J.; Li, Y. Photoluminescence Properties of Anodic Aluminum Oxide Formed in a Mixture of Ammonium Fluoride and Oxalic Acid. *Optical Engineering* **2017**, *56* (6), 067107. https://doi.org/10.1117/1.oe.56.6.067107.

[36] Kim, J.-H.; Bryan, W. W.; Randall Lee, T. Preparation, Characterization, and Optical Properties of Gold, Silver, and Gold−Silver Alloy Nanoshells Having Silica Cores. *Langmuir* **2008**, *24* (19), 11147–11152. https://doi.org/10.1021/la8016497.

[37] Raoufi, M.; Schönherr, H. Improved Synthesis of Anodized Aluminum Oxide with Modulated Pore Diameters for the Fabrication of Polymeric Nanotubes. *RSC Advances* **2013**, *3* (32), 13429. https://doi.org/10.1039/c3ra41165f.

[38] Alhusaini, Q.; Scheld, W. S.; Jia, Z.; Das, D.; Afzal, F.; Müller, M.; Schönherr, H. Bare Eye Detection of Bacterial Enzymes of Pseudomonas Aeruginosa with Polymer Modified Nanoporous Silicon Rugate Filters. *Biosensors* **2022**, *12* (12), 1064. https://doi.org/10.3390/bios12121064.

[39] Altuntas, S.; Buyukserin, F. Fabrication and Characterization of Conductive Anodic Aluminum Oxide Substrates. *Applied Surface Science* **2014**, *318*, 290–296. https://doi.org/10.1016/j.apsusc.2014.06.007.

[40] Le Coz, F.; Arurault, L.; Datas, L. Chemical Analysis of a Single Basic Cell of Porous Anodic Aluminium Oxide Templates. *Materials Characterization* **2010**, *61* (3), 283–288. https://doi.org/10.1016/j.matchar.2009.12.008.

[41] Yamamoto, Y.; Baba, N.; Tajima, S. Colored Materials and Photoluminescence Centres in Anodic Film on Aluminium. *Nature* **1981**, *289* (5798), 572–574. https://doi.org/10.1038/289572a0.

[42] Vojkuvka, L.; Santos, A.; Pallarès, J.; Ferré-Borrull, J.; Marsal, L. F.; Celis, J. P. On the Mechanical Properties of Nanoporous Anodized Alumina by Nanoindentation and Sliding Tests. *Surface and Coatings Technology* **2012**, *206* (8–9), 2115–2124. https://doi.org/10.1016/j.surfcoat.2011.09.040.

[43] Aman, J. N. M.; Wied, J. K.; Alhusaini, Q.; Müller, S.; Diehl, K.; Staedler, T.; Schönherr, H.; Jiang, X.; Schmedt auf der Günne, J. Thermal Hardening and Defects in Anodic Aluminum Oxide Obtained in Oxalic Acid: Implications for the Template Synthesis of Low-Dimensional Nanostructures. *ACS Applied Nano Materials* **2019**, *2* (4), 1986–1994. https://doi.org/10.1021/acsanm.9b00018.

[44] Gao, T.; Meng, G.; Zhang, L. Blue Luminescence in Porous Anodic Alumina Films: The Role of the Oxalic Impurities. *Journal of Physics: Condensed Matter* **2003**, *15* (12), 2071–2079. https://doi.org/10.1088/0953-8984/15/12/324.

[45] Li, S.-Y.; Wang, J.; Li, Y.; Zhang, X.-Q.; Wang, G.; Wang, C.-W. Photoluminescent Properties of Anodic Aluminum Oxide Films Formed in a Mixture of Malonic and Sulfuric Acid. *Superlattices and Microstructures* **2014**, *75*, 294–302. https://doi.org/10.1016/j.spmi.2014.07.018.

[46] Yamashita, K.; Kikkawa, Y.; Kurokawa, K.; Doi, Y. Enzymatic Degradation of Poly(l-lactide) Film by

---

K: Quartz Crystal Microbalance and Atomic Force Microscopy Study. *Biomacromolecules* **2005**, *6* (2), 850–857. https://doi.org/10.1021/bm049395v.

[47] Tarazona, N. A.; Wei, R.; Brott, S.; Pfaff, L.; Bornscheuer, U. T.; Lendlein, A.; Machatschek, R. Rapid Depolymerization of Poly(ethylene Terephthalate) Thin Films by a Dual-enzyme System and its Impact on Material Properties. *Chem Catalysis* **2022**, *2* (12), 3573–3589. https://doi.org/10.1016/j.checat.2022.11.004.

[48] Mortimer, R. J.; Graham, K. R.; Grenier, C. R. G.; Reynolds, J. R. Influence of the Film Thickness and Morphology on the Colorimetric Properties of Spray-Coated Electrochromic Disubstituted 3,4-Propylenedioxythiophene Polymers. *ACS Applied Materials & Interfaces* **2009**, *1* (10), 2269–2276. https://doi.org/10.1021/am900431z.

[49] Yamashita, K.; Kikkawa, Y.; Kurokawa, K.; Doi, Y. Enzymatic Degradation of Poly(l-lactide) Film by Proteinase K: Quartz Crystal Microbalance and Atomic Force Microscopy Study. *Biomacromolecules* **2005**, *6* (2), 850–857. https://doi.org/10.1021/bm049395v.

[50] Holmes, J. L.; Bachus, K. N.; Bloebaum, R. D. Thermal Effects of the Electron Beam and Implications of Surface Damage in the Analysis of Bone Tissue. *Scanning* **2000**, 22 (4), 243–248. https://doi.org/10.1002/sca.4950220403.

[51] Janorkar, A. V.; Metters, A. T.; Hirt, D. E. Modification of Poly(lactic acid) Films: Enhanced Wettability from Surface-Confined Photografting and Increased Degradation Rate Due to an Artifact of the Photografting Process. *Macromolecules* **2004**, *37* (24), 9151–9159. https://doi.org/10.1021/ma049056u.

[52] Lee, S. H.; Kim, I. Y.; Song, W. S. Biodegradation of Polylactic Acid (PLA) Fibers Using Different Enzymes. *Macromolecular Research/Macromolecular Research* **2014**, *22* (6), 657–663. https://doi.org/10.1007/s13233-014-2107-9.

[53] Ateş, S.; Baran, E.; Yazıcı, B. The Nanoporous Anodic Alumina Oxide Formed byTwo-step Anodization. *Thin Solid Films* **2018**, *648*, 94–102. https://doi.org/10.1016/j.tsf.2018.01.013.

[54] Lee, J.; Jung, S.-Y.; Kumbhar, V. S.; Uhm, S.; Kim, H.-J.; Lee, K. Formation of Aluminum Oxide Nanostructures via Anodization of Al$_3$10$_4$ Alloy and Their Wettability Behavior for Self-Cleaning Application. *Catalysis Today* **2021**, *359*, 50–56. https://doi.org/10.1016/j.cattod.2019.04.062.

[55] Roy, S.; Ansari, K. J.; Jampa, S. S. K.; Vutukuri, P.; Mukherjee, R. Influence of Substrate Wettability on the Morphology of Thin Polymer Films Spin-Coated on Topographically Patterned Substrates. *ACS Applied Materials & Interfaces* **2012**, *4* (4), 1887–1896. https://doi.org/10.1021/am300201a.

[56] Frolova, A.; Ksendzov, E.; Kostjuk, S.; Efremov, Y.; Rochev, Y.; Kukanova, V.; Kotova, S.; Timashev, P. Phase Behavior of P(NIPAM-g-PLA) Films for Cell Sheet Technology Assessed with Atomic Force Microscopy. *Colloids and Surfaces. A, Physicochemical and Engineering Aspects* **2024**, 134854. https://doi.org/10.1016/j.colsurfa.2024.134854.

Chapter 6. Optimizing the Response of a PLA-AAO Sensor: Towards the Detection of Bacterial Enzymes

6.1 Introduction

As discussed in Chapter 2, nanoporous materials, such as AAO, have been considered suitable candidates as transducers for sensing due to the signal enhancement that can be achieved by their large surface area compared to planar substrates[1]. Furthermore, they can be coupled with a wide range of chemical species to design label or label-free sensors for chemical sensing or biosensing[2,3]. For instance, AAO functionalized with polyelectrolyte multilayers has been used as host materials for enzyme-responsive polymers to detect enzymes[4]. These polymers can be specifically degraded by the target bacteria enzymes, which may be exploited to indicate the presence of targeted bacteria[5].

In this Chapter, the response of polymer-modified AAO for sensing enzymes[6] was optimized. The nanopores of AAO were filled with PLA via the droplet evaporation method. Unlike the functionalization approach discussed in Chapter 5, the PLA layer on the top side of the AAO was removed before performing the enzymatic degradation. This optimizes the performance of the sensor by eliminating the undesired signal generated due to the presence of the PLA on the top surface of AAO from the signal obtained due to the enzymatic reaction inside the pores (Scheme 6.1). Furthermore, the modification process of PLA inside the pores was investigated using the reflectometric interference spectroscopy (RIfS) technique[7].

As discussed in Chapters 2 and 5, the PLA can be degraded by selected proteases such as proteinase K[8,9,10]. Thus, the enzymatic degradation of PLA inside the pores can be discernible, inducing a change in the refractive index of the AAO and leading to a change in the *EOT*. The deposition and degradation of PLA by proteinase K were analyzed using RIfS. The shifts observed in the characteristic RIfS fringe pattern following pore filling and enzymatic degradation of the PLA film were quantitatively analyzed. The pore filling was evaluated by analyzing the RIfS spectra. This sensor, which is comprised of AAO and filled with PLA, explored a promising approach for both *in-situ* and *ex-situ* enzyme detection.

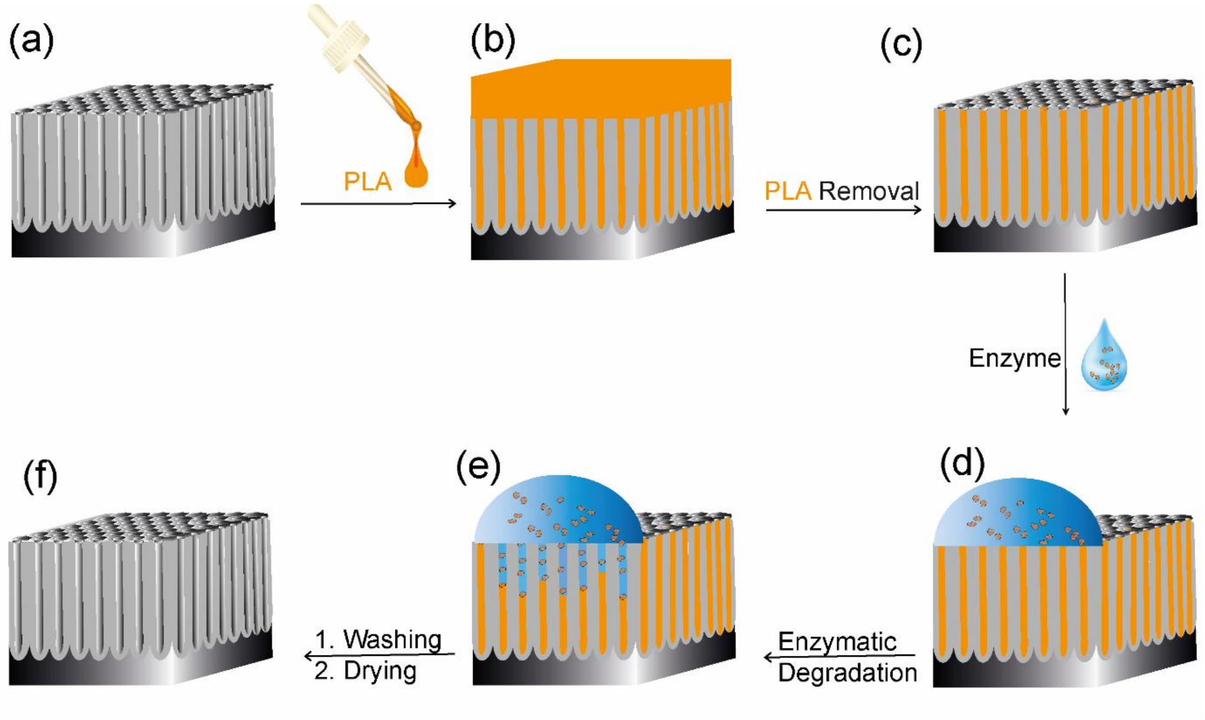

Scheme 6.1: *Schematic of the AAO-based sensor for enzyme detection: a) neat AAO; b) AAO after deposition of PLA; c) removal of PLA from the top side of the AAO and leaving behind PLA inside the pores; d) incubation of PLA-filled AAO with enzyme; e) degradation of PLA inside the pores by enzyme; f) AAO after the enzymatic reaction followed by washing and drying.*

6.2 Modification and Characterization of AAO with PLA by Casting Method

The solvent casting method, also known as droplet evaporation, is a direct and simple method to functionalize the AAO pores. Russell et al. also investigated this method[11]. They reported the fabrication of poly(methyl methacrylate) (PMMA) nanotubes through the wetting of AAO with PMMA solution in chloroform. Other researchers have demonstrated that this method offers a simple approach to preparing polymer nanostructures inside AAO pores, provided the solution can infiltrate and wet the AAO pore walls, as with acetone as a polymer solvent[12]. Thus, in this Chapter, the AAO pores were modified with PLA using this method, as illustrated in Scheme 6.1. The PLA solution was dropped onto the top AAO surface, and the solvent (i.e., chloroform) evaporated under ambient conditions, leaving behind a solidified PLA film. The applied PLA solution on AAO partially infiltrated the pores, and the majority of the polymer was located on the top side of the AAO surface. After the completion of the drying process, FESEM was conducted and revealed that a substantial amount of PLA was observed on the top side of AAO, as shown in Figure 6.1a,b. To optimize the AAO sensor, by confirming that any characteristic observed due to PLA degradation was strictly from PLA deposited into the AAO pores, the PLA film on the top AAO surface was removed by wiping the AAO surface with chloroform-wetted tissue. Figure 6.1c confirmed that the layer of PLA was removed from the top surface of AAO, showing that the majority of the pores were opened.

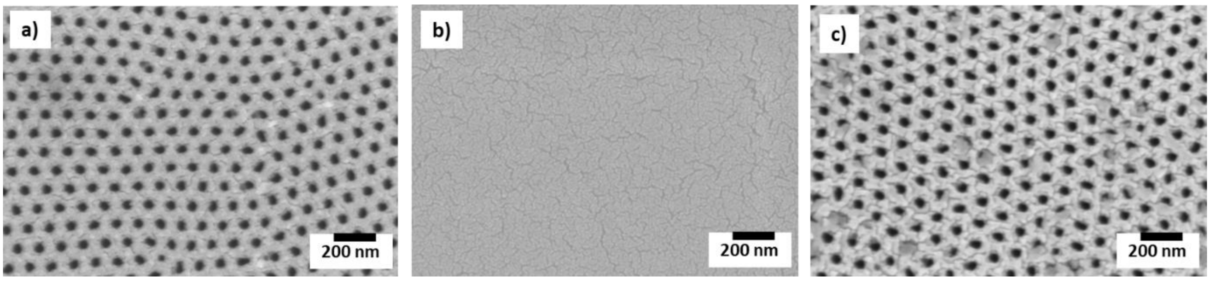

Figure 6.1: *Top view FESEM images of AAO nanopores (D_i = 103 nm, D_p = 42 nm, l = 3.2 µm; 40 V, 0.3 M oxalic acid, 2nd anodization: 60 min, widening: 7 min in H_3PO_4 at 35 °C) a) bare, b) after the casting of PLA (5 wt% in chloroform), c) after surface cleaning.*

Figure 6.2a,b displays cross-sectional FESEM images before and after the PLA deposition on the AAO surface. The FESEM image estimated the PLA film thickness on the top side of the AAO to be approximately 5.7 µm. This thick layer was removed to prevent it from affecting the response of the AAO-PLA sensor since this layer must be degraded prior to the degradation of the confined PLA inside the pores. Figure 6.2c also confirms the cleaning efficiency of the PLA from the AAO surface. The magnified image of Figure 6.2c reveals that PLA can be seen at the bottom of the pores, which emphasizes the penetration of the PLA solution deep into the pores (Figure 6.2d). The pore filling with PLA will be discussed later in this Chapter.

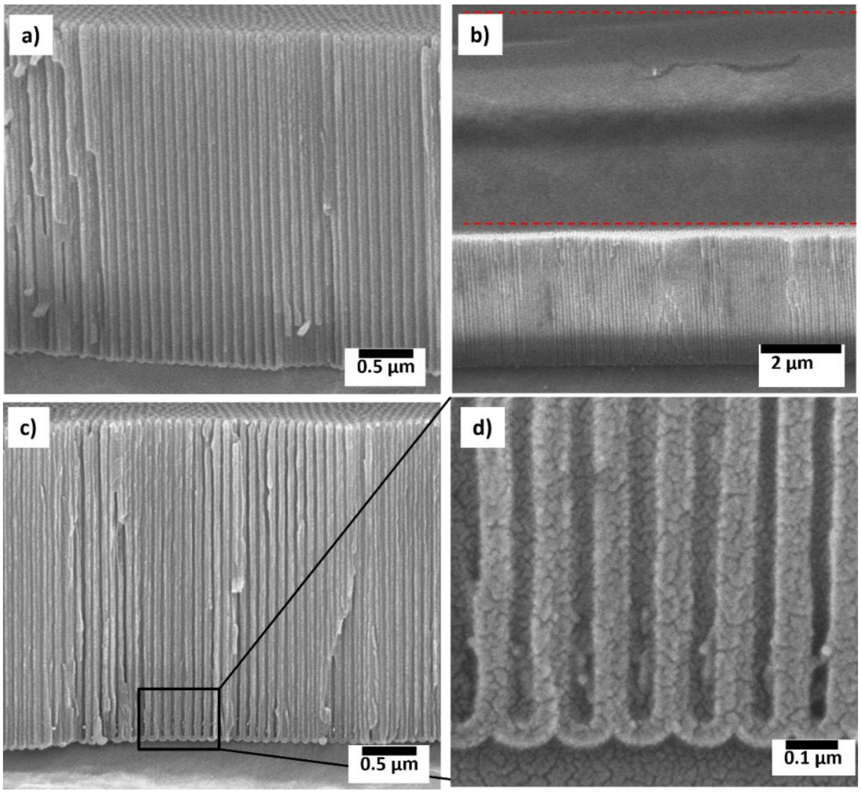

Figure 6.2: *Cross-sectional FESEM images of AAO nanopores (D_i = 103 nm, D_p = 42 nm, l = 3.2 µm; 40 V, 0.3 M oxalic acid, 2nd anodization: 60 min, widening: 7 min in H_3PO_4 at 35 °C; a) bare, b) after casting of PLA, c,d) after surface cleaning at low and high magnification, respectively.*

6.3 Characterization of PLA inside the Pores by RIfS

The pore filling (volume fraction) of PLA in the AAO pores was determined by RIfS measurements. Different concentrations of PLA were drop-casted onto AAO substrates with similar pore geometry, and the AAO surface was cleaned before RIfS measurements. The filling percentage was calculated by employing the Maxwell-Garnett equation described in Chapter 2 and comparing the maximum *EOT* of the neat AAO to the functionalized AAO.

The RIfS spectra before and after PLA deposition into AAO pores are shown in Figure 6.3 a-d. The values of Δ*EOT* increased with PLA concentrations due to an increase in the amount of PLA in the pores (pore filling). The calculation of pore filling percentage was detailed in section 6.6, Materials and Methods.

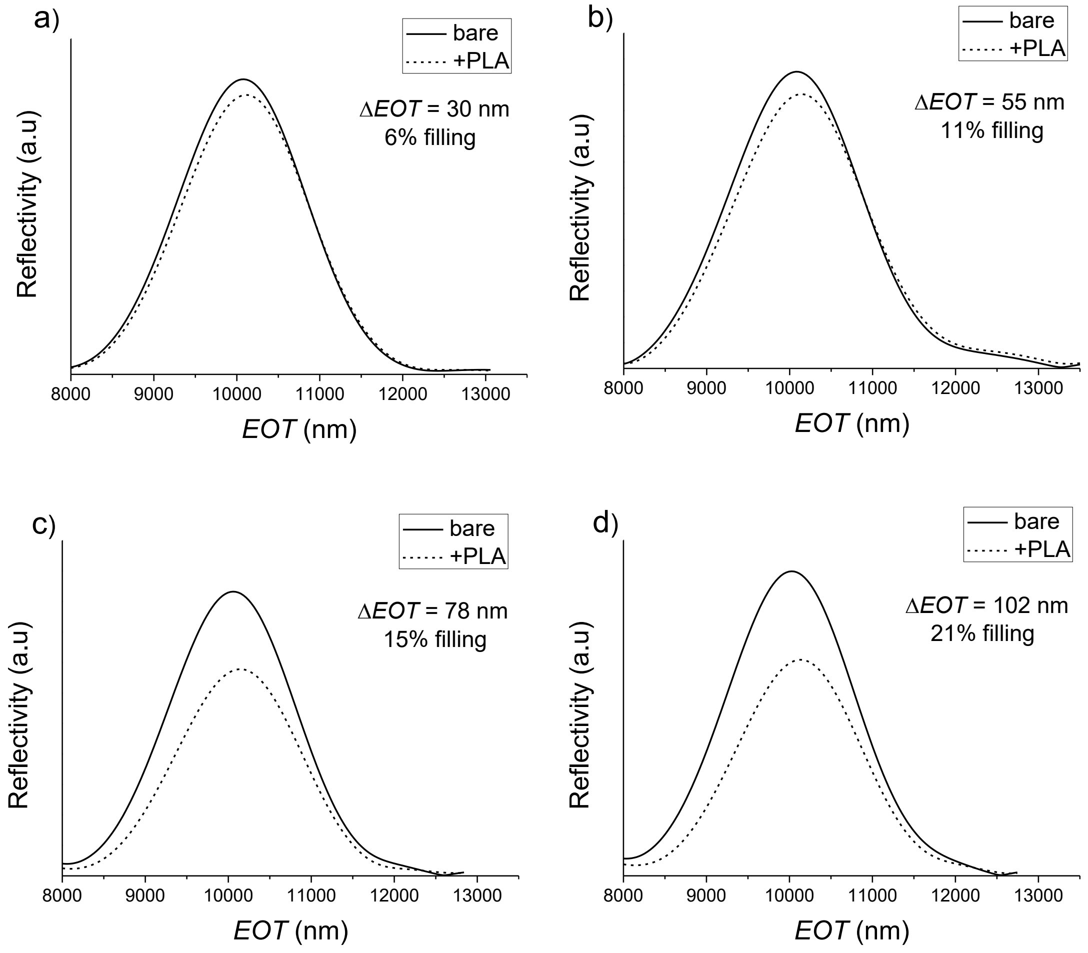

Figure 6.3: *Change of EOT upon loading with different PLA concentrations a) 1 wt%, b) 3 wt%, c) 4 wt%, and d) 5 wt%. AAO: pore diameter = 42 nm (widening: 7 min in* H_3PO_4 *at 35 °C), pore length = 3.2 µm (anodization: 60 min); 40 V, 0.3 M oxalic acid,* 2^{nd} *anodization: 60 min). All samples were surface cleaned after casting the PLA. The pore filling was calculated using the Maxwell-Garnett equation. All measurements were performed on dried AAO-PLA samples (the pores were air/PLA-filled).*

Figure 6.4 displays a plot of the Δ*EOT* versus the pore filling, revealing a linear relationship within this concentration range. It was reported that as the polymer concentration increases, the viscosity of the polymer solution also increases[13]. The high viscosity of the polymer solution hinders its penetration by clogging the pores, leading to less polymer filling the pores of AAO[14].

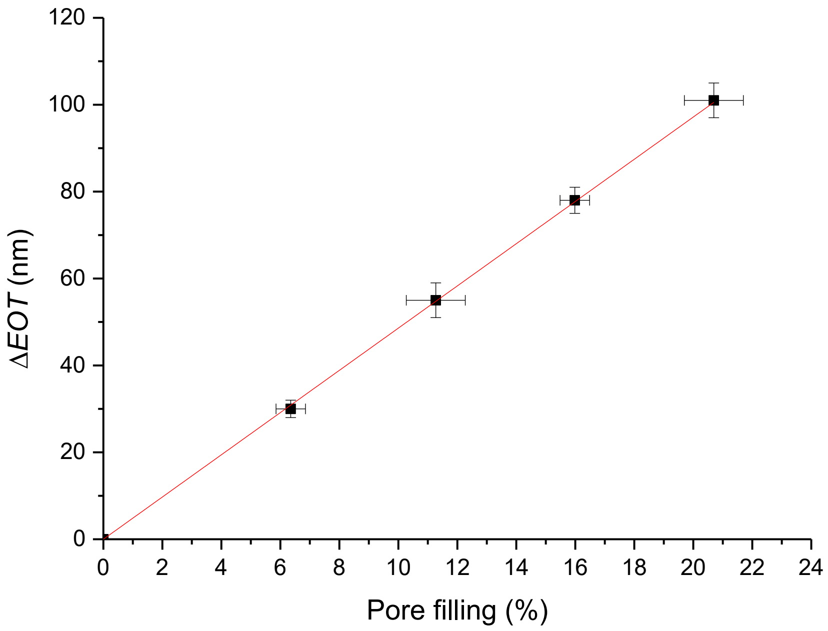

Figure 6.4: *Plot between the ΔEOT and pore filling (%) extracted from Figure 6.3 a-d. The error bars are the standard deviations (n=3).*

6.4 Enzymatic Degradation of PLA inside the Pores of AAO

As previously discussed, the deposition of PLA in AAO causes an increase in *EOT* due to an increase in n_{eff} of the AAO film. The PLA-modified AAO could be used to design a sensor to detect enzymes such as proteinase K. As discussed in Chapter 2, the reduction in the amount of deposited material inside the pores of AAO caused a blue shift in peaks (also referred to as fringes) in the interferometric spectrum. Therefore, the enzymatic degradation of PLA in the pores by proteinase K or bacterial enzymes should lead to a change in the n_{eff} of the AAO film. The reflectance spectrum was recorded before and after the incubation of PLA-modified AAO with proteinase K for different internal times (Figure 6.5). As shown in Figure 6.5, a blue shift in the maxima wavelength of the interferometric spectrum was observed, indicating that PLA was removed from the pores of AAO, confirming the occurrence of enzymatic degradation on PLA inside the pores.

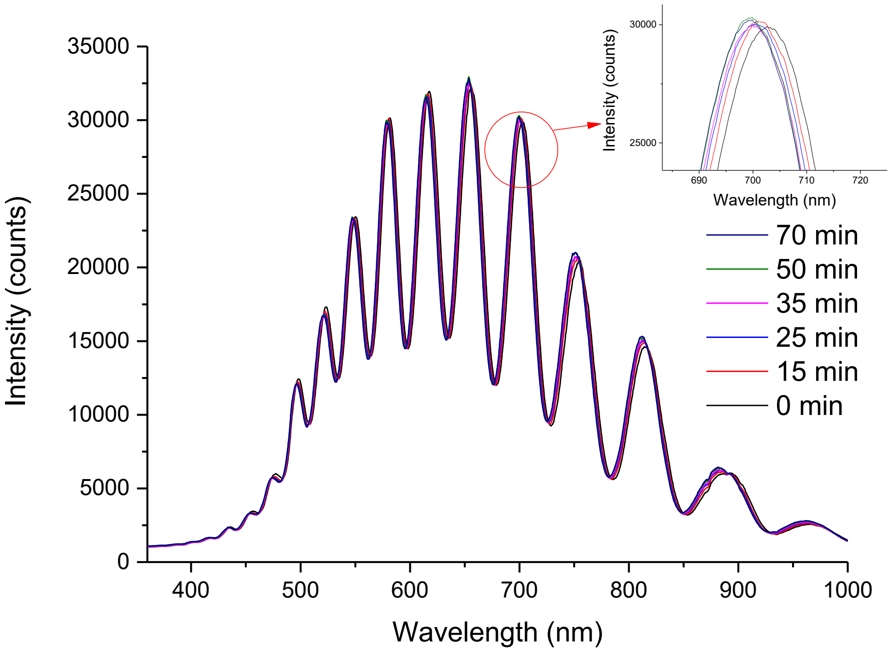

Figure 6.5: *RIfS spectra of PLA-modified AAO before and after enzymatic degradation of PLA with proteinase K (1 mg mL^{-1}) at different times. The inset figure is the zoomed fringes to show the shift due to the degradation.*

In the RIfS technique, a fast Fourier transform (FFT) analysis was applied to the interferometric spectrum to obtain the *EOT* value. Figure 6.6 shows *EOT* curves obtained after the enzymatic reaction at different times. As can be seen, the maxima of the *EOT* curves were blue-shifted with the degradation time. The spectrum of the PLA-modified AAO shows an *EOT* value of 10121 nm at time zero (t = 0). Fifteen minutes after starting the enzymatic reaction, the *EOT* value was reduced by ~17 nm, which attributed to a decrease in the refractive index after partially removing PLA from the pores. The *EOT* value reduced (by ~44 nm) up to 50 min. A slight reduction (by only 2 nm) was recorded at longer incubation times, providing 100 % degradation of the loaded PLA, and the *EOT* of unloaded AAO was significantly restored. This observation indicated that the PLA in AAO was degraded by proteinase K, and the resulting degraded fragments were removed in the washing step.

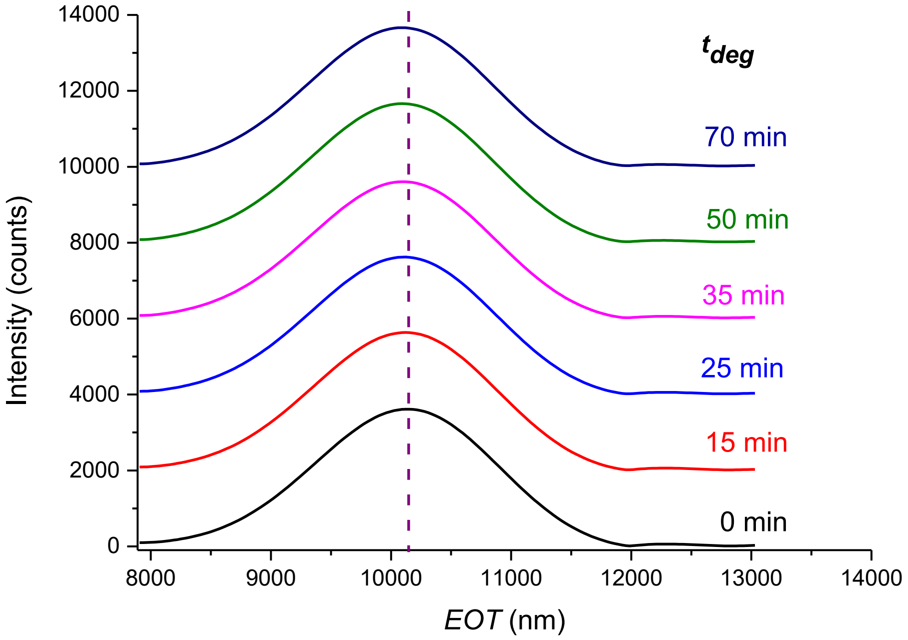

Figure 6.6: *EOT curves of PLA-modified AAO before and after enzymatic degradation of PLA with proteinase K (1 mg mL^{-1}) at different times. The maxima of EOT curves were shifted with the degradation time. The PLA/AAO samples were measured by RIfS after washing and drying steps for each degradation time (15, 25, 35, 50, and 70 min).*

Next, the response of the PLA-modified AAO sensor was investigated for different proteinase K concentrations. As shown in Figure 6.7, the decrease in *EOT* values obtained after applying proteinase K to the PLA-modified AAO sensor for a given time exhibited an increase with increasing enzyme concentration. Furthermore, there was no significant change in the Δ*EOT* value of the PLA-modified AAO incubated in a buffer solution compared to the enzyme. This data suggested that the proteinase K could degrade the PLA film.

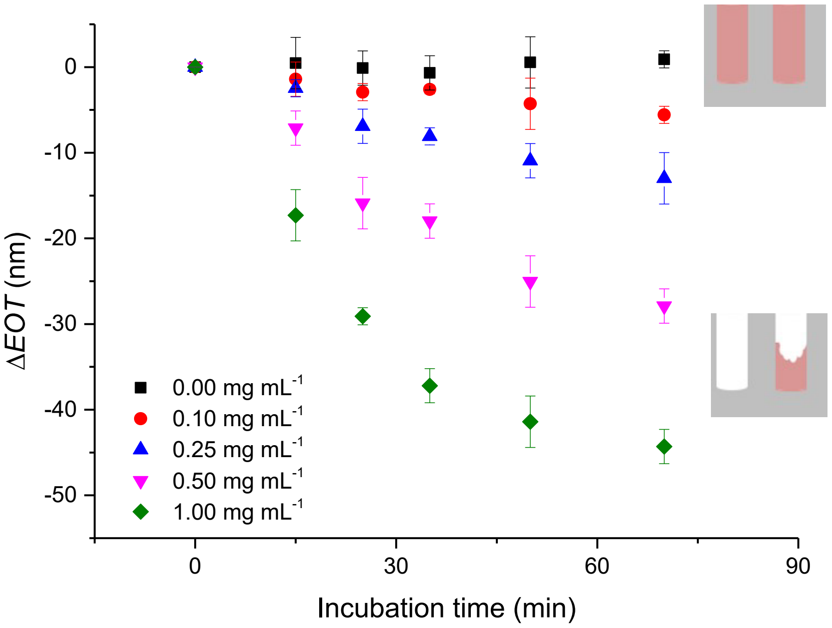

Figure 6.7: *Plot of EOT shift of four sets of PLA-modified AAO in the dry state, after incubation in 0.10, 0.25, 0.50, and 1.00 mg mL^{-1} of proteinase K solution for 0, 15, 25, 35, 50, and 70 min at 25 °C. The error bars are the standard deviations (n=3). The inset scheme represents the filled AAO with PLA before and after PLA degradation.*

The extent of the reaction x can be expressed as a function of incubation time[15].

$$x = \frac{\Delta EOT_0 - \Delta EOT_t}{\Delta EOT_0 - \Delta EOT_\infty} \quad \text{..............................} \text{ (Eq. 6.1)}$$

where ΔEOT_0 is the shift in the *EOT* at time zero, ΔEOT_t at time *t* and ΔEOT_∞ at infinite time.

Figure 6.8 illustrates the course of the enzymatic degradation ([1 − x], with the extent of reaction (x) as a function of reaction time), along with the change in the pore filling. The pore filling was determined by applying the Maxwell-Garnett equation described in Chapter 2. The PLA pore filling was reduced with the incubation time following the reduction in the refractive index in the pores. Furthermore, Figure 6.8 shows that the extent of the reaction increased substantially with an elevated concentration of proteinase K. In contrast, the sensor had no significant response in the absence of the proteinase K (Tris-HCl buffer). Hence, since the response is due to the enzymatic reaction, we may conclude that the PLA film in the AAO was stable in the buffered medium for at least 1 h. The data were least-squares fitted to evaluate the apparent rate constants.

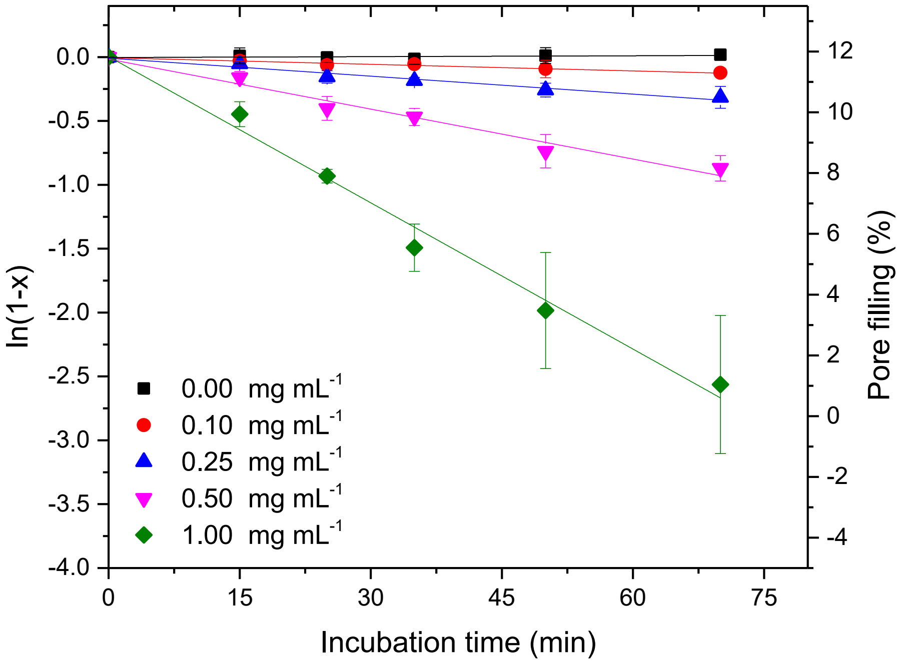

Figure 6.8: *Plot of ln(1-x) (x: extent of reaction) and the pore filling as a function of incubation time for the degradation of PLA inside pSiRF in 0.10, 0.25, 0.50 and 1.00 mg mL*$^{-1}$ *proteinase K solution at 25 °C for 0, 15, 25, 35, 50, and 70 min. The pore filling was determined by applying the Maxwell-Garnett equation. The data are presented as mean ± standard deviation. The solid lines correspond to the linear least squares fit of RIfS data. All measurements were conducted in the dried state.*

The apparent rate constants (k) were plotted against the proteinase K concentrations (Figure 6.9). It was observed that k increased linearly for the lower proteinase K concentrations. For higher proteinase K concentration, i.e., 1 mg mL^{-1}, the k value deviated from linearity, recording a higher degradation rate. The latter observation could be attributed to the substrate (PLA) availability inside the AAO pores to proteinase K, which may be because of the low pore filling (12 %), providing more free space in the pores. The confined pores of nanostructures may affect the kinetics of enzymatic reaction by influencing the diffusion of the degraded polymer fragments out of the pores. The size of the pores might hinder the mobility of PLA molecules, impacting the substrate's accessibility to enzyme molecules and thus affecting the enzymatic reaction rate. Furthermore, if the pores are too narrow, an interaction between the enzyme and the substrate may occur, inhibiting the enzyme's mobility inside the pores.

Unfortunately, no higher concentrations were applied to determine whether this behavior (drift from linearity) continues with increasing enzyme concentration.

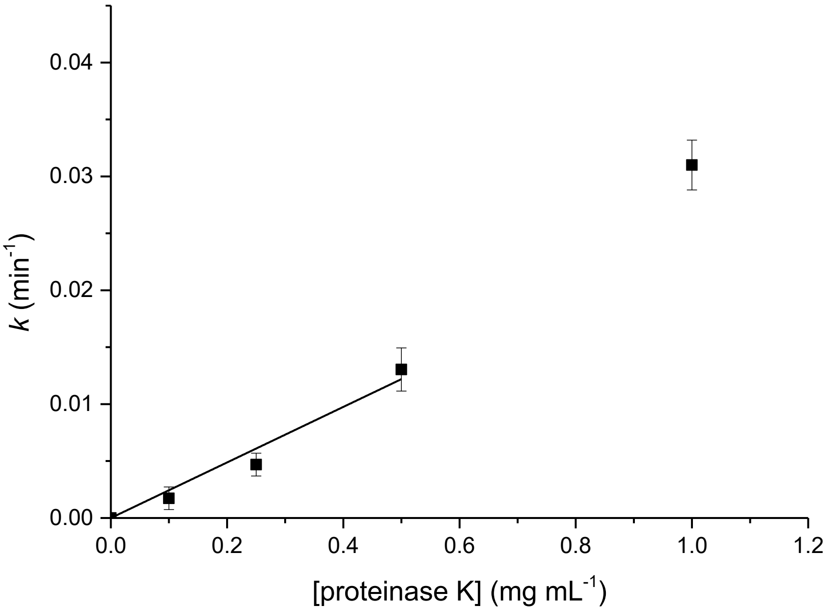

Figure 6.9: *Plot of apparent rate constant (k) versus proteinase K concentrations (0.10, 0.25, 0.50, and 1.00 mg* mL^{-1}*). The values for k were obtained from linear fits in Figure 6.8; the error bars denote the standard deviation from these fits. The solid line corresponds to the linear least-squares fit of the first three data points to estimate the corresponding slope (0.024 mg* mL^{-1} min^{-1}*).*

The enzymatic reaction of the PLA-modified AAO with proteinase K was conducted *in-situ* by RIfS. Figure 6.10 shows two ΔEOT and degradation time datasets: one is for PLA-modified AAO incubated with Tris-HCl buffer (as a blank), and the other is for PLA-modified AAO incubated in proteinase K solution (1 mg mL^{-1}). Before the enzymatic degradation, Tris-HCl buffer was injected over PLA-modified AAO for 10 min, followed by injecting enzyme solution. The data shows no significant change in ΔEOT with incubation in the buffer for 260 min. In contrast, an instantaneous decrease in ΔEOT was observed after the injection of the enzyme solution. The reduction in ΔEOT is due to the reduction in the refractive index of the medium in the pores because of the replacement of the PLA by the enzyme solution. A value for *k* of 0.003 min^{-1} was calculated from Figure 6.10. This value of k is smaller than that obtained in *ex-situ* measurements, where the samples were removed from the incubation solutions, washed, dried, and then measured with RIfS (Figure 6.7). In contrast, in this *in-situ* experiment, no washing or drying steps were applied; hence, no convection took place, and degraded PLA may have remained trapped inside the pores of AAO, resulting in a lower observed degradation rate.

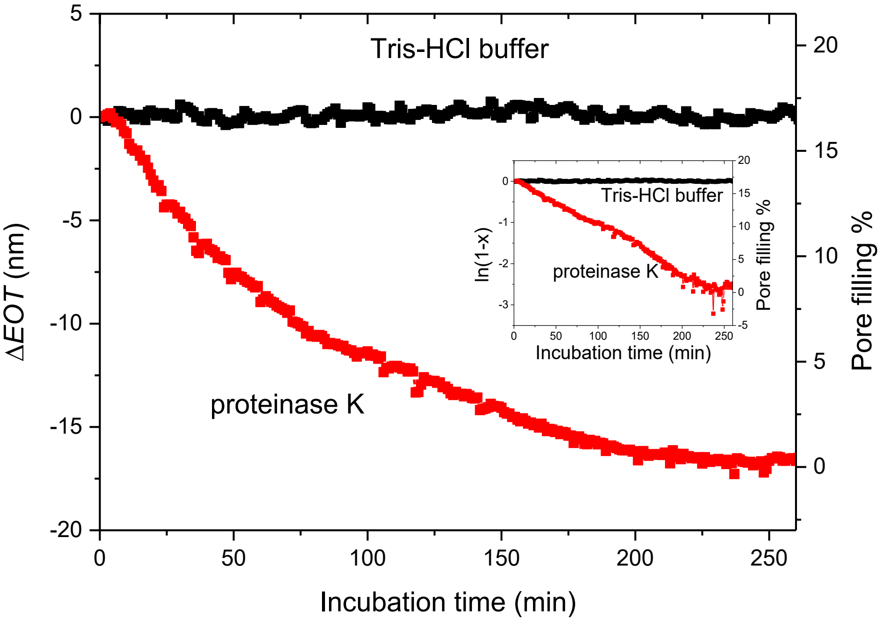

Figure 6.10: *Plot of in-situ RIfS measurement of enzymatic reaction on PLA-modified AAO with proteinase K solution (1 mg mL^{-1}) and Tris-HCl buffer. The inset is a Plot of ln(1-x) and the pore filling as a function of incubation time for the degradation of PLA inside AAO in 1 mg mL^{-1} of proteinase K solution at 25 °C.*

The PLA-modified AAO sample was also used as a biosensing platform in a biological environment. The PLA-modified AAO was treated with a sterile filtered supernatant of *P. aeruginosa* (PAO1) in the LB medium. The pure LB medium was chosen as a blank. Figure 6.11 shows the RIfS measurement carried out during incubation in the sterile bacterial supernatant and in the pure LB medium, respectively. It was observed that the Δ*EOT* was reduced for the *P. aeruginosa* supernatant by 20 nm (30 %), whereas the Δ*EOT* value was reduced only by 2 nm (3 %) in LB for the same incubation time (360 min). The results confirm that PLA was stable in the LB medium and degraded in the *P. aeruginosa* (PAO1) supernatant, thus indicating that enzymes secreted by *P. aeruginosa* in this medium can be detected by this sensor. The results showed that the reaction was slow compared to that of the highly concentrated proteinase K solution, possibly due to a lower enzymes concentration in the supernatant than in the case of pure proteinase K. Moreover, the supernatant composition is more complex and will contain different proteinases that may have different capabilities for PLA hydrolysis.

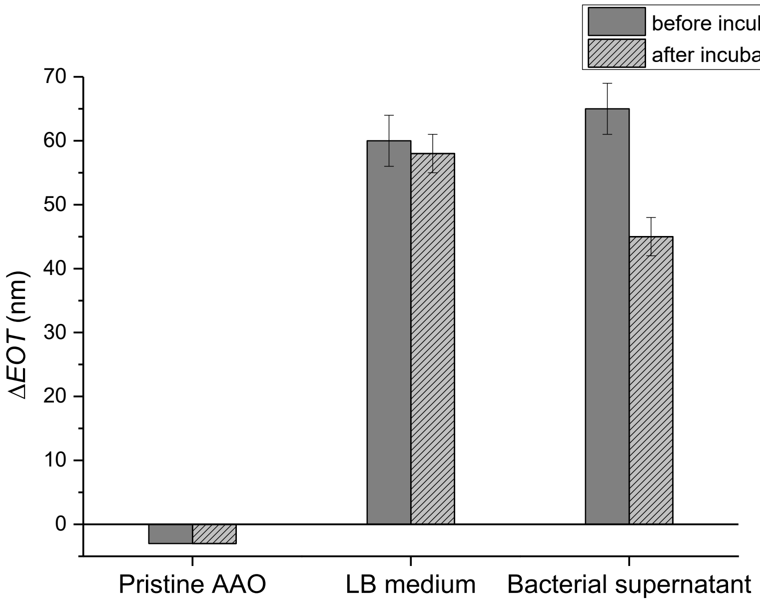

Figure 6.11: *Plot of ex-situ RIfS measurement before (solid) and after (stripes) incubation of a PLA-modified AAO in sterile P. aeruginosa (PAO1) supernatants obtained from a* 1.9×10^9 *CFU* mL^{-1} *suspension and in pure LB medium for 360 min at 25 °C. The ΔEOT before the incubation was calculated by subtracting the EOT values before and after PLA deposition in AAO, whereas ΔEOT after degradation was calculated by subtracting the EOT values before and after PLA degradation. The RIfS measurements were conducted in the dried state (after washing and drying steps). The error bars are the standard deviations (n=3).*

The PLA-modified AAO sample was also measured *in-situ* during the incubation in the LB medium and sterile *P. aeruginosa* (PAO1) supernatants. The RIfS were measured for 900 min in Figure 6.12. The result revealed that Δ*EOT* was relatively stable in LB compared to samples incubated in the supernatant. In the latter, Δ*EOT* decreased with time. Furthermore, Figure 6.12 shows that the Δ*EOT* measured in the LB medium initially increased by ~ 2 nm and decreased by ~ 2 nm after a few minutes. This fluctuation in Δ*EOT* continued for the entire reaction. A possible explanation for this behavior upon initial incubation may be due to the penetration of the solution into the blocked pores with PLA.

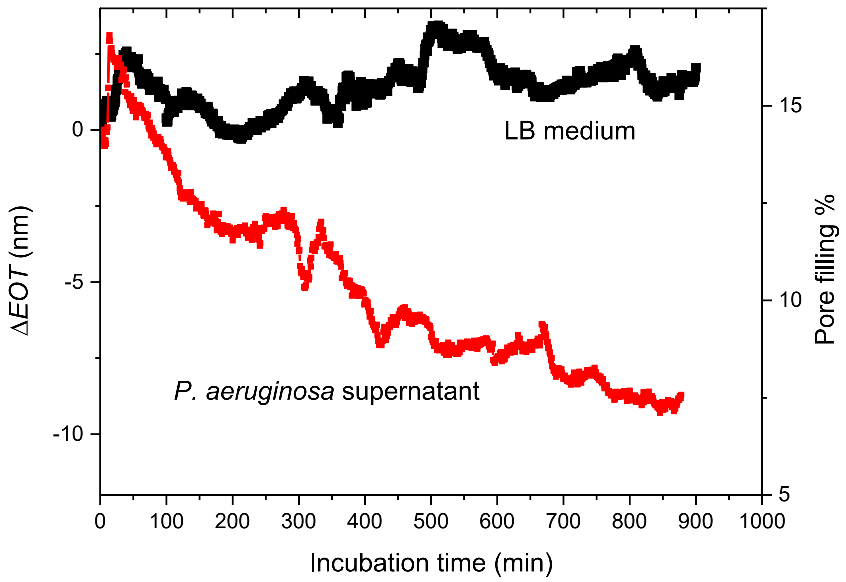

Figure 6.12: *Plot of in-situ RIfS measurement during incubation of a PLA-modified AAO in sterile P. aeruginosa (PAO1) supernatants obtained from a 1.9 × 10^9 CFU mL^{-1} suspension by filtration (red line) and in pure LB medium (black line). The measurement was conducted at 25 °C. The pore filling was determined by dividing the measured ΔEOT values by the calculated ΔEOT value obtained by applying the Maxwell-Garnett equation described in Chapter 2. The porosity and the pore length of AAO were determined with FESEM to be 13 % and 3,2 µm, respectively.*

6.5 Conclusion

This Chapter investigated the modification of AAO pores with PLA and the enzymatic degradation of the PLA inside the AAO pores. The PLA modification process was performed using the casting method. Different concentrations of PLA solution were cast on AAO, followed by removing the remaining PLA from the top side of the AAO surface. Pore filling was determined based on the Δ*EOT* measured by RIfS and Δ*EOT* calculated by the Maxwell- Garnett equation. The data showed that the Δ*EOT* increased linearly with the pore filling.

The FESEM was conducted on the AAO sensor before and after PLA deposition and after surface cleaning. The FESEM images confirmed that the PLA covered the AAO, and the consequent cleaning was successful. The cross-sectional FESEM also suggests the presence of PLA inside the pores. PLA degradation was conducted by immersing the AAO sensor in proteinase K solution for a given time. The RIfS measurement was conducted on the AAO sensor after washing and drying. The RIfS spectra showed a blue shift in the fringes with degradation time. The FFT was applied to the RIfS spectra to obtain the *EOT*. The *EOT* values also decreased over time when incubated in proteinase K. This reduction was attributed to a decline in the n_{eff} inside the pores, which results from enzymatic degradation of PLA, involving the cleavage of ester bonds along the PLA backbone and subsequent fragmentation of PLA into smaller entities capable of diffusing out of the pores.

The enzymatic degradation of PLA was also tested on an AAO sensor at different enzyme concentrations. The result revealed that the rate of enzymatic reaction increased with enzyme concentration. Finally, the AAO sensor was tested in the sterile *P. aeruginosa* (PAO1) supernatant. The reaction was conducted both *in-situ* and *ex-situ* and monitored by RIfS. In both cases, the Δ*EOT* decreased when the AAO sensor was treated with *P. aeruginosa* supernatant compared to the LB medium. The last finding suggests that the AAO sensor could be used as a versatile sensor platform in the biological environment to detect bacterial enzymes.

6.6 Materials and Methods

Modification of AAO with PLA

The procedure for fabricating the AAO sensors was discussed in Chapter 5. The filling process of AAO pores with PLA was performed using the solvent casting method. A series of PLA concentrations (1, 3, 4, and 5 wt%) were prepared in chloroform (99 %, purchased from Carl Roth). Prior to the modification, the AAO sensors were sputtered with ~ 8 nm gold. Then, 80 µL of PLA solution was cast on the surface of the AAO sensor and was left for 24 h under ambient temperature for drying. After solvent evaporation, the PLA film covering the AAO sensor was removed by carefully cleaning the top surface of AAO with chloroform-soaked tissue. Finally, the AAO sensor was heated on a hot plate at 70 °C for 1 min and cooled to ambient temperature. Prior to each experiment, the samples were vacuumed at 5 mbar for 2 h for further drying.

Calculation of Pore Filling based on the EOT Values

The Theoretical *EOT* was calculated according to the Maxwell-Garnett equation (Chapter 2), assuming 100% pore filled by air or PLA. The pore length and porosity were obtained from FESEM measurements. The experimental *EOT* for AAO before and after PLA modification was determined from RIfS. By comparing these *EOT* values, the volume fraction (fractional pore filling in %) can be obtained by applying Eq. 6.2.

$$\text{pore filling \%} = \frac{\Delta EOT_{\text{experimental}}}{\Delta EOT_{\text{theoretical}}} \quad \text{........................... (Eq. 6.2)}$$

where $\Delta EOT_{\text{experimental}}$, and $\Delta EOT_{\text{theoretical}}$, are the changes in *EOT* before and after the changing of void in the pores, respectively.

Enzymatic Degradation of PLA with Proteinase K

The AAO sensors coated with PLA were placed in a transparent polystyrene 6-well plate (Sarstedt, Nümbrecht, Germany) containing 2 mL of Tris-HCl buffer (pH 8.5) or proteinase K solutions (in Tris-HCl buffer, pH 8.5). For the *ex-situ* experiment, the samples were kept in the enzyme solution at 25 °C for 0, 15, 25, 35, 50, and 70 min. Prior to the RIfS measurement, the AAO sensors were washed with Milli-Q water, dried in a stream of nitrogen, and then kept in the desiccator at 5 mbar for 2 h. For *in-situ* RIfS measurements, the PLA-modified AAO sensor was placed in a homemade flow cell (volume 0.3 mL), and the proteinase K or Tris-HCl buffer solutions were introduced for 260 min.

Enzymatic Degradation of PLA with Bacterial Supernatant

One single colony of *P. aeruginosa* (PAO1 strain, (ATCC 15692)), provided by M. Laabei at the University of Bath, UK, Jenkins group, was transferred from an agar plate to a 15 mL reaction tube within 5 mL LB medium, then incubated under 200 rpm for 24 h at 37 °C. The absorbance (Abs) of the resulting bacterial suspension was measured by UV–Vis spectroscopy (see below) at λ = 600 nm in transparent 96-well plates containing 100 µL of the bacterial suspension. UV-Vis measurement was performed by Dr. Zhiyuan Jia, whereas the preparation of *P. aeruginosa* (PAO1) suspension and supernatant was conducted by M.Sc. Faria Afzal. The absorbance at λ (Abs_{600}) = 600 nm of *P. aeruginosa (PAO1)* grown for 24 h is shown in Figure 6.13. Afterwards, the bacterial suspension was diluted to Abs_{600} = 0.8 with fresh LB medium. The diluted bacterial suspension (200 µL) with Abs_{600} = 0.8 was transferred to 50 mL reaction tubes containing 20 mL of LB medium and further incubated under 200 rpm for another 24 h at 37 °C for the growth of *P. aeruginosa*. A 0.2 µm syringe filter (CME) was used to remove all the bacteria and the resultant sterile supernatant was used for further analysis. The AAO sensors coated with PLA were placed in a 6-well plate containing 2 mL sterile *P. aeruginosa* (PAO1) supernatant or LB medium for 360 min.

The AAO sensors were gently washed with LB medium and Milli-Q water and dried in a stream of nitrogen, and kept in the desiccator at 5 mbar for 2 h. For *in-situ* measurements (sterile *P. aeruginosa* (PAO1) supernatant or LB medium), the same protocol for proteinase K was followed except for the incubation time.

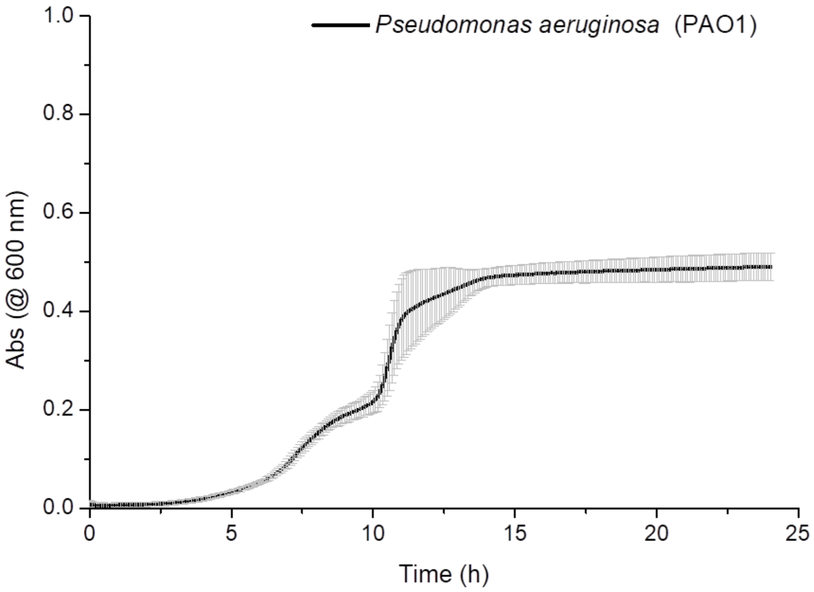

Figure 6.13: *Bacterial growth curve of P. aeruginosa (PAO1) grown at 37 °C, 200 rpm, for 24 h. The error bars indicate standard deviation (n=3 technical replicates: wells filled with bacterial cultures). This figure was reproduced with permission from reference [16]: Alhusaini, Q.; Scheld, W. S.; Jia, Z.; Das, D.; Afzal, F.; Müller, M.; Schönherr, H. Bare Eye Detection of Bacterial Enzymes of P. aeruginosa with Polymer Modified Nanoporous Silicon Rugate Filters. Biosensors* ***2022****, 12 (12), 1064. Copyright 2014. MDPI.*

UV−Visible Spectroscopy

UV−Vis spectroscopy measurements were carried out on a microplate reader (Tecan SAFIRE, Tecan, Switzerland) at 25 °C. The absorbance of the cultured bacterial suspension at 600 nm was recorded using a 96-well plate (transparent, polystyrene, flat bottom, Sarstedt, Germany) as a sample holder with a clear view seal sealer (Greiner Bio-One, Austria).

6.7 References

---

[1] Li, S.-J.; Xia, N.; Yuan, B.-Q.; Du, W.-M.; Sun, Z.-F.; Zhou, B.-B. A Novel DNA Sensor Using a Sandwich Format by Electrochemical Measurement of Marker Ion Fluxes across Nanoporous Alumina Membrane. *Electrochimica Acta* **2015**, *159*, 234–241. https:// doi.org/10.1016/ j.electacta.2015.02.010.

[2] Santos, A.; Kumeria, T.; Losic, D. Nanoporous Anodic Aluminum Oxide for Chemical Sensing and Biosensors. *TrAC Trends in Analytical Chemistry* **2013**, *44*, 25–38. https://doi.org/10.1016/j.trac.2012.11.007.

[3] Choma, P.; Bazin, I.; Cerutti, M.; Vena, A.; Sorli, B. Capacitive Immunosensor Based on Grafted Anodic Aluminum Oxide for the Detection of Matrix Metalloproteinase 9 Found in Chronic Wounds. *Analytical Biochemistry* **2023**, *678*, 115282. https://doi.org/10.1016/j.ab.2023.115282.

[4] Krismastuti, F. S. H.; Bayat, H.; Voelcker, N. H.; Schönherr, H. Real Time Monitoring of Layer-by-Layer Polyelectrolyte Deposition and Bacterial Enzyme Detection in Nanoporous Anodized Aluminum Oxide. *Analytical Chemistry* **2015**, *87* (7), 3856–3863. https://doi.org/10.1021/ac504626m.

[5] Escosura-Muñiz, A. de la; Ivanova, K.; Tzanov, T. Electrical Evaluation of Bacterial Virulence Factors Using Nanopores. *ACS Applied Materials & Interfaces* **2019**, *11* (14), 13140–13146. https://doi.org/10.1021/acsami.9b02382.

[6] Tücking, K.; Grützner, V.; Unger, R. E.; Schönherr, H. Dual Enzyme-Responsive Capsules of Hyaluronic Acid-block-Poly(Lactic Acid) for Sensing Bacterial Enzymes. *Macromolecular Rapid Communications* **2015**, *36* (13), 1248–1254. https://doi.org/ 10.1002/marc.201500076.

[7] Kumeria, T.; Kurkuri, M. D.; Diener, K. R.; Parkinson, L.; Losic, D. Label-Free Reflectometric Interference Microchip Biosensor Based on Nanoporous Alumina for Detection of Circulating Tumour Cells. *Biosensors and Bioelectronics* **2012**, *35* (1), 167–173. https://doi.org/10.1016/j.bios.2012.02.038.

[8] Shi, K.; Ma, Q.; Su, T.; Wang, Z. Preparation of Porous Materials by Selective Enzymatic Degradation: Effect of in Vitro Degradation and in Vivo Compatibility. *Scientific Reports* **2020**, *10* (1). https://doi.org/10.1038/s41598-020-63892-x.

[9] Williams, D. F. Enzymic Hydrolysis of Polylactic Acid. *Engineering in Medicine* **1981**, *10* (1), 5–7. https://doi.org/10.1243/emed_jour_1981_010_004_02.

---

[10] Seok, J. H.; Enomoto, Y.; Iwata, T. Synthesis of Paramylon Ester-Graft-PLA Copolymers and Its Two-Step Enzymatic Degradation by Proteinase K and β-1,3-Glucanase. *Polymer Degradation and Stability* **2022**, *197*, 109855. https://doi.org/10.1016/j.polymdegradstab.2022.109855.

[11] Chen, J.-T.; Zhang, M.; Russell, T. P. Instabilities in Nanoporous Media. *Nano Letters* **2007**, *7* (1), 183–187. https://doi.org/10.1021/nl0621241.

[12] Chen, J.-T.; Wei, T.-H.; Chang, C.-W.; Ko, H.-W.; Chu, C.-W.; Chi, M.-H.; Tsai, C.-C. Fabrication of Polymer Nanopeapods in the Nanopores of Anodic Aluminum Oxide Templates Using a Double-Solution Wetting Method. *Macromolecules* **2014**, *47* (15), 5227–5235. https://doi.org/10.1021/ma500568j.

[13] Zielinski, J. M.; Duda, J. L. Predicting Polymer/Solvent Diffusion Coefficients Using Free-volume Theory. *AIChE Journal* **1992**, *38* (3), 405–415. https://doi.org/10.1002/aic.690380309.

[14] Pasquali, M.; Liang, J.; Shivkumar, S. Role of AAO Template Filling Process Parameters in Controlling the Structure of One-Dimensional Polymer Nanoparticles. *Nanotechnology* **2011**, *22* (37), 375605. https://doi.org/10.1088/0957-4484/22/37/375605.

[15] Dordi, B.; Schönherr, H.; Vancso, G.J. Reactivity in the Confinement of Self-Assembled Monolayers: Chain Length Effects on the Hydrolysis of Self-Assembled Monolayers of N-Hydroxy-Succinimide Ester Disulfides of Gold. *Langmuir* **2003**, *19*, 5780-5786. https://doi.org/10.1021/la0343066.

[16] Alhusaini, Q.; Scheld, W. S.; Jia, Z.; Das, D.; Afzal, F.; Müller, M.; Schönherr, H. Bare Eye Detection of Bacterial Enzymes of *Pseudomonas aeruginosa* with Polymer Modified Nanoporous Silicon Rugate Filters. *Biosensors* **2022**, *12* (12), 1064. https://doi.org/10.3390/bios12121064.

Chapter 7. Fabrication and Characterization of PSi and PSi Rugate Filters (pSiRF) and their Modification with Polymers

7.1 Introduction

Porous silicon (pSi) and porous silicon Rugate Filter (pSiRF) have become attractive materials for biosensing due to their structural properties, such as the high surface area and controllable structure coupled with suitable optical properties[1,2]. For instance, sensing with pSiRF exploits both the large internal surface area and the photonic properties of these nanomaterials, making it a suitable material platform in many sensing protocols. In this Chapter, pSiRF was investigated as a photonic material in conjunction with a biodegradable polymer to detect bacteria via sensing of particular bacterial enzymes.

The synthesis of pSi can be achieved by electrochemical etching of Si in hydrofluoric acid (HF). The desirable structures (i.e., the pore diameter, pore length, porosity) of pSi depend on the synthesis conditions, such as the concentration of HF, applied current, resistivity of the Si, and type of doping (N-type or P-type). For instance, increasing the applied current leads to an increase in the porosity of pSi[3,4,5]. The latter is an essential factor for fabricating pSi photonic structures, such as pSiRF[6].

In this Chapter, the synthesis of pSi/pSiRF substrates is described. Starting with the etching of pSi, the etching parameters, such as applied electric current density and etching time, are discussed. Furthermore, the period time, the number of cycles, and the offset current density, critical parameters in the synthesis of pSiRF, were also investigated. The pore diameter and pore length of the fabricated samples were demonstrated and measured by field emission scanning electron microscope (FESEM) and reflectometric interference spectroscopy (RIfS). Finally, the modification of the nanomaterials with a known bacterial enzyme-labile polymer is addressed.

7.2 Fabrication and Characterization of PSi and PSiRF

Fabrication of PSi

The applied electric current density and etching time are two critical parameters that influence the structures of pSi[7,8]. To evaluate the effect of these two parameters, a series of pSi samples were prepared. Firstly, three current densities (15, 55, and 75 mA cm^{-2}) were applied to fabricate three sets of porous silicon whose structures were examined by FESEM. Figure 7.1a-c represents the top views of these samples. The FESEM images for the same sample show that the pores have different diameters and circularity. Furthermore, the pore diameters for those three samples are also different.

An increase in pore size was observed with increasing applied current density. A similar observation was also reported in the literature[9]. It was also seen that the pores of pSi are not uniform in terms of their diameters, while they are typically uniform in AAO[10]. Figures 7.1 d-f show that the pore sizes (equivalent diameters) in pSi were 12 ± 4, 48 ± 5, and 63 ± 6 nm when the applied current densities were 15 , 55, and 75 mA cm^{-2}, respectively.

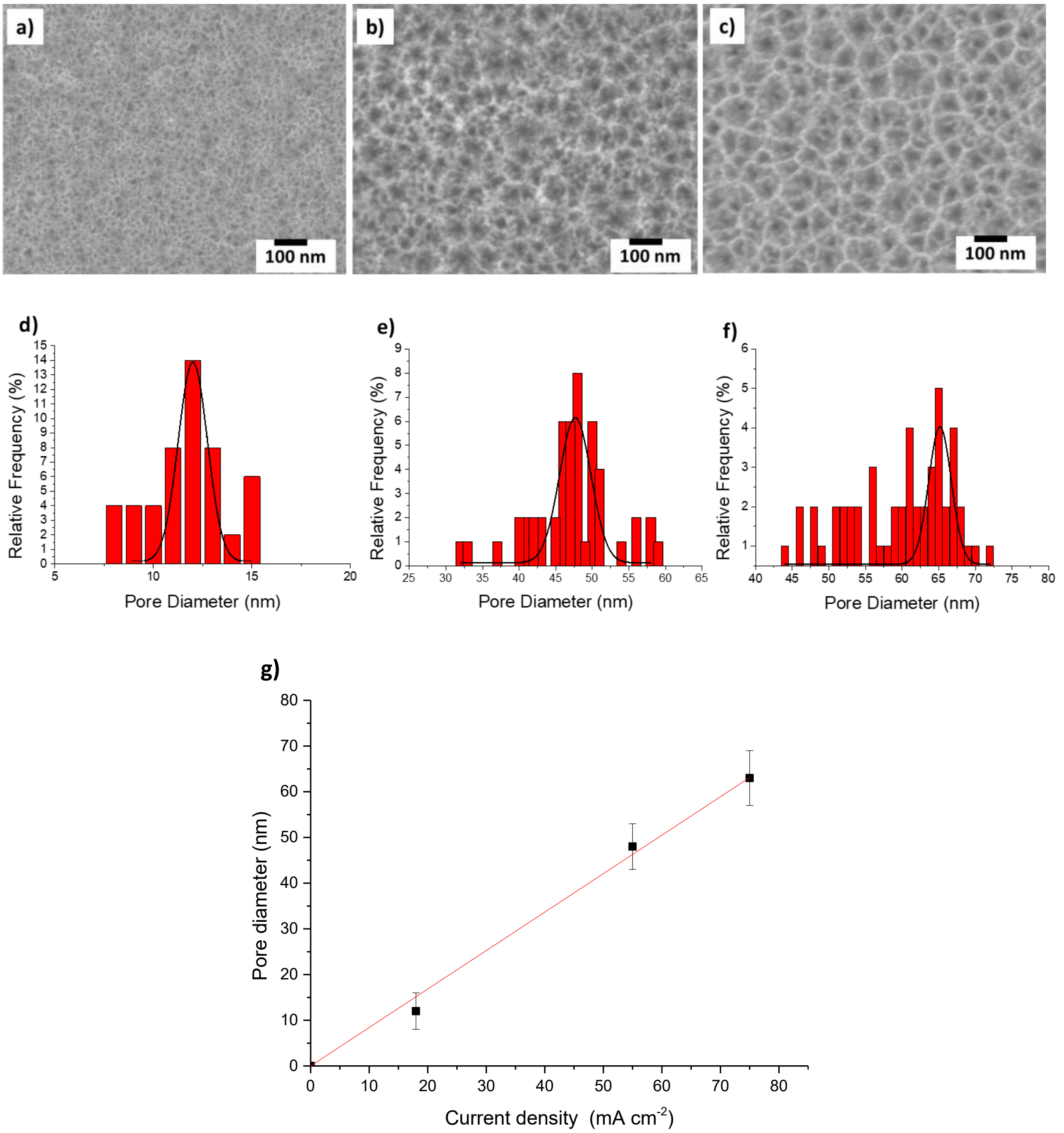

Figure 7.1: *FESEM images of top views of prepared pSi at current densities of a) 15 mA cm^{-2}, b) 55 mA cm^{-2} and c) 75 mA cm^{-2}, d-f) Histograms of pores diameter, and g) Linear fitted graph between mean pore diameter of pSi and applied current density. The error bars are the standard deviation (n=3). The solid line corresponds to a linear least squares fit of 0 to 75 mA cm^{-2} revealing a slope of 0.84 nm mA^{-1} cm^{-2}.*

Figure 7.2 a-c depicts the cross-sectional FESEM images of the fabricated pSi after 60, 120, and 240 sec of etching at a current density of 55 mA cm^{-2}. The pores were grown perpendicularly in the silicon sample from top to bottom, as seen in Figure 7.2a-c. The longer duration of the etching increases the length of the pores. A smaller pore length of 2.18 ± 0.03 µm was obtained after 60 sec of etching in ethanol/HF, while an increased pore length (8.04 ± 0.03 µm) was achieved after 240 sec of etching. As shown in Figure 7.2d, the length of the pores was found to increase linearly with the etching time.

Huber and his group also found that the thickness of the pSi increased linearly with the etching time[11]. They reported a value of 0.011 µm sec^{-1}, less than the value reported in this Thesis. Numerous parameters, other than the etching time, must be considered to compare these values, such as the applied current density, HF concentration, and temperature. In Huber´s study, the current density was 12.5 mA cm^{-2}, which was smaller than ours by a factor of ~4 (55 mA cm^{-2}), also, they used a more concentrated HF solution. Additionally, and with unreported reaction temperature, the comparison may not be accurate unless the electrochemical etching of Si is performed in identical reaction conditions. The long pores produced with longer etching time showed a slight drift from the linearity due to the impact of mass transport in the longer pores, which slows down the etching of pSi[11].

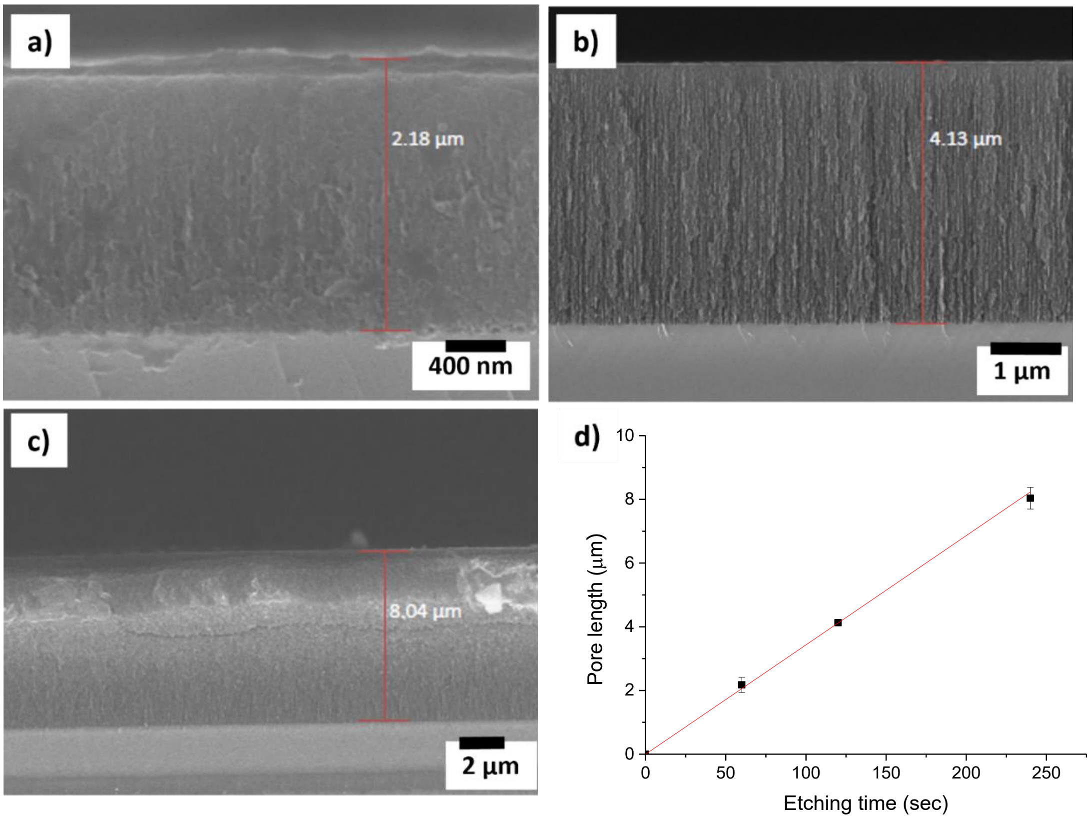

Figure 7.2: *FESEM cross-sectional images of pSi obtained by etching at 55 mA cm^{-2} of current density for a) 60 sec, b) 120 sec and c) 240 sec. d) Linear fitted graph between mean pore length of pSi and etching time. The error bars are the standard deviation (n=3). The solid line corresponds to a linear least squares fit of 0 to 240 sec, revealing a slope of 0.033 µm sec^{-1}.*

Fabrication of PSiRF

pSiRF was prepared via the electrochemical etching of p-type Si (<100>) wafers in ethanolic hydrofluoric acid by applying two current densities in a sinusoidal manner to produce a structure with periodic layers. Figure 7.3 shows the FESEM image of pSiRF, prepared at the minimum current density of 15 mA cm^{-2} and maximum current density of 50 mA cm^{-2} with a period of 7 sec and 100 repeats.

The pore length was 14.6 ± 0.5 µm, which was determined from the analysis of cross-sectional FESEM images (Figure 7.3a). The magnified image shown in Figure 7.3a revealed a periodic nanostructure with a spacing of 148 ± 3 nm, which was oriented perpendicular to the surface of the pSiRF. The total thickness of the pSiRF structure is consistent with the thickness of one layer (148 ± 3 nm), and the number of repeats (cycles) was 100.

However, the pSiRF is a photonic structure and has a band gap, which results in total reflection with a specific wavelength[2]. The peak position of this band gap at a normal incident angle defines the color of the pSiRF. Therefore, pSiRF with different colors can be produced by varying the number of repeating layers and applying current density and period time during the etching process.

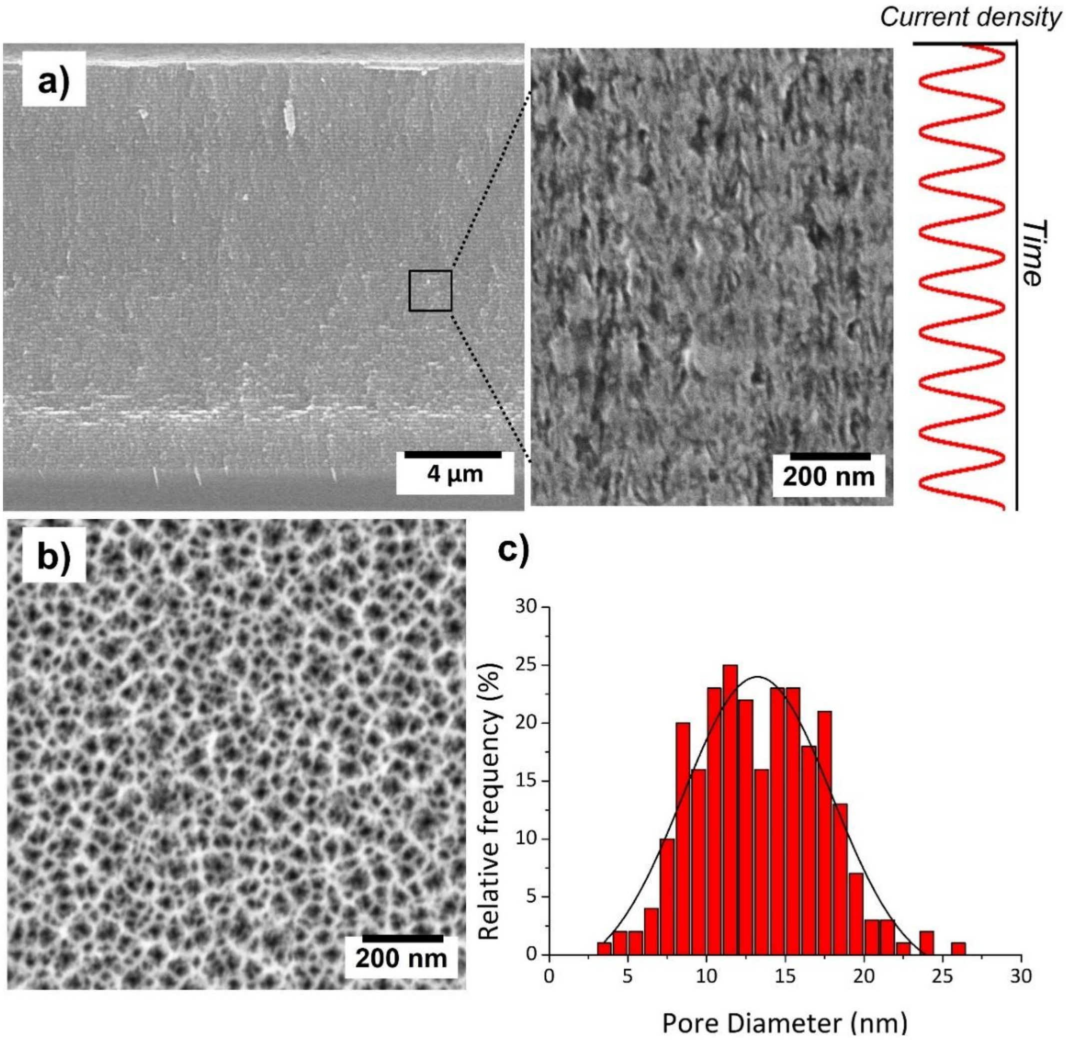

Figure 7.3: *SEM images of pSiRF with a current modulation of 15 – 50 mA cm^{-2} with a period time of 7 sec and 100 cycles. a) Cross-sectional FESEM image of the resulting pSiRF structure, the inset is a magnified image showing the periodic nanostructures along the pores. The schematic of the temporal current density profile corresponds to the data in the magnified image. b) Top view FESEM image of the sample; c) Histogram of pore sizes obtained by analyzing top view FE-SEM images of oxidized pSiRF with ImageJ software.*

The porosity of the pSiRF was also investigated. The pSiRF sample had a mean pore diameter of 12 ± 5 nm, which was determined from the top view of the FESEM image measured on the thermally oxidized pSiRF[12] (Figure 7.3b,c). This image shows nanopores that are randomly distributed across the surface. The average porosity was obtained by analyzing the FESEM image and additionally by the Spectroscopic Liquid Infiltration Method (SLIM)[13]. In SLIM, the effective optical thickness is measured by RIfS before and after injecting ethanol, which completely wets the surface and efficiently and completely fills the pores, infiltrates the pores, and displaces the air inside. The values of the porosity thus determined were 45 ± 5 % and 44 ± 4 % by FESEM and SLIM, respectively.

The influence of the above parameters on the generated structures was investigated. Firstly, the effect of the number of repeating layers on the position and width of the band gap peak was studied. A series of pSiRF were etched in 5, 15, 25, 50, 75, 100, and 150 cycles. The samples were then measured with RIfS and the interferograms were recorded (Figure 7.4). As shown in Figure 7.4, each spectrum showed a maximum value of reflectance at a particular wavelength, which is the characteristic peak of the pSiRF, whereas other peaks (patterns) belong to the Fabry-Pérot interference. The latter is because of the interference of reflected light at the air/pSi and the pSi/bulk Si interfaces.

The spectra show that the width of the maximum peak became narrower with the increasing number of etching cycles. The width of the maximum peak is related to the difference in refractive indices of the repeated layers (index contrast) and the number of these layers (number of cycles) within the pSiRF structure. The small peak width indicates a high-quality factor. The latter is recommended to enhance the sensor's performance[14]. The quality factor can be determined from the quotient of the peak position and the full width at half maximum (FWHM)[3].

It is anticipated that light can be transmitted less efficiently through the thicker porous silicon. Thus, the achievement of a narrow peak width is desired to enhance the sensitivity of pSiRF towards the sensing application.

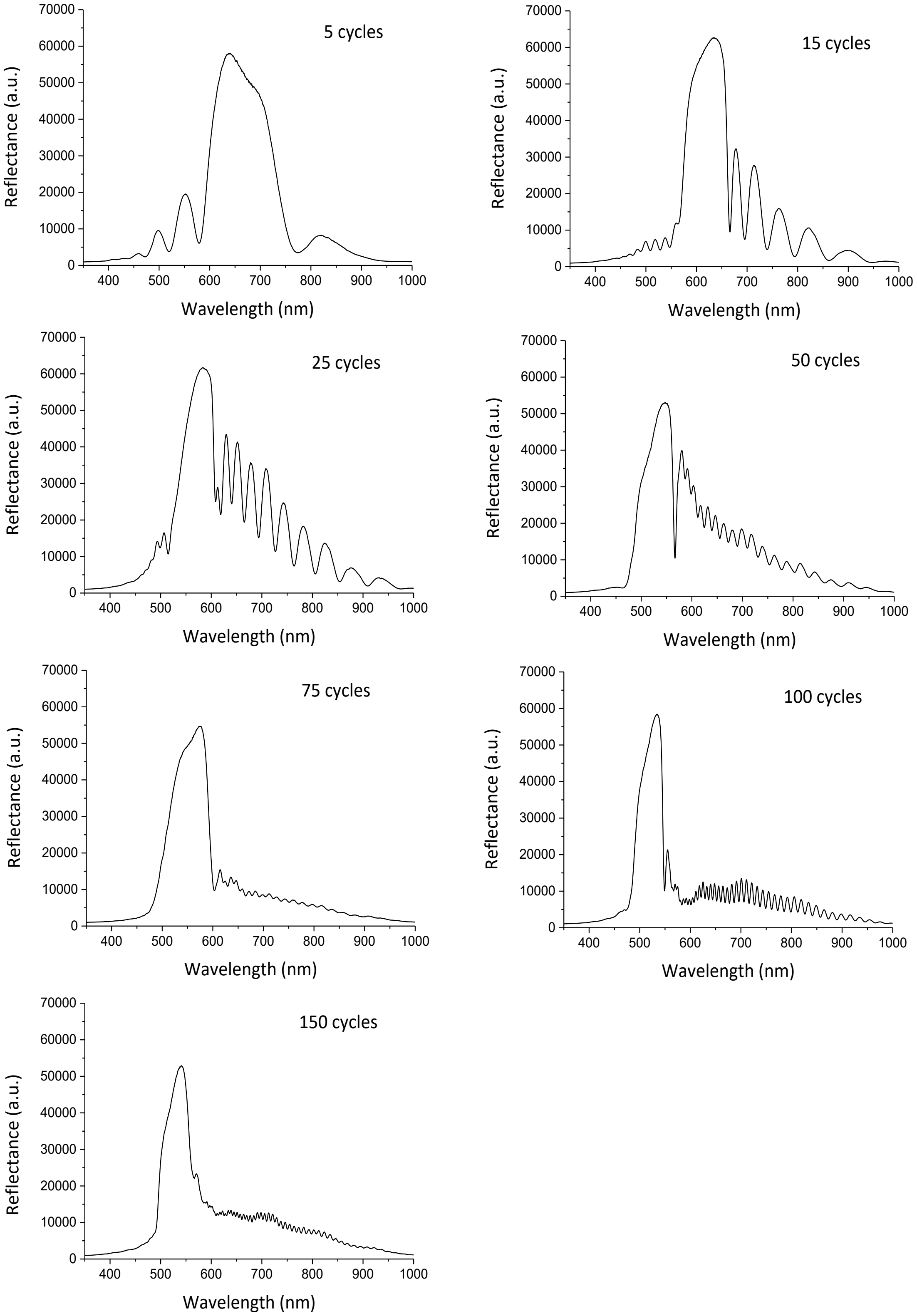

Figure 7.4: *RIfS spectra of pSiRF prepared by application of a sinusoidal current density-time profile (minimum current density: 15 mA cm^{-2} and maximum current density: 50 mA cm^{-2}) using 5, 15, 25, 50, 75, 100 and 150 cycles etching for 7 sec for each cycle (period time).*

The FWHM of the maximum peak for each sample described in Figure 7.4 was determined using Gaussian regression. Figure 7.5 shows that the determined FWHM of the maximum peak decreased with increasing cycles (from 5 to 150). Furthermore, the number of cycles beyond 100 caused an increase in FWHM. The increase in FWHM for the longer pores (prepared in 150 cycles) could be attributed to the mass transport limitation of the electrolyte solution into those pores, affecting the film's porosity and, consequently, the index contrast. Therefore, in this work, pSiRF sensors were prepared by etching a sinusoidal waveform with 100 cycles, providing the optimal quality factor for pSiRF sensors compared to the other sensors whose FWHM were shown in Figure 7.5. Moreover, partial dissolution of the pSi in the top could occur due to the longer exposure time to the HF, which affects the fabricated structure.

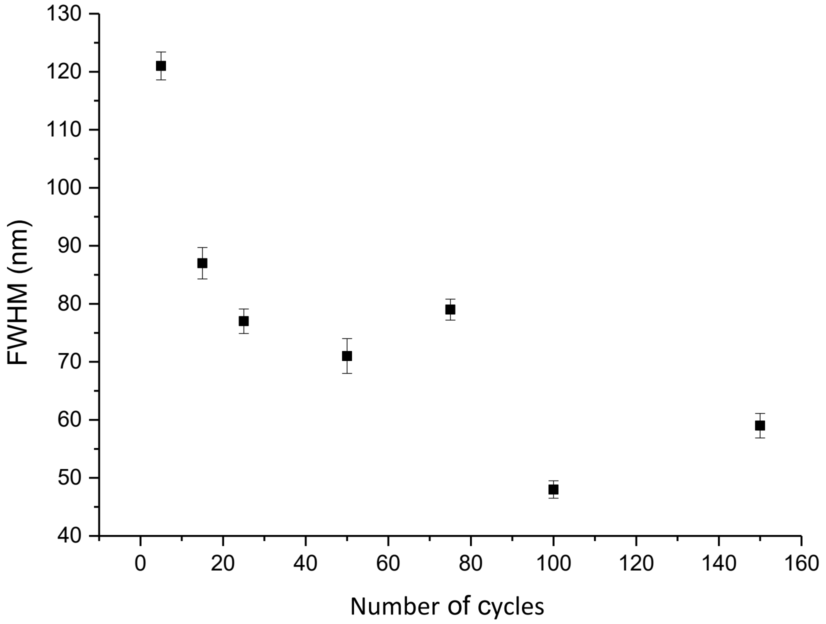

Figure 7.5: *Full-width half maximum (FWHM) of the maximum peak of pSiRF sensors determined from the spectra in Figure 7.4 versus the number of cycles. The errors were calculated as 3 × the standard deviation from the* Gaussian *fit of the curves.*

To study the effect of the current density on the optical properties of pSiRF, a series of pSiRF were fabricated at the current densities of 15, 30, and 45 mA cm^{-2}. The amplitude (the difference between the minimum and maximum currents) was kept constant during the fabrication of these samples; therefore, the variated offset is independent of a variation of the average current, which finally generates the change of the peak position. These fabricated structures were measured by RIfS, and the recorded spectra are shown in Figure 7.6a-c. The spectra show that the peak position of pSiRF was red-shifted with the increase of the offset current. The peak shifted from 500 to 690 nm when the offset current density varied from 15 to 45 mA cm^{-2}. Furthermore, it can be observed that the reflectance of those peaks increased along with the peak position. Li and coworkers investigated such observations on the prepared pSiRF at different current densities. They reported that the reflectance of the maximum peak was caused by the increase in the number of photons due to an increase in the thickness of the layer resulting from the application of higher current densities. Additionally, they stated that the reduction in photonic diffraction was observed at the higher peak positions[15]. It can also be seen in Figure 7.6a-c that a smoother peak of characteristic pSiRF was observed with a lower current density compared to the elevated current densities, which was also observed elsewhere[16].

Figure 7.6d reveals that the wavelength of the pSiRF was increased linearly with the increase of the offset current, where the change in the currents caused a change in porosity and, thus, in refractive index contrast in the pSiRF structure, which is consistent with the literature[17,18]. Furthermore, broader peaks were noticed for the larger pores (Figure 7.6e). As mentioned earlier in this Chapter, the change in the porosity of pSi leads to a change in the refractive index contrast within the structure. The latter and the discussed parameters that dominate the reflectivity led to a change in the peak width[19].

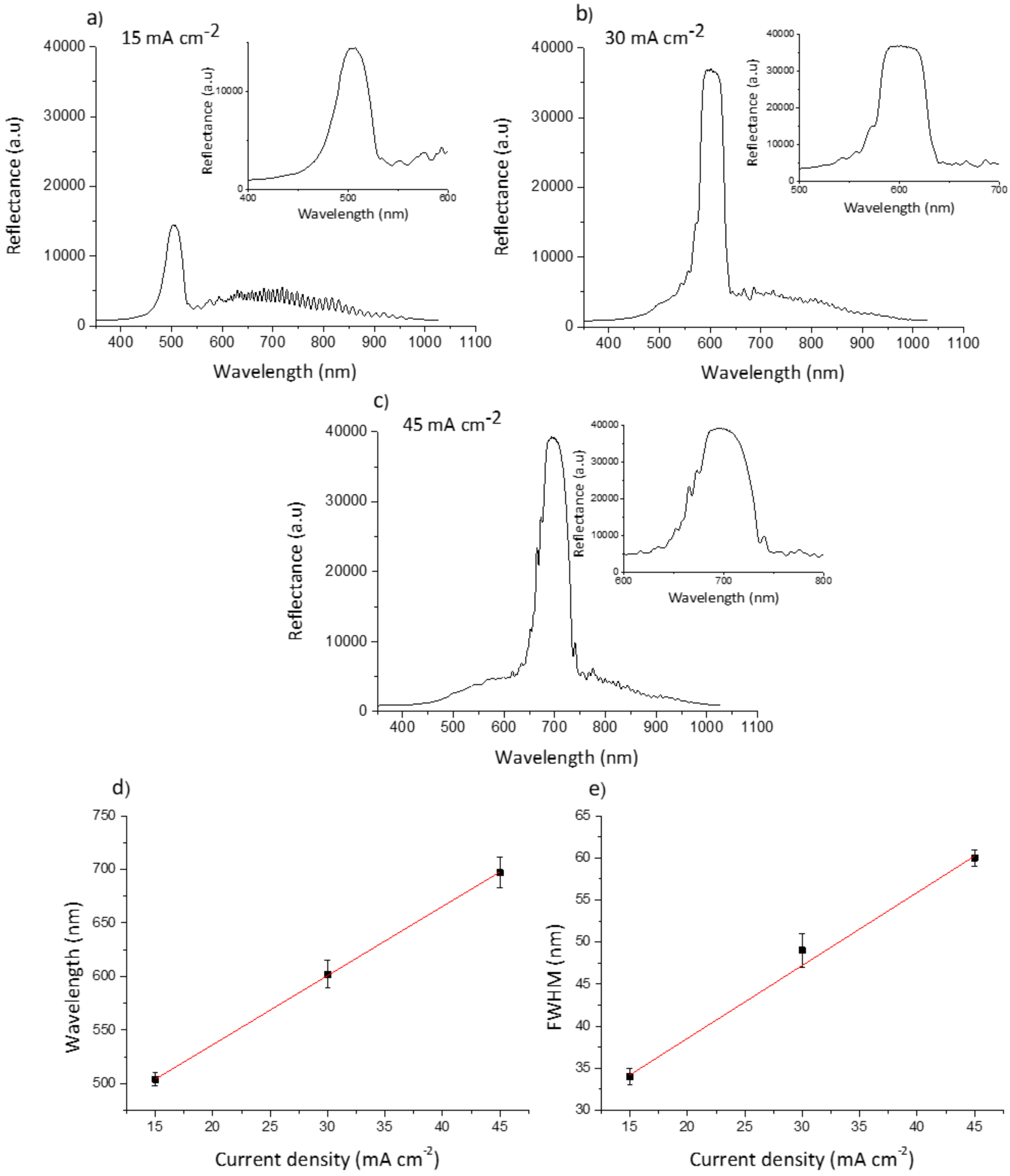

Figure 7.6: *RIfS spectra of oxidized pSiRF produced for 100 cycles with period time 7 sec at offset current density a) 15 mA cm^{-2}, b) 30 mA cm^{-2}, and c) 45 mA cm^{-2}. The insets are the magnified of the maximum peaks, d) Peak wavelength versus offset current. e) FWHM, obtained from the Gaussian fitting on the maximum peaks, versus offset current density. The errors were calculated as standard deviation from the* Gaussian *fit of the curves for three sets of samples.*

The effect of the period time in the sinusoidal current oscillation was also investigated. Therefore, pSiRF samples were fabricated in three different period times (7, 8, 9 sec). The single layer thickness in all three pSiRF samples was measured by FESEM. Figure 7.7 shows the corresponding FESEM images. It was observed that the thickness increased linearly with the period time, which is consistent with the literature[3]. The prepared pSiRF thickness for period 7 sec was 144 ± 5 nm, whereas 8 and 9 sec provided 174 ± 3 nm and 210 ± 6 nm thicker pSiRF, respectively.

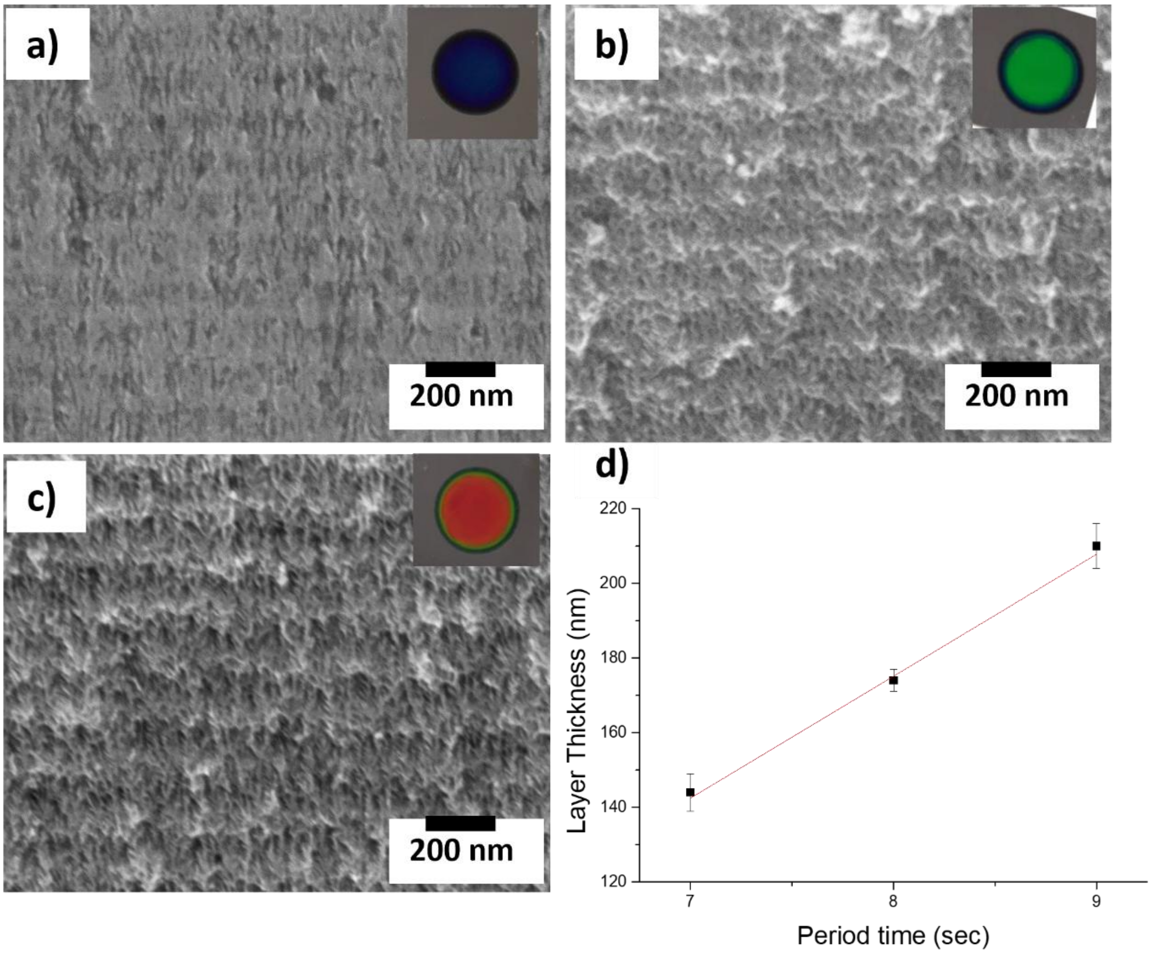

Figure 7.7: *FESEM cross-sectional images of pSiRF prepared by the application of a sinusoidal current density-time profile (minimum current density: 15 mA cm^{-2} and maximum current density: 50 mA cm^{-2}, a period of a) 7, b) 8 and c) 9 sec. The insets are photographs of pSiRF fabricated in periods of 7, 8, and 9 sec, respectively. d) Linear fitted graph between mean periodic layer thickness of pSi and period time (slope is 33 nm sec^{-1}). The error bars are the standard deviation (n=3).*

RIfS measurements were also performed for those samples. Figure 7.8a-c displays three RIfS spectra of the prepared pSiRF for a period time of 7, 8, and 9 sec. The pSiRF produced with a period time of 7 sec shows more intense Fabry-Pérot fringes than other samples. This can be explained by the difference in the total pSi film thickness, which leads to a low reflectance of the interference light at the air/pSi and pSi/bulk pSi interfaces. However, the central peak positions (photonic band gap), calculated with a Gaussian regression, exhibit a linear behavior when plotted versus period time (Figure 7.8d). This trend indicates that the red-shift in wavelength with increasing periods of time was due to an increase in the light pathway within the single layer. The RIfS spectra confirmed that the sample prepared for 7 sec had higher quality than others; therefore, it was utilized in further experiments.

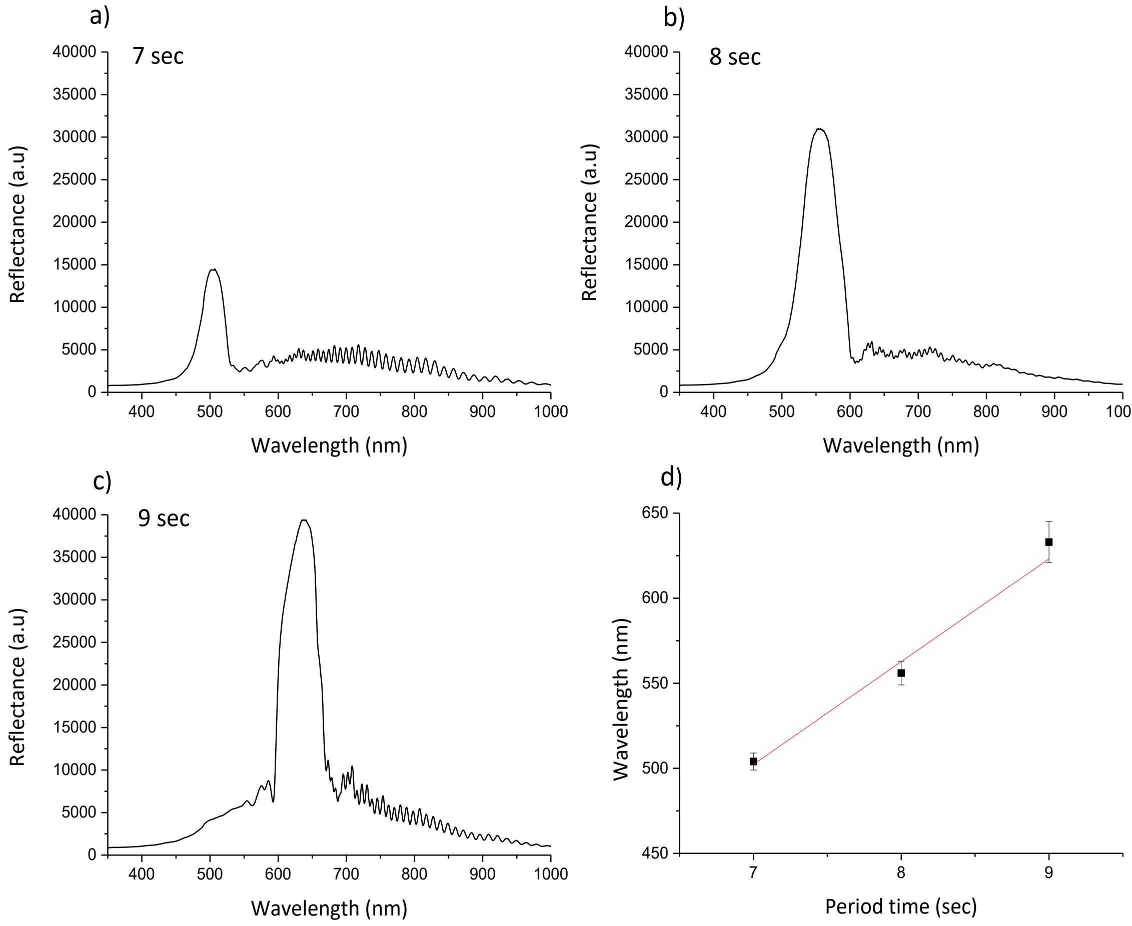

Figure 7.8: *RIfS spectra of dried pSiRF produced by application of a sinusoidal current density-time profile (minimum current density: 15 mA cm^{-2} and maximum current density: 50 mA cm^{-2}, a period of a) 7, b) 8 and c) 9 sec. d) Dependence of the peak position on period time, the red line represents the linear fit, revealing the slope of 60 nm sec^{-1}). The error bars are the standard deviation (n=3).*

7.3 Stabilization of PSiRF

The freshly prepared pSi and other pSi structures, such as pSiRF, are highly reactive due to the presence of Si-H and Si-Si bonds[20]. Both of these species are reducing agents and can reduce water. Moreover, in the case of Si-Si bonds, new Si-H and Si-O bonds can be generated as a result of the reduction reaction. In this case, the dissolution of pSi can occur in aqueous solutions and subsequently reduce the sensitivity or stability of the pSi sensor[21]. Several approaches have been developed to stabilize the freshly etched pSi. These include thermal, ozone, or chemical treatments. The most common method is thermal oxidation, in which the Si-Si and Si-H bonds are stabilized at high temperatures[22].

In this Thesis, all pSiRF sensors were thermally oxidized at 600°C for 1 h in the air, as it was exhibited to be a suitable protocol to stabilize pSi for biological applications[23,24]. The RIfS spectra in Figure 7.9 show an apparent blue shift of the peak position from 570 to 513 nm due to the thermal treatment on the optical properties of the freshly prepared pSiRF. This blue shift of 57 nm is due to the transformation of Si to SiO_2, which reduces the refractive index from 3.5 for Si to 1.4 for amorphous SiO_2[25]. Therefore, the shift in the reflectance spectrum upon thermal treatment was consistent with the formation of SiO_2, which agrees with previous studies[26,27].

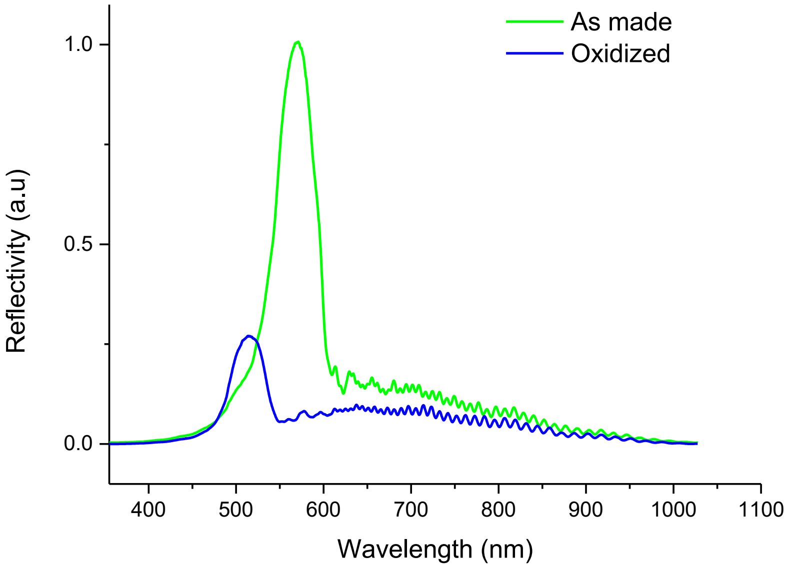

Figure 7.9: *RIfS spectra of pSiRF measured in air at 23 °C before (green) and after (blue) thermal oxidation in air at 600 °C for 1 h.*

7.4 Modification of pSiRF with PLA by Casting Method

pSiRF pores were filled with PLA by placing a droplet of PLA solution prepared in chloroform onto the surface of the sensors, which was allowed to evaporate. Figure 7.10a shows the FESEM of the pristine pSiRF exhibiting the open pores with a mean diameter of 12 ± 5 nm. The deposition of the PLA led to covering the top side of the pSiRF surface, and no pores could be observed (Figure 7.10b).

As can be seen in Figure 7.10c, the PLA film covering the pores was successfully removed by cleaning the top surface with chloroform-soaked tissue, and most of the pSiRF pores were opened.

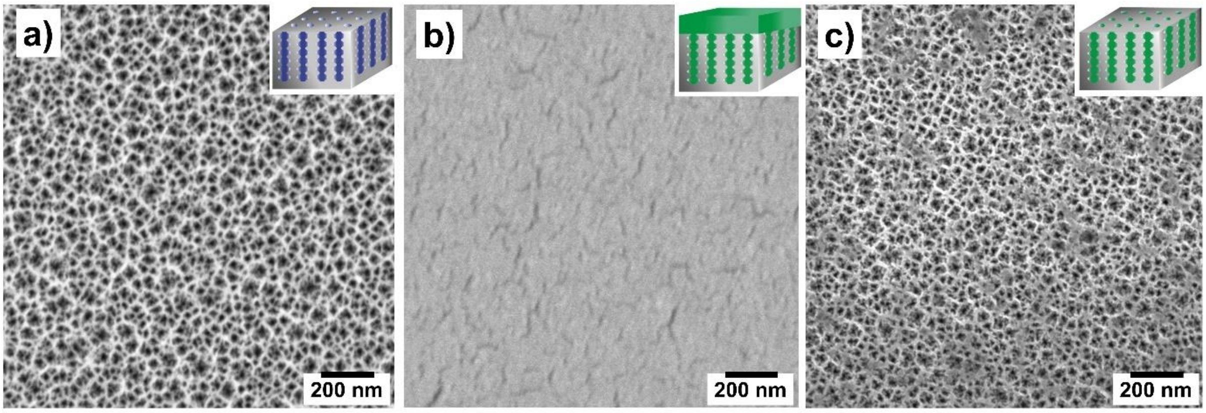

Figure 7.10: *FESEM images of: a) neat pSiRF, b) pSiRF after PLA deposition, and c) PLA-coated pSiRF after cleaning of the top surface with a chloroform-soaked tissue. The insets show schematics of the pSiRF sensors before and after PLA deposition/removal of PLA.*

Similarly, the PLA-filled pSiRF nanopores exhibited a shift in the RIfS spectra compared to the neat air-filled pSiRF sensors. The position of the peak in the reflectance spectrum of the empty (air-filled, before PLA deposition) pSiRF was centered at 513 nm (Figure 7.11). The fringes in the reflectivity spectrum were caused by the interference of reflected light at the Si-SiO_2 (bottom side) and air-SiO_2 (top side) interfaces of the pSiRF. After the PLA deposition, the peak (blue) was red-shifted by 37 ± 2 nm due to an increase in the effective refractive index (n_{eff}) of the pSiRF.

The n_{eff} values of the empty and PLA-modified pSiRF can be determined using the Bragg–Snell law (Eq. 7.1)[28].

$$m\lambda = 2L\sqrt{n^2_{eff} - \sin^2\theta} \qquad \text{.......................................} \text{ (Eq. 7.1)}$$

where m is the interference order, λ is the wavelength, L is the periodic thickness obtained from the FESEM images (148 nm), and θ is the incidence angle of light with respect to the normal (0°).

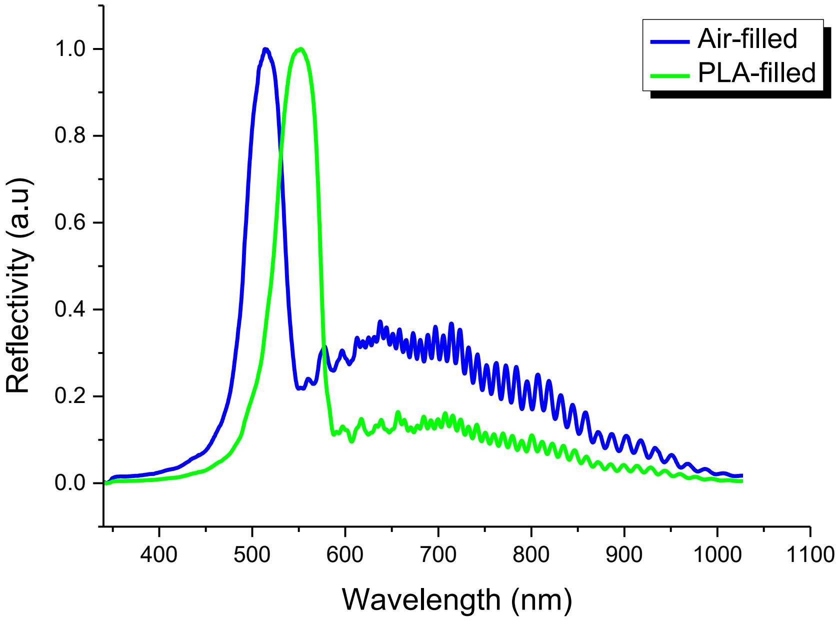

Figure 7.11: *RIfS spectra dried pSiRF: The blue spectrum represents air-filled pSiRF, and the green spectrum represents PLA-filled pSiRF.*

Knowing the peak position before and after PLA deposition in pSiRF shown in Figure 7.11, the values of n_{eff} were determined to be 1.73 and 1.96 for empty pSiRF (air-filled) and PLA-filled pSiRF, respectively. The increase of n_{eff} after PLA infiltration in pSiRF is due to the replacement of air, which has a small refractive index (1.000)[29], with the polymer PLA, which possesses a high refractive index (1.459)[30]. The Bruggeman effective-medium approximation was used to predict how much the spectral position of the stop-band peak would shift if the polymer infiltrates the pores of pSiRF (Eq. 7.2)[31].

$$P\,\frac{n^2_{void} - n^2_{eff}}{n^2_{void} + 2n^2_{eff}} + (1 - P)\,\frac{n^2_{SiO_2} - n^2_{eff}}{n^2_{SiO_2} + 2n^2_{eff}} = 0 \quad \text{..........................} \quad \text{(Eq.7.2)}$$

Where P is the porosity, n_{void} is the refractive index of the medium filling the pores, n_{SiO_2} is the refractive index of the SiO_2 that makes up the porous structure[3].

If the pores are completely occupied with PLA, the peak of empty pSiRF shifts from 513 to 580 nm, according to Eq. 7.1. However, the observed shift of 37 nm in the reflectance peak in the PLA-modified pSiRF is smaller; hence, the PLA did not fill the pores completely; the pore filling was 55 %. It is worth mentioning that the reflectance spectrum of both PLA-modified pSiRF and empty (air-filled) pSiRF did not show any sign of additional peaks (stop bands) or superposition of RIfS response. Additional or multiple peaks in the reflectance spectrum can appear if a modified pSiRF exists as a biphasic system. This refers to systems in which PLA fully occupies a part at the bottom or top of pores, and the rest remains air-filled[32].

Energy-dispersive X-ray spectroscopy (EDX) measurements were also conducted to assess the polymer penetration into pSiRF. Several positions across the PLA-filled pores were measured by the point mode of EDX. Points of the carbon/Si signal ratio demonstrate that PLA was loaded successfully into the pores (Figure 7.12). It can also be seen that the major amount of PLA was located close to the top side of the pSiRF, which was expected due to the evaporation of the polymer solution leaving the PLA blocking the mouth of the pores, sequentially, a non-uniform modification of pores with PLA. It is worth mentioning that the carbon signal in the spectra came only from PLA because the neat Si did not show any carbon signal. The last assumption was proven by measuring neat pSiRF by EDX. The data showed no carbon signal in the spectrum, as shown in Figure 7.13.

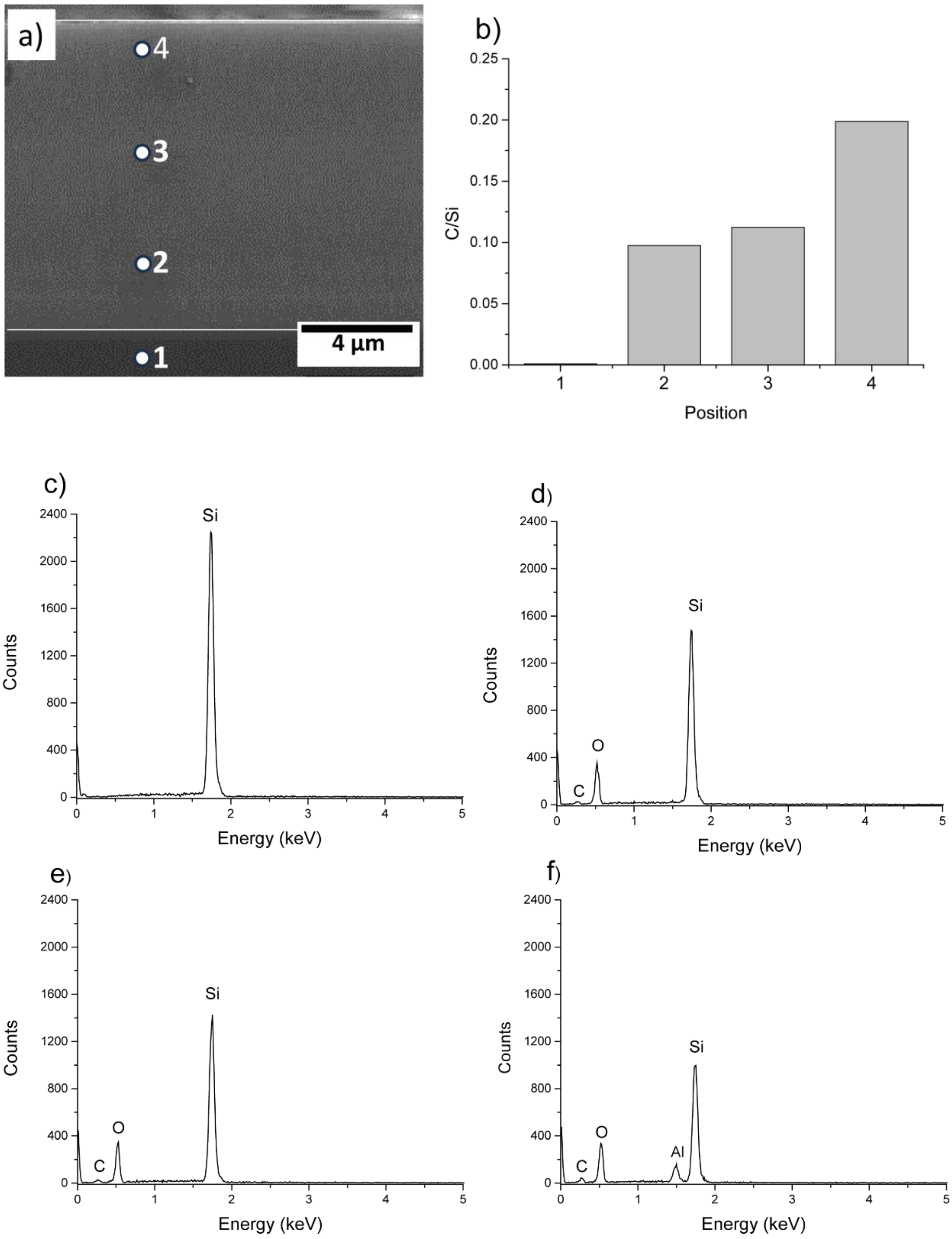

Figure 7.12: *a) Cross-sectional FESEM image of PLA-modified pSiRF showing points (1-4) where EDX was measured, b) measured EDX carbon/Silicon ratio obtained from a. c-f) EDX spectra of points 1-4 in SEM image, respectively.*

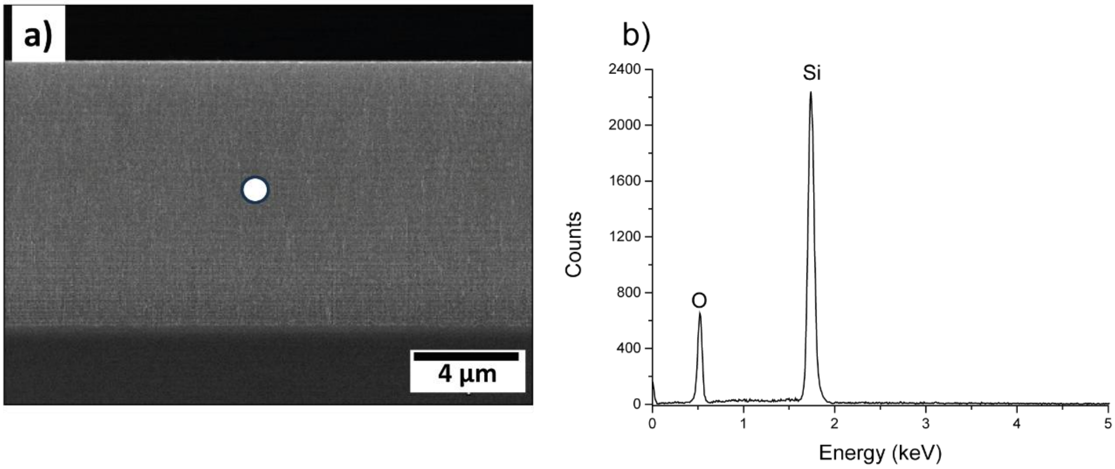

Figure 7.13: *a) Cross-sectional FESEM image of neat pSiRF showing one point where EDX was measured, b) EDX spectrum obtained from a.*

The pore filling was also determined by thermogravimetric analysis (TGA). The PLA decomposition in the nitrogen atmosphere began at around 250 °C before a rapid decomposition occurred. Almost all of the PLA (bulk) was degraded below 410 °C (Figure 7.14a), whereas the PLA inside the pores, the decomposition, i.e., mass loss, continued beyond 410 °C (Figure 7.14b). This scenario can be explained by the limitation of mass transport of thermally degraded products inside the pores compared to the degradation of pure PLA. Based on the TGA data, the pore filling was 54 ± 14 %, which is identical to the value determined by RIfS (55 %), as discussed previously in this Chapter.

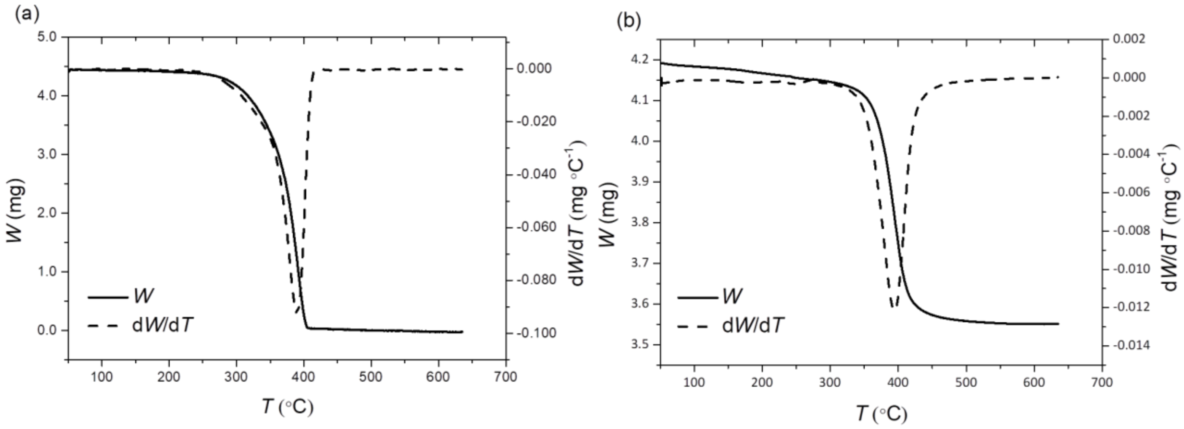

Figure 7.14: *TGA thermograms of PLA a) in bulk, b) inside the pores of pSiRF with an average pore diameter of 12 ± 5 nm and pore length of 14.6 ± 0.5 µm. The heating ramp was conducted from 50 to 650 °C with a heating rate of 10 °C per minute in a 15 mL min^{-1} nitrogen gas flow. The terms W and dW/dT are the mass and the mass derivative, respectively.*

7.5 Conclusion

In this Chapter, the fabrication of pSi and pSiRF was performed. The etching process was optimized to obtain the desired structures. The electrochemical etching of pSi/pSiRF was carried out in an HF/ethanol mixture (1:2 (v/v)). Pore diameters scaled linearly with the current densities from 12 ± 4 to 63 ± 6 nm. The length of the pores increased linearly with the etching time up to 8.04 ± 0.03 µm. pSiRF sensors were successfully fabricated with a small FWHM of the stop-band peak, which was achieved with 100 cycles. Similarly, a narrow peak with a small FWHM in the RIfS spectrum was obtained with a small current density (minimum current density in the sinusoidal mode), which enhances the sensitivity of the pSiRF. The period time on the pSiRF structure had a prominent effect on the peak position; a red shift was recorded when the samples were etched at a higher period. Optimal parameters were applied to the pSiRF synthesis used in this Thesis. The minimum and maximum current densities were 15 and 50 mA cm^{-2}, respectively, with a 7 sec period time and repeated 100 times. All the pSiRF samples were stabilized by thermal treatment in the air. Finally, the PLA was loaded into the pores of pSiRF using the casting method. The EDX, RIfS, and TGA data revealed that the polymer was successfully loaded inside the pores. The pSiRF samples loaded with PLA were further utilized in Chapter 8 for the detection of fungal and bacterial enzymes.

7.6 Materials and Methods

Chemicals, materials, and instruments, which have already been mentioned in Chapter 4, will not be stated here again.

Materials

P-type silicon wafers (<100> orientation, resistivity 0.01–0.02 mΩ cm, Siegert Wafer), Hydrofluoric acid (48 % aqueous, VWR Chemicals), ethanol absolute (99.8 %, VWR).

Fabrication of PSi and PSiRF

The pSi and pSiRF samples were etched into highly doped Si wafers (P-type) by an anodic electrochemical method[33]. A controllable current source (digital source meter model 2400, Keithley, USA) was used to supply the desired current. The Si wafer was washed with ethanol and Milli-Q water and then dried in a stream of nitrogen. Afterwards, the pre-cleaned Si wafers were oxidized using a UV/ozone cleaner (Procleaner^{TM}, BIO FORCE, UK). The electrochemical etching was performed in a homemade Teflon cell with a 2 × 2 cm^2 piece of Si used as anode and a circular Pt wire immersed in the HF solution (see below) acted as a cathode (*Caution: HF is highly toxic and contact with the skin must be prevented. Adequate safety measures must be taken*)[3]. To remove the surface contaminations, an initial sacrificial etch was performed at constant current density (55 mA cm^{-2}) for 30 sec in HF/EtOH 1:2 (v/v)[34]. Afterwards, the sacrificial layer was dissolved by dipping the specimens into 0.5 M aqueous sodium hydroxide (NaOH) solution, followed by rinsing with Milli-Q water and ethanol. The pSi samples were prepared at 25, 55, and 75 mA cm^{-2} for 60, 120, and 240 sec.

In contrast, the pSiRF films were prepared by application of a sinusoidal current density-time profile (minimum current density: 15 mA cm^{-2} and maximum current density: 50 mA cm^{-2}, a period of 7 sec was repeated 100 times). Then, the sensors were thoroughly rinsed with ethanol and dried in a stream of nitrogen. Freshly etched sensors were stored under vacuum (≤ 10 mbar, 4 h). Next, the sensors were thermally oxidized at 600 °C for 1 h in the air in a muffle furnace (Thermo Fisher, USA) with a heating ramp of 10 °C min^{-1} from/to ambient for both the heating and cooling phases[35]. The thermal treatment of the sensors was performed by M.Sc. Jamal N. M. Aman.

Modification of PSiRF with PLA by Solvent Casting Method

The pre-oxidized pSiRF was modified with PLA by the solvent casting method (also called the droplet evaporation method). At first, 150 µL of PLA solution (4 wt% in chloroform) was dropped from a glass pipette onto a pSiRF sample, followed by drying at ambient temperature (≈ 23 °C) for 4 h. The PLA layer, which remained on the top of the pSiRF sensor, was removed by carefully wiping the sensor surface 3 times with a paper tissue (Kimberly-Clark) soaked with chloroform under a fume hood. Then, the PLA-modified pSiRF was dried in a stream of nitrogen and was kept in a desiccator at 5 mbar for 2 h. Finally, it was heated on a hot plate at 70 °C in the ambient atmosphere for 1 min and allowed to cool to ambient temperature.

7.7 References

---

[1] Macias, G.; Ferré-Borrull, J.; Pallarès, J; Marsal, L. 1-D Nanoporous Anodic Alumina Rugate Filters by Means of Small Current Variations for Real-time Sensing Applications. *Nanoscale Research Letters* **2014**, 9 (1), 315. https://doi.org/10.1186/1556-276X-9-315.

[2] Janshoff, A.; Dancil, K.-P. S.; Steinem, C.; Greiner, D. P.; Lin, V. S.-Y.; Gurtner, C.; Motesharei, K.; Sailor, M. J.; Ghadiri, M. R. Macroporous p-Type Silicon Fabry−Perot Layers. Fabrication, Characterization, and Applications in Biosensing. *Journal of the American Chemical Society* **1998**, 120 (46), 12108–12116. https://doi.org/10.1021/ja9826237.

[3] Sailor, M.J. Porous Silicon in Practice: Preparation, Characterization and Applications, First Edition, **2012**, *Wiley-VCH*, Weinheim, Germany.

[4] Lang, W.; Steiner P.; Sandmaier H. Porous silicon: A Novel Material for Microsystems. *Sensors and Actuators A: Physical* **1995***,* 51 (1), 31–36. https://doi.org/10.1016/0924-4247(95)01066-1.

[5] Li; M.; Hu, M.; Zeng, P.; Ma, S.; Yan, W.; Qin, Y. Effect of Etching Current Density on Microstructure and NH_3-sensing Properties of Porous Silicon with Intermediate-Sized Pores. *Electrochimica Acta* **2013**, 108, 167–174. https://doi.org/10.1016/j.electacta.2013.06.106.

[6] Li, S.; Hu, D.; Huang, J.; Cai, L. Optical Sensing Nanostructures for Porous Silicon Rugate Filters. *Nanoscale Research Letters* **2012***,* 79 (7). https://doi.org/10.1186/1556-276X-7-79

[7] Diaz, D. C.; Osmanski, M.; Guan, H.; Das, B. An Improved Fabrication Technique for Porous Silicon. *Review of Scientific Instruments* **1993**, 64 (2), 507–509. https://doi.org/10.1063/1.1144223.

[8] Gong, X.; Bustillo, J.; Blanc, L.; Gautier, G. FEM Simulation on Elastic Parameters of Porous Silicon with Different Pore Shapes. *International Journal of Solids and Structures* **2020**, 190, 238–243. https://doi.org/10.1016/j.ijsolstr.2019.11.001.

[9] Chiang, C. C.; Lee, B. T. H. Annihilating Pores in the Desired Layer of a Porous Silicon Bilayer with Different Porosities for Layer Transfer. *Scientific reports* **2019**, 9 (1), 12631. https://doi.org/10.1038/s41598-019-49119-8.

[10] Schulte, A.; Alhusaini, Q.F. M.; Schönherr, H. Anodic Aluminum Oxide Nanopore Template-Assisted Fabrication of Nanostructured Poly(vinyl alcohol) Hydrogels for Cell Studies. *ACS Applied Bio Materials* **2020**, 3 (4), 2419–2427. https://doi.org/10.1021/acsabm.0c00153.

[11] Kumar, P.; Huber, P. Effect of Etching Parameter on Pore Size and Porosity of Electrochemically Formed Nanoporous Silicon. *Journal of Nanomaterials* **2007**, *2007*, 1–4. https://doi.org/10.1155/2007/89718.

[12] El-Gamal, A. A.; Ibrahim, S. M.; Amin, M. Impact of Thermal Oxidation on the Structural and Optical Properties of Porous Silicon Microcavity. *Nanomaterials and Nanotechnology* **2017,** *7*, 184798041773570https://doi.org/10.1177/1847980417735702.

[13] Kumeria, T.; Wang, J.; Chan, N.; Harris, T. J.; Sailor, M. J. Visual Sensor for Sterilization of Polymer Fixtures Using Embedded Mesoporous Silicon Photonic Crystals. *ACS Sensors* **2018,** *3* (1), 143–150. https://doi.org/10.1021/acssensors.7b00764.

---

[14] Mohammed, N. A.; Hamed, M. M.; Khalaf, A. A. M.; Alsayyari, A.; El-Rabaie, S. High-Sensitivity Ultra-quality Factor and Remarkable Compact Blood Components Biomedical Sensor Based on Nanocavity Coupled Photonic Crystal. *Results in Physics* **2019**, *14*, 102478. https://doi.org/10.1016/j.rinp.2019.102478.

[15] Li, S.; Hu, D.; Huang, J.; Cai, L. Optical Sensing Nanostructures for Porous Silicon Rugate Filters. *Nanoscale Research Letters* **2012**, *7* (1). https://doi.org/10.1186/1556-276x-7-79.

[16] Salem, M. S.; Sailor, M. J.; Sakka, T.; Ogata, Y. H. Electrochemical Preparation of a Rugate Filter in Silicon and its Deviation from the Ideal Structure. *Journal of Applied Physics* **2007**, *101* (6). https://doi.org/10.1063/1.2710339.

[17] Casanova, F.; Chiang, C. E.; Ruminski, A. M.; Sailor, M. J.; Schuller, I. K. Controlling the Role of Nanopore Morphology in Capillary Condensation. *Langmuir* **2012**, 28 (17), 6832–6838. https://doi.org/10.1021/la204933m.

[18] Khardani, M.; Bouaïcha, M.; Bessaïs, B. Bruggeman Effective Medium Approach for Modelling Optical Properties of Porous Silicon: Comparison with Experiment. *Physica Status Solidi* **2007**, 4 (6), 1986–1990. https://doi.org/10.1002/pssc.200674420.

[19] Rakhimov, R. A.; Osipov, E. V.; Dovzhenko, D. S.; Martynov, I. L.; Chistyakov, A. A. Influence of Electro-chemical Etching Parameters on the Reflectance Spectra of Porous Silicon Rugate Filters. *Journal of Physics Conference Series* **2016**, *737*, 012026. https://doi.org/10.1088/1742-6596/737/1/012026.

[20] Sailor, M.J. Chemical Reactivity and Surface Chemistry of Porous Silicon. Handbook of Porous Silicon,**2014** *Springer*, Cham, Switzerland. https://doi.org/10.1007/978-3-319-04508-5_37-1.

[21] Naveas, N; Costa, V.; Gallach, D.; Hernandez-Montelongo, J.; Palma R.J.M.; Garcia-Ruiz J.P; Manso-Silván, M. Chemical Stabilization of Porous Silicon for Enhanced Biofunctionalization with Immunoglobulin. *Science and Technology of Advanced Materials* **2012**, 13:4, https://doi.org/10.1088/1468-6996/13/4/045009.

[22] Aggarwal, G.; Mishra, P.; Joshi, B.; Islam S. S. H. Porous Silicon Surface Stability: a Comparative Study of Thermal Oxidation Techniques. *Journal of Porous Materials* **2014**, 21, 23–29. https://doi.org/10.1007/s10934-013-9742-y.

[23] Szili, E. J.; Jane, A.; Low, S. P.; Sweetman, M.; Macardle, P.; Kumar, S.; St. Smart, R. C.; Voelcker, N. H. Interferometric Porous Silicon Transducers Using an Enzymatically Amplified Optical Signal. *Sensors and Actuators B: Chemical* **2011,** *160* (1), 341–348. https://doi.org/ 10.1016/j.snb.2011.07.059.

[24] Shtenberg, G.; Massad-Ivanir, N.; Fruk, L.; Segal, E. Nanostructured Porous Si Optical Biosensors: Effect of Thermal Oxidation on their Performance and Properties. *ACS Applied Materials & Interfaces* **2014,** *6* (18), 16049–16055. https://doi.org/10.1021/am503987j.

[25] Shtenberg, G.; Massad-Ivanir, N.; Fruk, L.; Segal, E. Nanostructured Porous Si Optical Biosensors: Effect of Thermal Oxidation on their Performance and Properties. *ACS Applied Materials & Interfaces* **2014,** *6* (18), 16049–16055. https://doi.org/10.1021/am503987j.

---

[26] El-Gamal, A. A.; Ibrahim, S. M.; Amin, M. Impact of Thermal Oxidation on the Structural and Optical Properties of Porous Silicon Microcavity. *Nanomaterials and Nanotechnology* **2017,** *7*, 184798041773570. https://doi.org/10.1177/1847980417735702.

[27] Martín-Sánchez, D.; Kovylina, M.; Ponce-Alcántara, S.; García-Rupérez, J. Thermo-Optic Coefficient of Porous Silicon in the Infrared Region and Oxidation Process at Low Temperatures. *Journal of the Electrochemical Society* **2019,** *166* (6), B355-B359. https://doi.org/10.1149/2.0341906jes.

[28] Robbiano, V.; Surdo, S.; Minotto, A.; Canazza, G.; Lazzerini, G. M.; Mian, S. M.; Comoretto, D.; Barillaro, G.; Cacialli, F. C-Si Hybrid Photonic Structures by Full Infiltration of Conjugated Polymers into Porous Silicon Rugate Filters. *Nanomaterials and Nanotechnology* **2018**, 8, 184798041878840. https://doi.org/10.1177/1847980418788404.

[29] Olsen, T. On the Calculation of Power from Curvature of the Cornea. *The British journal of ophthalmology* **1986,** *70* (2), 152–154. https://doi.org/10.1136/bjo.70.2.152.

[30] Hutchinson, M. H.; Dorgan, J. R.; Knauss, D. M.; Hait, S. B. Optical Properties of Polylactides. *Journal of Polymers and the Environment* **2006,** *14* (2), 119–124. https://doi.org/ 10.1007/s10924-006-0001-z.

[31] Bruggeman, D. A. G. Berechnung Verschiedener Physikalischer Konstanten von Heterogenen Substanzen. I. Dielektrizitätskonstanten und Leitfähigkeiten der Mischkörper aus isotropen Substanzen. *Annals of Physics* **1935,** *416* (7), 636–664. https://doi.org/ 10.1002/andp.19354160705.

[32] Wang, J.; Lee, G. Y.; Kennard, R.; Barillaro, G.; Bisiewicz, R. H.; Cortez Lemus, N. A.; Cao, X. C.; Anglin, E. J.; Park, J. S.; Potocny, A.; Bernhard, D.; Li, J.; Sailor, M. J. Engineering the Properties of Polymer Photonic Crystals with Mesoporous Silicon Templates. *Chemistry of Materials* **2017,** *29* (3), 1263–1272. https://doi.org/10.1021/acs.chemmater.6b04670.

[33] Orosco, M.M.; Pacholski, C.; Sailor, M.J. Real-Time Monitoring of Enzyme Activity in a Mesoporous Silicon Double Layer. *Nat. Nanotechnol*. **2009**, *4*, 255-258. https://doi.org/ 10.1038/nnano.2009.11.

[34] Tong, W. Y.; Sweetman, M. J.; Marzouk, E. R.; Fraser, C.; Kuchel, T.; Voelcker, N. H. Towards a Subcutaneous Optical Biosensor Based on Thermally Hydrocarbonised Porous Silicon. *Biomaterials* **2016,** *74,* 217–230. https://doi.org/10.1016/j.biomaterials.2015.09.045.

[35] Pap, A. E.; Kordás, K.; George, T. F.; Leppävuori, S. Thermal Oxidation of Porous Silicon: Study on Reaction Kinetics. *The Journal of Physical Chemistry B* **2004,** *108* (34), 12744–12747. https://doi.org/10.1021/jp049323y.

Chapter 8. Bare Eye Detection of Bacterial Enzymes of *Pseudomonas aeruginosa* with PLA Modified PSiRF[a]

8.1 Introduction

With the increasing prevalence of antibiotic-resistant bacteria, including multi-drug resistant strains,[1,2] research efforts worldwide are now concentrated on developing targeted diagnostics and therapies. Despite the development of ultrasensitive detection and identification techniques, such as mass spectrometry-based approaches,[3] the vast plethora of challenges cannot be addressed satisfactorily.

As discussed in Chapter 2, and in particular in Chapter 7, photonic materials become an attractive strategy for bacterial detection due to the absence of any chromophore for obtaining a strong color response. Hence, no bleaching occurs, if the sensors are irradiated (which results in vastly increased shelf-life) and no irritating and potentially toxic dyes are being released. Since pSi photonic structures possess a stop bandgap that limits reflected light to specific wavelengths[4]. This property makes them exceptionally responsive to changes in the refractive index of the photonic structure.

In this context, our research focuses on the development of enzyme-responsive polymer-modified pSiRF (porous silicon with reflective film) for the rapid optical detection of bacterial enzymes and bacteria. Specifically, we explore the potential for detecting enzymes secreted by *Pseudomonas aeruginosa* (PAO1) (*P. aeruginosa (*PAO1)) using this innovative approach (Scheme 8.1). By utilizing pSiRF as an optical transducer and incorporating the enzyme-sensitive polymer poly(lactic acid) (PLA), we have successfully detected bacterial enzymes, including proteinase K and those secreted by *P. aeruginosa*. This detection results in a noticeable color change, easily discerned by the naked eye. Importantly, this approach offers a simple and direct method for detecting *P. aeruginosa* (PAO1) based on the enzymatic activity of its secreted enzymes without interference from other PLA-degrading enzymes.

---

[a] Part of this Chapter was published in "Alhusaini, Q.; Scheld, W. S.; Jia, Z.; Das, D.; Afzal, F.; Müller, M.; Schönherr, H. Bare Eye Detection of Bacterial Enzymes of *Pseudomonas aeruginosa* with Polymer Modified Nanoporous Silicon Rugate Filters. *Biosensors* **2022**, *12* (12), 1064".

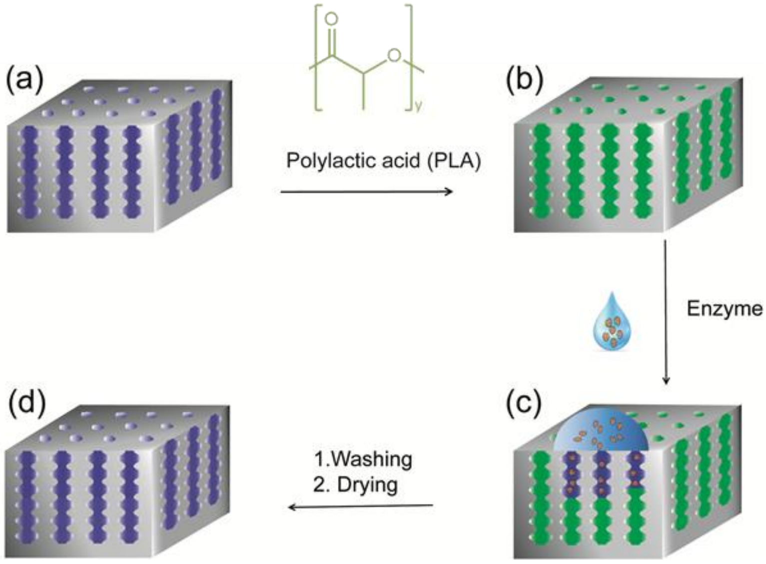

Scheme 8.1: *Schematic of the pSiRF-based sensor for bacterial enzymes: a) neat nanoporous pSiRF; b) pSiRF after deposition of PLA inside the pores; c) enzymatic degradation of PLA inside the pores; d) pSiRF after the reaction. The color change of the pSiRF from blue (bare) to green (pores modified with PLA) is due to the increase of the effective refractive index of the sensor caused by the compositional change inside the pores. The original color is recovered after enzymatic degradation of PLA. This Scheme was reproduced with permission from reference [5]: Alhusaini, Q.; Scheld, W. S.; Jia, Z.; Das, D.; Afzal, F.; Müller, M.; Schönherr, H. Bare Eye Detection of Bacterial Enzymes of Pseudomonas aeruginosa with Polymer Modified Nanoporous Silicon Rugate Filters. Biosensors* ***2022****, 12 (12), 1064. Copyright 2014. MDPI.*

8.2 Enzymatic Degradation of PLA with Proteinase K

As mentioned in Chapter 7, the deposition of PLA in pSiRF not only caused a red shift in the spectral position but also led to a color change from blue to green due to the concomitant increase in n_{eff} of pSiRF (Figure 8.1a,c). Figure 8.1b shows a photograph of the empty pSiRF, which showed a blue color in reflection, and later was changed to green after loading PLA into the pores. Additionally, the peak intensity increased after PLA modification due to the refractive index contrast at the interfaces (e.g., from air to polymer). This effect was also observed in the literature[6]. However, the PLA-infiltrated pSiRF can, thus, be used to detect the enzyme proteinase K, which is known to cleave the ester bonds of PLA[7,8,9]. The degradation of PLA by proteinase K in the pores should lead to a change in n_{eff} of the pSiRF.

The reflectance spectrum was recorded after the incubation of PLA-modified pSiRF with proteinase K for 7 h.

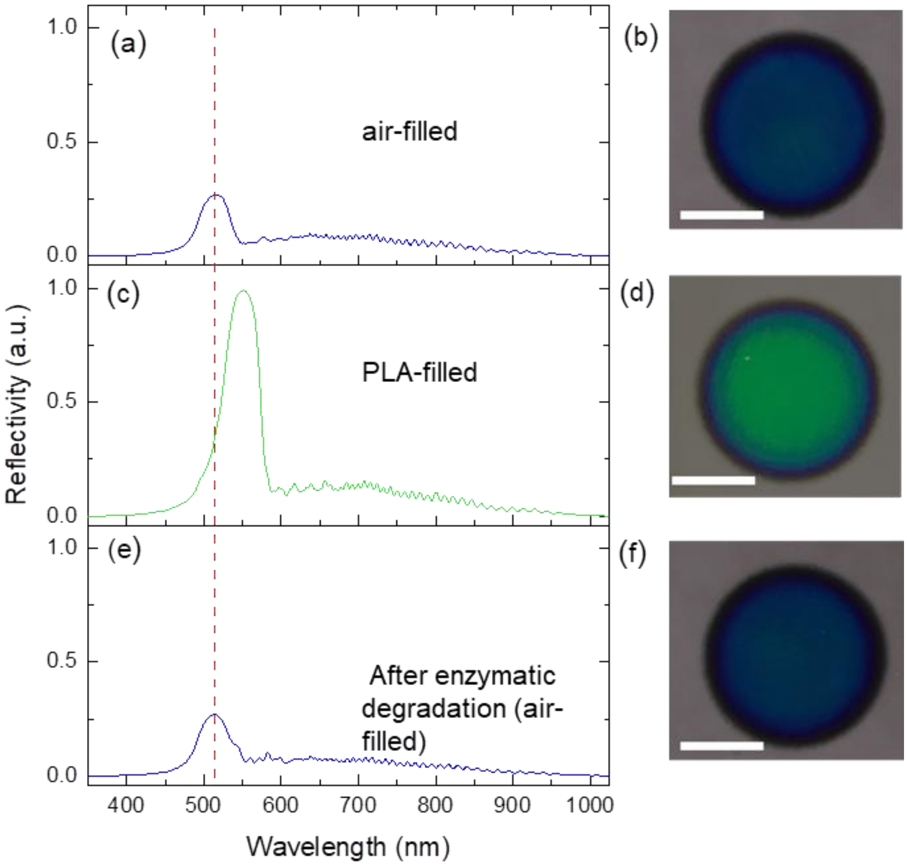

Figure 8.1: *RIfS spectra and photographs of dried pSiRF: a,b) air-filled pSiRF, c,d) PLA-filled pSiRF, and e,f) pSiRF after enzymatic degradation of PLA with proteinase K (scale bars = 0.5 cm). This Figure was reproduced with permission from reference [5]: Alhusaini, Q.; Scheld, W. S.; Jia, Z.; Das, D.; Afzal, F.; Müller, M.; Schönherr, H. Bare Eye Detection of Bacterial Enzymes of Pseudomonas aeruginosa with Polymer Modified Nanoporous Silicon Rugate Filters. Biosensors* ***2022****, 12 (12), 1064. Copyright 2014. MDPI.*

As can be seen in Figure 8.1e, the position of the peak is blue-shifted to the original position. This observation indicates that the PLA in pSiRF was indeed degraded by proteinase K, and the resulting degraded fragments were removed during the washing step. Figure 8.1f displays a photograph of the pSiRF, confirming a color change from green to blue, which was readily discernible by the bare eye after PLA degradation.

This enzymatic reaction was also studied for different degradation times. As shown in Figure 8.2, the spectrum of the PLA-modified pSiRF shows a peak centered at 550 nm at time zero (t = 0). Thirty minutes after starting the enzymatic reaction, the peak was blue-shifted by ~ 6 nm, which is attributed to a decrease in the refractive index after partial removal of PLA from the pores. The peak was blue-shifted by ~37 nm up to 240 min and remained unchanged at longer incubation times, providing 100 % degradation of the loaded PLA, and the peak position of unloaded pSiRF was restored. Moreover, the intensity of the peak decreased as the reaction progressed.

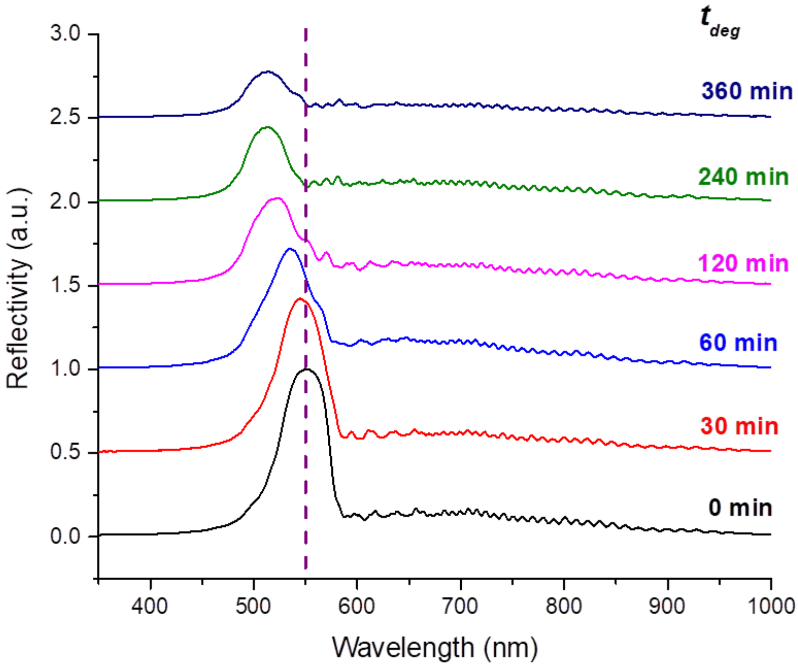

Figure 8.2: *RIfS spectra of PLA coated pSiRF after incubation with 1.00 mg mL^{-1} proteinase K for 0, 30, 60, 120, 240, and 360 min. The RIfS measurement was performed after the washing and drying steps of pSiRF. This Figure was reproduced with permission from reference [5]: Alhusaini, Q.; Scheld, W. S.; Jia, Z.; Das, D.; Afzal, F.; Müller, M.; Schönherr, H. Bare Eye Detection of Bacterial Enzymes of Pseudomonas aeruginosa with Polymer Modified Nanoporous Silicon Rugate Filters. Biosensors* ***2022****, 12 (12), 1064. Copyright 2014. MDPI.*

Next, the response of the PLA-modified pSiRF sensor was investigated for different enzyme concentrations. As shown in Figure 8.3, the shift in the peak positions obtained after applying proteinase K to the PLA-modified pSiRF sensor for a given time exhibited an increase with increasing enzyme concentration. In contrast, there was no shift in the peak position when the PLA-modified pSiRF sensor was exposed to the enzyme-free solution, indicating that no enzymatic degradation took place and the PLA was stable during this time frame.

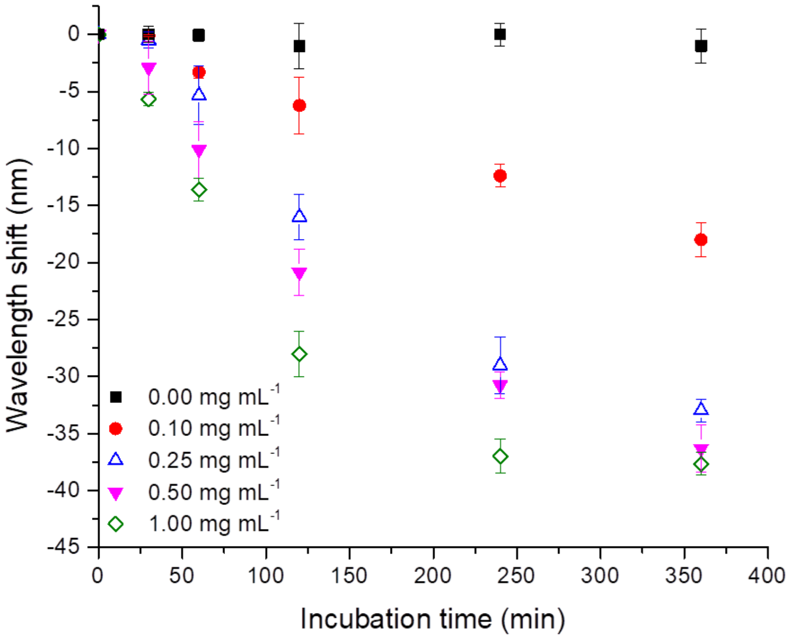

Figure 8.3: *Plot of wavelength shift of four sets of PLA-modified pSiRF sensors in the dry state after incubation in 0.10, 0.25, 0.50, and 1.00 mg mL^{-1} of proteinase K solution at 25 °C for 0, 30, 60, 120, 240, and 360 min. The error bars are the standard deviation (n=3). This Figure was reproduced with permission from reference [5]: Alhusaini, Q.; Scheld, W. S.; Jia, Z.; Das, D.; Afzal, F.; Müller, M.; Schönherr, H. Bare Eye Detection of Bacterial Enzymes of Pseudomonas aeruginosa with Polymer Modified Nanoporous Silicon Rugate Filters. Biosensors* ***2022****, 12 (12), 1064. Copyright 2014. MDPI.*

The extent of the reaction *x* can be expressed as a function of incubation time[10].

$$x = \frac{\Delta\lambda_0 - \Delta\lambda_t}{\Delta\lambda_0 - \Delta\lambda_\infty} \quad \text{..} \text{ (Eq. 8.1)}$$

where $\Delta\lambda_0$ is the shift in the wavelength shift at time zero, $\Delta\lambda_t$ at time t, and $\Delta\lambda_\infty$ at infinitive time. Figure 8.4 illustrates the course of the enzymatic degradation ([1 - *x*], with the extent of reaction (*x*) as a function of reaction time), along with the change in the pore filling. The PLA pore filling was reduced with the incubation time, following the reduction of the refractive index in the pores.

Furthermore, Figure 8.4 shows that the extent of the reaction increases substantially with an elevated concentration of proteinase K. In contrast, the sensor did not respond significantly in the absence of proteinase K (Tris-HCl buffer). Hence, the response was due to the enzymatic reaction. We may conclude that the PLA-modified pSiRF is stable in the buffered medium for at least 6 h. The data were least-squares fitted to evaluate the apparent rate constants *k*.

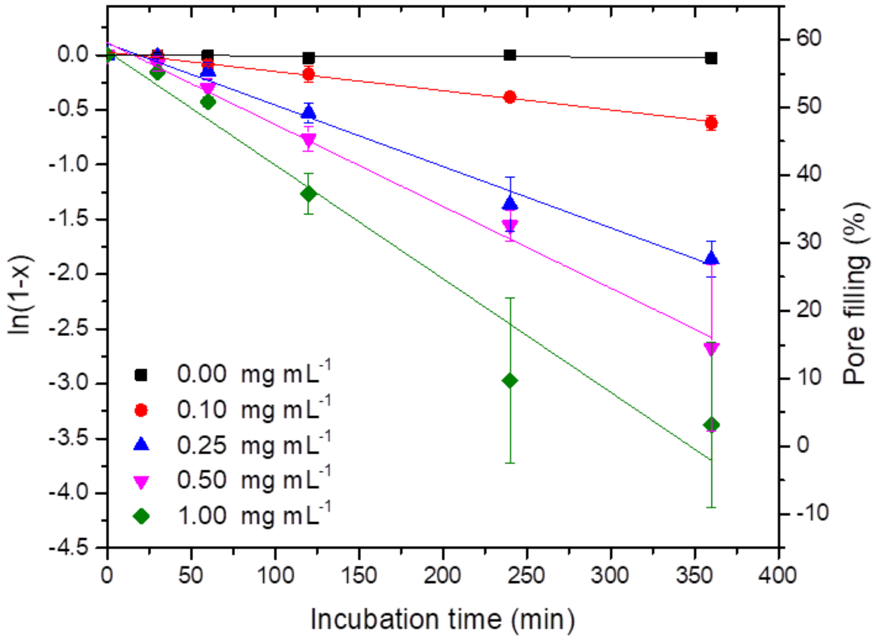

***Figure 8.4**: Plot of ln(1 − x) (x: extent of reaction) and the pore filling as a function of incubation time for the degradation of PLA inside pSiRF in 0.10, 0.25, 0.50, and 1.00 mg mL^{-1} of proteinase K solution at 25 °C for 0, 30, 60, 120, 240 and 360 min. The pore filling was estimated based on Figure 8.5. The data were presented as mean ± standard deviation. The solid lines correspond to the linear least-squares fit of RIfS data. All measurements were conducted in the dried state. This Figure was reproduced with permission from reference [5]: Alhusaini, Q.; Scheld, W. S.; Jia, Z.; Das, D.; Afzal, F.; Müller, M.; Schönherr, H. Bare Eye Detection of Bacterial Enzymes of Pseudomonas aeruginosa with Polymer Modified Nanoporous Silicon Rugate Filters. Biosensors **2022**, 12 (12), 1064. Copyright 2014. MDPI.*

The pore filling in Figure 8.4 was estimated from the relation between the refractive index and peak shift. It was reported that the spectral peak position increased linearly with the refractive index of the void in the pores; therefore, a series of solvents were employed to estimate the pore filling[11,12]. The organic solvents were used in previous studies to ascertain how pSi sensors respond to changes in their porous medium[13,14]. In this Chapter, methanol, ethanol, ethyl acetate, hexane, isopropanol, and ethylene glycol were used to infiltrate the pores of pristine pSiRF, and the changes were monitored by RIfS. The refractive indices of the solvents outside the pSiRF pores were measured with an Abbe refractometer. The positions of the peaks observed in RIfS were plotted against the refractive indices of the solvents (Figure 8.5). Based on a fit of these data, the refractive index of the dried PLA-modified pSiRF was calculated (Table 8.1 and Figure 8.6).

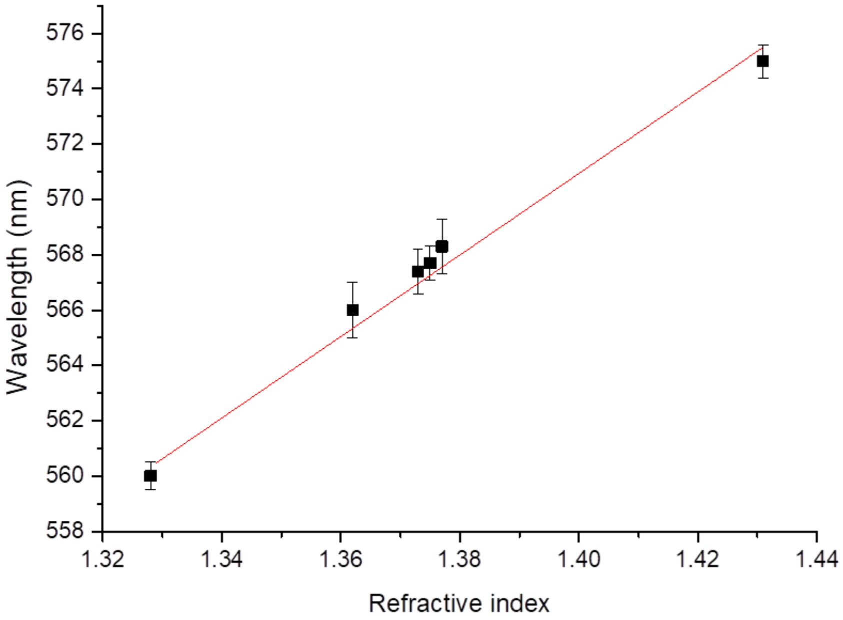

Figure 8.5: *Plot of the wavelength shift of neat pSiRF versus refractive indices of methanol, ethanol, ethyl acetate, hexane, isopropanol, and ethylene glycol infiltrated the pores, (λ (nm) = 147.38 nm × n + 364 nm, $R^2 = 0.98$). The data are presented as a mean value of three measurements with the standard deviation as an error. The solid red line corresponds to a linear least-squares fit of the data. This Figure was reproduced with permission from reference [5]: Alhusaini, Q.; Scheld, W. S.; Jia, Z.; Das, D.; Afzal, F.; Müller, M.; Schönherr, H. Bare Eye Detection of Bacterial Enzymes of Pseudomonas aeruginosa with Polymer Modified Nanoporous Silicon Rugate Filters. Biosensors* ***2022****, 12 (12), 1064. Copyright 2014. MDPI.*

***Table 8.1.** Calculated refractive index of the void (PLA plus air) in pSiRF (dried state) from Figure 8.5. The refractive index shift was calculated by subtracting n values at a given time (n_t) from the n at time zero (n_{ref}). This Table was reproduced with permission from reference [5]: Alhusaini, Q.; Scheld, W. S.; Jia, Z.; Das, D.; Afzal, F.; Müller, M.; Schönherr, H. Bare Eye Detection of Bacterial Enzymes of Pseudomonas aeruginosa with Polymer Modified Nanoporous Silicon Rugate Filters. Biosensors **2022**, 12 (12), 1064. Copyright 2014. MDPI.*

Incubation time (min)	Refractive index of the void n_{void} (PLA+air) in pSiRF	Refractive index shift (n_t-n_{ref})
0	1.262	0.000
30	1.224	-0.038
60	1.170	-0.092
120	1.072	-0.190
240	1.011	-0.251
360	1.006	-0.256

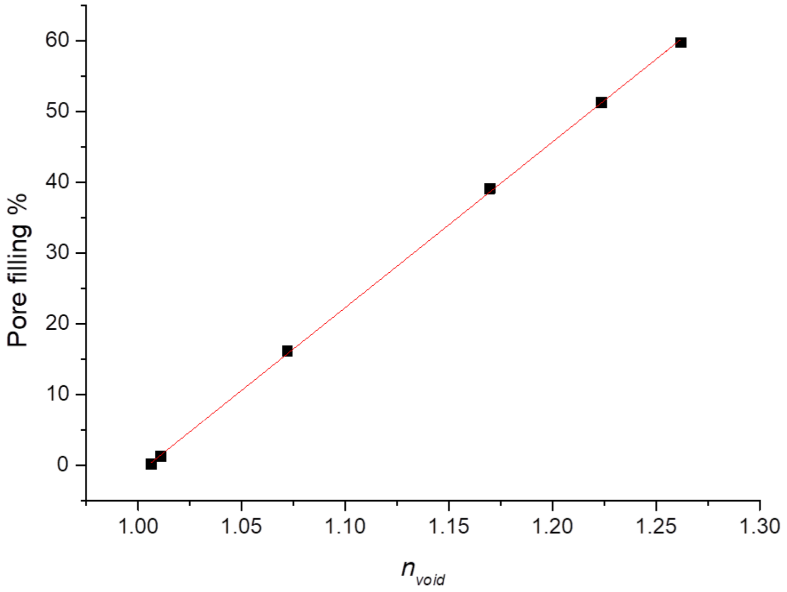

***Figure 8.6:** Plot of pore filling vs. refractive index of the voids (filling % = 234 × n_{void} - 235, R^2 = 0.99). The solid red line corresponds to a linear least-squares fit of the pore filling data. This Figure was reproduced with permission from reference [5]: Alhusaini, Q.; Scheld, W. S.; Jia, Z.; Das, D.; Afzal, F.; Müller, M.; Schönherr, H. Bare Eye Detection of Bacterial Enzymes of Pseudomonas aeruginosa with Polymer Modified Nanoporous Silicon Rugate Filters. Biosensors **2022**, 12 (12), 1064. Copyright 2014. MDPI.*

The *k* values were plotted against the proteinase K concentrations (Figure 8.7). It was observed that *k* increased linearly for the lower proteinase K concentrations and then leveled off. The latter observation is attributed to the limited fraction of exposed PLA inside the nanopores. For higher proteinase K concentrations, the amount of PLA became saturated with enzymes for the hydrolysis of ester bonds, and consequently, the rate did not increase further.

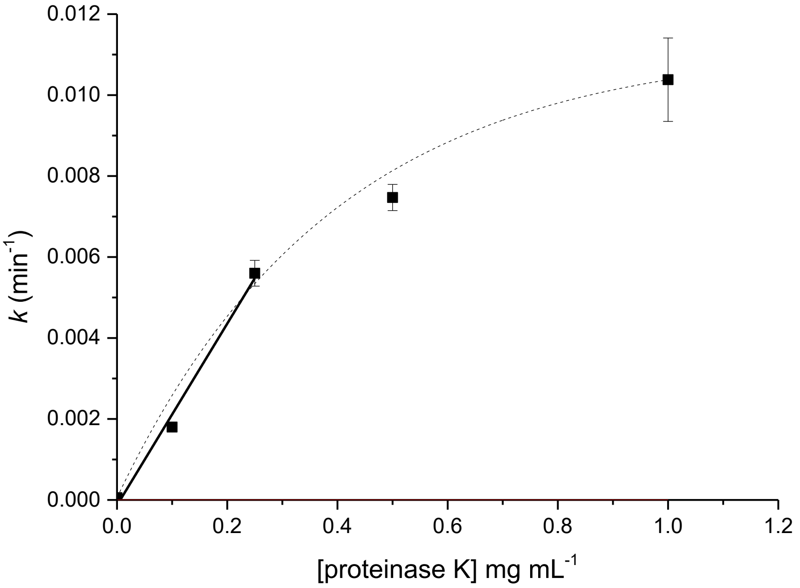

Figure 8.7: *Plot of apparent rate constant (k) versus proteinase K concentrations (0.10, 0.25, 0.50, and 1.00 mg mL^{-1}). The values for k were obtained from linear fits in Figure 8.4, the error bars denote the standard error from these fits. The solid line corresponds to the linear least-squares fit of the first three data points used to estimate the corresponding slope (0.022 mg mL^{-1} min^{-1}) and serves, similar to the dotted line, as a guide to the eyes only. This Figure was reproduced with permission from reference [5]: Alhusaini, Q.; Scheld, W. S.; Jia, Z.; Das, D.; Afzal, F.; Müller, M.; Schönherr, H. Bare Eye Detection of Bacterial Enzymes of Pseudomonas aeruginosa with Polymer Modified Nanoporous Silicon Rugate Filters. Biosensors **2022**, 12 (12), 1064. Copyright 2014. MDPI.*

The enzymatic reaction of the PLA-modified pSiRF with proteinase K was also followed under conditions identical to the previous experiment by RIfS. Figure 8.8 shows two wavelength-incubation time data sets: one is for PLA-modified pSiRF exposed to Tris-HCl buffer (blank), and the other is for PLA-modified pSiRF exposed to proteinase K solution.

Before the enzymatic reaction, Tris-HCl buffer was injected over PLA-modified pSiRF for 120 min, followed by the injection of proteinase K solution.

In contrast to the virtually constant wavelength observed in the blank experiment during 1050 min, a blue shift in the wavelength was observed almost instantaneously after injection of the proteinase K. The blue shift of the peak position is due to the reduction in the refractive index of the void in the pores because of the replacement of the PLA by the buffer. A value for *k* of 0.003 min^{-1} was calculated from Figure 8.8. This value of *k* is three times smaller than that obtained in *ex-situ* measurements (compare Figure 8.4). This variation resulted from the procedures employed in performing the enzymatic reaction and the sample handling prior to the analysis. For instance, after each incubation of the sensor in the *ex-situ* experiment, the sensor was taken out of the medium, washed and dried, and then characterized with RIfS. By contrast, no washing or drying steps were applied in the *in-situ* experiment, hence, no convection took place, and degraded PLA may have remained trapped inside the pores.

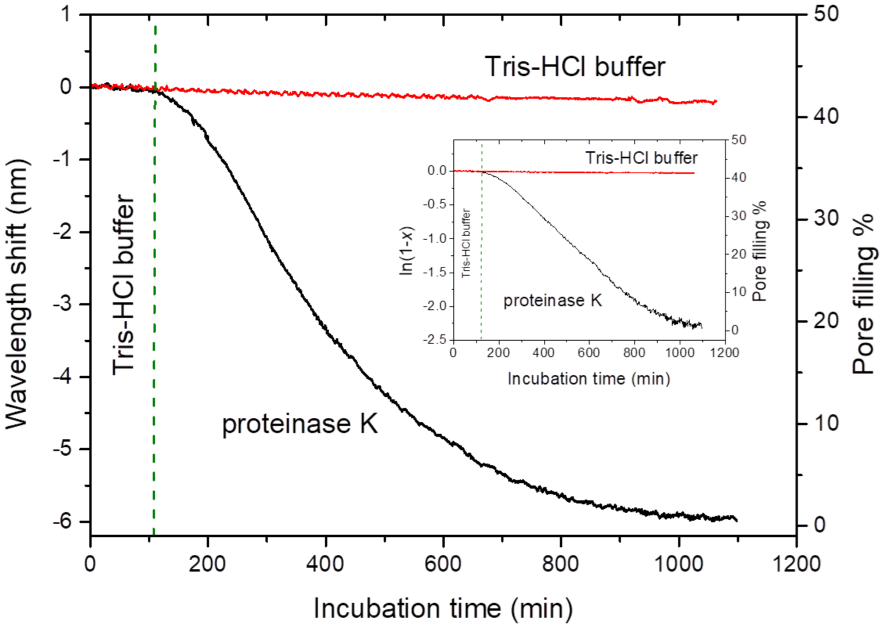

Figure 8.8: *Plot of in-situ RIfS measurement of enzymatic reaction in PLA-modified pSiRF with proteinase K solution (1.00 mg* mL^{-1}*) and Tris-HCl buffer at 25°C. This Figure was reproduced with permission from reference [5]: Alhusaini, Q.; Scheld, W. S.; Jia, Z.; Das, D.; Afzal, F.; Müller, M.; Schönherr, H. Bare Eye Detection of Bacterial Enzymes of Pseudomonas aeruginosa with Polymer Modified Nanoporous Silicon Rugate Filters. Biosensors* ***2022****, 12 (12), 1064. Copyright 2014. MDPI.*

8.3 Enzymatic Degradation of PLA with *Pseudomonas aeruginosa*

The essential step to demonstrate the functionality of bacterial enzyme detection is a test with the living target bacteria. The experiment was performed by immersing the PLA-modified pSiRF sensor directly into a suspension of *P. aeruginosa* (PAO1) (cultured for 24 h) in a 6-well plate. The color changes due to the enzymatic reaction were documented with a conventional smartphone camera. As can be seen in Figure 8.9, a strong color change from green to blue was observed after exposing the PLA-modified pSiRF sensor to the suspension of *P. aeruginosa* in the LB medium for 24 h. As a control experiment, a PLA-modified pSiRF sensor was immersed in a bacteria-free LB medium under the same conditions. Here, no significant color change was observed after 24 h. These results indicate that the color change on pSiRF occurs only when the target bacteria are present, which are known to secrete enzymes (proteases) that digest the PLA[15,16].

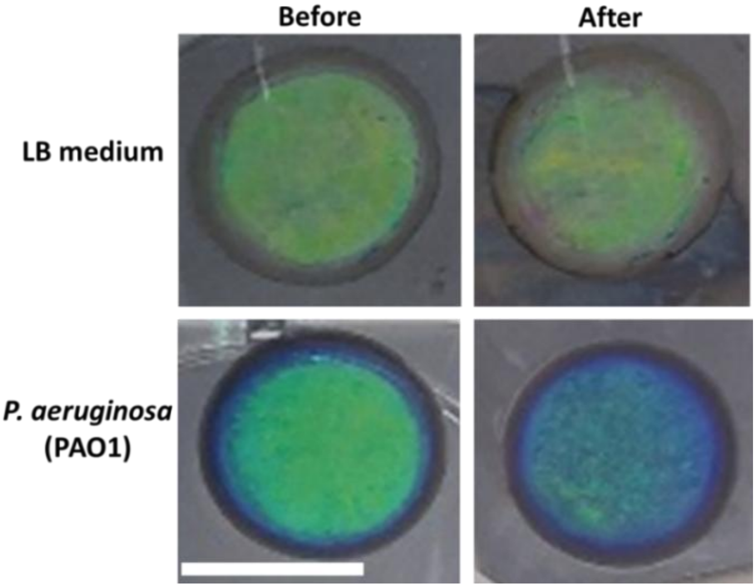

Figure 8.9: *Photographs of the pre-dried PLA-modified pSiRF before and after the immersion in bacteria-free LB medium and P. aeruginosa (PAO1) suspension (bacteria starting concentration:* 1.9×10^9 *CFU* mL^{-1} *in LB medium at 37 °C for 24 h (end concentration:* 3.7×10^9 *CFU* mL^{-1}*). Scale bar = 1 cm. This Figure was reproduced with permission from reference [5]: Alhusaini, Q.; Scheld, W. S.; Jia, Z.; Das, D.; Afzal, F.; Müller, M.; Schönherr, H. Bare Eye Detection of Bacterial Enzymes of Pseudomonas aeruginosa with Polymer Modified Nanoporous Silicon Rugate Filters. Biosensors* ***2022****, 12 (12), 1064. Copyright 2014. MDPI.*

Finally, the PLA-modified pSiRF sensor was also tested *in-situ* in the corresponding sterile filtered supernatant of *P. aeruginosa* (PAO1). Again, the LB medium was chosen as a blank. Figure 8.10 shows the RIfS measurement carried out during the incubation in the sterile bacterial supernatant and in the LB medium, which has not been in contact with any bacteria, respectively. It was observed that the peak was blue-shifted for the *P. aeruginosa* supernatant, whereas no significant change in the peak position was recorded in LB medium, even after 1350 min of incubation. The results confirm that PLA was stable in the LB medium and degraded in the *P. aeruginosa* supernatant, thus indicating that enzymes secreted by *P. aeruginosa* in this medium can-still be detected after removing the bacteria.

Not surprisingly, the results revealed that the reaction in the bacterial supernatant was slower compared to the reaction in the bacterial suspension. A possible explanation for these results may be the lower enzyme concentration in the supernatant compared to those in the bacterial suspension, which is due to adsorption to the filters used. Further, it was reported that the filtration process caused an effect on enzyme activity due to the enzyme denaturation and/or the reduction in the concentration of enzyme[17,18]. Also, the increase in the bacteria concentration (from 1.9×10^9 to 3.7×10^9 CFU mL^{-1}) after 24 h incubation of the PLA-modified pSiRF sensor in bacterial suspension cannot be neglected, which leads to an enhancement in the concentration of secreted enzymes. Thus, no further enzymes were consistently produced in bacterial supernatants, in contrast to metabolically active bacterial suspensions (presence of bacteria).

The results underlined the feasibility of this sensing platform to be potentially used as a PoC system for bacterial enzyme detection by the bare eye. The response times and sensitivities are currently inferior compared to other nanocapsule or hydrogel-based approaches[19,20], but the sensor design and the materials render this macro(molecule)-nano(porous) platform extremely robust.

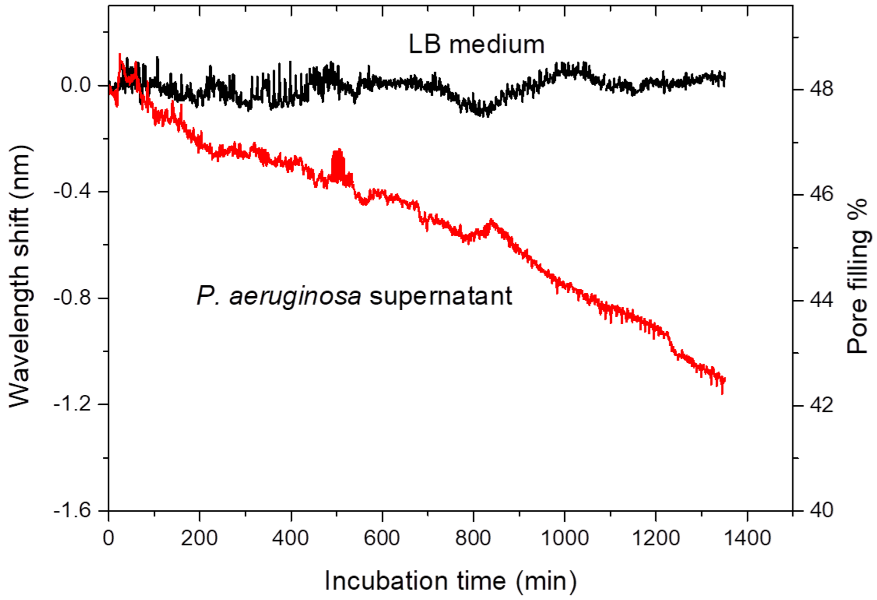

Figure 8.10: *Plot of in-situ RIfS measurement during incubation of a PLA-modified pSiRF sensor in sterile P. aeruginosa (strain: PAO1) supernatants obtained from a 1.9 × 10^9 CFU mL^{-1} suspension by filtration (black line) and in pure LB medium (red line). The PLA-modified pSiRF sensor was stable in LB for more than 22 h, whereas incubation in P. aeruginosa supernatant caused a quasi-linear blue shift in the wavelength. The spectral positions of the characteristic peaks were corrected by subtracting the wavelength obtained before incubation in the bacterial supernatant or the LB medium. This Figure was reproduced with permission from reference [5]: Alhusaini, Q.; Scheld, W. S.; Jia, Z.; Das, D.; Afzal, F.; Müller, M.; Schönherr, H. Bare Eye Detection of Bacterial Enzymes of Pseudomonas aeruginosa with Polymer Modified Nanoporous Silicon Rugate Filters. Biosensors* ***2022****, 12 (12), 1064. Copyright 2014. MDPI.*

The color change of the sensor from green to blue may be challenging to discern, depending on the lighting conditions in a real application, but the colors can be adapted by changing the Rugate structure. Additionally, objective detection utilizing smartphone-based detection is an already demonstrated option[21]. The response time depends on the enzyme concentration, hence, LOD values (not determined here) are time-dependent, as discussed before[22]. Moreover, this approach could be employed for real-time detection of secreted enzymes from a broad range of bacteria if PLA is replaced by, e.g., hyaluronan or poly(ε-caprolactone) or other labile polymers specifically prone for degradation by bacterial enzyme selective for other clinically labile bacteria, such as hyaluronidase or lipases from *Staphylococcus aureus*[23,24,25].

8.4 Conclusion

This Chapter demonstrates a poly(lactic acid) (PLA)-modified porous silicon with reflective film (pSiRF) nanoporous sensor for the visual detection of bacterial enzymes produced by *P. aeruginosa*. This macro-molecule-nano-porous platform, achieved through the functionalization of pSiRF with the biodegradable polymer PLA using a solvent casting method, showcases promising results.

The role of pSiRF as an optical transducer is evident through significant changes in wavelength observed in the reflectometric interference spectroscopy (RIfS) spectra and the noticeable color shifts in the sensor, transitioning from blue to green when exposed to pure proteinase K solution, *P. aeruginosa* (PAO1) cultures, and their corresponding sterile culture supernatants. This change is attributed to an increase in the effective refractive index caused by the infiltration of PLA into the nanopores of pSiRF. Moreover, the wavelength can be reversed, shifting from 550 nm back to 513 nm upon enzymatic degradation of PLA, resulting in the sensor returning to a blue color. The color transition of the pSiRF sensor from green to blue could be detected by the bare eye after incubation in a suspension of *P. aeruginosa* immersion, washing it, and drying it.

The combined results of *ex-situ* and *in-situ* RIfS measurements, on the one hand, and the visual inspection of the photonic sensors, on the other hand, indicate that this principle may be utilized for sensing bacterial enzymes of clinically relevant bacterial pathogens.

8.5 Materials and Methods

Chemicals, materials, and instruments, which have already been mentioned in Chapter 4 and Chapter 7, will not be stated here again.

Enzymatic Degradation of PLA with Proteinase K

The PLA-modified pSiRF sensors were placed in a 6-well plate containing 300 µL of Tris-HCl buffered proteinase K solution (pH 8.5) with varying concentrations (0.10, 0.25, 0.50, and 1.00 mg mL^{-1}). After 0, 30, 60, 120, 240, and 360 min, the reacted sensor was washed with Milli-Q water, dried in a stream of nitrogen, and then kept in the desiccator at 5 mbar for 2 h, followed by RIfS analysis. For *in-situ* RIfS measurements, the PLA-modified pSiRF was inserted in a homemade flow cell (volume 0.3 mL), and the proteinase K or Tris-HCl buffer solutions were injected.

Bacteria Tests

The preparation of the suspension and sterile supernatant of sterile *P. aeruginosa* (PAO1) was detailed in Chapter 6. Dr. Zhiyuan Jia participated in performing the bacteria test on pSiRF sensors. The enzymatic reaction was conducted by adding 3 mL of resulting bacterial suspension into the well of the transparent 6-well plates containing a PLA film-coated pSiRF, followed by incubation for 24 h at 37 °C. A part of the suspension was diluted and spread out onto an LB agar plate and incubated at 37 °C overnight to determine the bacterial colony forming units mL^{-1} (CFU mL^{-1}) of the inoculums. The PLA-modified pSiRF was removed from the bacterial suspension or the LB medium and washed gently with the LB medium and Milli-Q water. Finally, the pSiRF was dried in a laminar flow cabinet for 1 h. For *in-situ* analysis, PLA-coated pSiRF sensors were inserted in a homemade flow cell (volume 0.3 mL) and incubated in the LB medium or the supernatant solution.

8.6 References

---

[1] MacFadden, D. R.; McGough, S. F.; Fisman, D.; Santillana, M.; Brownstein, J. S. Antibiotic Resistance Increases with Local Temperature. *Nature Climate Change* **2018,** *8* (6), 510–514. https://doi.org/10.1038/s41558-018-0161-6.

[2] Center for Disease Control and Prevention. Antibiotic Resistance Threats in the United States, *CDC Office of Infectious Diseases* **2019**, 19, 1-150. https://doi.org/10.15620/cdc:82532.

[3] Moore, J. L.; Caprioli, R. M.; Skaar, E. P. Advanced Mass Spectrometry Technologies for the Study of Microbial Pathogenesis. *Current Opinion in Microbiology* **2014**, 19, 45–51. https://doi.org/ 10.1016/j.mib.2014.05.023.

[4] Reece, P. J.; Gal, M.; Tan, H. H.; Jagadish, C. Optical Properties of Erbium-Implanted Porous Silicon Microcavities. *Applied Physics Letters* **2004,** *85* (16), 3363–3365. https://doi.org/ 10.1063/1.1808235.

[5] Alhusaini, Q.; Scheld, W. S.; Jia, Z.; Das, D.; Afzal, F.; Müller, M.; Schönherr, H. Bare Eye Detection of Bacterial Enzymes of *Pseudomonas aeruginosa* with Polymer Modified Nanoporous Silicon Rugate Filters. *Biosensors* **2022**, *12* (12), 1064. https://doi.org/10.3390/ bios12121064.

[6] Wang, J.; Lee, G. Y.; Kennard, R.; Barillaro, G.; Bisiewicz, R. H.; Cortez Lemus, N. A.; Cao, X. C.; Anglin, E. J.; Park, J. S.; Potocny, A.; Bernhard, D.; Li, J.; Sailor, M. J. Engineering the

---

Properties of Polymer Photonic Crystals with Mesoporous Silicon Templates.*Chemistry of Materials* **2017,** *29* (3), 1263–1272. https://doi.org/10.1021/acs.chemmater.6b04670.

[7] Krismastuti, F.S.H.; Bayat, H.; Voelcker, N.H.; Schönherr, H. Real Time Monitoring of Layer-by-Layer Polyelectrolyte Deposition and Bacterial Enzyme Detection in Nanoporous Anodized Aluminum Oxide. *Analytical Chemistry* **2015**, *87*, 3856–3863. https://doi.org/ 10.1021/ac504626m.

[8] Vichaibun, V.; Chulavatnatol, M. A New Assay for the Enzymatic Degradation of Polylactic Acid*. Science Asia* **2003**, *29*, 297. https://doi.org/10.2306/scienceasia1513-1874.2003.29.297.

[9] Yamashita, K.; Kikkawa, Y.; Kurokawa, K.; Doi, Y. Enzymatic Degradation of Poly(L-Lactide) Film by Proteinase K: Quartz Crystal Microbalance and Atomic Force Microscopy Study. *Biomacromolecules* **2005**, *6*, 850–857. https://doi.org/10.1021/bm049395v.

[10]. Dordi, B.; Schönherr, H.; Vancso, G. J. Reactivity in the Confinement of Self-Assembled Monolayers: Chain Length Effects on the Hydrolysis of Self-Assembled Monolayers of N-Hydroxy-Succinimide Ester Disulfides of Gold. *Langmuir* **2003**, *19*, 5780-5786. https://doi.org/ 10.1021/la0343066.

[11] Pham, V. H.; Nguyen, T. V.; Nguyen, T. A.; Pham, V. D.; Bui H. Nano Porous Silicon Microcavity Sensor for Determination Organic Solvents and Pesticide in Water. *Advances in Natural Sciences: Nanoscience and Nanotechnology* **2014,** *5* (4), 45003. https://doi.org/10.1088/2043-6262/5/4/045003.

[12] Salem, M. S.; Sailor, M. J.; Harraz, F. A.; Sakka, T.; Ogata, Y. H. Electrochemical Stabilization of Porous Silicon Multilayers for Sensing Various Chemical Compounds. *Journal of Applied Physics* **2006,** *100* (8), 83520. https://doi.org/10.1063/1.2360389.

[13] Pham, V. H.; Van Nguyen, T.; Nguyen, A.; Pham, V. D.; Bui, H. Nano Porous Silicon Microcavity Sensor for Determination Organic Solvents and Pesticide in Water. *Advances in Natural Sciences: Nanoscience and Nanotechnology* **2014,** *5* (4), 45003. https://doi.org/10.1088/2043-6262/5/4/045003.

[14] Salem, M. S.; Sailor, M. J.; Harraz, F. A.; Sakka, T.; Ogata, Y. H. Electrochemical Stabilization of Porous Silicon Multilayers for Sensing Various Chemical Compounds. *Journal of Applied Physics* **2006,** *100* (8), 83520. https://doi.org/10.1063/1.2360389.

[15] Engel, L. S.; Hill, J. M.; Caballero, A. R.; Green, L. C.; O'Callaghan, R. J. Protease IV, a Unique Extracellular Protease and Virulence Factor from *Pseudomonas aeruginosa*. *Journal of Biological Chemistry* **1998,** *273* (27), 16792-16797. https://doi.org/10.1074/jbc.273.27.16792.

[16] Galdino, A.C.M.; Branquinha, M.H.; Santos, A.L.S.; Viganor, L. *Pseudomonas aeruginosa* and Its Arsenal of Proteases: Weapons to Battle the Host. In: *Pathophysiological Aspects of Proteases*, Chakraborti, S., Dhalla, N., Eds.; Springer, Singapore, **2017**; 381–397. https://doi.org/10.1007/978-981-10-6141-7_16.

---

[17] Bowen, W. R.; Gan, Q. Properties of Microfiltration Membranes: the Effects of Adsorption and Shear on the Recovery of an Enzyme. *Biotechnology and bioengineering* **1992,** *40* (4), 491–497. https://doi.org/10.1002/bit.260400407.

[18] Hernandez-Pinzon, I.; Millan, F.; Bautista, J. Study of the Loss of Streptokinase Activity during Cross-Flow Microfiltration: I. Immunologic Approach. *Enzyme and Microbial Technology* **1995,** *17* (10), 911–914. https://doi.org/10.1016/0141-0229(94)00124-A.

[19] Laabei, M.; Jamieson, W. D.; Lewis, S. E.; Diggle, S. P.; Jenkins, A. T. A. A New Assay for Rhamnolipid Detection-Important Virulence Factors of *Pseudomonas aeruginosa*. *Applied Microbiology and Biotechnology* **2014,** *98* (16),7199–7209. https://doi.org/10.1007/s00253-014-5904-3.

[20] Thet, N. T.; Mercer-Chalmers, J.; Greenwood, R. J.; Young, A. E. R.; Coy, K.; Booth, S.; Sack, A.; Jenkins, A. T. A. SPaCE Swab: Point-of-Care Sensor for Simple and Rapid Detection of Acute Wound Infection. *ACS Sensors* **2020,** *5* (8), 2652–2657. https://doi.org/ 10.1021/acssensors.0c01265.

[21] Kaur, K.; Chelangat, W.; Druzhinin, S.I.; Karuri, N. W.; Müller, M.; Schönherr, H. Quantitative E. coli Enzyme Detection in Reporter Hydrogel-Coated Paper Using a Smartphone Camera. *Biosensors* **2021**, *11*, 25. https://doi.org/10.3390/bios11010025.

[22] Jia, Z.; Gwynne, L.; Sedgwick, A. C.; Müller, M.; Williams, G. T.; Jenkins, A. T. A.; James, T. D.; Schönherr, H. Enhanced Colorimetric Differentiation between *Staphylococcus aureus* and *Pseudomonas aeruginosa* Using a Shape-Encoded Sensor Hydrogel. *ACS Applied Bio Materials* **2020,** *3* (7), 4398–4407. https://doi.org/10.1021/acsabm.0c00403.

[23] Tücking, K.-S.; Vasani, R.B.; Cavallaro, A.A.; Voelcker, N.H.; Schönherr, H.; Prieto-Simon, B. Hyaluronic Acid-Modified Porous Silicon Films for the Electrochemical Sensing of Bacterial Hyaluronidase. *Macromol. Rapid Commun.* **2018**, *39*, e1800178. https://doi.org/10.1002/marc.201800178.

[24] Haas, S.; Hain, N.; Raoufi, M.; Handschuh-Wang, S.; Wang, T.; Jiang, X.; Schönherr, H. Enzyme Degradable Polymersomes from Hyaluronic Acid-blockpoly(ε-caprolactone) Copolymers for the Detection of Enzymes of Pathogenic Bacteria. *Biomacromolecules* **2015,** *16* (3), 832-841. https://doi.org/10.1021/bm501729h.

[25] Tam K.; Torres VJ. *Staphylococcus aureus* Secreted Toxins and Extracellular Enzymes. *Microbiol Spectrum* **2019,** *7* (2), 7.2.16. https://doi.org/10.1128/microbiolspec.GPP3-0039-2018.

Chapter 9. Summary and Conclusion

This Thesis focused on anodic aluminum oxide (AAO) and porous silicon rugate filter (pSiRF) nanoporous substrates and studied their potential use in biological contexts. The main aim was to modify these porous materials to generate functional nanocomposites that could potentially benefit enzyme or bacteria detection approaches. The AAO/pSiRF sensors were modified with a biodegradable polymer, i.e., poly(lactic acid) (PLA), to design a composite system to detect a bacterial enzyme. The fungal enzyme proteinase K was used as a model enzyme for proteases secreted, e.g., by *Pseudomonas aeruginosa (P. aeruginosa).* The AAO or pSiRF sensors modified with PLA were also tested in a bacterial environment.

Firstly, the AAO substrates were fabricated under optimized conditions to obtain homogenous circular pores with pore diameters and interpore distances ranging from 20 to 130 nm and 64 to 450 nm, respectively. The synthesized AAO samples obtained via the two-step anodization were well-ordered with hexagonal pore shapes. Next, the anodization parameters were adjusted, and the formed AAO was investigated. The pores of the synthesized AAO were widened in phosphoric acid. The FESEM data confirmed that the pore diameters increased linearly with the widening time. The pore diameter was widened from 32 nm to 85 nm after immersion in phosphoric acid for 35 min. The porosity was also calculated and was found to scale linearly with widening time. The pore length's dependence on the anodization time was also studied. AAO synthesized in oxalic acid at 40 V exhibited pores ranging from 1.6 to 12.8 µm in length when the anodization was conducted from 0.5 to 4.0 h.

The wetting and filling of the AAO pores were investigated using RIfS. The *EOT* value dramatically increased when the pores were filled with water. Based on the calculated and experimental Δ*EOT*, the pore filling was found to be 99.5 %. Later, it was proved that the pores of AAO were filled completely with water. Furthermore, the dependence of Δ*EOT* on the refractive index of the filling solution was studied in RIfS, showing a linear trend of *EOT* with the refractive index of the pore content. The wetting of AAO covered with a PLA sheet was also investigated. The top side of AAO was covered with a 350 ± 20 nm thin, free-standing PLA sheet. The PLA sheet was successfully prepared on a pre-treated Si wafer using the spin-coated method and transferred to AAO, which covers the top side with the exposed pore mouth. The impact of the PLA sheet on the wetting on AAO was evaluated using RIfS.

Two identical AAO samples were used for comparison, covering one with the PLA sheet. The RIfS was conducted during the infiltration of water into the pores. The data showed that the *EOT* measured on AAO covered with PLA gradually increased and reached a plateau after 35 min. In contrast, on the bare AAO (uncovered), the *EOT* increased rapidly and reached a plateau in a few seconds. The latter indicates that the pores were filled with water faster than in the case of covered pores, where the PLA sheet altered the filling of the pores, but did not affect the wettability of the pores, which was proven by the *EOT* values for these samples. The fabrication of pSi and pSiRF nanostructures was also performed. The etching process was optimized to obtain the desired structures. The electrochemical etching of pSi/pSiRF was carried out in HF/ethanol mixtures. Pore diameters scaled linearly with the current densities from 12 ± 4 to 63 ± 6 nm. Also, the length of the pores increased linearly with the etching time up to 8.04 ± 0.03 µm. The pSiRF sensors were successfully fabricated; the etching process was optimized by controlling the FWHM of the stop-band peak, the number of repeating cycles, and the period time. The result revealed that the narrow FWHM of the peak was obtained with a small current density. The data showed that with a 7 sec period time and repeated 100 cycles, an optimal pSiRF structure for the sensing protocol was prepared in this Thesis.

The deposition and enzymatic degradation of PLA on planar Si, AAO, and pSiRF were investigated. Firstly, the PLA deposition process on planar Si was performed using the spin coating. Ellipsometry showed that the dry thickness of the PLA film on a flat Si increased linearly with the PLA concentration. The water contact angle data confirmed the presence of the PLA on the surface due to the change in wettability. Moreover, the FTIR data were consistent with the ellipsometric and contact angle data where the PLA layer was successfully deposited on the Si surface. The carbonyl band area increased linearly with the dry PLA thickness.

For AAO sensors, two protocols were used to deposit PLA; one was done by spin coating and the other by the solvent casting method. The spin-coated PLA on the AAO sensor was examined using contact angle, FESEM, ATR-FTIR spectroscopy, EDX, and TGA. Different concentrations of the PLA solutions were used to ensure optimal pore coverage. The optimal PLA concentration was 5 wt% in chloroform, equivalent to ~ 300 nm film thickness estimated from FESEM images. The FTIR spectroscopy data revealed that a deviation from the linear dependence was observed as the PLA concentration increased. The TGA data also confirmed the presence of the PLA on the AAO. The EDX measurement was conducted on the coated AAO at four points along the AAO (from top to bottom). The EDX analysis confirmed the presence of PLA inside the pores and on the pore gate/top side of AAO, and it was concluded that the PLA was distributed along the pores, but the quantity of PLA was low in regions placed more profoundly into the pores. In the cast solvent approach, different concentrations of PLA solution were cast on AAO, followed by removing the PLA film from the top side of the AAO surface, leaving part of the PLA loaded into the pores. The FESEM data suggests that the PLA covered the AAO, and the consequent cleaning was successful. The cross-sectional FESEM also suggests the presence of PLA inside the pores. The volume fraction of the pores after PLA modification (pore filling) was determined based on the ΔEOT measured by RIfS and ΔEOT calculated by the Maxwell-Garnett equation. The data showed that the ΔEOT increased linearly with the pore filling.

The prepared pSiRF sensor was loaded with PLA using the solvent casting method. The PLA film was removed from the top side of pSiRF. The EDX, RIfS, and TGA data revealed that the PLA was successfully loaded inside the pores. After the comprehensive investigation of the presence of PLA on planar Si and AAO substrates, the enzymatic degradation of PLA on those substrates was investigated. The degradation was conducted using proteinase K. Firstly, the enzymatic degradation of PLA was tested on planar Si substrates. A reduction in dry thickness was observed with an increase in degradation time. Moreover, the contact angle showed a slight change in the wettability after the enzymatic degradation, with no further significant change in wettability throughout the degradation process. The FTIR data supported the ellipsometric data by showing a linear trend with the degradation time. FESEM and AFM were performed on the PLA film before and after degradation. The FESEM could not qualitatively differentiate between the PLA film before and after treatment with the enzyme, suggesting that the degradation was homologous on the entire surface. AFM could provide more information about the surface roughness, whereas the PLA film treated with the enzyme was rougher than the untreated one.

The enzymatic degradation of the spin-coated PLA on the AAO was then investigated. The FESEM data showed that the enzyme degraded the PLA film on the AAO surface, whereas the enzyme-free solution showed no degradation. The contact angle data also confirmed this process, where a significant reduction in the contact angle was observed before and after the degradation (from 73 ± 2 to 37 ± 3˚). The AFM data showed a slight increase in *Rq* value after immersion in the buffer solution for 300 min. The RIfS data exhibited that the *EOT* decreased after treatment with proteinase K due to the occurrence of the degradation of PLA film. PLA degradation in AAO pores (prepared using the solvent casting method) was conducted. The RIfS spectra showed a blue shift in the fringes with degradation time. The Δ*EOT* values also showed a blue shift with incubation time in proteinase K. The RIfS data revealed that the enzymatic reaction increased with enzyme concentration. Finally, the AAO sensor was tested in the sterile *P. aeruginosa* (PAO1) supernatant. The reaction was conducted in *in-situ* and *ex-situ* and monitored by RIfS. In both cases, the Δ*EOT* decreased when the AAO sensor was treated with *P. aeruginosa* supernatant compared to the LB medium. The last finding suggests that the AAO sensor could be used as a versatile sensor platform in the biological environment to detect bacterial enzymes.

Finally, the enzymatic degradation of PLA-modified pSiRF was investigated. The pSiRF sensor provides a visual detection approach to bacterial enzymes. The noticeable color shifts in the sensor, transitioning from blue to green, were observed when exposed to pure proteinase K solution, *P. aeruginosa* cultures, and their corresponding sterile-filtered culture supernatants. RIfS measurement exhibited that the wavelength in the pSiRF sensor shifted from 550 to 513 nm upon enzymatic degradation of PLA, resulting in the sensor returning to a blue color. The pSiRF sensor's color transition from green to blue could be detected by the naked eye after incubation in a suspension of *P. aeruginosa*, washing, and drying. The combined results of *ex-situ* and *in-situ* RIfS measurements, on the one hand, and the visual inspection of the photonic sensors, on the other hand, indicate that this principle may be utilized for sensing bacterial enzymes of clinically relevant bacterial pathogens.

This research lays the foundation for in-depth studies of the detection of bacterial enzymes employing porous structures combined with biodegradable polymers. For instance, using different biodegradable polymers may provide a deep understanding of the sensor's spontaneous response to different analytes or how varying pore morphologies affect sensor efficiency.

Acknowledgments

First and foremost, I am sincerely grateful to Prof. Dr. Holger Schönherr for giving me the opportunity to pursue my PhD in his group. He guided, advised, and supported me throughout my research studies. I am truly thankful for his encouragement and for keeping me motivated throughout my research and writing. In addition, I would like to express my gratitude to Prof. Dr. Ulrich Jonas for access to the ATR-FTIR instrument and to Dr. Maximilian Meier for performing ATR-FTIR measurements. Many thanks to Prof. Dr. Jörn Schmedt auf der Günne for access to the muffle furnace and M.Sc. Jamal N. M. Aman for the thermal treatment of porous silicon films. I would like to thank Prof. Dr. Xin Jiang for granting me access to the FESEM instrument, Dr. Yilmaz Sakalli, Dr. Thorsten Staedler, Dr. Marc Steuber, and Mrs. Petra auf dem Brinke for training and supporting me in using the FESEM. Also, I would like to thank Prof. Dr. Toby Jenkins (University of Bath, UK) for providing PAO1 (ATCC 15692). Thanks to Dr. Sergey Druzhinin, Dr. Stephanie Müller, Dr. Anna Schulte, Dr. Qimeng Song, and Dr. Daniel Wesner for scientific discussions. Special thanks to Dr. Mareike Müller, Dr. Zhiyuan Jia, M.Sc. Faria Afzal, and Dipl. Sabine Wenderhold-Reeb for helping in the bacteria lab and supporting the bacteria experiments. Additionally, I would like to express my thanks to the people who corrected my publication/Thesis, especially Dr. Mareike Müller, Dr. Lars Birlenbach, Dr. Mohammad Raoufi, Dr. Dipankar Das, M.Sc. Kawaljit Kaur, M.Sc. Aysha Awan, M.Sc. Winny Chelangat, M.Sc. Ernest Maina, M.Sc. Joshua Schumacher. Also, thanks to M.Sc. Aysha Awan and Dr. Anna Schulte for measuring some of my samples with FESEM and AFM, respectively. I want to thank Dipl.-Ing. Gregor Schulte and the mechanical workshop, especially Mr. Dieter Gaumann, Mr. Bernd Meyer, and Mr. Markus Rabe, for excellent technical support. Furthermore, I am grateful for the administrative support provided by Dr. Lars Birlenbach, Mrs. Sandra Johnson, and Mrs. Rosi Neidhardt. Many thanks to M.Sc. Walter Sebastian Scheld, M.Sc. Diana Hebel, Dr. Willis Collins Akeyo Muganda, M.Sc. Max Müller, M.Sc. Alexander Kleimann, M.Sc. Ratka Hoferick, and all members of the Physical Chemistry I group for the nice atmosphere during my study. Furthermore, this dissertation would not have been completed without the support of the German Academic Exchange Service (Deutscher Akademischer Austauschdienst, DAAD), the Iraqi Ministry of Higher Education and Scientific Research, and the University of Kufa. Part of this work was also performed at the Micro and Nanoanalytics Facility (MNaF) at the University of Siegen.

Finally, this dissertation would not have been possible without the support of my lovely wife, my parents, and my beloved children. You stood beside me throughout my study and encouraged me to overcome the difficult times. With your love, I will always be able to achieve my goals! Thank you!.